The History and Rate of Star Formation Within the G305 Complex

Alessandro Daniele Faimali

Centre for Astrophysics Research

University of Hertfordshire

A thesis submitted to the University of Hertfordshire in partial
fulfilment of the requirements of the degree of

Doctor of Philosophy

July 2013

The most exciting phrase to hear in science, the one that heralds new discoveries, is not "Eureka" but "Thats funny..." - Isaac Asimov.

Abstract

Within this thesis, we present an extended multiwavelength analysis of the rich massive Galactic star-forming complex G305. We have focused our attention on studying the both the embedded massive star-forming population within G305, while also identifying the intermediate-, to low-mass content of the region also. Though massive stars play an important role in the shaping and evolution of their host galaxies, the physics of their formation still remains unclear. We have therefore set out to studying the nature of star formation within this complex, and also identify the impact that such a population has on the evolution of G305.

We firstly present a *Herschel* far-infrared study towards G305, utilising PACS 70, 160 μm and SPIRE 250, 350, and 500 μm observations from the Hi-GAL survey of the Galactic plane. The focus of this study is to identify the embedded massive star-forming population within G305, by combining far-infrared data with radio continuum, H_2O maser, methanol maser, MIPS, and Red MSX Source survey data available from previous studies. From this sample we identify some 16 candidate associations are identified as embedded massive star-forming regions, and derive a two-selection colour criterion from this sample of $\log(F_{70}/F_{500}) \geq 1$ and $\log(F_{160}/F_{350}) \geq 1.6$ to identify an additional 31 embedded massive star candidates with no associated star-formation tracers. Using this result, we are able to derive a star formation rate (SFR) of 0.01 - 0.02 $M_\odot$ yr^{-1}. Comparing this resolved star formation rate, to extragalactic star formation rate tracers (based on the Kennicutt-Schmidt relation), we find the star formation activity is underestimated by a factor of ≥ 2 in comparison to the SFR derived from the YSO population.

By next combining data available from 2MASS and VVV, *Spitzer* GLIMPSE and MIPSGAL, MSX, and *Herschel* Hi-GAL, we are able to identify the low-, to intermediate-mass YSOs present within the complex. Employing a series of stringent colour selection criteria and fitting reddened stellar atmosphere models, we are able remove a significant amount of contaminating sources from our sample, leaving us with a highly reliable sample of some 599 candidate YSOs. From this sample, we derive a present-day SFR of $0.005 \pm 0.001\,M_\odot$ yr^{-1}, and find the YSO mass function (YMF) of G305 to be significantly steeper than the standard Salpeter-Kroupa IMF. We find evidence of mass segregation towards G305, with a significant variation of the YMF both with the active star-forming region, and the outer region. The spatial distribution, and age gradient, of our 601 candidate YSOs also seem to rule out the scenario of propagating star formation within G305, with a more likely scenario of punctuated star formation over the lifetime of the complex.

Acknowledgements

Firstly, I want to thank my supervisor, Mark Thompson, for giving me this opportunity to continue my interest in astronomy, and pursue a career in the field. Without this, I would have never had the chance to travel to some truly amazing places across the world, and experience some truly awe inspiring sights. Thank you for your continued support and advice throughout, always being available for a quick chat and sanity check, and putting up with my quasi-hermit presence, only to reappear with a stack of work to run past you.

To my friends, what can I say expect thanks for all the laughs! Both Jose, Mahesh, and Sunil have kept me sane through all these years; from stupidly long hours in the library as undergrads, to some of the most bizarre and comical chats we seems to have everyday! I don't think there could have been any other way that would have helped me through the low points, and kept all of us going.

To my mother and father, Laura and Daniele, I have nothing than my eternal thanks. Without both of you I could never have envisaged getting to where I am today; your unshakable support and love throughout has been at the bedrock of everything I have done. Since childhood you have always encouraged my love of science and astronomy, and helped develop my inquisitive nature, even when it led to some long and never-ending questions that you were always happy to listen to. Finally, I am eternally grateful to Gina for her loving support and patience, especially the patience! Be it having to travel to the other side of the globe, or locking myself away in my room to finish my thesis, you have always be so understanding and helped me throughout at every step.

Contents

List of Figures

List of Tables

Chapter 1

Introduction

"I thought I'd begin by reading a poem by Shakespeare, but then I thought, Why should I? He never reads any of mine." - Spike Milligan

1.1 Introduction

When we observe the night sky, the overwhelming feature we notice is the prevalence of stars within the great swathe of light that stretches from horizon to horizon; our Galaxy, the Milky Way. Its appearance as a stream of diffuse white light let the ancient Greeks to describe it as a river of flowing milk from Hera, the wife of Zeus. The very word "galaxy" derives from the Greek word for milk. It was not until 1610, that Galileo turned a telescope towards the Milky Way, and found that this great structure was comprised of a huge number of individual, faint stars, and the implication that the Milky Way was at heart a stellar system. Our Galaxy, like many others, comprises a large system of some 10^{11} stars, while also containing interstellar clouds of both gas and dust. We find that many of these stars are aggregated into clusters, themselves containing up to 10^5 stars within.

The study of stellar sources only truly became an empirical one from the middle of the last century. In 1945, Alfred Joy identified a sample of variable sources, residing within dark clouds, that exhibited highly irregular changes in their optical light curves, sometimes up to three orders of magnitude. It became clear that these sources represented a primitive phase for solar-type stars, that had condensed out of the dark clouds they were found to lay within. This new sample of stellar sources would go on to be known as T Tauri stars. This class of object was most commonly found within the constellations of Taurus and Auriga, and as such this stellar classification was named after the brightest in the sample, T-Tau (Joy, 1945). Through the mid 1950's, theories were beginning to be constructed, to model the pre-main-sequence evolutionary phases of a star (Herbig, 1952, 1957). The pace of scientific discovery rapidly increased through the 1970's, with the advent of infrared astronomy allowing us to peer into dust obscured regions (Mendoza V., 1968; Harper & Low, 1971; Cohen, 1973), while advances in millimeter dishes, X - ray observations, and the optical regimes have also contributed. By the 1980's, star formation was one of the most active fields of astrophysics (Neugebauer et al., 1984), with studies focusing on the chemical reactions in cloud environments (Benson & Myers, 1989), to the interiors of newly formed stars. This leads us to the present state of affairs where, for the formation of low-mass stars, an empirical framework of the various evolutionary stages is well established for solitary YSOs (Shu, Adams & Lizano, 1987; Shu et al., 1991), yet a similarly resilient theory for high-mass stars is still rather lacking.

We define a massive star as an OB star that has sufficient mass to produce a detectable HII region (i.e. $\mathrm{M}_* > 8\,\mathrm{M}_\odot$). They play a key role in the Universe; their presence has a profound affect on the stellar and planetary formation process, while also on the physical, chemical, and morphological structure of galaxies (Kennicutt, 2005). Their UV radiation output ionises the surrounding interstellar neighbourhood providing the principle source of heating in the ISM, while also having an impact on subsequent star formation. Through various process, such as stellar winds, and supernovae, their mechanical energy output serves as the energy and momentum inputs to the surrounding ISM, helping to sculpt the structure and energetics of the ISM, and hence the host galaxies (Zinnecker & Yorke, 2007).

Though they are important, in the shaping and evolution of their host galaxies, the physics of the formation and evolution of massive stars is unclear. Firstly, there is the issue of high dust extinction making direct observation difficult; with sites of massive star formation tending to be embedded within very opaque cloud cores, which suffer from visual extinction greater than 100 magnitudes (Bally et al., 2005). Related to this also, is the fact that massive stars are predominantly found to form within dense, stellar clusters (Minier et al., 2005). Massive stars also tend to be rare, on average with lifetimes of the order 10^6 - 10^7 yr. Their main-sequence lifetime is preceded by an embedded period, which is found to be roughly 15% of an OB stars lifetime, with the individual key evolutionary phases being short lived

To combat the difficulty in observing such environments, to which massive stars reside within, we can combine both sub-millimetre (sub-mm), infrared (IR), and radio observations to peer through the plentiful amount of dust and gas that obscures our other attempts to observe, in wavelengths such as the optical. Previous studies of star-forming regions have tended to suffer in two key areas: either a limited wavelength coverage, and/or an inadequate spatial resolution. This has lead to restricted studies of star-forming objects, on a case by case basis, which makes extrapolating such results across multiple sites of star formation in the Milky Way unwise. Only recently have improvements to instruments made such analysis a reality, allowing us to map entire star-forming regions in unprecedented resolution, across multiple wavelengths. These new studies will allow us to investigate the nature of star formation across numerous Galactic environments, the mechanism(s) involved, and the star formation history of Galactic complexes.

We dedicated the remainder of this chapter in reviewing the current knowledge of star formation, and lay out the scientific theory behind the study we have conducted, and present in this thesis.

1.2 The Initial Conditions Of Star Formation

Since they were first observed by Bok & Reilly (1947), molecular clouds have been recognised as the initial sites of star formation. Stars are comprised primarily of hydrogen, and the material to which they form from is contained within the interstellar medium (ISM); therefore it stands to reason that star formation will be contained within regions of dense concentrations of hydrogen. The ISM itself has a very low density, some one atom per cubic centimetre, therefore it is only within these dense clouds of hydrogen that gravity can play a significant role in

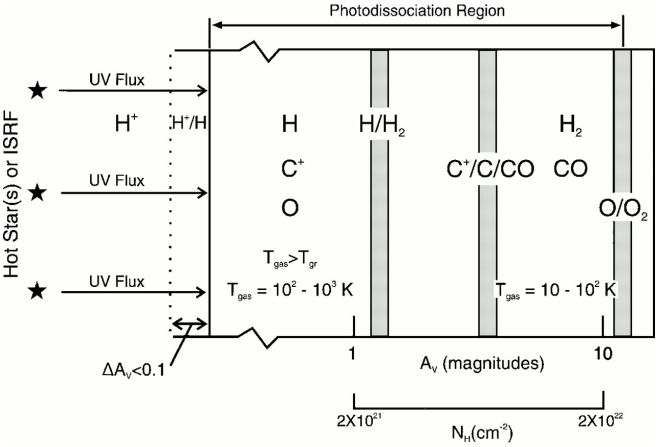

Figure 1.1: A schematic diagram of a photodissociation region (PDR); the PDR is illuminated from the left, with an atomic/ionised hydrogen surface. With increasing extinction, the transition from H/H_2 to $C^+/C/CO$ can be seen within the molecular cloud (Hollenbach & Tielens, 1997).

inducing collapse, and eventually star formation. The densest concentrations of hydrogen tend to be those of molecular hydrogen, H_2, and these molecular clouds are predominately located within the spiral arms of our Galaxy (Cohen et al., 1980); the term molecular clouds derives it's name from this high concentration of molecular hydrogen.

Molecular clouds tend to be comprised of both gas ($\approx 99\%$), and a small quantity of dust ($\approx 1\%$), of grain size $\approx 0.1\,\mu$m. The dust present within these regions comprises mostly of carbon and silicon, and tends to be cold, T 20 K, thus can be detected through thermal emission in the sub-mm; it's presence also aids in shielding the molecular environment from photoionising radiation. Given a high enough surface density, $n \approx 2 \times 10^{-3}\,\mathrm{g\,cm^{-2}}$ (Krumholz, McKee & Tumlinson, 2009), the dust and gas can provide a shielding mechanism to interstellar UV radiation allowing molecules to form; molecules such as carbon monoxide (CO), water (H_2O), ammonia (NH_3), hydroxide (OH), and hydrogen cyanide (HCN). The ionising radiation that hits the periphery of the molecular cloud destroys any present, and prevents further formation, of molecules, creating what is known as a photodissociation region (PDR); this surface layer is predominately ionised and atomic hydrogen, and the UV radiation is able to excite Polycyclic Aromatic

Hydrocarbons (PAH) emission (Fig.1.1).

Observationally, we can identify the properties of molecular clouds by observing the dust content rather than the gas, and then convert between the two, assuming a dust to gas ratio, typically a ratio of 100 is employed. The dust content within these clouds is also responsible for the scattering and absorption of radiation, and is known as the extinction, A_v. We can use this to produce extinction maps, taking advantage of the fact that any clouds, lying between the observer and background stars, will absorb both optical and near-IR emission, since absorption of shorter wavelengths are favoured. By measuring the colour excess of these background sources, we can deduce the extinction along the line of sight, and thus the dust properties of the cloud. Finally, the rich molecular chemistry that lies beyond the surface layer of the PDR can provide insights into the physical properties of the cloud; each molecule has a different set of excitation criteria required for formation, so the presence of certain molecular emission allows us to infer physical and chemical properties of the cloud.

1.2.1 Molecular Cloud Types

Molecular clouds comprise of a broad base of physical properties, from their densities (10^2 - 10^4 cm^{-3}), sizes (0.1 - 50 pc), mass (10 - 10^5 M$_\odot$), and temperature (0.1 - 50 K). Structurally, these clouds tend not to be spherical in nature, but rather have an irregular and filamentary structure, an example of this is shown in Fig.1.2 for the Eagle Nebula.

The physical properties are used to provide a classification scheme for clouds within our Galaxy, which are shown in Table 1.1; we use these classifications to discuss the properties of each cloud type below.

1.2.1.1 Bok Globules

At the low mass end we find dark globules, also known as Bok globules, named after the astronomer who first observed them. They are observed as small patches of visual extinction in the night sky, and appear relatively isolated structures; their properties resemble those of dense cores located within larger complexes, and as a result, are believed to be sites of only low mass star formation. A

Figure 1.2: A three-colour image of the Eagle Nebula (M16), from the *Hubble Space Telescope*, taken in 2004. The structure is about 3 pc high, at a distance of 1800 pc.

Table 1.1: The physical properties of molecular clouds (Stahler & Palla, 2005).

Cloud Type	A_v (mag)	$n_{\rm tot}$ (cm^{-3})	L (pc)	T (K)	M ($M_\odot$)
Bok Globules	10	10^4	0.1	10	10
Diffuse Clouds	1	500	3	50	50
Dark Cloud Complexes	5	500	10	10	10^4
Giant Molecular Clouds	2	100	50	15	10^5

well-studied example of a Bok globule is that of B335; being at a distance of 250 pc, and consisting of a visually opaque core of 11 $M_\odot$ with an associated elongated envelope of 22 $M_\odot$ also (Frerking, Langer & Wilson, 1987). Near the peak intensity of the cloud, a far-IR star of 3 $L_\odot$ is found, which is driving an extended molecular outflow.

1.2.1.2 Diffuse Clouds

Further up in the mass scale we have the structures known as diffuse clouds. These tend to be isolated structures, that comprise of similar amounts of both atomic and molecular hydrogen. Within such clouds, the extinction is found close to unity, allowing the majority of background stellar emission to traverse through these clouds; absorption lines, particularly in the UV, have proved useful in studying the molecular abundances and chemical environment. These structures do represent a minor fraction of interstellar gas, and there is no evidence to suggest they support star formation (Welty et al., 1999).

1.2.1.3 Dark Cloud Complexes

Moving up in the mass scale, we reach dark clouds, which are similar to Bok globules in that they are observed as patches of visual extinction, yet are found at greater masses. A well known example of this subtype is the Taurus-Auriga molecular cloud; measuring some 30 pc across, at a distance of 140 pc, the complex is found in a collection of molecular clouds that are collectively known as the Gould belt. The complex has been studied in detail by many authors (Ungerechts

& Thaddeus, 1987; Kenyon et al., 1990; Abergel et al., 1994; Mizuno et al., 1995), and what is found is a total molecular mass of $10^4\,\mathrm{M}_{\odot}$ with no signs that indicate the presence of massive O and B stars forming within. Studies have identified young stars, with luminosities of $\approx 0.5\,\mathrm{L}_{\odot}$ indicating that the region is in fact a low-mass star forming complex.

1.2.1.4 Giant Molecular Clouds

Found at the top end of the mass scale, giant molecular clouds (GMCs) are the behemoths of the molecular cloud types. It is within these complexes, that high-mass star formation is favourable, with the sheer size of the clouds being conducive to gravitational collapse. Within the Milky Way, up to 80 % of the molecular hydrogen content resides within GMCs (Stahler & Palla, 2005). As a structure, they comprise of smaller units of clumps, that themselves range in masses of $10 - 10^3\,\mathrm{M}_{\odot}$, sizes of 0.5 - 3 pc, and densities of $10^3 - 10^5\,\mathrm{cm}^{-3}$ (Shu, Adams & Lizano, 1987). A well known example of GMCs is that of the Orion GMC; at a distance of $\approx 400\,\mathrm{pc}$, and mass of $10^5\,\mathrm{M}_{\odot}$. This GMC is a site of high-mass star formation, where O and B stars have been forming over the last $10^6\,\mathrm{yr}$ (O'dell, 2001).

1.2.2 The Formation And Evolution Of Molecular Clouds

The formation of GMCs is still an issue of contention, with no clear mechanism identified, let along to being to consider the role that gravity, magnetic fields, and radiation have in the formation process also. The theory of their formation is marked with either a "bottom-up" or "top-down" process. In the bottom-up scenario, smaller clouds are thought to combine via inelastic collisions (Dobbs & Pringle, 2013; Dobbs, Pringle & Burkert, 2012; Kwan, 1979); this process would be rather slow, and as a result, the destructive processes associated with star formation would prevent the further growth of the GMC, once the first generation of star formation had begun. The second top-down scenario, seems the likelier of the two, involves the formation of GMCs via large scale, self-gravitating instabilities within the ISM (Dobbs & Pringle, 2013; Dobbs, Pringle & Burkert, 2012; Elmegreen, 1979); either compression of the ISM via supernovae and expanding

HII regions, and large-scale gravitational instability in the galactic disk (spiral wave shocks) have been put forward as mechanisms for these self-gravitating instabilities (Dobbs, 2009; McKee & Ostriker, 2007).

GMCs tend to be unbound, temporary structures, that exist for $\approx 10\,\mathrm{Myr}$ (Leisawitz, 1990); this would be backed up by the low star formation efficiencies that are observed for GMCs, some 1 - 2% (Vázquez-Semadeni, 2010). GMCs do not exhibit uniform density, but rather a hierarchical structure that can be described as fractal (Stutzki et al., 1998); sub-structures with masses of $\approx 100\,\mathrm{M}_{\odot}$ and a few parsecs in size are known as clumps, further sub-structures of $1 - 10\,\mathrm{M}_{\odot}$ with sizes in the region of 0.5 pc are known as cores. The evolution of such a structure goes through broad phases of cloud formation, formation of clumps and core, the gravitational collapse of sub-structures that leads to protostellar formation, and the eventual dispersal of the complex following star formation.

We find that with the most massive and dense GMCs, all have some tracer of formation apparent, while some 10% of GMCs within the Milky Way have no associated signs of star formation occurring within (Murray, 2011; Dobbs & Pringle, 2013). Statistically, this would suggest that these clouds were young, 3 Myr, and that there is only a short period of time between the formation of a cloud and the subsequent star formation activity within. What is also unclear, with regards to the evolution of a GMCs, is the part that the first generation of star formation has on succeeding generations; particularly how star formation propagates within a GMC on local levels, and whether tiggering mechanisms from this initial massive stellar generation either aids or inhibits further formation (Blitz, 1993). Clearly this issue and the clumpy, hierarchical nature of GMCs, are fundamental areas that need further study and understanding with regards to star formation.

1.2.3 Interstellar Dust

The total mass of molecular clouds consists primarily of molecular hydrogen, yet they also contain a small fraction of dust, around 1% in total. Though there is a clear dominance in the mass of molecular clouds, fundamentally molecular hydrogen remains invisible at optical, infrared, and sub-mm wavelengths; it is the small presence of dust that is responsible for the observed scattering, and absorption of this radiation.

When considering the properties of dust, the key factors include: *i)* the shape of the dust grain, *ii)* the size distribution of the particles, *iii)* chemical composition; it is a combination of these properties that dictate the extinction and absorption of dust. It is thought that dust grains consist mainly of particles of graphite, silicates and amorphous carbons, which can then stick together, forming larger grain sizes between 0.01 - 0.25 μm (Mathis & Whiffen, 1989). The presence of dust grains can lead to the absorption and scattering of radiation in the both the optical and UV, this effect is known as interstellar extinction. Extinction can render a cloud opaque, yet fortunately this phenomena is wavelength dependent, meaning clouds become increasingly transparent at longer wavelengths; this allows us to observe objects embedded within, and background stars to be observed also. Aside from this, astronomers have also to contend with interstellar reddening. The presence of dust leads to strong absorption and scattering of shorter wavelength radiation (i.e. blue light), while the transmission of longer wavelength radiation (i.e. red light) is unaffected; the result being that observed stars appear redder than they in fact are.

The interstellar extinction observed along a given line of sight can be determined through observations of background stars; using the extinction curve between 0.11 - 1 μm, Mathis, Rumpl & Nordsieck (1977) determined the size distribution and grain composition of dust grains. By assuming spherical grains, it was found that the interstellar extinction could be accounted for by two dust grain distributions, one of which being graphite with a size distribution of 0.005 - 1 μm; the second distribution being accounted for by grains of sizes 0.025 - 0.25 μm. Within the interstellar extinction curve, a broad 10 μm absorption feature is seen, suggesting the presence of a non-graphite composition of dust; this feature being accounted for by SiO bending and vibration modes of silicates, which accounts for the second dust grain distribution. As a result of this, the composition of interstellar dust is favoured by a mix of graphite and silicate particles. This composition is challenged however, particularly whether graphite does indeed constitute a major component of the dust composition. One issue with importance placed on graphite can be observed from carbon stars, which themselves are known major producers of the carbon component of interstellar dust. Results from Jura (1986) found that dust grains, within the circumstellar envelopes of carbon stars, are found to be in amorphous form rather than graphitic. Taking this result, it seems difficult to determine a mechanism for amorphous carbonaceous grains ejected from these stellar envelopes to be processed into layer-lattice graphitic structures in interstellar space (Li & Greenberg, 2003). In addition to this, the failure to detect graphite in the solar system, in bodies such as comets and meteorites, has cast some doubt on whether graphite is a major constituent of interstellar dust (Pollack et al., 1994).

We also observe within the interstellar medium, a series of unidentified infrared emission (UIR) bands, with emission lines observed at 6.2, 7.7, 8.6, and 11.6 μm; these features are now known to originate from polycyclic aromatic hydrocarbon (PAH) molecules (Leger & Puget, 1984a; Allamandola, Tielens & Barker, 1985). PAHs are found to be smaller than dust grains, being large carbon molecules of some 50 - 1000 carbon atoms in ring-like structures, that are excited by the absorption of a single UV photon and tend not to be in local thermal equilibrium (Sellgren, 1984). We find that when temperatures exceed $\approx$1000 - 2000 K within these environments, both silicate, graphite, and amorphous carbon dust grains are found to sublimate (Duschl, Gail & Tscharnuter, 1996). As a result, we can describe the properties of dust grains through the extinction of starlight through the ISM or clouds at UV, optical, and infrared, while we can also study dust via emission features at infrared wavelengths; where significant UV flux is observed we can extend the grain distribution down to PAH molecules that reveal their presence in the mid-IR.

Dust grains also play a key part in the environments of molecular clouds, and protostellar cores, where grain growth through coagulation (Ossenkopf, 1993) leads to an increase in the opacity at sub-mm wavelengths (Ossenkopf & Henning, 1994). In addition to this, dust grains play an important role in enhancing the chemistry of clouds, through the ‘freezing’ of molecules onto the surface of grains, leading to the production of ice ‘mantles’. Within the dense regions of molecular clouds, dust grains are shielded from interstellar UV radiation, and as a result various types of ices can form on the outer layers of dust grains, such as H_2O, CO, CO_2, molecular hydrogen, methane, and ammonia. Both ammonia and water ice constitute the bulk of the mantles observed, with the abundance of ammonia only a few percent of water (Whittet, 1992); a strong absorption feature at 3 μm is observed for all dark clouds with $\mathrm{A}_V \geq 3.0$ mag (Whittet et al., 2004). Such molecules evaporate when temperatures of ≈ 100 - 200 K are reached (Fraser et al., 2001), and prove valuable tools for mapping the structure of molecular clouds and protostellar cores, in providing information on internal mass, density, and temperature.

1.3 Star Formation

In the following sections we outline the initial stages, and physical processes of, both low-, and high-mass star formation, however it is first ideal to define what a star is, and how are stars defined in mass regimes. We define a star as a body that satisfies two criteria: *i)* a body bound by self-gravity; *ii)* a body that radiates energy, which is supplied by an internal source. The first condition implies that the shape of such a source would be spherical, with gravity being a spherically symmetrical force field. Secondly, the source of internal energy emanates from thermonuclear reactions that occur deep within the stellar interior, and sometimes also gravitational potential energy released in contractions or collapse. A star must produce energy in order to maintain hydrostatic equilibrium, with the force of gravity acting towards the centre of mass being balanced by the internal radiation pressure. In equilibrium, the forces of gravitation and pressure are in exact balance, giving us the equation of hydrostatic equilibrium:

$$\frac{dP}{dr} = -\rho \frac{GM_*}{R_*^2} \tag{1.1}$$

where G is the gravitational constant ($6.673 \times 10^{-11}\,\mathrm{m}^3\,\mathrm{kg}^{-1}\,\mathrm{s}^2$), M_* is the mass of the star, ρ is the stellar density, and R_* is the stellar radius.

The structure, and evolution of stars, are therefore dictated by these two factors: gravity, tending to collapse the star; pressure, tending to expand the star. Eventually, the demise of a star will be the result of these two conditions; violation of self-gravity, with the star ending in a violent breakup and scattering of material into interstellar space, or the gradual depletion of the internal energy source that causes the star to slowly fade away, and cool off. Gravitation is initially responsible for the formation of stellar sources from protostellar material, and it is ultimately because of gravitational collapse that it is responsible for stellar destruction.

Stellar classification is most easily grouped according to stellar mass, which itself has implications for stellar temperature and luminosity, and as a result greatly affects the structure, formation, and evolution of a star. Using the stellar mass, we can group sources into three classification groups: low-mass, intermediate-mass, and high-mass stars. In general, these three categories follow mass intervals of: $0.1 \leq \mathrm{M}_{*} < 2\,\mathrm{M}_{\odot}$ for low-mass stars, $2 \leq \mathrm{M}_{*} \leq 8\,\mathrm{M}_{\odot}$ for intermediate-mass stars, and finally $\mathrm{M}_{*} > 8\,\mathrm{M}_{\odot}$ for high-mass stars.

1.3.1 Fragmentation In Star Formation

The concept of fragmentation and collapse of cores, to form protostars, is not a new concept; Jeans (1902) first proposed that gravity can amplify any small perturbations present within a uniform medium. A molecular cloud will remain in hydrostatic equilibrium until any density enhancements begin to attract additional mass, through gravitation, and grow into an over-dense region. We define the minimum mass to overcome the conditions of hydrostatic equilibrium and collapse as the Jeans mass, M_J, and the minimum scale for gravitational fragmentation as the Jeans length, λ_J. In the case of an isothermal sphere, of uniform density, we can define:

$$M_J \,=\, 1.0\,M_{\odot}\left(\frac{T}{10\,K}\right)^{\frac{3}{2}}\left(\frac{n_{H_2}}{10^4\,cm^{-3}}\right)^{-\frac{1}{2}} \tag{1.2}$$

While, we also have:

$$\lambda_J \,=\, 0.19\,\mathrm{pc}\left(\frac{T}{10\,\mathrm{K}}\right)^{\frac{3}{2}}\left(\frac{}{10^4\,\mathrm{cm}^{-3}}\right)^{-\frac{1}{2}} \tag{1.3}$$

Once the criteria are met, a molecular cloud will begin to collapse, breaking ever smaller fragments. As this collapse continues, both the temperature and pressure will increase, and the fragments will become optically thick; making them less efficient at radiating away the potential energy as heat, meaning that further collapse is inhibited (Blitz, 1993; Williams, Blitz & McKee, 2000). This fragmentation process of a molecular cloud leads to the observed structure of filaments, and irregular clumps; globally the temperature remains roughly constant, while density increases locally, meaning that within these filamentary structures we find clumps known as molecular cores, where the Jeans conditions are satisfied locally, and star formation can take place. One of the issues with collapse is the effect that many physical processes, including rotation, turbulence, magnetic fields, radiation pressure etc., can have on collapse, and the need to include these effects when attempting to simulate the initial conditions and collapse of molecular clouds. Another issue regarding the Jeans mass concerns density perturbations that exceed the Jeans length; in such a scenario these perturbations grow exponentially, meaning that at the largest scales we observe the fastest growth rates, hence the quickest collapse rates. The direct result of this faster collapse, at the largest scales, means fragmentation into smaller pieces becomes much more difficult (Larson, 1985). These smaller sub-structures are known as clumps, and are self-gravitating structures where star clusters are likely to form. Taking this one step further, these clumps have densities of the order of 10^3 - $10^5\,\mathrm{cm}^{-3}$, and have an associated Jeans length $\lambda_J \approx 0.01\,\mathrm{pc}$. These smaller subdivisions are known as molecular cores, and are found to be the densest parts within molecular clumps; average densities of 10^5 - $10^7\,\mathrm{cm}^{-3}$, and it is within these dense cores that a star or stellar system will form.

1.3.2 The Clump/Core Mass

One of the physical properties that we derive from the modified blackbody fitting is the total mass (gas + dust) for each source (see Section 3.3.2), were we obtain the mass following the approach of Hildebrand (1983).

We firstly consider an idealised cloud, comprised of spherical dust grains, of uniform size, composition, and temperature. This cloud is found to be optically thick to stellar radiation, but optically thin to far-IR emission, and is heated by internal processes. The flux density, F_ν, from this cloud at distance D containing N spherical dust grains of cross-section σ, temperature T, and emissivity Q_ν is given by:

$$F_\nu \,=\, \left(\frac{N\, Q_\nu\, B_\nu(T)\, \sigma}{D^2}\right) \tag{1.4}$$

The volume of dust is given by:

$$V \,=\, N\, v \tag{1.5}$$

where v is the volume of an individual dust grain. By substituting for N we have:

$$V \,=\, \frac{F\, v\, D^2}{\sigma\, Q_\nu\, B_\nu(T)} \tag{1.6}$$

If we assume a grain density of ρ, then we have that $V \,=\, M/\rho$, meaning that:

$$M_d \,=\, \frac{F_\nu\, D^2}{B_\nu(T)\, Q_\nu}\, \frac{v}{\sigma}\, \rho \tag{1.7}$$

We can state that $v \,=\, 4/3\, \pi\, a^3$, and that $\sigma \,=\, \pi\, a^2$, where a is the dust grain radius (typically $\approx 1\, \mu$m or smaller) then:

$$M_d \,=\, \frac{F_\nu\, D^2}{B_\nu(T)\, Q_\nu}\, \frac{4/3\, \pi\, a^2}{\pi\, a^2}\, \rho \tag{1.8}$$

$$M_d \,=\, \frac{F_\nu\, D^2\, 4/3\, a\, \rho}{B_\nu(T)\, Q_\nu} \tag{1.9}$$

The above result is the dust mass, however we wish to determine the clump/core mass. Therefore, we need to take into consideration that typically the ISM is composed of 99 % gas, and 1 % dust. To account for this we introduce the dust mass coefficient, C_ν, to obtain a clump/core mass of M_c. We next introduce the ratio $M_g \,/\, M_d$, the gas to dust mass, where $M_g \,\approx\, M_{cloud}$, then we have that the clump/core mass is:

$$M_c \,=\, \frac{F_\nu\, D^2\, 4/3\, a\, \rho}{B_\nu(T)\, Q_\nu}\, \frac{M_g}{M_d} \tag{1.10}$$

where:

$$C_\nu \,=\, \frac{4/3\, a\, \rho}{Q_\nu}\, \frac{M_g}{M_d} \tag{1.11}$$

The value of C_ν is typically a power law in frequency, and allows us to convert between quoted values at various frequencies using (Kerton et al., 2001):

$$C_\nu = C_{\nu_0} \left(\frac{\nu_0}{\nu}\right)^\beta \tag{1.12}$$

This produces the final function to derive the clump/core mass for each source:

$$M = \frac{F_\nu D^2}{B_\nu(T)} C_\nu \tag{1.13}$$

1.4 Low-Mass Star Formation

The formation of stars in different mass regimes is believed to happen by different mechanisms, and in the case of low-mass stars, the process is fairly well understood (Shu, Adams & Lizano, 1987; Shu et al., 1991). The initial process involves the fragmentation of clumps within a molecular cloud, and how dense cores form from the result of this; it is within these cores that star formation begins.

Initially, gravitational forces acting towards the centre of the core are counterbalanced by rotation, thermal pressure, and weak magnetic fields. Over time this balance is lost, and the central region begins to increase in density and temperature, leading to the ‘inside-out’ collapse of the core, with the collapse forced outwards as a front travelling at the speed of sound through gas. The core now increases in rotation, forming a spherical core with an accompanying, slower rotating, extended envelope of gas and dust. At this stage, the core is a pre-protostellar core.

What follows is an accretion phase, in which the material within this extended envelope falls down onto the pre-protostar, and slowly raises the temperature of the source. As the temperature increases to around 2000 K, molecular hydrogen begins to dissociate into its atomic counterpart, disrupting hydrostatic equilibrium, and forcing the core to collapse further to restore equilibrium. The core has yet to attain all of it’s final mass, with the majority still held within the surrounding envelope. The core is now know as a protostar, and can be observed at infrared wavelengths.

The continued collapse leads to an increase in the rotation of the core and the surrounding envelope, and the conservation of angular momentum results in the infalling material being pushed out to form a dusty circumstellar disk, which continues to accrete mass onto the protostar. The emergence of highly collimated jets and flows along the polar axes of the protostar, known as bipolar outflows, marks the shift of angular momentum dissipating into the surrounding medium.

Once the source has accreted sufficient mass, and a central temperature of $\approx 10^6\,$K is reached, the protostar can begin burning deuterium; the source is now considered a pre-main-sequence star, or T Tauri star, and is optically visible. The surrounding material has been exhausted through accretion or dispersed by the bipolar outflows, and the remnants of the circumstellar disk are slowly dissolved away by both stellar winds, and the radiation pressure of the star as it evolves towards the main-sequence.

1.4.1 The Evolutionary Stages Of Low-Mass Star Formation

The evolution of low-mass young stellar objects (YSOs) has been observationally divided into four distinct stages, according to the changes present within their SEDs. The term YSO refers to a stellar object whose luminosity is derived from accretion, as opposed to a traditional stellar source that relies on nuclear process to drive it's luminosity. These four distinct stages represent protostellar phases (class 0 and I), a classical T Tauri star (class II), and a weak T Tauri star (class III).

Lada (1987) first defined the evolution of the low-mass SED, based on the variation of the spectral index of a source's emission, between 10 - 100 μm. The three evolutionary phases were defined according to:

$$a = \frac{d\,log(\lambda\,F_\lambda)}{d\,log(\lambda)} \tag{1.14}$$

where for a class I source, $0 < a \leq 3$, class II represented by $-2 \leq a \leq 0$, and class III for $-3 \leq a \leq -2$.

A further evolutionary stage was proposed by Andre, Ward-Thompson & Barsony (1993), which corresponded to an earlier stage than those of Lada (1987),

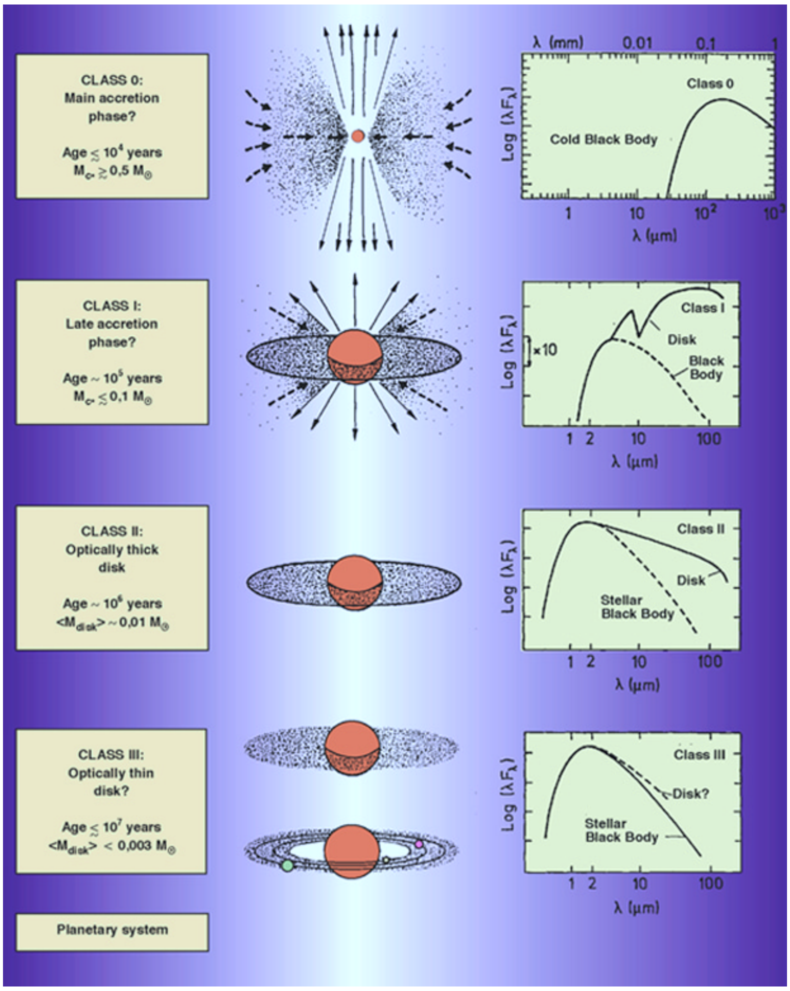

Figure 1.3: A schematic illustration of the evolutionary stages of low-mass star formation (Fuente, 2001).

for a class of protostars detected in the sub-mm with a ratio of $L_{sub-mm}/L_{bol} > 5 \times 10^{-3}$; this indicated a new class of object, placed ahead in the evolutionary phases of Lada (1987).

The final proposed evolutionary phases of low-mass star formation are shown in Fig.1.3, and we outline the observational stages below:

- *Class 0*: This is a protostar, which has formed a hydrostatic core, but has yet to accumulate the majority of its final mass; some half of the final mass remains in the circumstellar envelope. The SED is best described by a blackbody, with temperatures of 20 - 30 K, and is characterised by a strong peak in emission at sub-mm wavelengths ($\lambda > 100\,\mu$m). Many class 0 sources are associated with bipolar outflows, that signify the non-spherical nature of infall, and that disk-like structures have begun to form; from the angular momentum excess in the core.
- *Class I*: At this stage, the source is said to be a relatively evolved protostar ($\approx 10^5$ yr), while continued accretion has increased the dust temperature, pushing the peak emission towards $\lambda \approx 100\,\mu$m. Residual rotation causes the infalling material to form into an accretion disk, while continued bipolar outflows and jets transfer excess momentum and energy into the surroundings. The SED is now characterised by a 50 - 100 K blackbody component from the accreting envelope, while a further 200 - 400 K component that originates from the accretion disk is observed too. A silicate absorption feature at 10 μm is observed, indicating an optically thick envelope of dust. At this stage, the source has accreted more than half the total mass of the circumstellar envelope, onto the protostellar core.
- *Class II*: After $\approx 10^6$ yr the majority of the circumstellar material has either been accreted onto the star, or a combination of winds and bipolar outflows have swept the material away, exposing the circumstellar dusty disk (also known as a proto-planetary disk, from where planets may possibly form). As a result of this material clearing, the central pre-main-sequence core is exposed, and tends to be visible in the optical and near-IR; this object is typically known as a classical T Tauri star. The SED now peaks at $\approx 2\,\mu$m,

while flux longward of this peak is dominated by emission from the dusty circumstellar disk; which is found to be optically thick at $\lambda \leq 10\,\mu$m.

- *Class III*: Finally, these sources are observed as stars in the near-IR and optical, where their SED is found to peak. Some circumstellar material may still be present, in the form of an optically thin disk, however the SED is best described by a reddened blackbody, of little to no IR excess emission. This SED is consistent with a reddened stellar photosphere, of a star on the zero-age-main-sequence stage.

1.5 High-Mass Star Formation

As mentioned earlier, gravitation is the major factor in the creation of stars, with the gravitational contraction of interstellar clouds of gas and dust being the birthplace of new stars. The major factor that distinguishes low-mass stars, and high-mass stars, is the timescales over which they form. If gravity was the sole force acting on a cloud, then the timescale for collapse would be defined by the free-fall time (Shu, Adams & Lizano, 1987):

$$t_{\mathrm{ff}} = \left(\frac{3\pi}{32G\rho}\right)^{1/2} = 3.4 \times 10^{7}\, n^{-0.5} \quad (\mathrm{yr}) \tag{1.15}$$

where G is the gravitational constant, ρ is the average density, and n is the number density. Typically, for a molecular cloud, the number density $n \geq 50\,\mathrm{cm}^{-3}$, leading to a free-fall time $\mathrm{t_{ff}} \leq 5 \times 10^{6}$ yrs, which sets a lower limit to the timescale of stellar evolution.

As this mass of gas contracts under self-gravity, we have a conversion from gravitational potential energy to thermal and radiative energy; the timescale to which this occurs is known as the Kelvin-Helmholtz timescale. This timescale provides an estimate for the time taken for a star to evolve towards temperatures sufficient for fusion reactions within, known as the pre-main-sequence phase:

$$t_{\mathrm{KH}} \approx \frac{GM_{*}^{2}}{R_{*}L_{*}} \quad (\mathrm{yr}) \tag{1.16}$$

where R_{*} is the stellar radius, and $L*$ is the stellar luminosity.

From this timescale we can see for a star of $1\,\mathrm{M}_\odot$ such as our Sun, the time is exceptionally long, at $t_{\mathrm{KH}} \approx 3 \times 10^7$ yrs, which implies that $t_{\mathrm{KH}} > t_{\mathrm{ff}}$, and stars evolve onto the main-sequence once they have accreted all their material; the case found for the majority of stars. However, for a high-mass O6 star of $40\,\mathrm{M}_\odot$ for example, that timescale would result as $t_{\mathrm{KH}} \approx 2.5 \times 10^4$ yrs. The implication is that high-mass stars have a $t_{\mathrm{KH}} < t_{\mathrm{ff}}$, meaning that such stars will reach fusion ignition before gravitational collapse has ceased. This has important implications for star formation via accretion, specifically how do massive stars continue to accrete mass while also undergoing nuclear fusion that itself produces radiation pressure that will prevent further collapse. Placing the mechanics aside, we are aware of massive stars in the order of $\approx 300\,\mathrm{M}_\odot$ that are observable (Crowther et al., 2010), and have $t_{\mathrm{KH}} < t_{\mathrm{ff}}$, so the question remains as to how these sources exist.

1.5.1 Possible Formation Mechanisms

The formation of high-mass stars is less understood than their low-mass brethren; the process is thought to differ considerably from that of low-mass stars. As we showed earlier, if we simply try to scale-up the mechanisms of low-mass star formation we hit the issue of feedback affecting the formation mechanisms for high-mass stars. The protostellar object will reach a stage where it is still accreting material, yet has reached the main-sequence, and consequently both radiation pressure and associated stellar winds can slow or even halt further accretion from the surrounding envelope (Davies et al., 2011; Wolfire & Cassinelli, 1987). This should, theoretically, place an upper limit on the stellar mass that can be assembled, but as discussed earlier, we observe stars with $\approx 300\,\mathrm{M}_\odot$. Clearly, a vanilla accretion and infall mechanism can explain the assembly of low-, to intermediate-mass stars, yet falls short for the high-mass regime.

High-mass stars are preferentially formed within dense regions of giant molecular clouds, these dense regions known as cores tend to mass $\approx 100\,\mathrm{M}_\odot$, and sizes of $\leq 0.1\,\mathrm{pc}$ (Kurtz et al., 2000; Zinnecker & Yorke, 2007). The formation of high-mass stars is less understood that low-mass stars due to a multitude of reasons. Firstly, high-mass stars are rare (due to the steep mass dependence in the IMF), and also tend to spend far less time in their protostellar phase, evolving far more quickly than low-mass stars. High-mass stars also tend to form deep within dense molecular clouds, where the optically thick layers of dust and gas obscures direct observation. In addition to this, we find that these regions tend to be at much greater distances, making the task of resolving out the stellar population far more challenging. Finally, high-mass stars tend to cluster in formation; one star-forming region may contain several stars at differing stages of evolution. The processes involved in their evolution, such as outflows and stellar winds, may disrupt the evolution of their younger compatriots, making decoupling this feedback from the natural evolution of high-mass stars a difficult task.

Three mechanisms have been put forward as the theoretical model which defines the mechanism of high-mass star formation, and overcomes the limitations mentioned above. We outline the details of these models below.

1.5.1.1 Monolithic Collapse

This proposed model is essentially a scaled up version of low-mass star formation (Shu, Adams & Lizano, 1987), yet with much higher accretion rates. In this method, high-mass stars form via the accretion of gas from a rotationally supported disk, which results from conservation of angular momentum.

The molecular core collapses under self gravity, with the gravitational force acting centrally but being counterbalanced through numerous means, such as rotation and thermal pressure. Over time this balance is lost, thereby causing the central density to increase, resulting in a collapse that is forced outwards. Accretion from this extended envelope falls onto the central star, while residual angular momentum in the infalling material causes the extended envelope to spin into a circumstellar disk. This process is accompanied by radiation jets along the polar axis, as angular momentum is cast off into the surroundings. The resulting final mass of the star is therefore determined by the mass of the collapsing molecular core; the meaning being that a high-mass star would directly form from a high-mass molecular core (McKee & Tan, 2003).

There are two main limitations to this model however: *i)* The requirement for high accretion rates to overcome the shorter evolution timescales of high-mass stars; *ii)* Prevention of further fragmentation of molecular cores into sites of low-mass protostars (Bonnell, Vine & Bate, 2004). In regards to limitation *i)*, assuming spherical accretion will limit the the mass reached by the central source. However, much work has been recently conducted on this point, utilising three-dimensional simulations to model the collapse of a massive pre-stellar core. Simulations by Krumholz et al. (2009) and Kuiper et al. (2010) find for the accretion of material onto a pre-stellar core, that accretion through a non-axisymmetric circumstellar disk driven by gravitational and Rayleigh-Taylor instabilities can channel gas onto the central star. Filaments that then form within the disk are found to be self shielding against radiation, allowing radiation to escape through optically thin bubbles, thus allowing accretion to continue; such a process is known as the “flashlight effect”, where radiation within the circumstellar disk will preferentially escape along the poles (Krumholz, McKee & Klein 2005; Yorke & Sonnhalter 2002). The non-axisymmetric accretion originates from instabilities caused by companion stars, that themselves formed from gravitational instabilities within the disk (Krumholz et al., 2009); such a result may explain the observed multiplicity of massive stars. The issues addressed in point *ii)*, with cores fragmenting before a massive star can form, can be addressed provided there are sufficiently high levels of turbulence (McKee & Tan, 2003).

Observationally, some support can be found for the model from the clump mass distribution (CMF), which has been seen to bear a resemblance to the IMF (André et al., 2011; Reid & Wilson, 2006), while observed disks and outflows around massive protostars, similar to those seen in low-mass star formation (Beuther, Linz & Henning, 2012; Sandell, Wright & Forster, 2003) also provides observational support for such a mechanism.

1.5.1.2 Competitive Accretion

This model was first proposed by Bonnell et al. (1997), and argues that all stellar formation occurs from the same material within the collapsing molecular cloud core. The collapse is inhomogeneous, in that certain areas reach stellar densities while the remaining material is still infalling; the result being the formation of a stellar core of fractional solar mass, which then begins to grow through the accretion of the infalling material (Bonnell et al., 2001). Since the majority of massive stars do not form in isolation, but rather prefer to form in clusters, each star will compete for the reservoir of material; with up to 90 % of the mass within clusters being gas.

As the gas continues to collapse into a centrally-condensed system, the overall potential of the cluster deepens, causing the stars that accrete gas to sink towards the centre of this potential. The result leads to mass segregation, in that those centrally located stars will accrete more gas as the density will be highest at the bottom of the potential well. Therefore the position of a star, in respects to the clusters potential well, will dictate its overall mass (Bonnell, Vine & Bate, 2004).

Mass segregation leads to a hierarchical substructure, where the most massive protostar will form in the centre, and proceeding out from this source, stars of increasingly lower mass will surround the central source. Observationally, this model is supported by the fact that almost all massive stars do indeed form within a cluster, where the most massive counterpart is found towards the centre, with a surrounding intermediate-, to low-mass component (Sung, Sana & Bessell, 2013; Preibisch et al., 2000). However mass segregation may simply be an observational affect; where we are unable to distinguish true segregation from incompletenesses, due to overcrowding towards the core of a cluster that leads us to believe all clusters are segregated (Ascenso, Alves & Lago, 2009).

1.5.1.3 Stellar Mergers

The final proposed model, suggested as part of the competitive accretion model, is that of the stellar mergers model of Bonnell, Bate & Zinnecker (1998); the model emerged as a means to account for the high density of massive stars that are present within clusters, and radiation possibly impeding accretion. It is possible that collisions of massive stars can occur within the densest parts of clusters, and it may be a component that explains the formation of the most massive stars that are observed, however there are some key limitations. Firstly, the model requires exceptionally high, and unobserved, stellar densities of $> 10^8$ stars pc^{-3} for grazing collisions. Secondly, a prerequisite is the presence of high-mass stars already, that collide to form the most massive stars; therefore the theory cannot explain the formation of these high-mass stars (Zinnecker & Yorke, 2007). Crucially also, there are strong observational factors that limit the testing of this theory, namely the need for very high angular resolution to observe the phenomena.

Recent work has shown a convergence of the monolithic collapse and competitive accretion models, where both models now seemingly predicting the involvement of outflows and circumstellar disks. Undoubtedly, the theory of high-mass star formation will advance with improved observations, yielding a stronger set of conditions and characteristics in massive star-forming regions, that can be fed into ever complex simulations to test various models.

1.5.2 Observational Stages Of High-Mass Star Formation

As was discussed earlier, the environment to which high-mass stars are found to form within, can prove difficult for direct observation; inhibiting direct analysis of their formation and evolution. However, there are certain known tracers, which are the direct result that high-mass star formation has on the surroundings, that betray the presence of high-mass star-forming regions. Observations from infrared through to radio have suggested a basic evolutionary sequence, comprised of several stages in the embedded phase, highlighted by both Menten, Pillai & Wyrowski (2005) and van der Tak & Menten (2005), which we outline below (see Fig.1.4). However, the evolutionary stages to which an embedded source is observed does depend of the mass. Davies et al. (2011) observe for YSOs, of masses $< 20\,\mathrm{M}_{\odot}$, an average embedded lifetime of 0.1 - 0.3 Myr, while for high luminosity sources with a mass $> 20\,\mathrm{M}_{\odot}$, lifetimes of $\approx 10^4$ are found; the shorter lifetime being the direct result of a reduction in the Kelvin-Helmholtz timescale. As a result of this, higher mass sources will evolve straight to a UC HII stage, where the central source has reached the main-sequence, and has begun to ionise its surroundings.

1.5.2.1 Hot Molecular Cores

The collapse of a cold core leads to the eventual formation of a central protostar. The resultant heating from this central source leads to the formation of a hot molecular core that comprises a large mass of warm, dense gas. These hot

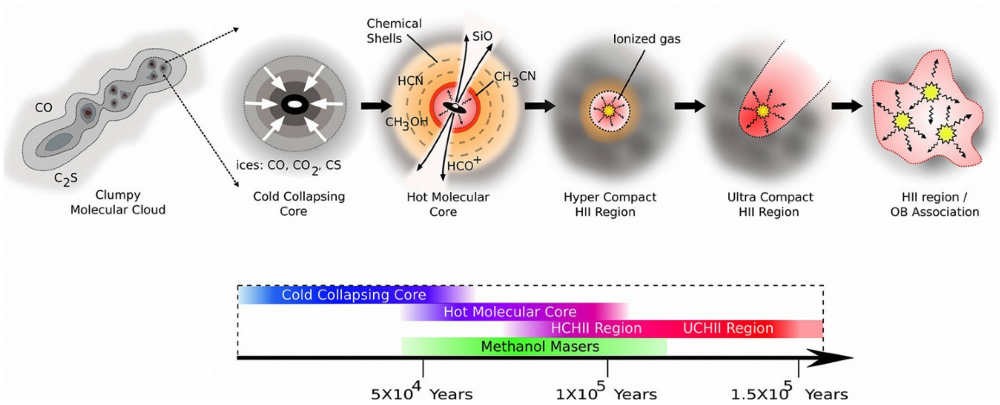

Figure 1.4: Illustration of the possible evolutionary sequence for high-mass stars, along with suggested time line and tracers (Purcell, 2007).

molecular cores have temperatures $\geq 100\,\mathrm{K}$, and this heat causes the evaporation of large abundances of molecules that have formed on the surface of dust grains, and had previously been frozen out of the gas phase, making hot cores identifiable sites of rich complex chemistry (Cesaroni, 2005).

Hot molecular cores are characterised as compact regions, of warm molecular gas, with diameters $\leq 0.1\,\mathrm{pc}$, and particle densities of $\geq 10^7\,\mathrm{cm}^{-3}$ (Kurtz et al., 2000; Fontani et al., 2007). Aside from the central source heating the surrounding gas, hot cores are though to be also surrounded by an accretion disk (Molinari et al., 1996a), and have also been found with associated massive bipolar outflows. Maser emission is also typically detected towards many hot cores, with their presence indicating an early stage of infall and outflow (Longmore et al., 2007). Based on the rich chemistry present within hot cores, models have suggested that the age of such regions is 10^5 yr (Hatchell, Millar & Rodgers, 1998).

1.5.2.2 Masers

Masers are compact sites of intense and narrow molecular line emission, where radiation from certain atomic and molecular transitions is greatly amplified via stimulated emission. A requirement for masers are regions of high density, some 10^6 - $10^{11}\,\mathrm{cm}^{-3}$, and a pumping mechanism to form and sustain an inverted population of masing species; this pumping mechanism can be either collisional, thermal/radiative, or produced via shocks.

Maser emission is known to associate with star formation, and the very bright emission that results from masers makes them excellent tracers of star formation. It is thought that the embedded protostellar source provides the necessary heat and photon flux to maintain the population inversions for masing, and the variations in the pumping mechanisms means that masers trace the environments to which they form within (Churchwell, 2002b).

The variation in the environment for different masers suggests that different masers will be associated with different evolutionary stages of high-mass star formation. Surveys of species, such as H_2O, OH, and CH_3OH have been conducted, and have revealed different associated stages of formation:

- Hydroxyl masers (OH) have to date been observed in many differing environments, such as evolved stars, and supernovae remnants, however they have also been found to associate with UC HII regions. OH masers have been detected towards the edges of UC HII regions, within the material of the accreting circumstellar envelope, but outside of the expanding ionisation front of the region; the suggestion is therefore, that OH masers are tracers of the advanced stages of high-mass star formation (Garay, Reid & Moran, 1985; Bloemhof, Reid & Moran, 1992).
- Water masers (H_2O) are believed to originate from collisional excitation in shocked gas within outflows and accretion disks (Torrelles et al., 1996, 1997), and are found to be good tracers of both low-, and high-mass stars formation.
- Methanol masers (CH_3OH) are subdivided into two classes, class I which are found to associate with both high-, and low-mass star formation, and class II which are found to be exclusively associated with massive star formation (Menten, 1991). Class I masers are collisionally pumped by outflows, as they interact with ambient high density material; they tend to be found offset from the central protostar, rather than being detected centrally (Ellingsen et al., 2007). Class II masers, however, are believed to be radiatively pumped (Sobolev et al., 2007), and provide a unique tool to tracer

high-mass star formation. They tend to be located towards, or against, the edge of UC HII regions, and are thought to arise when a protostar evolves towards a UC HII phase, tentatively suggesting a statistical age of $< 10^5$ yr (Caswell, 2009; van der Walt, 2005; Menten, 1991).

1.5.2.3 Ultracompact HII Regions

Ultracompact (UC) HII regions comprise newly formed massive stars, that are still embedded within their natal molecular clouds. The presence of dust means that such objects are only observable at infrared/sub-mm wavelengths, while also having a detectable component in the radio. A standard model of these regions is a spherically symmetric object, that comprises of two major components: an inner ionised hydrogen region surrounding the massive embedded star, and an outer thick cocoon of molecular dust and gas.

As their name suggest, UC HII regions tend to be compact, small objects, typically with radii ≤ 0.1pc, and densities of $\geq 10^4\,\mathrm{cm}^{-3}$. Their natal molecular clouds, which UC HII regions are deeply embedded within also tend to be small, with radii ≤ 0.5pc, densities of $\geq 10^5\,\mathrm{cm}^{-3}$, temperatures of 100 - 200 K, relatively massive, some $\times\,10^3\,\mathrm{M}_\odot$, and particular bright objects in the far-infrared at 10^4 - $10^6\,\mathrm{L}_\odot$ (Churchwell, 2002a).

The newly formed stars within UC HII regions tend to be observable from their radio free-free emission due to the ionised HII region that surrounds the embedded star. The absorption of the UV emission, from the massive star, by the surrounding dust cocoon tends to heat the dust grains to temperatures that range from sublimation near to the star, out to interstellar temperatures in the surrounding natal cloud (Hoare et al., 2007).

Figure 1.5 outlines the characteristic spectral energy distribution of a UC HII region. Typically UC HIIs are detected in the IR, with the dominant emission being due to thermal emission from the hot dust in a shell around the ionised gas, which surrounds the embedded star. The radiation from the central source heats the dust, and it is this warm dust within the ionised gas that re-emits in the infrared, with a pseudo-blackbody spectrum peaking at $\approx 100\,\mu$m. Most of this dust emission comes from dust of temperatures ≈ 30 K, yet those grains nearer to

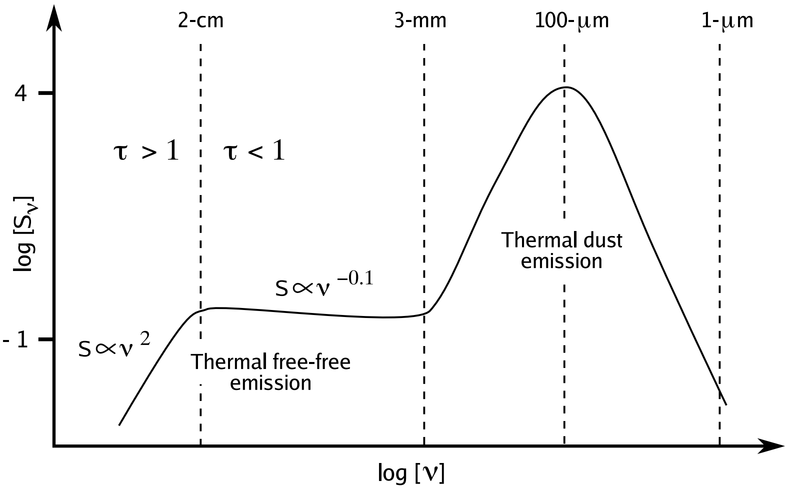

Figure 1.5: Spectral energy distribution of a UC HII region, highlighting the contributing two components. The dominant component is dust emission, while from 3 mm onwards the contribution is from thermal free-free emission from the ionised gas (Purcell, 2007).

the central star may reach temperatures closer to ≈100 K.

At wavelengths greater than 3 mm, this thermal dust emission drops off, and the dominant detection is due to thermal free-free radio emission from the ionised gas in the inner region surrounding the massive star. The Lyman continuum photons that are emitted from the central star are used up within the volume of ionised hydrogen, producing the detected radio emission. For this emission, its believed stars of spectral index B3 or earlier are only capable of producing the required ionising flux of Lyman continuum photons ($E > 13.6$eV, i.e. $912\mathring{A}$.) (Crowther & Conti, 2003). Such a spectral type is selected, because the Lyman continuum flux then begins to rapidly drop off with decreasing effective temperatures (Panagia, 1973).

A consequence of the production of Lyman photons is the production, and expansion of a HII region. When a massive star first emits ionising UV photons, the expansion of the HII region is rapid, as the ionisation front moves through the ISM. Since the ionising photon flux is an inverse square law with distance, the initial expansion will eventually come to a halt as the rate of ionisation is balanced by the rate of recombination. The ionising photons that drive this expansion consequently raise the number density within the HII region (i.e. each ionised molecular hydrogen atom will produce two protons and two electrons), and combining this with an increase in the temperature ($\approx 10^4$ K within the HII region, as opposed to $\approx$ 10 - 100 K in the surrounding environment), the result is pressure gradient (i.e. considering an ideal gas $p = nkT$). This pressure between the hot ionised gas, and the surrounding cool gas, drives a further phase of expansion of the HII region into the natal molecular cloud, at the speed of sound within the HII region (10 kms^{-1}). This expansion of the HII region is underpinned by several factors, such as the spectral class/ionising potential of the embedded stellar source, whether the system is a singular or multiple ionising star, and the size and density of the natal cloud. Aside from UC HII regions, other classes of HII region are defined according to the expansive driving force of the HII region: evolving from hypercompact (HC) HII regions, radii $\leq$ 0.01pc, UC HII, compact HII, radii $\leq$ 0.5pc, and classical HII regions, radii $\approx$ 10pc (Davies et al., 2011; Kurtz & Hofner, 2005; Churchwell, 2002a; Comerón & Torra, 1996).

Studying these regions provides a primary means to identify the earliest phases of massive OB star formation. By definition, the compact nature of UC HII regions suggests that these regions are sites of young star formation. However this phase is short lived; if we assume that the surrounding HII shell expands at around the sound speed of an ionised material, we obtain lifetimes in the order of 10^4 - 10^5 yr (Kurtz et al., 2000). This age, however, seems to conflict with the observed number of UC HII regions present within the Galaxy. The statistical argument suggests that if we assume a population of some 17,000 O stars within the Milky Way, as suggested by Wood & Churchwell (1989a), and taking a UC HII age of 10^4 yr (suggesting some 2 % of O star main-sequence lifetime is spent within this evolutionary phase), then in total we would expect to identify $\approx$ 300 UC HII regions throughout the Galaxy. Yet, current number estimates of the UC HII population place a figure of $\approx$ 1000 such regions within the Galaxy (Wood & Churchwell, 1989b), proposing that a main-sequence star can indeed spend a greater proportion of its lifetime in such an embedded phase, up to 10 % in fact. If this scenario is the case, with typical O star main-sequence lifetimes of 10^6 yr, then a more reasonable age for the UC HII phase would be in the order of 10^5 yr

(Davies et al., 2011; Comerón & Torra, 1996).

1.6 Triggered Star Formation

As mentioned earlier, one area of interest with massive stars is their interaction with their surrounding environment; what affect does the energy and momentum input from a massive star, and its associated HII region, having on the surrounding natal cloud? This is of particular interest, as the expansion of a HII region may trigger a new generation of star formation; sequential star formation within the cloud. The classic theory of triggered star formation was first proposed by Elmegreen & Lada (1977), in which induced star formation is the direct result of a interaction between the massive stellar population, and the surrounding environment. Their proposed theory comprises an advancing ionising shock front, caused by a HII region, that provides a pressure on surrounding layers of molecular gas, causing this material to compress and heat. As a result of this interaction, the shock front will stimulate gravitational instability in pre-existing overdensities within the cloud, or cause new sites as a direct result of the sweeping up of material, eventually leading to the formation of massive stars. This classical approach in all likelihood does not account for the formation of low-mass stars; if this were the case, the process would lead to an anomalous IMF, with only massive stars present - known as 'Bimodal Star Formation' (Guesten & Mezger, 1982).

What is key in the proposed triggering models, is the suggestion that if the triggered population produces massive stars, then the process could conceivably be repeated for another generation. The implication of this would be a sequential process of star formation, generation after the next, until no more material were present within the natal cloud. If such a scenario were the case, then massive stars would prove a key factor in both the star formation efficiency (SFE) and rate (SFR) of their host GMC; be it triggering, or exhausting star formation.

1.6.1 Models Of Triggering

In total, some three models have been proposed as triggering mechanisms:

- Cloud-cloud collisions: where two pre-existing molecular clouds collide resulting in gravitational instabilities.
- Radiative-driven implosions (RDI): where pre-existing clumps are further compressed, due to a propagating shock front.
- Collect and collapse: where the accumulation of gas into a dense ridge leads to the collapse of dense cores as a result of gravitational instability.

Of all the models proposed, the final two are considered the main proponents; both have their origins in expanding HII, or supernovae, due to pre-existing massive stars, that provide the main driving force. It is noted that these two main mechanisms do not necessarily occur in isolation, indeed Deharveng, Zavagno & Caplan (2005) have suggested both processes may have occurred within a single HII region.

Below we outline the two main proposed models in further detail.

1.6.1.1 Radiative-Driven Implosions

The RDI model (Bertoldi, 1989; Lefloch & Lazareff, 1994), concerns the expansion of a HII region into a pre-existing cloud, which drives an ionisation front and shock wave through the cloud; a schematic of the process is shown in Fig.1.6. This advancing front will generate an inward pressure that causes the collapse of pre-existing dense cores, or triggers the formation of new subcritical clumps, both of which lead to the formation of a new generation of stars.

In this model the UV radiation of nearby OB stars drives an ionisation front, and photoionsation induced shock front, into the surface of the neighbouring cloud. If the internal pressure of the neighbouring cloud is lower that the external ionising gas, then the cloud is said to be under-pressure; this causes the compression of the gas until it reaches pressure equilibrium. The gas immediately ahead of the ionising front is compressed by the shock, allowing a density-critical ionisation front to form behind the shock that further propagates into the cloud (a density, or D-critical front refers to the density of the medium the ionisation front is propagating into). This continued propagation causes the temperature and pressure of the ionising shell to increase, and ionised gas begins to stream

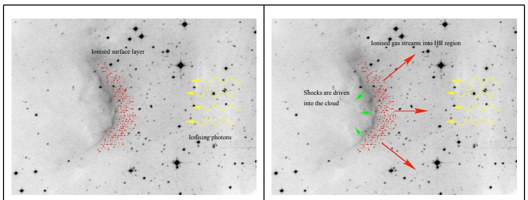

(a) Ionisation of the cloud's surface by Lyman photons.

(b) The ionised gas expands into the low density HII region, compressing the molecular gas via the rocket effect.

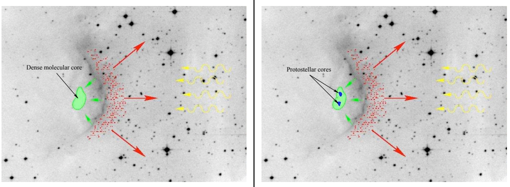

(c) Photoionisation induced shocks lead the formation of a dense clump at the focus of the cloud rim.

(d) The cores collapse and fragment into protostellar objects.

Figure 1.6: A diagram depicting the radiative-driven implosion model of triggered star formation. The ionisation from of the HII region drives into the molecular cloud, triggering the gravitation collapse of pre-existing cores, leading to further star formation. Image courtesy of James Urquhart.

into the lower density HII region that is behind the front; the cloud eventually accelerates away from the OB stars via the 'rocket effect' (Oort & Spitzer, 1955), producing a cometary like morphology. At this state the shocks can either induce the collapse of the cloud, or the cloud can undergo a prolonged period of slow evolution, as the front propagates into the cloud. The eventual result of this propagation is the formation of dense clumps within the cloud, that will go on to collapse under self-gravity, to form a new generation of stars (Urquhart et al., 2006).

The usefulness of the RDI model is that it can accurately explain the morphology of bright-rimmed clouds; where the persistent UV radiation from the OB stars leads to a dense shell of ionising gas that forms around the surface of the cloud, with a bright rim that is directed towards the source of the ionising radiation (Bisbas et al., 2009, 2011; Miao et al., 2009).

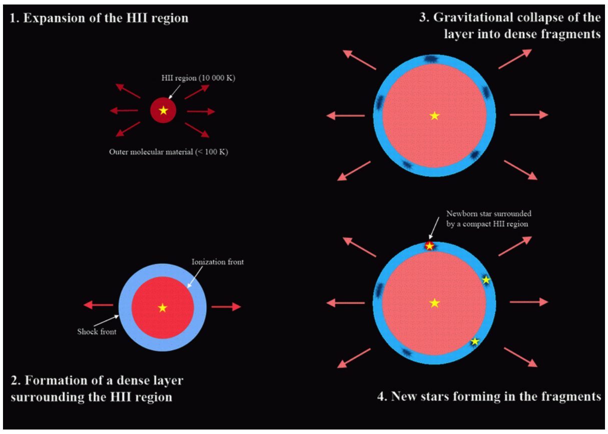

Figure 1.7: A diagram depicting the collect and collapse model of triggered star formation. In this model, the stellar winds of the present massive stellar population causes the expansion of the HII region, which in turn triggers a second generation of star formation. Image courtesy of Lise Deharveng and Annie Zavagno.

1.6.1.2 Collect And Collapse

The collect and collapse model of star formation was first proposed by Elmegreen & Lada (1977), and differs from the RDI model in that it does not require a pre-existing molecular structure. Instead, this model concerns the expansion of a HII region, that sweeps up any surrounding low-density material into a shell surrounding the expanding HII region; the model requires a period of time after the formation of the centrally ionising source(s) for surrounding material to be swept up by the HII region.

Starting from the first massive stars present, their stellar winds and ionising radiation begin to drive the expansion of the HII region. The initial clearing disperses the immediate surroundings, thus preventing further star formation within close proximity. Moving further out, both the ionisation front and shock front produced by the expanding HII region begin to gather up all surrounding material, and compress this into an increasing dense shell of gas. As this 'snowplough' affect continues, the surrounding material reaches a stage at which point the shell itself becomes self gravitating; it is then at this stage that the shell can begin to fragment, and enter a phase of collapse, possibly leading to the formation of new stars (Dale, Bonnell & Whitworth, 2007). Fig.1.7 outlines the main processes involved in the model.

One conclusion that can be drawn from the model is, that given a sufficient reservoir of material, this sequential process can continue, provided successive generations of massive stars are formed (Whitworth et al., 1994b); the time-scale between successive generations will measure in the $\approx 10^6$ yr. This staggered star formation may explain the hierarchical nature of massive stellar clusters, where one would expect an age gradient, of two to three generations, that spreads out from the initial site of massive star formation (Bastian et al., 2005; Oey et al., 2005). If the collect and collapse model were to exist, observationally we would expect to see the oldest shell with a younger expanding region at its edge, which itself would have a far younger star formation site on its edge.

1.6.2 Significance Of Triggering

One issue at present with proposed triggered star formation, is how confidently you can identify a site *as* triggered, or not; a 'chicken or the egg' scenario. It is difficult to determine whether observed star formation is the direct result of triggering, or whether we are merely observing an underlying population that has already formed. Evidence for triggering via both collect and collapse, and RDI mechanisms have been observed in some selective studies to date (Dewangan & Ojha, 2013; Dewangan et al., 2012; Dirienzo et al., 2012; Thompson et al., 2004; Urquhart, Morgan & Thompson, 2009; Zavagno et al., 2010; Zavagno et al., 2006, 2010), however the fact still remains that an unbiased identification of triggered star formation, and how important its perceived effect is, still remains to be seen.

Aside from observational studies to identify triggering, much theoretical modelling and simulation work has been conducted, that attempts to incorporate the physical process that occur within GMCs into simulations of triggering (Dale, Bonnell & Whitworth, 2007; Dale, Clark, P. C. & Bonnell, 2007; Dale & Bonnell, 2012; Dale, Ercolano & Bonnell, 2012, 2013). These models attempt to incorporate affects such as external irradiation onto a molecular cloud, and internal feedback effects from massive stars such as stellar winds and ionising shocks, to begin to recreate observable phenomena. A combination of more detailed and predictive simulations, along with large-scale Galactic surveys (Thompson et al., 2012; Kendrew et al., 2012) that allow us to apply statistical techniques to sights of potential triggering, will ultimately be needed to rigorously test the models, and move beyond the theories to a more predictive stage.

1.7 Star Formation Rates & The Initial Mass Function

The advent of large-scale, multi-wavelength studies, allows us to begin to test some fundamental concepts in astronomy, across our Galaxy and beyond, to extragalactic regimes. Two of these key questions are the motivators for some of the work conducted within this thesis: *i)* what is the nature of the initial mass function in Galactic star-forming regions; *ii)* and how do star formation rates (SFR) vary in Galactic regions, and can we apply the same SFR tracers to Galactic and extragalactic regimes. Below we outline the the main concepts involved in both these questions.

1.7.1 The Initial Mass Function

The initial mass function (IMF) defines the distribution of stellar masses formed during one event; measured by various authors, and shown in Fig.1.8. As a quantity, it was first measured by Salpeter (1955), who showed that the number of stars $\xi(m)\,dm$, in the mass interval between m and $m\ dm$ can be approximated by a power law:

$$\xi\,(m)\,dm\;\approx\;m^{-\alpha}\,dm \tag{1.17}$$

where $\alpha\;\approx 2.35$, known as the Salpeter value, for stars in the mass range of $0.4 \leq m\;\leq 10\,\mathrm{M}_{\odot}$ this approach however is slightly simplistic, and a more lognormal form has been proposed. Miller & Scalo (1979) conducted a study of the form of the IMF, outside of the Salpeter limits, and proposed a flattening IMF below a value of $\approx 0.5\,\mathrm{M}_{\odot}$ and that the IMF had a lognormal form of:

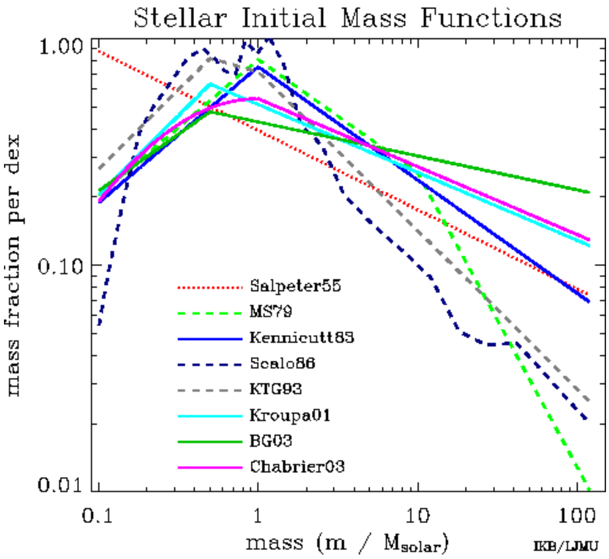

Figure 1.8: The Initial Mass Function measured by various authors: Salpeter (1955), Miller & Scalo (1979), Kennicutt (1983), Scalo (1986), Kroupa, Tout & Gilmore (1993), Baldry & Glazebrook (2003), and Chabrier (2003).

$$\frac{dn}{d(log\, m)} = \frac{A}{\sqrt{2\pi\sigma}} exp\left[-\frac{(log\, m - log\, m_c)^2}{2\sigma^2}\right] \tag{1.18}$$

with m_c the mean mass, and $\sigma^2 = \langle(log\, m - \langle log\, m\rangle)^2\rangle$ the variance in $log\, m$.

At present, the more commonly accepted IMF it that of the power law in Equation 1.17, but broken down into three components, that comprise differing mass regimes (Kroupa, 2002; Chabrier, 2003):

$$\xi(m) = \begin{cases} 0.26m^{-0.3\pm0.7} & 0.01 \leq m \leq 0.08\, M_\odot \\ 0.035m^{-1.3\pm0.5} & 0.08 \leq m \leq 0.5\, M_\odot \\ 0.019m^{-2.3\pm0.7} & 0.5 \leq m \lesssim 150\, M_\odot \end{cases} \tag{1.19}$$

The shape of the Galactic IMF is shown in Fig.1.9, along with the associated uncertainties; Scalo (1998) proposed that the uncertainties found within the IMF exponent were in a large part due to observational constraints, being due to Poisson uncertainties and dynamical effects, falling out from the biases through unresolved multiple stars.

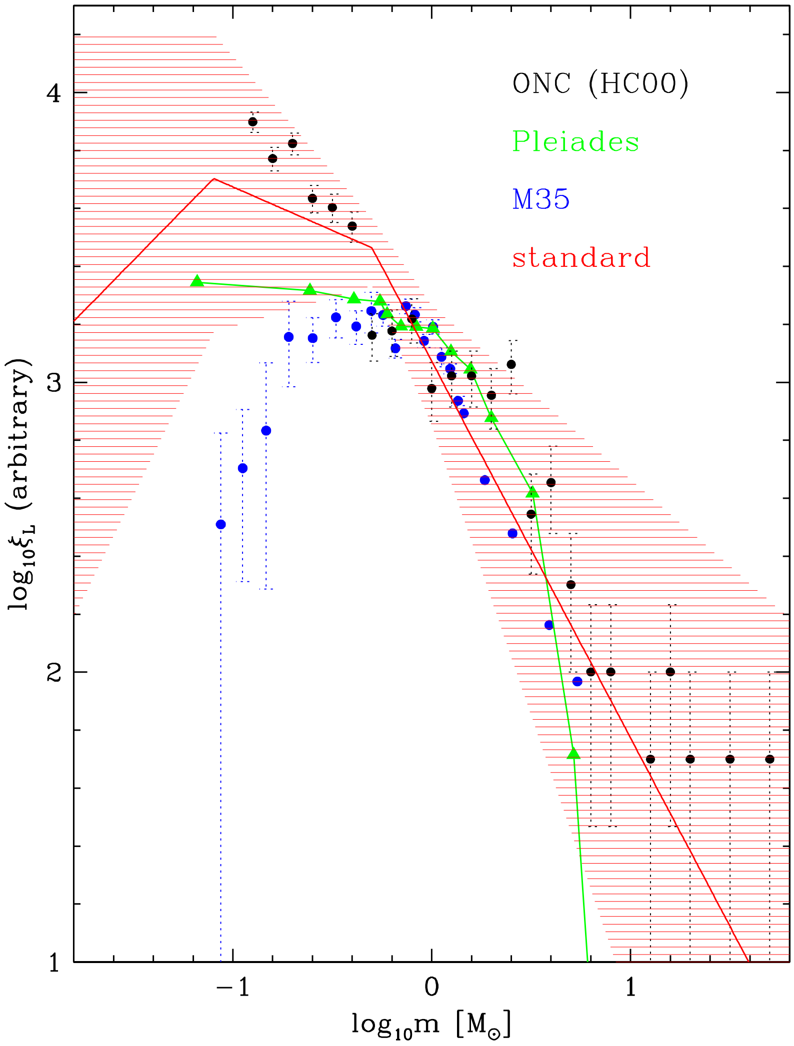

Figure 1.9: The shape of the averaged Galactic IMF, shown as the solid red line, with the associated uncertainties shown also (Kroupa & Weidner, 2005).

Why the nature of the IMF is an important phenomena for astronomers is as it appears that the observed distribution within the IMF is common across all star-forming regions, across a range of environments (Kroupa, 2001). Particularly at the high mass tail of the IMF, the distribution is found to be near universal, despite environmental factors such as the metalicity or density, which themselves could have changed the distribution. This ubiquitous distribution not only extents to Galactic realms, but has also been found to be the case at moderate, to high redshift, where the IMF is found to be constant with the Salpeter power-law (Baldry & Glazebrook, 2003).

1.7.2 Star Formation Rates

As we have mentioned earlier, massive stars produce vast quantities of radiation that photoionises their surroundings, and produce detectable HII regions; hence HII regions can be used as the bright way-points that demarcate sites of active star formation in galaxies. Normally, within these regions, it is the most massive source(s) that ionise the accompanying HII region, and with issues of resolving individual populations in extragalactic studies, use of the stellar IMF is needed. The classical SFR relations, such as Kennicutt (1998b) employ the IMF to extrapolate the young stellar population from SFR tracers such as optical/near-IR recombination lines or far-IR continuum, which themselves are only sensitive tracers of the most massive stellar component. The result of this is that the extrapolation can prove to be enormous, and prone to error.

The necessity to obtain an accurate SFR is paramount; the most massive stars account for the majority of luminosity in galaxies, and inject both energy and heavy elements into their surroundings, through feedback processes such as stellar winds, radiation, and ultimately supernovae. Galaxy evolution models require an accurate SFR as an input parameter to their models, with these feedback mechanisms determining the energy and composition of the surrounding ISM. The issue with solely tracing the massive stellar content, is the fact that both intermediate-, to low-mass stars are neglected. Their presence is also important, as the more evolved of these sources tend to manufacture and provide the best-part of interstellar dust, and chemical enrichment of abundances such as carbon. Low-mass stars also dominate the bulk of stellar matter, and have far longer lifespans on the main-sequence, as opposed to their vigorous higher-mass counterparts, meaning that their continued presence has a profound impact on galactic dynamics and structure. An accurate account of not just the SFR, but also the intermediate-, to low-mass content is required for accurate galaxy models.

It was Schmidt (1959) that first proposed, in his pioneering work, that the SFR could be related to the gas surface density in the form of a power-law:

$$\sum_{\text{SFR}} = A \sum_{\text{gas}}{}^{N} \tag{1.20}$$

where A is the absolute star formation efficiency (SFE), $\sum_{\text{SFR}}$ is the SFR surface density (in $\text{M}_{\odot}\,\text{yr}^{-1}\,\text{kpc}^{-2}$), N is a power-law of the ISM gas surface density $\sum_{\text{gas}}$ (in $\text{M}_{\odot}\,\text{pc}^{-2}$).

It was Kennicutt (1998b) that presented the various SFR tracers that could be used in extragalactic scenarios, all of which relied on stellar population synthesis models. These models generate integrated spectra of stellar populations, as functions of mass and age, which are then compared to the observations to determine the underlying population. In this situation, the IMF provides the weighting used to select the stellar population from grids of stellar evolutionary tracks.

The main tracers, to which the SFR is calculated, is provided by optically visible $\text{H}\,\alpha$ lines, which trace the young stellar population; their brightness and easy accessibility to ground-based observations makes them ideal also. However, for every advantage there is the major drawback of the environment that these young sources are found within. The star-forming regions tend to enshroud their YSO content within layers of dust and gas, meaning that $\text{H}\,\alpha$ observations are next to impossible; the infrared radiation that is produced by UV photon absorption is the staple in contributing the luminosity in these environments. This situation means that the thermal IR emission is a strong probe for the SFR, at the bare minimum on an individual HII region basis, or particularly also in starburst galaxies where the stellar radiation field is dominated by young stellar sources (Kennicutt, 1998a).

Taking the synthesis models of Leitherer & Heckman (1995), for a continued burst of star formation over a period of 10 - 100 Myr, and with the assumption of a solar metallicity, Kennicutt (1998b) derived the classical IR tracer of:

$$SFR = 4.5 \times 10^{-44} \, L_{\mathrm{FIR}} \; [\mathrm{M}_{\odot} \; \mathrm{yr}^{-1}] \tag{1.21}$$

where L_{FIR} is the FIR luminosity (in erg s^{-1}) measured over the entirety of the far-IR range that carries the bolometric luminosity of the HII region/starburst (i.e. $\lambda = 10 - 100\,\mu$m) , and the value 4.5×10^{-44} is a constant derived from the population synthesis models.

In terms of the gas surface density, a significant fraction of the interstellar hydrogen content is found to be in molecular form, H_2. However, the observation of H_2 is difficult, and thus the density of the second most abundant molecule, CO, is used as a proxy for the H_2 density by assuming a fixed abundance ratio between CO and H_2 (Lacy et al., 1994):

$$\frac{[CO]}{[H_2]} \sim 2 \times 10^{-4} \tag{1.22}$$

Combining a sample of some 61 normal spiral galaxies, and 36 IR selected starburst galaxies that spanned five orders of magnitude in gas surface density, and over six orders of magnitude in SFR surface density, Kennicutt (1998b) showed that star-forming galaxies followed a Schmidt Law, with an index $N = 1.4 \pm 0.15$; this has come to be known as the Schmidt-Kennicutt Law (shown in Fig.1.10).

The above relation is strictly empirical in nature; it appears that the Schmidt-Kennicutt Law applies over a wide range of galaxy types and conditions, however as we mentioned earlier, this is not a completely reliable measure of the SFR in a galaxy. From Fig.1.10 we can clearly see that there is a noticeable scatter about the line of best-fit, that increases at larger gas surface densities.

The Milky Way should serve as the best SFR calibrator that is available to us; the proximity affords us superb resolution to identify individual stellar populations embedded within clusters. This high resolution data allows us to directly analyse the young stellar population that ionise Galactic HII regions, allow us the constrain the IMF, and ultimately probe the physical processes that govern star formation. The logical conclusion from this data would be to calibrate against the more diffuse, and global tracers, that extragalactic SFR investigations

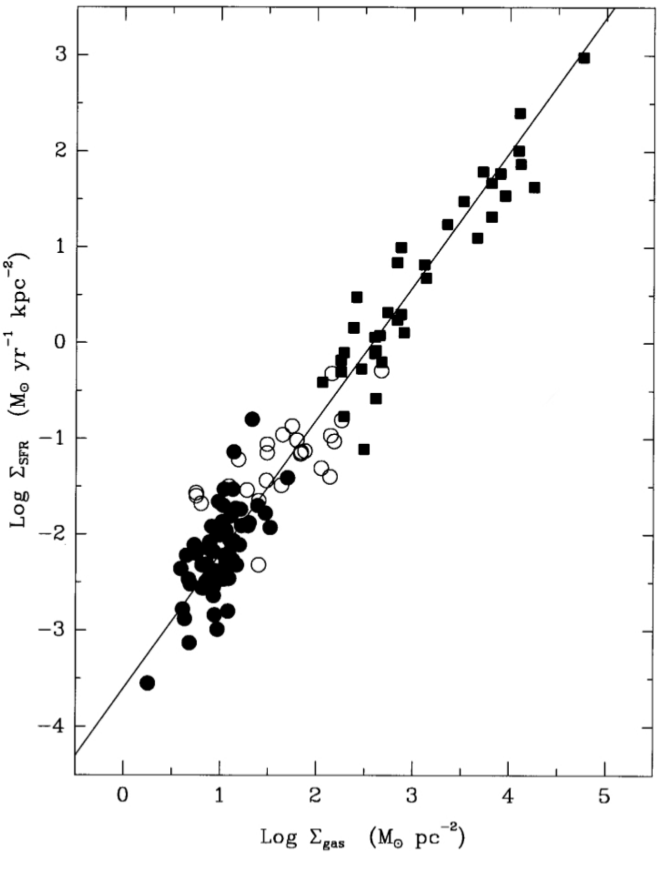

Figure 1.10: The Schmidt-Kennicutt Law of Kennicutt (1998b), where the SFR surface density is plotted against gas surface density for normal spiral galaxies (filled circles), starburst galaxies (filled squares), and the centres of the normal spiral galaxies (open circles). The least-square fit power law of $N = 1.4$ is shown also.

call upon. However, as we later discuss in Chapter 3, recent work has highlighted the clear disparity between the two regimes (Kennicutt & Evans, 2012); Galactic and extragalactic SFR tracers do not seem to agree.

1.8 Stellar Characterisation

The study of stars doesn't lend itself to experimental study, conducting experiments to test or valid theories; to validate theories we gather information through observations. This information typically is the apparent brightness of a source, being the amount of radiation from the source falling per unit time, on unit area of a collector, which normally is a telescope. This radiation flux is not an intrinsic property of the source, for it depends on the distance of the source from the observer.

One mainstay of analysis within this thesis, concerns the spectral energy distribution of sources, known as the SED. Below we aim to describe the physics and techniques use to analyse the radiation measured from each source.

1.8.1 Definitions

Before we progress, we firstly define some fundamental concepts and definitions.

1.8.1.1 Intensity

The intensity, or sometimes known as the specific intensity, depends on the direction, in that for a source it is the amount of energy emitted per unit time, per unit area of the source, per unit frequency, per solid angle in a given direction (see Fig.1.11 for a diagram of the definition). Therefore we define the amount of energy as:

$$dE_\nu \;=\; I_\nu cos\,\theta\,dA\,d\nu\,d\omega\,dt \tag{1.23}$$

where I_ν is the specific intensity of radiation with units of $\mathrm{W\,m^{-2}\,Hz^{-1}\,sr^{-1}}$, dE is the power in Watts, $d\nu$ is the bandwidth in Hz, dA is the area of the surface element in m, and $d\omega$ is the solid angle at an angle of θ to the surface, in sr. We

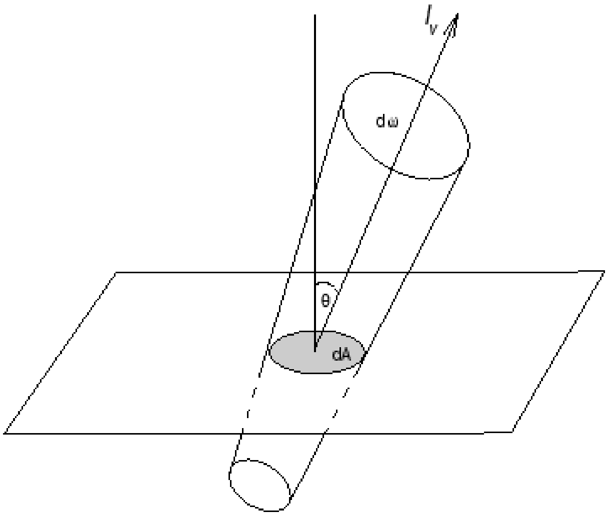

Figure 1.11: The relationship between the specific intensity, I_ν, and the energy passing through a surface element of area dA.

can obtain the intensity over all possible frequencies, known as the total intensity I, by integrating Equation (1.23) over all frequencies.

We next consider the change in intensity, I_ν, passing through a medium of density ρ, such as a molecular cloud; as shown in Fig.1.12. Over a small distance, of ds, many processes can take place, namely: *i)* Absorption - in which the radiative energy is absorbed by dust grains along the line of sight; *ii)* Scattering - here, the incident photon is scattered by a dust grain, and moves off at a angle θ to the direction of propagation of the incident beam; *iii)* Thermal excitation - in this, photons are added to the beam by being scattered from beams propagating in other directions.

The result of these interactions leads to a change in the intensity, known as the equation of radiative transfer, and can be quantified as:

$$\frac{dI_\nu}{ds} = -\rho\,\kappa_\nu\,I_\nu + \varepsilon_\nu \tag{1.24}$$

where κ_ν is the opacity (in $\mathrm{cm^2\,g^{-1}}$), which depends on the incident frequency, the number of dust grains and their physical properties, while ε_ν is the emissivity, and is the energy per unit volume, per unit time emitted along the line of sight.

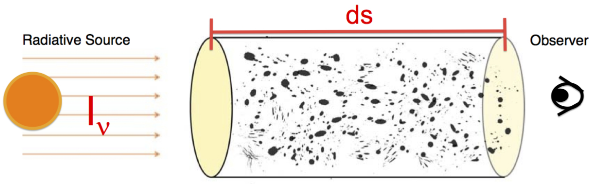

Figure 1.12: The passage of radiation, with intensity I_ν, through a medium of length ds, and total density ρ.

Usually the equation of radiative transfer is defined in terms of the optical depth along the line of sight, which gives the number of mean free paths along the line of sight, and is a dimensionless quantity:

$$d\tau_\nu = \frac{1}{\rho\,\kappa_\nu} \tag{1.25}$$

With the inclusion of the optical depth, two cases can result:

- Optically thick medium: $d\tau_\nu \gg 1$ - in the case of thermal equilibrium, the emergent intensity will be identical to the Planck blackbody function.
- Optically thin medium: $d\tau_\nu \ll 1$ - the emergent intensity will be the product of the optical depth, and the source function (the ratio of total emissivity to extinction coefficient). As the optical depth has a frequency dependency, the emergent intensity will not be identical to the source function.

1.8.1.2 Flux Density

From an observational point of view, we are generally more interested in the flux, which is what we directly measure with a telescope. This quantity is the flux density, which provides us with the energy of the incident radiation per unit time, passing through a unit area of the surface, per unit frequency. We relate the intensity and the flux by noting that the energy passing through a certain area is composed of beams exiting at different angles to the normal; thus by integrating the intensity over the total solid angle subtended by the source, we obtain:

$$F_\nu \, = \, \int_0^{4\pi} I_\nu(\theta) \, cos \, \theta \, d\omega \tag{1.26}$$

where the units for flux density are $\mathrm{W\,m^{-2}\,Hz^{-1}}$. Observed flux densities tend to be extremely small, particularly in radio astronomy, and thus the units of flux density are often expressed in units of Jansky (Jy), where $1\,\mathrm{Jy} = 10^{-26}\,\mathrm{W\,m^{-2}\,Hz^{-1}}$.

If we consider a star as the source of radiation, then the isotropic radiation emitted by the star, at a distance r, we be distributed evenly across a spherical surface of area $4\,\pi\,r^2$, and hence the luminosity is defined as:

$$L \, = \, 4\,\pi\,r^2\,F_\nu \tag{1.27}$$

1.8.2 Spectral Energy Distribution

Observations of young stars tend to be difficult, mainly due to the prohibitive environments that they are found within. Young stellar sources tend to be embedded within highly obscuring clouds, and generally are place far away from the observer. Rather than relying purely on imaging these sources, we instead rely on the measurement of the total energy emitted by the stellar source, and its surrounding environment, per wavelength/frequency interval; this is know as the spectral energy distribution (SED) of the source. The bulk of the energy, for embedded stellar sources, is found to be emitted in the 1 mm to $1\,\mu$m interval; the shape of the SED, in relation to the wavelength, can provide us with information on the nature and evolutionary stage of the source being observed (e.g. temperature, luminosity).

Below we outline the physics behind interpreting the incident radiation from these sources.

1.8.2.1 Blackbody Radiation

An important first concept to understand is that of blackbody radiation - this underpins the the work achieved with SED fitting and modelling. We define a blackbody as a system that absorbs all electromagnetic radiation incident upon

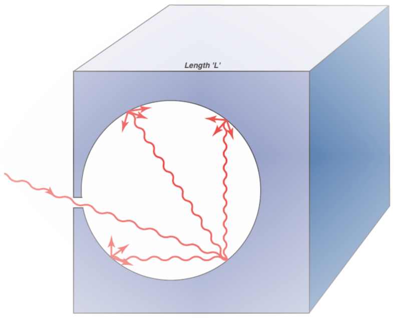

Figure 1.13: Realisation of a blackbody, as a perfectly insulated enclosure, within which radiation is in thermal equilibrium with the enclosure walls. Radiation is incident, and re-radiated, through a tiny hole within the the cavity.

it, and re-radiates this energy at the exact same rate of absorption, to remain in thermal equilibrium. The spectrum of such a system will depend solely on the temperature, and the emitted radiation will be isotropic, homogeneous, and unpolarised.

Thermodynamic equilibrium (TE) is an important assumption made throughout our work, and greatly simplifies the analysis of radiation. The basic assumption of TE is that a state which is found to be in TE will experience no net flows of energy within the system over time, and experiences no changes when in isolation from its surroundings, i.e. the temperature of a system is unchanging in time and uniform in space. This assumption is unlikely to apply over large regions, such as molecular clouds, where the temperature is likely to be variable, but is more applicable at local scales, such as individual clumps or cores. At this local thermodynamic equilibrium (LTE), a region can be modelled as a blackbody.

Under this condition of TE, the radiation energy density is given by the Planck function, and the derivation of said function is shown below.

We firstly consider a cavity, as a one-dimensional box, of side L (see Fig.1.13). In equilibrium, only standing waves are possible, and these have ends at nodes $x=0, L$.

$$\frac{L}{\lambda} = \frac{n_x}{2} = 1,\, 2\ldots \tag{1.28}$$

and since we have that $\lambda\,\nu\,=\,c$ for all wave motion, then we have that:

$$\nu\,=\,n_x\,\frac{c}{2L} \tag{1.29}$$

For each dimension, n_x, n_y, n_z there will be two modes; to find the number of modes in the frequency interval ν and $\nu\ d\nu$ we note that the cavity has sides of length $\frac{c}{2L}$. There is one point per cube of volume $\left(\frac{c}{2L}\right)^3$, and only positive integers n_x, n_y, n_z are acceptable. Therefore, we have that the number of triplets of positive integers, is equivalent to the volume of one octant of the space, divided by the volume $\left(\frac{c}{2L}\right)^3$:

$$\text{no.modes}\,=\,\frac{2\times\frac{1}{8}\times 4\pi\nu^2\mathrm{d}\nu}{\left(\frac{\mathrm{c}}{2\mathrm{L}}\right)^3}\,=\,\frac{8\pi\mathrm{V}}{\mathrm{c}^3}\nu^2\mathrm{d}\nu \tag{1.30}$$

The factor of $4\pi\nu^2 d\nu$ is the volume of a thin spherical shell, and L^3 has been replaced by the volume V.

If we next assume that each mode of oscillation represents a harmonic oscillator, with $\frac{1}{2}kT$ each potential and kinetic energy on average, we obtain the Rayleigh-Jeans law:

$$\frac{\text{Energy}}{\text{Volume}}\,=\,u_\nu d\nu\,=\,\frac{8\pi}{c^3}kT\nu^2 d\nu \tag{1.31}$$

The divergence of this relation, at high frequency, is known as the ultraviolet catastrophe - the prediction that a blackbody, at thermal equilibrium, will emit radiation with infinite power. To work around this problem, Planck postulated that the possible energies of the oscillators were quantised:

$$E_n\,=\,nh\nu\quad\text{with n}\,=\,0,\,1,\,2,\,... \tag{1.32}$$

in this, h is a new constant that was introduced, now known as the Planck's constant; determined by fitting the theoretical curve to the experimental data.

The average energy per oscillator is calculated from the Maxwell-Boltzmann distribution:

$$\bar{E} \;=\; \frac{\sum_n E_n e^{\frac{-E_n}{kT}}}{\sum_n e^{\frac{-E_n}{kT}}} \tag{1.33}$$

where the denominator is known as the partition function, and is represented as Z; which can be evaluated by summing the geometric series:

$$Z \;=\; \sum_{n=0}^{\infty} e^{\frac{-E_n}{kT}} \;=\; \sum_{n=0}^{\infty} e^{-nx} \;=\; \frac{1}{1 \;-\; e^{-x}} \quad \text{where x} \;=\; \frac{\mathrm{h}\nu}{\mathrm{kT}} \tag{1.34}$$

The numerator is then found to be:

$$\sum_{n=0}^{\infty} nh\nu e^{-nx} \;=\; h\nu \left(-\frac{dZ}{dx}\right) \;=\; \frac{h\nu e^{-x}}{(1 \;-\; e^{-x})^2} \tag{1.35}$$

and the average energy per oscillator is found as:

$$\bar{E} \;=\; \frac{h\nu}{e^x \;-\; 1} \;=\; \frac{h\nu}{e^{\frac{h\nu}{kT}} - 1} \tag{1.36}$$

Thus, the energy per unit volume of the radiation in the cavity is given by:

$$u_\nu(T)d\nu \;=\; \frac{8\pi}{c^3}\frac{h\nu^3}{e^{\frac{h\nu}{kT}} \;-\; 1}d\nu \tag{1.37}$$

We have that the flux propagating from the surface of the blackbody is isotropic, then we find that:

$$F_\nu \;=\; \frac{u_\nu(T)\,c}{4\pi} \tag{1.38}$$

where $F_\nu d\nu \;=\; \text{flux} = \frac{\text{energy}}{\text{area} \times \text{time}}$.

$$\therefore\; B_\nu(T) \;=\; \frac{2h\nu^3}{c^2}\frac{1}{e^{\frac{h\nu}{kT}} \;-\; 1} \tag{1.39}$$

Or in terms of wavelength:

$$B_\nu(T) \;=\; \frac{2hc^2}{\lambda^5}\frac{1}{e^{\frac{hc}{\lambda kT}} \;-\; 1} \tag{1.40}$$

where we define B_ν as the Planck function, with c the speed of light ($2.998 \times 10^8\,\mathrm{m\,s^{-1}}$), k the Boltzmann constant ($1.380 \times 10^{-23}\,\mathrm{J\,K^{-1}}$), and h the Planck constant ($6.626 \times 10^{-34}\,\mathrm{J\,s}$).

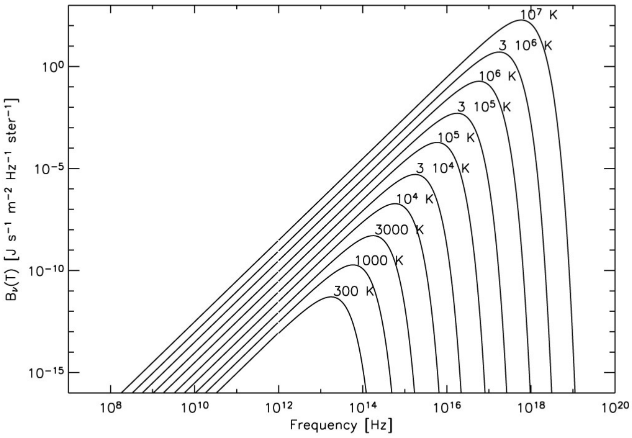

Figure 1.14: A log-log plot of the Planck curves, for blackbodies with differing temperatures.

The result of the Planck function is shown in Fig.1.14, where we can see that a blackbody emits at a peak intensity that shifts to higher frequencies, as its temperature increases. To determine the peak intensity, we solve the the Planck function for $\frac{dB_\lambda}{d\lambda} = 0$, which provides us with Wien's displacement law:

$$\lambda_{\max} = \frac{2.898 \times 10^{-3}}{T} \tag{1.41}$$

where $\lambda_{\max}$ is the maximum wavelength in m, when T is in K.

The area represented under the Planck curve, Fig.1.14, represents the total energy flux (W m^{-2}) emitted by a blackbody when summed over all wavelengths, and solid angles; this is known as the Stefan-Boltzmann law:

$$F = \sigma T^4 = \pi B(T) \tag{1.42}$$

where σ is known as the Stefan-Boltzmann constant ($5.670 \times 10^{-8}\,\mathrm{W\,m^{-2}\,K^{-4}}$), F is the flux, and T is the blackbody temperature.

1.8.2.2 Modified Blackbody Radiation

A true blackbody source will have an emissivity, ε, that was equal to unity, however when we fit the SED of embedded star-forming regions, this is not the case, with $\varepsilon < 1$ in most cases. With sources embedded within natal dust cocoons, we have to take on the form of a modified blackbody, which takes into consideration both the optical depth, τ_ν, and dust emissivity; clearly the emission will not be optically thick at all frequencies. The optical depth effectively defines the mean free path of a photon through a medium, and when a photon propagates through an optically thick medium, i.e. $\tau_\nu \gg 1$, there is a high probability of extinction. Conversely, radiation can travel freely within an optically thin environment, $\tau_\nu \ll 1$.

We define the emissivity as the energy per unit volume, per unit time, that is emitted into any one direction, and it is this physical property that must be taken into consideration when modifying the classical blackbody equation. If we consider a uniform medium, of optical depth τ_ν, then radiation passing through this medium will be reduced by a factor $e^{-\tau_\nu}$. In these scenarios, the emissivity of the medium is define as:

$$\varepsilon_\nu = 1 - e^{-\tau_\nu} \tag{1.43}$$

Taking this factor in account, the modified blackbody for an embedded source within a dust shrouded environment becomes:

$$F_\nu = \Omega \, B_\nu(T)(1 - e^{-\tau_\nu}) \tag{1.44}$$

where $B_\nu(T)$ is the classical Planck function, Ω is the effective solid angel of the emitting sources (in sr), and τ_ν is the optical depth. For dust grains, the optical depth is modelled as a power law, such that:

$$\tau_\nu = \left(\frac{\nu}{\nu_c}\right)^\beta \tag{1.45}$$

where β is the dust emissivity index, and ν_c is the critical frequency at which the source becomes optically thin, i.e. $\tau_\nu = 1$. The dust emissivity parameter directly reflects the physical properties of the dust grains, such as the grain size, shape, and coating (no mantles, thin ice mantle, thick ice mantle). From both model, and laboratory work, the value taken can vary considerably, and has been shown to range from $\beta = 2$ for amorphous silicate or graphitic grains, to values of $\beta = 1$ for amorphous carbon grains (Dupac et al., 2003).

1.9 Thesis Motivation & Goals

The broad aim of this work, and what we set out to investigate, is the nature of star formation within Galactic complexes such as G305, and the star formation history of such regions. In an effort to address these aims, we have gone about cataloguing both the embedded massive star-forming population of G305, and the low-, to intermediate-mass YSO population also, with a view to deriving the SFR of the region. In order to study the nature of star formation, and the possible interactions between various generations of star formation, we employ a detailed multi-wavelength analysis across the complex. With this detailed analysis of one Galactic region, we propose a scaling of our work across the Galactic plane, to both study the star formation history across all environments within the Milky Way, and to highlight the fundamental differences in Galactic and extragalactic star formation tracers, and derivations for SFRs.

The main questions that we aim to address in our work concern:

- To demonstrate the power of multi-wavelength observations when conducting a complete census of the star formation activity of a Galactic complex.
- Does the embedded massive star-forming population of a region exhibit similar properties, and can these be used to propose selection criteria?
- Completing a YSO census of the G305 region, and comparing the resulting SFR to other global SFR tracers. Do different approaches agree at a Galactic level?
- Do we see evidence for sequential star formation, emanating from the central HII region, throughout the GMC?

- Can we compare Galactic SFR tracers to extragalactic SFR tracers, and what are the differences between the two regimes? Is it possible to propose a unified SFR law across all scales?

To answer these questions we continue a body of work that has already been conducted in the G305 complex; including a near-IR *Hubble Space Telescope* study of the central Danks 1 & 2 open clusters (Davies et al., 2012), work focused towards the reservoir for star formation within the region through NH_3 observations, while identifying sites of active star formation from H_2O maser emission (Hindson et al., 2010), and more recently work towards identifying compact radio emission throughout the region that is indicative of UC HII regions (Hindson et al., 2012). Our work focuses on addressing these questions by combining present, multi-wavelength observations, with new far-IR observations of the G305 complex from the *Herschel* Infrared GALactic plane survey (Hi-GAL) survey (Molinari et al., 2010b).

This is an ideal time to conduct such a study, with a plethora of high-quality, multi-wavelength observations that are available across the Galactic plane, and put a case for future study of Galactic star-forming complexes using data including: Hi-GAL (Molinari et al., 2010b), GLIMPSE (Benjamin et al., 2003), UKIDSS GPS (Lucas et al., 2008), MIPSGAL (Carey et al., 2009), VVV (Minniti et al., 2010), CORNISH (Purcell & Hoare, 2010), MALT90 (Foster et al., 2011), ATLASGAL (Schuller et al., 2009), BOLOCAM GPS (Aguirre et al., 2011), MMB (Green et al., 2009), and SCUBA-2 (Holland et al., 2013).

1.10 Thesis Structure

The structure of this thesis is as follows: In Chapter 2 we introduce the main focus of this study, the G305 star-forming complex, and discuss its physical properties and the motivation behind an extended study of the region. In Chapter 3 we present a *Herschel* far-IR study towards the complex, with a view to identifying the embedded massive star-forming population found within. We also take this population in consideration when calculating a SFR of the region, and discuss the disparity in various SFR tracers. In Chapter 4 we address the issues of incompleteness at low-, to intermediate-mass YSOs, and complete a YSO census of G305. Finally, in Chapter 5, we summarise our findings and present the conclusions of our thesis, and suggest paths for future study.

Chapter 2

The G305 Star-Forming Complex

"I don't paint so that people will understand me, I paint to show what a particular scene looks like." - J. M. W. Turner

2.1 Introduction

The G305 star-forming complex is one of the most massive and luminous star-forming regions in the Galaxy (Clark & Porter, 2004; Hindson et al., 2010), centred on the two optically visible open clusters Danks 1 & 2 (Danks et al., 1984), and the Wolf-Rayet star WR 48a. G305 is located inside the Scutum-Crux arm within the Galactic plane at $l = 305^\circ$, $b = 0^\circ$, and found at a distance of $\sim 4\,\mathrm{kpc}$, it has a projected diameter of $\sim 30\,\mathrm{pc}$, and an estimated age of some 3 - 5 Myr (Clark & Porter, 2004). In this chapter we introduce the G305 star-forming region, and summarise the work that has been conducted on the complex.

2.2 Motivation To Study G305

Throughout this study, the focus has firmly been on studying the nature of star formation and the surrounding environment of the G305 complex. G305 was first identified and studied as part of a radio survey of some 70 star-forming regions in the Galactic plane conducted by Goss & Shaver (1970), and Shaver & Goss (1970), using the Parkes telescope at 5 GHz, and the Molonglo telescope at 408 MHz.

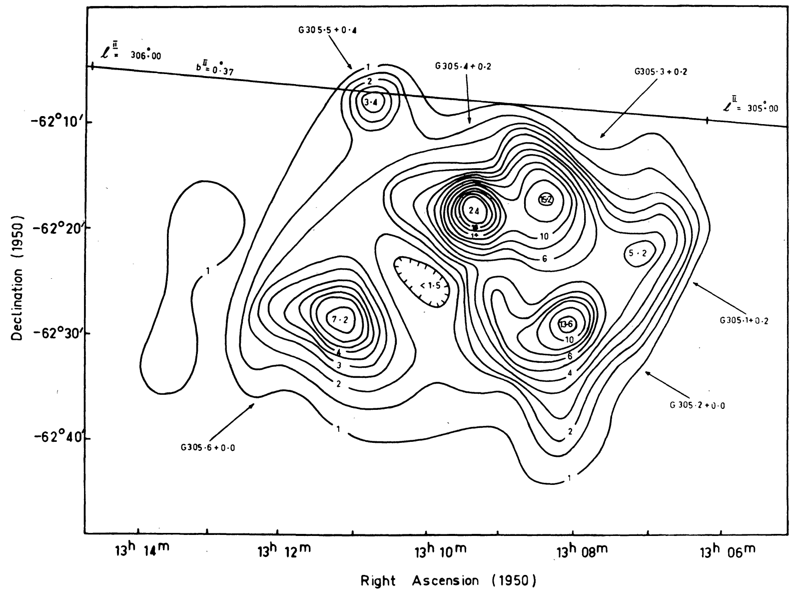

Figure 2.1: Low resolution 5 GHz observation of the G305 complex from Goss & Shaver (1970).

Initially, these low resolution observations, at 4' and 3' respectively, revealed five bright thermal radio sources, at 5 GHz, associated with a diffuse background radio structure, as shown in Fig.2.1. Of the 250 galactic radio sources presented in Table 1 of Shaver & Goss (1970), the combined 5 GHz thermal flux from the G305 complex places it as the tenth brightest star-forming region detected within their Goss & Shaver (1970) survey.

More recently, Murray & Rahman (2010) have conducted a study using the Wilkinson Microwave Anisotropy Probe (WMAP), to measure the free-free luminosity of the Galaxy between 10 - 100 GHz. The results showed that 18 of the most luminous star-forming regions within the WMAP survey constituted over half the total ionising flux of the Milky Way. This galactic ionising flux originates from the high-mass stellar content within the Galaxy, that tends to originate from a smaller number of GMCs; the Murray & Rahman (2010) results imply that half the population of O-type stars reside within this handful of star-forming regions. G305 is found to be the 15th brightest radio complex within the WMAP Milky

Way sample (Rahman & Murray, 2010), and is comparable in its free-free flux to other well-known GMCs and HII regions such as Westerlund 2 (Dame, 2007), the Rosette Nebula (Wang et al., 2008), W49A (de Pree, Mehringer & Goss, 1997), and NGC 3603 (Nürnberger et al., 2002). From this therefore, we can safely assume that G305 is a star-forming complex that is representative of the vigorous high-mass star-forming content within the Galaxy. Added to this, the numerous signposts of massive star formation, such as infrared hotspots, compact and ultra-compact (UC) HII regions, H_2O, OH, and methanol masers (Urquhart et al., 2007; Robitaille et al., 2008; Hindson et al., 2010; Hindson et al., 2012), is suggestive of a massive region of ongoing triggered star-formation (Clark & Porter, 2004).

With the availability of high resolution *Herschel* Hi-GAL observations of G305, combined with other multi-wavelength observations (outlined in Section 2.5), we are able to study at length the star-forming content of the G305 complex. Having the capacity to resolve the embedded star-forming population affords us an excellent chance to not only study the embedded massive star-forming population, but to also identify the evolutionary phases of the intermediate, to low-mass YSO content also. Using this, we are able to investigate the nature of the IMF within massive Galactic star-forming regions, while also being able to constrain the SFR of G305. As suggested earlier, with G305 being indicative of the general population of massive star-forming complexes within the Milky Way, our study serves as an example of what can be achieved in similar Galactic regions, and can begin to go some way towards a detailed analysis of the nature of star-formation, and the SFR, of our Galaxy.

Finally, a detailed analysis of the SFR of a Galactic HII region such as G305 has also implications for the determination of extragalactic SFRs. With dust obscured star formation within Galactic HII regions being similar in nature to the star-forming activity of starburst galaxies, we are able to compare SFR tracers and estimates between the two regimes. As is shown in Chapter 3, there is a clear disparity between Galactic - extragalactic SFR tracers, and therefore what is needed is a means to accurately compare the Milky Way to other galaxies. A multi-wavelength analysis of G305, and extension to other Galactic regions, will allow for an accurate determination of the SFR of the Galaxy, and will allow us

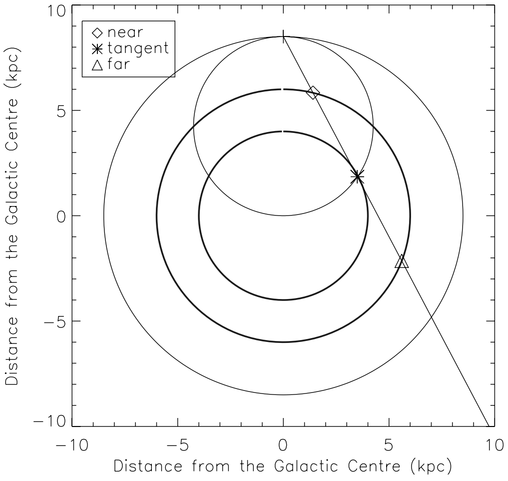

Figure 2.2: A diagram depicting the kinematic distance ambiguity, for an observer at (0, 8.5) kpc, with the line of sight shown as a solid line from the observer. Both near and far kinematic distances are shown also (Urquhart et al., 2012).

to extended our detailed Galactic analysis to extragalactic regimes. Ultimately, a firmer understanding and estimate of the Galactic SFR will help in bridging the gap between both Galactic and extragalactic scales, and may go some way towards a unified star formation law, if such a law is to exist.

2.3 Physical Properties Of G305

In the following subsections we outline the key physical properties of the complex, which are used throughout our studies in the following chapters.

2.3.1 The Distance To G305

Distances to Galactic objects tend to be poorly constrained, particularly for sources found within the inner Galaxy. One of the more common methods involves taking the measured radial velocity of a source, and assuming this arises from its differential Galactic rotation. From this, a rotation model of the Galaxy is employed, such as the Brand & Blitz (1993) model, to obtain a kinematic distance to the source. However, this measurement becomes ambiguous when applied to sources within the inner Galaxy. Each velocity measurement that is taken leads to two possible distance measurements, known as the near and far distance, that correspond to the two equidistant points from the point where the observer's line of sight is tangent to the circular orbit of the source; this scenario is shown in Fig.2.2. In this situation, the only possible way to resolve the distance ambiguity is using other information available along that line of sight, such as extinction maps (Russeil et al., 1998; Urquhart et al., 2012), HI self-absorption techniques (Busfield et al., 2006), and spectroscopic parallax methods (Damineli et al., 2005; Moisés et al., 2011).

In the case of the G305 complex, much work has already been conducted to determine the distance, both spectroscopic estimates (Danks et al., 1983; Danks et al., 1984; Leistra et al., 2005), or using kinematics (Georgelin et al., 1988; Russeil et al., 1998). Recent work within the G305 consortium has focused on providing two accurate independent measurements of both the kinematic and spectrophotometric distance to G305 (Davies et al., 2012). A estimate of the kinematic distance is first obtained from searching for known YSOs associated with the complex, from the Red MSX Source (RMS) survey (Hoare et al., 2005), that also have known radial velocities (Urquhart et al., 2007, 2009). Of these 15 objects, the mean radial velocity is found to be $v_{LSR} = -39.4 \pm 3.0\,\mathrm{km\,s^{1-}}$, and by applying the Galactic rotation curve of Brand & Blitz (1993), a kinematic distance of 4.2 ± 2.0 kpc is obtained. The spectrophotometric distance of G305 is calculated using the two optically visible open clusters Danks 1 & 2, by analysing the stellar population with an accurately determined luminosity. A final weighted mean of the distance to both Danks 1 & 2 of 4.16 ± 0.6, and 3.4 ± 0.2 kpc is found, being consistent with that determined through kinematics. We note that the main assumption in these estimates is that the stellar population used in the calculations is indeed associated with the wider G305 complex, and that it is one coherent structure.

With these results, we employ a distance to G305 of 3.2 - 4.4 kpc throughout our further studies, placing G305 within the Scutum-Crux arm of the Milky Way, as shown in Fig.2.3. The complex itself exhibits a trilobed cavity structure, and has a projected diameter of ≈ 30 pc, with the Wolf-Rayet star WR 48a some 2 pc

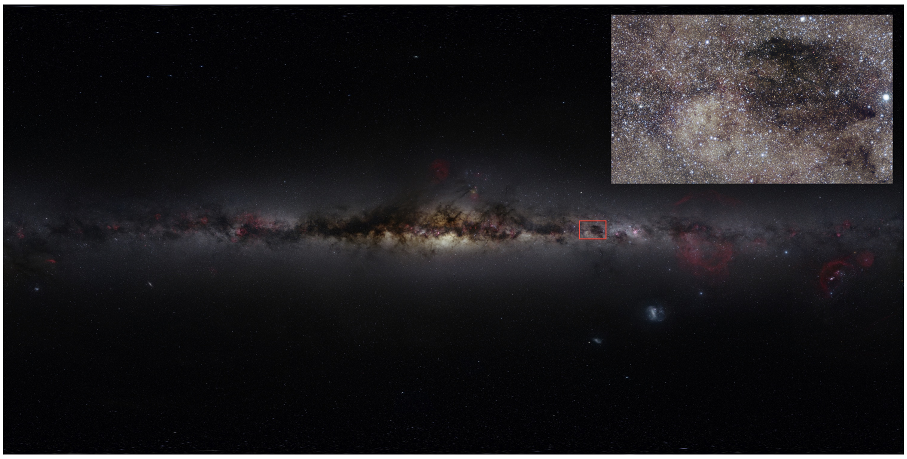

Figure 2.3: Location of the G305 complex within the Milky Way, show by the red box at $l = 305°$, $b = 0°$, with accompanying zoom window. Image courtesy of Nick Risinger, and the Photopic Sky Survey[2].

away from the two central open clusters of Danks 1 & 2, themselves separated by $\approx 3\,\mathrm{pc}$ (Clark & Porter, 2004; Davies et al., 2012).

2.3.2 The Age Of G305

We can begin to place limits on the age of the complex by studying the presence of particular stellar sources, and the lack of others. Firstly, there is a clear lack of supernova remnants within the G305 region as a whole, suggesting an age that is below some 8 Myrs (Bertelli et al., 1994; Martins, Schaerer & Hillier, 2005). In the case of Danks 1 & 2, Davies et al. (2012) identify the bulk of the stellar population within these clusters to be early-to-mid O dwarfs and supergiants, indicating an age of $\leqslant 6$ Myr. We also note the distinct lack of any luminous red supergiants present, which would have dominated the near-IR output of Danks 1 & 2 if such a population were to exist, suggesting an upper limit to the clusters of ≈ 4 - 5 Myr (Clark & Porter, 2004). Both Danks 1 & 2 represent the only optically visible clusters present within the complex, and as a result the most evolved state of the region. As a result, we can assume that the age of these clusters would be indicative of the age of the complex as a whole.

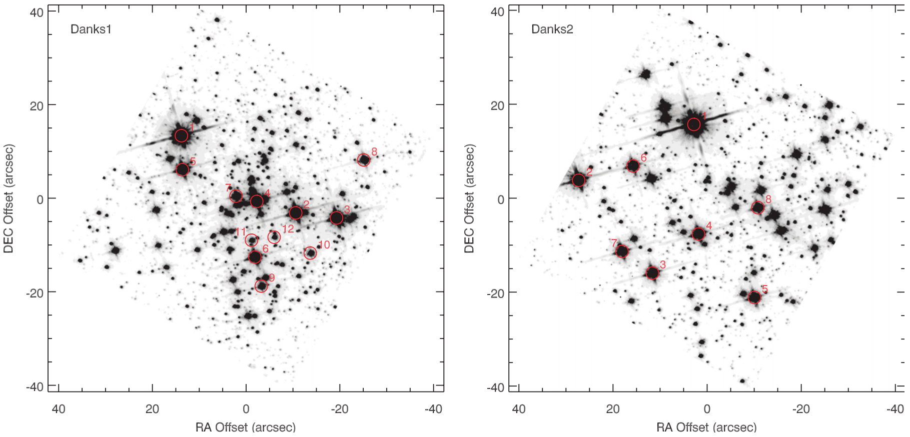

Figure 2.4: Hubble 1.4 - 1.8 μm mosaic of left: Danks 1, and right: Danks 2. The red circles correspond to the stellar identifications in Table 2 of Davies et al. (2012).

Davies et al. (2012) estimate the age of Danks 1 & 2 using near-IR observations from the *Hubble Space Telescope* Near Infrared Camera and Multi-Object Spectrometer (NICMOS); Fig.2.4 shows a 1.4 - 1.8 μm mosaic of both open clusters. The age of both Danks 1 and 2 is estimated using three separate methods: through analysis of each stellar populations in each cluster, by examining the main sequence turn-offs, and by also studying the low-mass pre-main sequence population found within also. From a combination of all these results, Danks 1 is found to be $1.5^{+1.5}_{-0.5}$ Myr, while Danks 2 is the elder at 3^{+3}_{-1} Myr.

2.3.3 The Mass Of G305

A calculation of the mass of the complex was first provided by Hindson et al. (2010), where an estimation of the amount of dense gas within the complex is obtained from estimating the physical properties of detected NH_3 clumps within the region. The amount of dense gas within the region provides an excellent estimate to the reservoir of material for future star formation, and NH_3 proves an excellent tracer with a critical density of $\approx 10^4\,\mathrm{cm}^{-3}$ (Stahler & Palla, 2005). Typically NH_3 emission is found to be associated with cool dense clouds, with

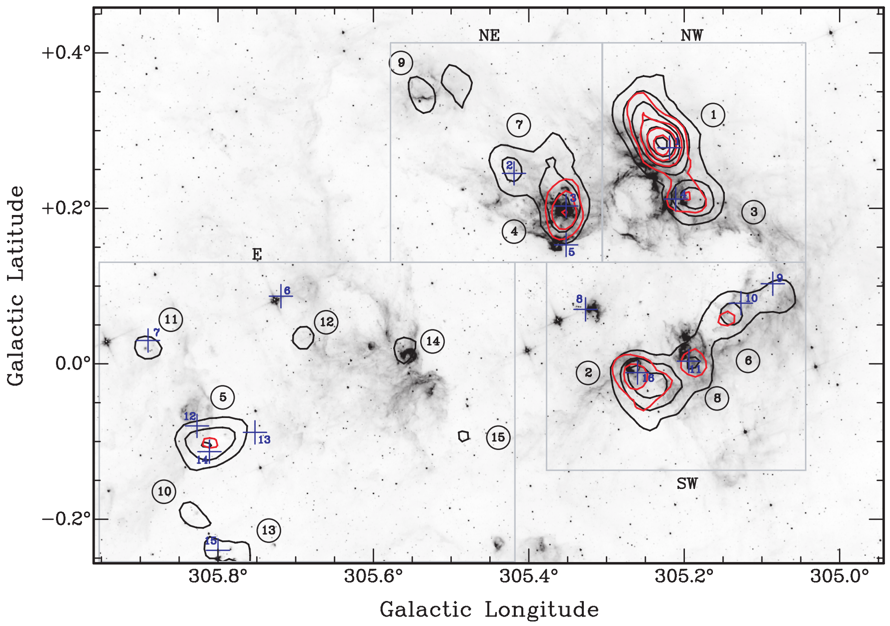

Figure 2.5: Contour map of the peak temperature of the 15 NH_3 clumps identified by Hindson et al. (2010), overlay on to a GLIMPSE 5.4 μm grey scale image; the contours begin at 0.15 K, increasing in 0.1 K increments. The locations of the 16 H_2O masers identified, and discussed in section 2.5.8, are also show as blue crosses.

temperatures <10 K (Molinari et al., 1996b; Urquhart et al., 2011a), and also with compact HII regions at temperatures >100 K (Cesaroni et al., 1994). In the case of cool dense clouds, such temperature are found to be too low for more common gas tracers, such as CO, to be released into the gas phase (Bergin et al., 2006).

As seen in Fig.2.5, Hindson et al. (2010) identify a sample of 15 NH_3 clumps distributed around the central cavity of the complex, with these clumps varying in sizes between 1.5 - 5.1 pc, and all found to be above $\approx 10^3\,M_\odot$. By summing the contribution of these NH_3 clumps, Hindson et al. (2010) derive a total mass of $\approx 6\times10^5\,M_\odot$. This result suggests that there is a significant reservoir of dense molecular gas, located along the periphery of the central cavity, to which future star formation can occur. However, star formation is a highly inefficient process, where on average some 2 - 17 % of this material will go on to form stars (Williams & McKee, 1997); adopting such an efficiency suggests a further $\approx 8 \times 10^3\,\mathrm{M}_\odot$ of material is likely to form stars.

2.3.4 The Morphology Of G305

Fig.2.6 provides a *Spitzer* Galactic Legacy Infrared Mid-Plane Survey Extraordinaire (GLIMPSE) three-colour image of the complex, and highlights the dynamic morphology apparent when observing G305. This mid-IR observation is particularly useful at the $8\,\mu$m filter, which is dominated by polycyclic aromatic hydrocarbon (PAH) features (Tielens, 2008); these being excited in the surface layers of molecular clouds that have been exposed to high amounts of UV radiation, and by extension are tracers of photodissociation regions (PDRs) (Leger & Puget, 1984b). As a result of this relationship, PDRs are considered good tracers of molecular clouds interacting with a surrounding HII region, and serve as good tracers of star formation (Urquhart et al., 2003).

What is apparent from both Figs.2.6 - 2.7, is the three distinct lobes of emission, surrounding a clearly non-spherical central cavity, of which both Danks 1 & 2 and WR 48a reside within. The location of these sources, and the almost blown and sculpted surrounding material, would strongly suggest that the powerful stellar winds and UV radiation that would originate from the central population, could be the driving force for the present morphology; a similar sculpted morphology is observed in other massive star-forming regions, such as M17 (Povich et al., 2007). In addition to this complex structure, numerous signposts of ongoing star formation have been identified along the periphery of the central cavity, in the form of embedded MYSOs, compact and ultracompact HII regions, H_2O, OH, and methanol masers (Urquhart et al., 2007; Urquhart et al., 2009; Hindson et al., 2010; Hindson et al., 2012; Clark, Davies & Thompson, 2011; Faimali et al., 2012). Combining the overall morphology, with the numerous epochs of sequential star formation, G305 is clearly a highly active and dynamic region, that strongly suggests some form of initiated and sustained interaction between the ionised and neutral environments.

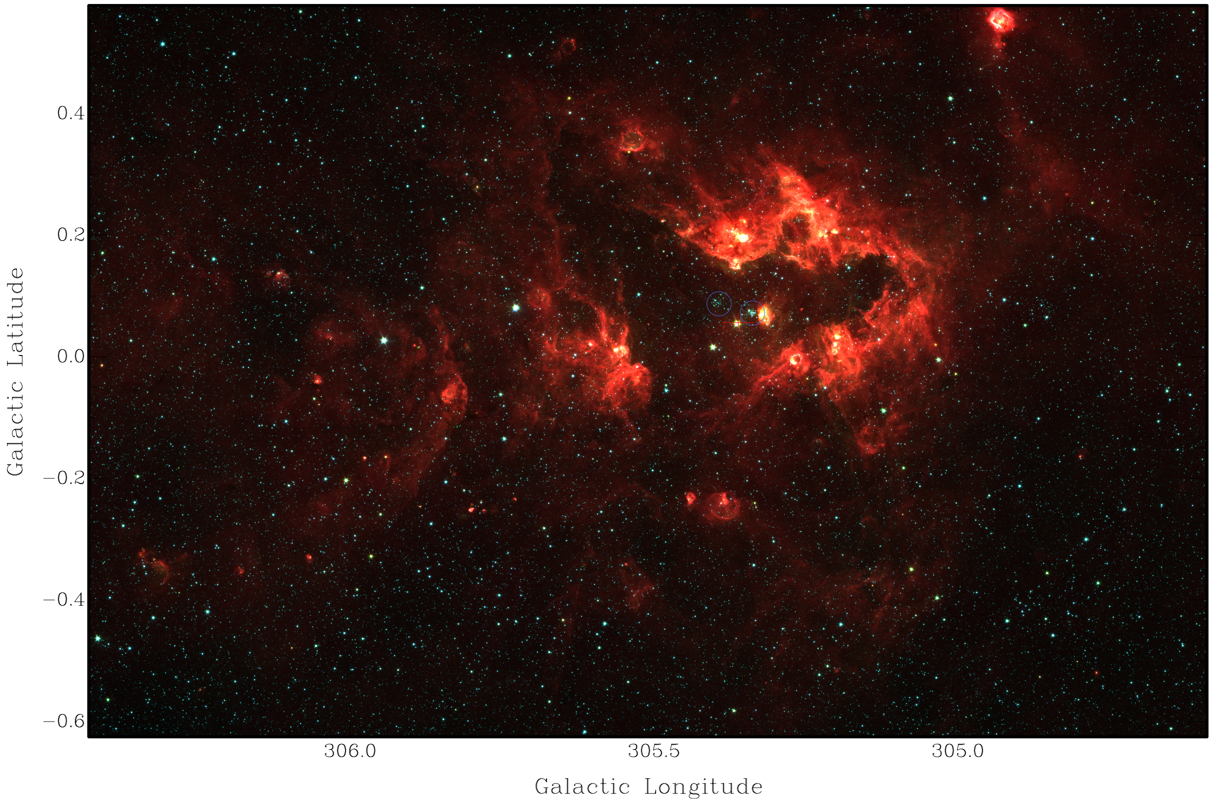

Figure 2.6: Three-colour (blue = 3.6 μm, green = 4.5 μm, red = 8 μm) GLIMPSE image of the G305 star-forming region. The positions of Danks 1 & 2 are shown as blue circles, while WR 48a is shown as a red cross.

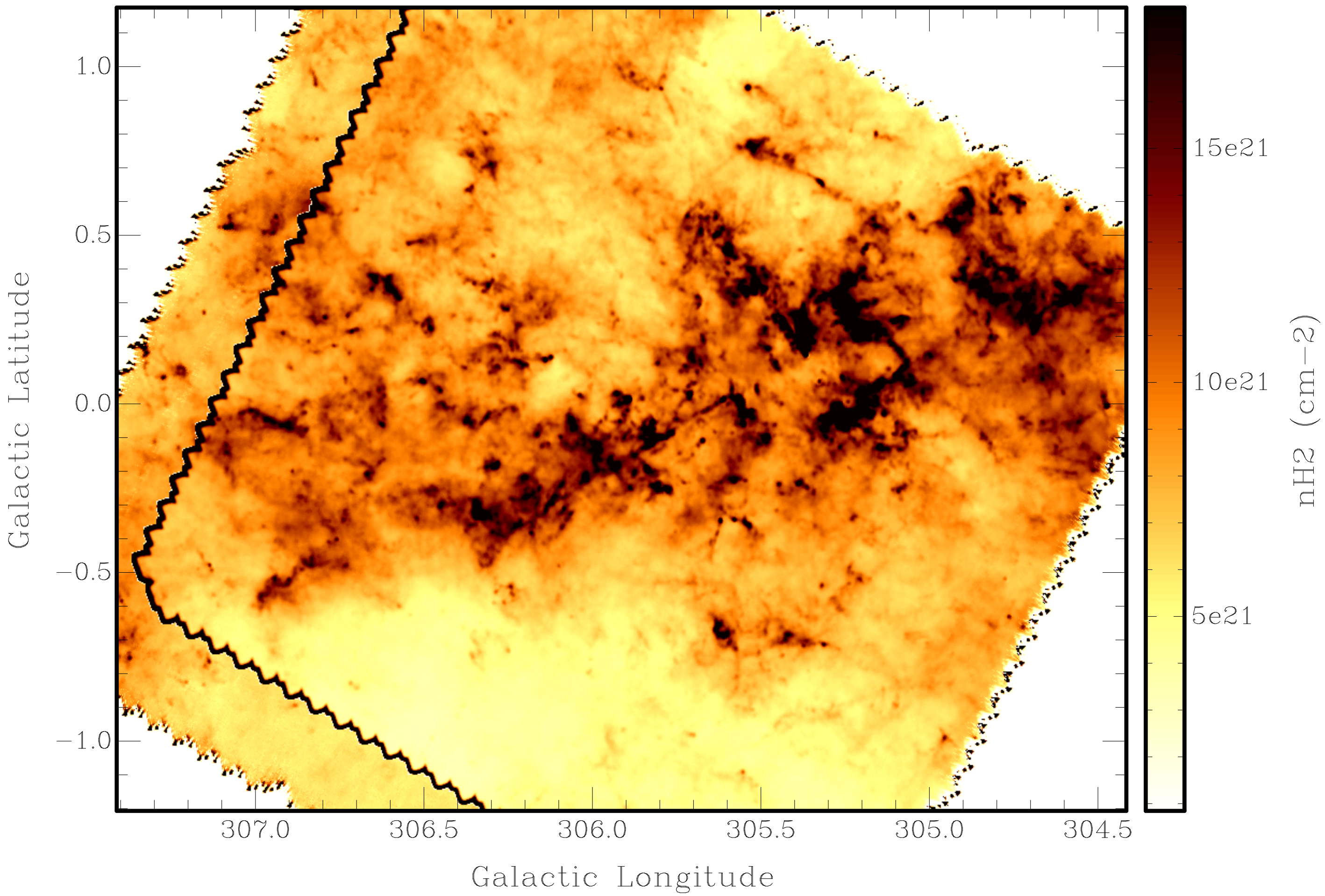

Figure 2.7: A *Herschel* Hi-GAL column density map, derived from PACS and SPIRE observations of G305. The column density map is produced via pixel-by-pixel modified blackbody SED fitting to all five PACS/SPIRE observed wavelengths, following the approach of Giannini et al. (2012), with a dust emissivity index $\beta = 2.0$.

2.4 Previous Studies Of G305

The work we have conducted on G305, and discuss in Chapters 3 and 4, follows in a series of previous studies of massive star formation within the G305 star-forming complex. Previously, Hindson et al. (2010) have focused on the reservoir for star formation within the region through observations of NH_3 emission, while tracing sites of active star formation through H_2O maser emission. To complement this, Davies et al. (2012) have recently carried out a near-infrared study of the two central open clusters Danks 1 and 2. Current work has focused on identifying compact radio emission that is indicative of UC HII regions towards G305 (Hindson et al., 2012). Below we outline a brief overview of the identified massive stellar population within G305, and known tracers of current star formation within the complex; we use Fig.2.8 as a reference for these sources.

As mentioned in Section 2.3.2, the central population of Danks 1 & 2 are likely the upper limit of the age of the complex, with star formation following on from this (in Chapter 3 we estimate a delay of $\approx 2.4\,$Myr after the formation of Danks 1 & 2, for the next generation of star formation to occur). Aside from the stellar content identified in Danks 1 & 2 by Davies et al. (2012), there is also a further subset of massive stars present within the complex. Firstly, Leistra et al. (2005) have identified a sample of three high-mass stars (Sources L05-A1, A2, and A3 in Table A.1) towards the HII region designated G305.254 + 0.204; these three stellar sources can clearly be seen in the top right of Fig.2.8. As noted by Leistra et al. (2005), this population of stars lies entirely within the $8\,\mu$m emission, with the general appearance being that of a windblown bubble, possibly the result of L05-A1, A2, and A3 driving the expansion of the HII region. Further to this population, located in proximity to Danks 1 & 2, Mauerhan, van Dyk & Morris (2009); Mauerhan, Van Dyk & Morris (2011) identify eight WR stars, in addition to WR 48a, within the G305 region (Sources MDM3 - 9, and J13125770 6240599 in Table A.1). It is found that the sources MDM3, 4, 5, 6, and WR48a are well separated from Danks 1 by ≈ 20" which, assuming a distance to G305 of $\approx 3.5\,$kpc, suggests a physical distance of ≈ 2 - $25\,$pc. This extended distribution may be the result of gravitational encounters within the cluster, causing this WR sample to runaway from their cluster birthplace; some 10 - 30 % of O-type stars form within clusters, only to be ejected due to dynamic interactions within the cluster (Moffat & Isserstedt, 1980; Moffat et al., 1998). Taking an upper limit to the ejection velocity of OB runaways stars, of 30 - 40 kms^{-1} (Gvaramadze et al., 2012), suggests it would take $\approx$ 0.7 - 0.5 Myr for this sample of WR stars to reach their present positions, a timescale well within the age of Danks 1 & 2.

Aside from this sample of massive stars, G305 has also a substantial sample of ongoing star formation tracers present. Towards G305 a total of some 38 sites of maser emission were found (see Table A.2 for maser positions), comprising of some 16 H_2O masers (Hindson et al., 2010), a further 17 methanol masers (Green et al., 2012), and finally some 5 OH masers (Caswell, 1998); in total some 4 sites of maser emission are found to be coincident with each other (as seen in Fig.2.8). Adding to this maser population, a further sample of some 14 MYSOs (see Table A.2) that are positionally associated with the complex, are identified from the RMS database[1] (Hindson et al., 2012). Finally, Hindson et al. (2012) have identified a sample of 6 UC HII regions present within the G305 region; their presence confirming the existence of a younger generation of massive star formation occurring, in comparison to the classical and compact HII population found within the complex.

Clark & Porter (2004) inferred from the radio flux of G305 that a minimum of 31 canonical O7V stars would be required to provide the necessary Lyman ionising flux. Previously, Davies et al. (2012) proposed that the massive stellar population of Danks 1 & 2 provided a sufficient ionising flux to power the observed radio emission towards G305. However, Hindson et al. (2012) suggest that it is in fact the population of classical and UC HII regions, identified around the periphery of the central cavity, that are responsible for the majority of the observable ionising flux. From Fig.2.8 we can see that the majority of the massive stars present within G305 are located within the central cavity of the complex, where their powerful winds and radiation has cleared away the natal molecular cloud that was in the immediate vicinity of Danks 1 & 2. This clearing of material around the central population has swept and compressed the gas, causing a second generation of star formation along the periphery of the central cavity; this idea is supported by the overwhelming presence of maser emission, UC HIIs, and RMS MYSOs present

---

[1] The RMS survey database can be found at http://www.ast.leeds.ac.uk/RMS/.

along the rim of the central cavity. This ordering of previous, and current star formation, along with the dynamic morphology of the complex is highly suggestive of triggered star-formation occurring within the G305 complex (Elmegreen & Lada, 1977; Elmegreen, 2002).

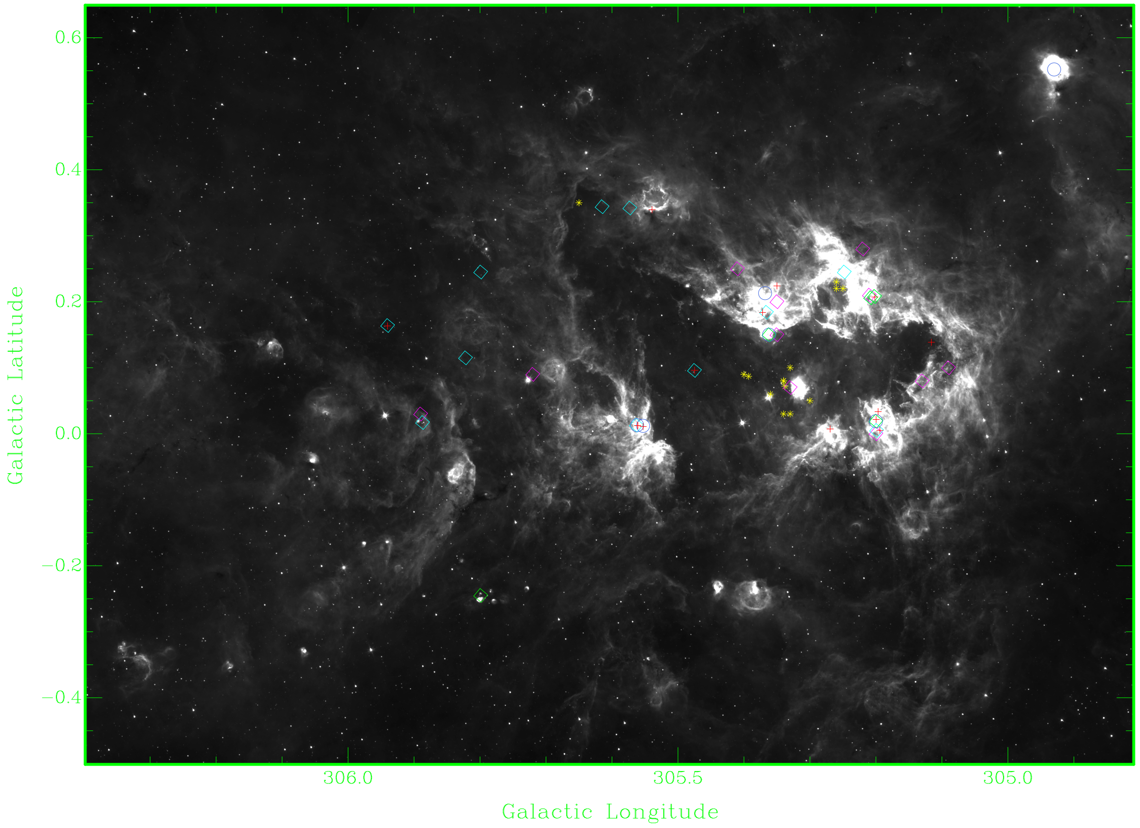

Figure 2.8: A GLIMPSE 8 μm image of the present state of star formation within G305. The positions of high-mass stars are shown with yellow asterisks. Maser emission is show with diamonds, with H_2O masers in magenta, methanol masers in cyan, and OH masers in green. The sample of UC HII regions identified within G305 are shown with blue circles, while finally RMS detected YSOs are shown with red crosses.

2.5 Ancillary Datasets For G305

Currently there is a plethora of datasets, over a broad range of wavelengths, covering the G305 complex that are publicly available. As a result of this, we are able to conduct a multi-wavelength analysis of the complex, allowing us to deeply probe the star formation activity, and surrounding environment of G305. Our results are presented in Chapters 3 and 4, while below we outline the various ancillary datasets that are utilised in our studies.

2.5.1 VISTA VVV

The VISTA variables in the Via Lactea (VVV) survey is a near-IR survey of the Milky Way, using the European Southern Observatory 4.1 m-class telescope located at the Cerro Paranal Observatory in Chile. In total, the survey will cover some 562 deg^2 of the Galactic bulge between $-10° < l < 10°$ and $-10° < b < 5°$, and the southern disk between $-65° < l < -10°$ and $-2° < b < 2°$, with an estimated 10^9 point sources in total. The VVV survey will be conducted over the period of 2010 2014, and will map the Galactic bulge and adjacent mid-plane over an estimated 189 epochs (Minniti et al., 2010).

VISTA is fitted with a single instrument, VIRCAM (VISTA InfraRed CAMera (Dalton et al., 2006; Emerson & Sutherland, 2010), and is equipped with five broad-band filters Z (0.87 μm), Y (1.02 μm), J (1.25 μm), H (1.64 μm), and K_s (2.14 μm), and two narrow-band filters centred at 0.98 and 1.18 μm. Using aperture photometry, the limiting magnitude for the majority of fields is $K_s \approx 18.0$ mag, while within crowded fields ($|\,b\,| \leq 1°$) a limit of $K_s \approx 16.5$ mag is reached (Saito et al., 2012). The VVV survey is foremost a survey of variability within the Galactic bulge, cataloguing some 10^6 variable objects in total (Minniti et al., 2010), but will also serve as a complementary survey to existing 2MASS *JHK* photometry (Cutri et al., 2003), by increasing the both the sensitivity, and adding two additional wavelength regimes (Z and Y).

2.5.2 2MASS

The Two Micron All Sky Survey (2MASS) comprises a near-IR survey of some 99.998 % of the celestial sphere, conducted between June 1997 and February 2001, utilising two 1.3 m telescopes at Mount Hopkins, Arizona, and Cerro Tololo, Chile. The survey provides uniform photometry, and precise astrometry in the J, H, and K_s photometric bands, with a $10\,\sigma$ point-source detection limit of 15.8, 15.1, and 14.3 mag at the J, H, and K_s bands respectively (Skrutskie et al., 2006).

In total, some 470,992,970 sources are recorded within the 2MASS Point Source Catalogue, with only 0.64 deg^2 of the celestial sphere missing (due to 50 mispointed tiles leaving narrow uncovered gaps between neighbouring tiles). Source extraction for bright sources has a $1\,\sigma$ uncertainty of < 0.03 mag, and an astrometric accuracy of 100 mas (Cutri et al., 2003).

2.5.3 *Spitzer* GLIMPSE

The *Spitzer* GLIMPSE survey covers an area of some 220 deg^2, between $10^\circ < l < 65^\circ$ and $|\,b\,| \leq 1^\circ$, including the outer ends of the Galactic bar, the Galactic molecular ring, inner spiral arms, and the spiral-arm tangencies. In total, some 10 million point sources are recorded in the GLIMPSE Point Source Catalogue (Benjamin et al., 2003). The survey utilises the *Spitzer* InfraRed Array Camera (IRAC), centred at 3.6, 4.5, 5.8, and 8.0 μm, and a high angular resolution of $\approx$1.2”, with a $1\,\sigma$ sensitivity of 0.92, 1.22, 6.0, and 9.0 μJy at 3.6, 4.5, 5.8, and 8.0 μm respectively (Fazio et al., 2004).

2.5.4 *Spitzer* MIPSGAL

MIPSGAL is a 278 deg^2 survey of the inner Galactic plane, comprising of two observing programmes: MIPSGAL I covers $10^\circ < l < 65^\circ$, and $295^\circ < l < 350^\circ$ with latitude $|\,b\,| \leq 1^\circ$. MIPSGAL II extends the survey to higher latitudes, $|\,b\,| \leq 3^\circ$ in the Galactic center region of $l = 350^\circ$ to $l = 10^\circ$ (Mizuno et al., 2008)

The survey makes use of the Multiband Imaging Photometer System (MIPS) aboard *Spitzer* (Rieke et al., 2004), imaging in two passbands of 24 and 70 μm, with resolutions of 6" and 18" and a 5 σ point source sensitivity of 1.3 and 73 mJy respectively. The principle focus of the survey was to provide a uniform, well-calibrated dataset of the inner Galactic Plane, to complement previous shorter wavelength *Spitzer* surveys, such as GLIMPSE (Carey et al., 2009).

2.5.5 RMS Survey

The Red MSX Source (RMS) survey[1] is an ongoing multi-wavelength programme, aiming to identify a genuine sample of MYSOs and UC HII regions located throughout the Galactic plane (Hoare et al., 2004; Urquhart et al., 2008b). The survey employs the mid-IR observations of the Midcourse Space Experiment (MSX), with the on board Spirit III instrument surveying the entire Galactic plane between $|\,b\,| \leq 5^{\circ}$ at 4.29, 4.35, 8.28, 12.13, 14.65, and 21.3 μm, at a spatial resolution of $\approx$ 18"(Price et al., 2001).

The RMS survey utilises a colour-cut selection, based on the colours of well-known MYSOs from the MSX and 2MASS Point Source Catalogues, to identify potential MYSOs within the survey area (Lumsden et al., 2002). Though the survey is limited by the resolution of the MSX data, a substantial multi-wavelength follow-up programme has been conducted by the RMS team, to remove contaminating sources that display similar colours to very red MYSOs, such as UC HII regions, planetary nebulae, evolved stars, and low mass YSOs (Urquhart et al., 2007; Urquhart et al., 2007; Urquhart et al., 2009; Urquhart et al., 2009; Urquhart et al., 2011b).

2.5.6 *Herschel* Hi-GAL

The *Herschel* Infrared GALactic plane survey (Hi-GAL) (Molinari et al., 2010b) is an Open Time Key Project on board the 3.5 m *Herschel* Space Observatory (Pilbratt et al., 2010), mapping a two degree wide strip of the inner Galactic plane, between $|\,l\,| \leq 60^{\circ}$ and $|\,b\,| \leq 1^{\circ}$. The survey combines both the PACS (Poglitsch et al., 2010) and SPIRE (Griffin et al., 2010) cameras aboard *Herschel*, to produce maps at 70 and 160 μm with PACS and 250, 350, and 500 μm with

---

[1] The RMS survey database can be found at http://www.ast.leeds.ac.uk/RMS/.

SPIRE. From the Hi-GAL survey, we find within the G305 region, that some 3288 infrared sources are detected by *Herschel* (Faimali et al., 2012). A detailed analysis of G305, employing the *Herschel* Hi-GAL results, is discussed at length in Chapter 3.

2.5.7 Australia Telescope Compact Array

The Australia Telescope Compact Array (ATCA) is an array of six 22 m antennas, at the Paul Wild Observatory, located some 25 km west of the town of Narrabri in New South Wales, Australia[1].

Hindson et al. (2012) have conducted a wide-area observation of the G305 complex at both 5.5 GHz and 8.8 GHz, placing the antennas in several configurations with maximum and minimum baselines of 6 km and 30 m. From these observations, a sensitivity of 0.07 and 0.15 mJy beam^{-1} are achieved at 5.5 GHz and 8.8 GHz respectively. We make use of the 5.5 GHz radio continuum observations towards G305, which at the longest baseline has a resolution of $\approx$ 1.4", and at the shortest baseline of 30 m has a resolution of $\approx$ 5'. In total, some 71 radio sources are found randomly distributed across the observed field, of which 15 are found to be associated with G305, while the remaining 56 sources are found to be background radio sources. Of this sample of 15 associated sources, six are identified as candidate UC HII regions, some eight sources are found to be stellar radio source, and one source is a bright rimmed cloud (Hindson et al., 2012).

2.5.8 Mopra Telescope

The Australia Telescope National Facility (ATNF) Mopra Telescope comprises a 22 m single-dish radio telescope , that is situated some 26 km outside the town of Coonabarrabran in New South Wales, Australia[2]. Mopra is situated at a latitude of -31°, and has an elevation of 866 m above sea level. We employ the 22 GHz H_2O maser observation conducted by Hindson et al. (2010) of the G305 complex,

---

[1] The Australia Telescope Compact Array is part of the Australia Telescope National Facility (ATNF), which is funded by the Commonwealth of Australia for operation as a National Facility managed by CSIRO.

[2] The telescope is operated by the Commonwealth Scientific and Industrial Research Organisation (CSIRO) Astronomy and Space Science division.

with a $\approx 2'$ angular resolution. In total, some 16 H_2O masers are observed within G305.

2.5.9 Methanol Multi-Beam Survey

The Methanol Multi-Beam Survey (MMB) is a project to survey the entire Galactic plane, to identify all 6.7 GHz methanol masers present within a positional accuracy of ≤ 0.4" (Green et al., 2009; Caswell et al., 2010). Observations for the MMB survey within the southern hemisphere, covering $-174° < l < 60°$, are firstly conducted using the Parkes 64 m radio telescope, situated some 20 km north of the town of Parkes, New South Wales, Australia. To complement these observations, further follow-up observations, to obtain accurate position measurements, are obtained using the ATCA. Within the G305 complex, the MMB survey identify some 17 methanol masers (see Green et al. (2012), Table 2 for their positions).

Chapter 3

Embedded Massive Star Formation, and The Star Formation Rate of G305

"The nitrogen in our DNA, the calcium in our teeth, the iron in our blood, the carbon in our apple pies were made in the interiors of collapsing stars. We are made of starstuff." - Carl Sagan

3.1 Motivation

As was shown in Chapter 2, within the G305 complex there are numerous signposts of massive star formation, some of which are located on the periphery of the central cavity, such as infrared hotspots, compact and ultra-compact (UC) HII regions, H_2O, OH, and methanol masers (Urquhart et al., 2007; Hindson et al., 2010). Fig.3.1 underlines the dynamic morphology of the region, with the central location Danks 1 & 2 and WR 48a thought to be the main source of energy input and the driving force behind the expansion and clearing of the central diffuse HII region in the complex (Clark & Porter, 2004). The suggestion is an interaction between the centrally embedded sources and the surrounding cloud, with an occurrence of ongoing massive star formation being located in the hot dust emission sites (seen in blue in Fig.3.1) on the periphery of the central cavity. With the presence of numerous and different epochs of star formation in one location, and the relative close proximity, the G305 star-forming complex affords us an exceptional opportunity to study the nature of massive star formation, and investigate the environmental impact this may have on the formation of future generations of stars (Elmegreen, 2002; Elmegreen & Lada, 1977).

In this chapter we present work from Faimali et al. (2012), involving a far-infrared (far-IR) study of the G305 complex using *Herschel* (Pilbratt et al., 2010), in conjunction with radio continuum, H_2O maser, methanol maser, MIPS, and Red MSX Source survey data, with the aim of identifying sites of embedded massive star formation. In this study we are able to identify the embedded population within G305, since the *Herschel* far-IR observations are unaffected by dust, and combined with mid-IR data, constrain the luminosities of individual YSOs. By incorporating the luminosities of the embedded massive star-forming population with the initial mass function (IMF), we are able to determine the SFR of G305 and investigate the star formation history of the region. This resolved, Galactic SFR can then be compared to extragalactic SFR indicators to test whether the two regimes are consistent with one another, and identify where fundamental differences may lie (Heiderman et al., 2010; Lada, Lombardi & Alves, 2010).

This work serves as an example of how *Herschel* data can be applied to Galactic star-forming regions, such as G305, in order to identify the high-mass stellar content of such complexes, and how the star formation activity can be inferred from this population. The *Herschel* observations provide an unbiased dataset that is ideal in conducing a Galactic wide survey; both the high spatial resolution (sub - 30") and wavelength coverage that traces the peak of the dust SED, allows us to identify sites of embedded high-mass star formation and accurately constrain both the temperatures and luminosities of such sources. Following from this, a comprehensive YSO counting approach, similar to that conducted by Povich et al. (2011) for the Carina complex, is conducted in Chapter 4, to tackle the incompletenesses present at the intermediate, and low-mass range.

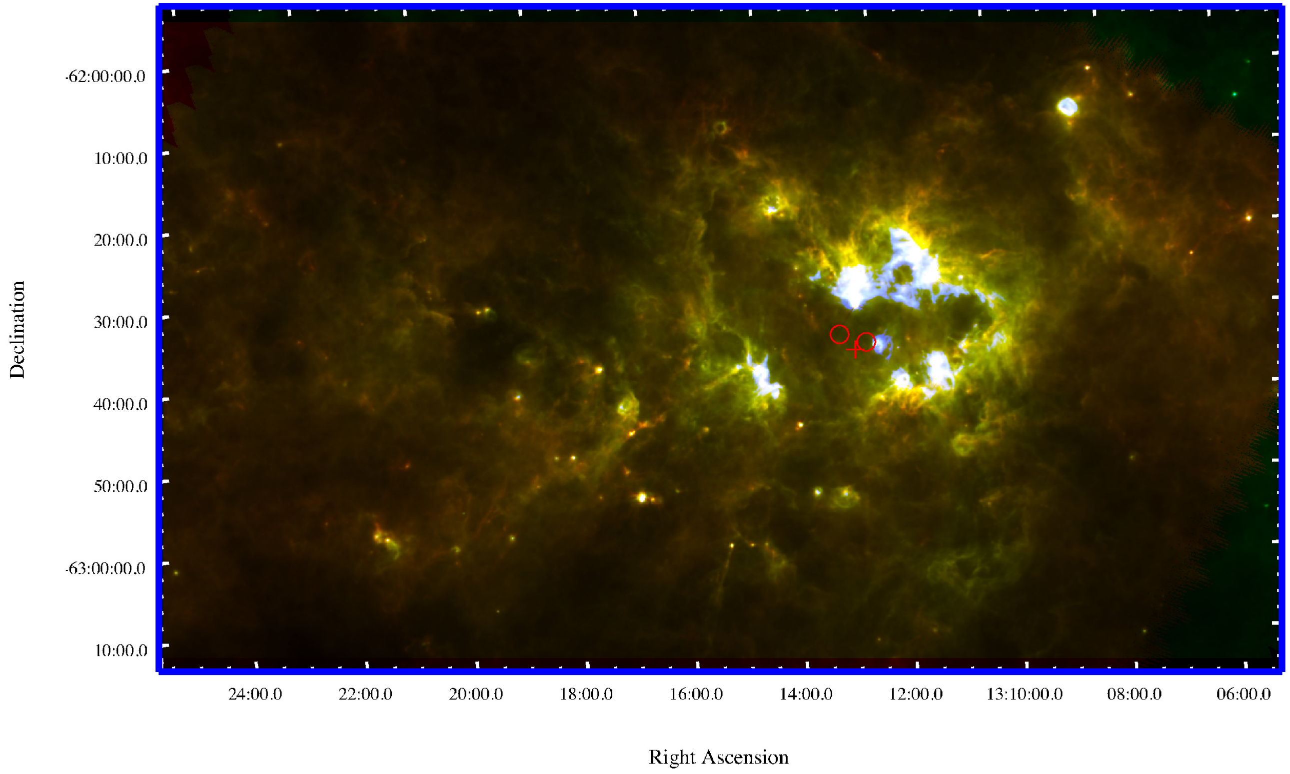

Figure 3.1: Three-colour (blue = 70 μm, green = 160 μm, red = 350 μm) *Herschel* Hi-GAL image of the giant HII region G305. The 70 μm emission corresponds to hot dust emission ($\geq$ 40 K), while the 350 μm emission emanates from more cold dust ($\leq$ 20 K). The positions of both Danks 1 & 2 (circles), and WR 48a (cross) are overplotted.

3.2 Observations & Data Analysis

3.2.1 Herschel Hi-GAL

The *Herschel* Infrared GALactic plane survey (Hi-GAL) (Molinari et al., 2010b) is an Open Time Key Project on board the ESA *Herschel* Space Observatory (Pilbratt et al., 2010), mapping a two degree wide strip of the inner Galactic plane, in the longitudinal range $|\, l \,| \leq 60^{\circ}$ and latitude range $|\, b \,| \leq 1^{\circ}$. The survey takes advantage of the PACS (Poglitsch et al., 2010) and SPIRE (Griffin et al., 2010) cameras operating in parallel mode, scanning the sky in a raster fashion at a rate of $60\,''\,\mathrm{s}^{-1}$, while PACS and SPIRE acquire data simultaneously. The survey has a total angular resolution, θ, of $10'' \leq \theta \leq 30''$ across five photometric bands at 70 and $160\,\mu$m with PACS and 250, 350, and $500\,\mu$m with SPIRE. The overall aim is to catalogue star-forming regions and study cold structures across the ISM. Using the broad spectral coverage available, the intention is to study the early phases of star formation, with particular focus on providing an evolutionary sequence for the formation of massive stars within the Galactic plane.

The catalogue of compact infrared sources for the G305 region is obtained using the CuTEx (CUrvature Thresholding EXtractor) code highlighted by Molinari et al. (2011). The detection technique considers the curvature properties of astronomical images, rather than source detection through signal intensity, by building a "curvature" image from the observed image using double-differentiation in four separate directions. The advantage of this approach is that resolved, compact sources are easily detected, while the diffuse thermal emission from cold dust associated with the fore/background is greatly reduced. Photometry estimates of candidate sources are then performed by fitting an elliptical two-dimensional Gaussian with an underlying planar inclined plateau.

The completeness of the infrared source catalogue is estimated using a simulated field of some 1000 artificial sources, initially at $250\,\mu$m, comprising both a compact dust component (such as YSO envelopes, or dense molecular cores or clumps), and the diffuse emission present towards the Galactic plane (Molinari et al., 2010a). In all, source recovery rate is found to be 90% for sources of peak fluxes of 0.2 Jy/pixel (equivalent to approximately 5σ), with peak fluxes being within 30% of their input value in 80% of recovered input sources (Molinari et al., 2011).

Identifying each source within the five different bands is obtained considering their basic positional association, starting with source extraction at the longest of the observed wavelengths, i.e. at 500 μm. From this first band, an association is established with the next band (i.e. 350 μm) if a source is present within a search radius that corresponds to the *Herschel* beam size at the longer of the two considered wavelength, in this case a radius of 18.1" at 500 μm. In the case where multiple associations are found, the closest one is kept. This is more frequent at 70 μm (Elia et al., 2010). At this stage the flux contribution at longer wavelengths has not been split up into contributions from multiple associations at 70 μm, however we find 87% of 500 μm sources are associated with a single 70 μm detection. Of the remaining 500 μm sources with multiple 70 μm associations, the majority are found to have the bulk of the 70 μm flux assigned to their primary 70 μm counterpart. We find only 3% of 500 μm sources to have lost a fraction of 70 μm flux through multiple associations. This loss is deemed negligible, being on the order of 1.5% of the total 70 μm flux.

Finally, the celestial coordinates assigned to the sources are those which correspond to the shortest wavelength association, which by definition will have the highest spatial resolution (Molinari et al., 2010a). As a result of this, in total some 3288 infrared sources are detected across the G305 region in Hi-GAL; of these some 1913 sources are detected at 70 μm, 1658 at 160 μm, 1257 at 250 μm, 856 at 350 μm, and 530 sources at 500 μm. Not all sources are detected in all wavebands, and this can be accounted for by either positional association failing, or that the flux obtained for a source in a particular band had been corrupted by factors such as source crowding, or confused background conditions (Molinari et al., 2010a).

3.2.2 Ancillary Data

To complement our data set we utilise mid-IR, radio, H_2O and methanol maser data matched to the Hi-GAL far-IR data to broaden our view of the G305 complex, aiding in the consideration of the morphology, and star formation within the region.

We firstly make use of the 5.5 GHz radio continuum observations towards G305 using the Australia Telescope Compact Array (ATCA) (Hindson et al., 2012), with a sensitivity of $\approx 0.07\,\mathrm{mJy\,beam^{-1}}$, as a means to distinguish UC HII regions across the complex. A key method of detecting HII regions is through the associated radio emission; at wavelengths greater than 3 mm, thermal dust emission drops off, and the dominant detection is due to thermal free-free radio emission from the ionised gas in the inner region surrounding the massive star. The Lyman continuum photons that are emitted from the central star are balanced by recombination within the volume of ionised hydrogen; it is these Lyman continuum photons that are responsible for the detected radio emission. For this emission, stellar models suggest stars of spectral type B3 or earlier are capable of producing the required ionising flux of Lyman continuum photons ($\mathrm{E} > 13.6\,\mathrm{eV}$, i.e. $912\,\mathring{A}$) (Crowther & Conti, 2003). Such a spectral type is selected since the Lyman continuum flux then begins to rapidly drop off with decreasing effective temperatures (Panagia, 1973).

To also locate areas of ongoing star formation, we employ both 22 GHz H_2O maser observations using the Australia Telescope National Facility (ATNF) telescope Mopra (Hindson et al., 2010), and the 6.7 GHz methanol maser observations of the Methanol Multi-Beam survey (Green et al., 2009; Caswell et al., 2010) with the Parkes 64 m radio telescope and follow ups by the ATCA. Since their discovery, methanol masers have been recognised as one of the most distinct signposts of massive star formation (Menten, 1991), and only found close to high-mass young stars (Minier et al., 2003). H_2O maser emission, on the other hand, has also been shown to provide a useful indicator of both low- and high-mass star formation, and are found to associate mainly with both hot molecular cores and UC HII regions (Furuya, 2003).

Finally, we also make use of mid-IR data from both the Red MSX Source (RMS) survey that aims to identify a large sample of genuine massive young stellar objects (MYSO) and UC HII regions located throughout the Galactic plane (Urquhart et al., 2008a), and the $24\,\mu$m point source catalogue from the *Spitzer* MIPS Galactic Plane Survey (MIPSGAL) (Mizuno et al., 2008; Carey et al., 2009) which aims to identify all high-mass protostars located in the inner

Galactic disk.

3.2.3 Identification Procedure

Our aim is to identify a statistically reliable sample of counterparts to the Hi-GAL infrared catalogue, by matching this catalogue to the ATCA radio, MMB, RMS, Mopra H_2O maser, and MIPSGAL catalogues. By using a frequentist technique, highlighted by Lilly et al. (1999), we can identify all associations found within G305, by establishing the probability that matches to Hi-GAL sources are not the result of a chance alignment. We approach this using a Monte Carlo method, with the technique outlined in the following subsection for the case of Hi-GAL infrared and ATCA radio counterparts.

3.2.3.1 Association Probabilities

Starting from the matching of both the Hi-GAL infrared and ATCA radio catalogues, we need to consider the possibility of chance alignments and provide an estimate as to how reliable each individual match may or may not be. We therefore need to derive some statistical argument that considers the probability that a candidate compact radio source is indeed correctly identified within the search radius of the associated infrared source. A method based on the positional coincidence, similar to that adopted by Downes et al. (1986) and Sutherland & Saunders (1992) is employed.

The necessity to work out a statistic which can inform whether an association is indeed true, or by chance can be shown by considering the ATCA radio data. A certain number of the 71 radio sources identified across the field will be accounted for by extragalactic background sources. We can estimate the total amount of background sources empirically from the extragalactic source count approach of Anglada et al. (1998). The number of background radio sources, $\langle N_{Radio} \rangle$, that would be expected to be observed given the region size, and frequency of observation is defined by:

$$\langle N_{Radio} \rangle \simeq \left(\frac{\theta_f}{\theta_A} \right) 1.1\, S_0^{-0.75} \tag{3.1}$$

where θ_f is the diameter of our observed field, θ_A is the FWHM of the primary beam (in arcminutes), and S_0 is the sensitivity of the radio observations at 5.5 GHz. Using this approach, we find that some 60 ± 8 background sources in total should be detected across the G305 field (Hindson et al., 2012).

As an example, to explain the positional coincidence method, we use our identified infrared-radio associations. For each association we calculate that for each ATCA compact radio source candidate with magnitude m at a distance r from the matched to the Hi-GAL infrared source, there is a surface density N_σ of radio sources brighter than m across the G305 field. We therefore obtain the mean number μ of chance sources that are closer and brighter than the matched to candidate ATCA radio source:

$$\mu = \pi r^2 N_\sigma \tag{3.2}$$

We utilise this statistic to suggest the fraction of sources within a sample size of n, that we would expect to have an incorrect candidate association identified within a matching radius r. In a sense, the probability of the association is:

$$P = [1 - \exp(-\mu)] \approx \mu \text{ for } \mu \ll 1 \tag{3.3}$$

From this, we find that if the P-statistic, $P \ll 1$ for an individual source, then that particular identified association is unlikely to be the result of a chance association.

However this statistic alone does not provide us with a firm argument to the reliability of associations; merely the chance that the particular source would have an association within the specific matching radius. Rather, a more reliable means to measure whether an individual association can be deemed correct, is to compare the number of identifications in the total sample with a particular P-statistic, against the amount of associations, nP, that would have been expected from a randomised association between the infrared and radio populations.

To do this, we run 5000 Monte Carlo simulations that follow the previous matching criteria between both Hi-GAL and ATCA catalogues; where the positions of each compact radio source have been randomized, with the only constraint being that they remain within the field. From these Monte Carlo results, we can then calculate the P '-statistic for each of the identified Monte Carlo candidate

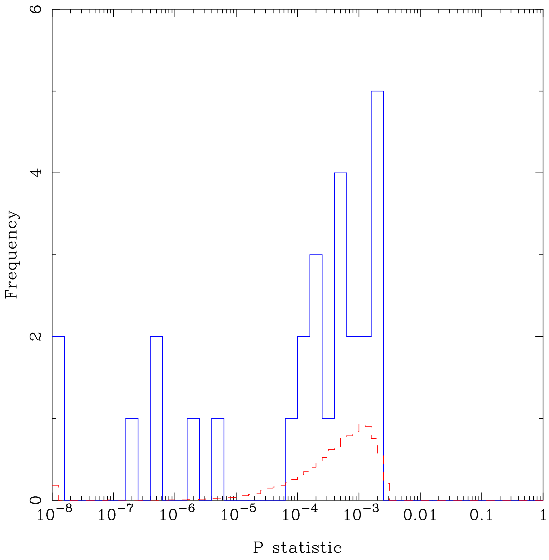

Figure 3.2: Distribution of P-statistics of identified associations (solid blue line), against the distribution of P '-statistics obtained from Monte Carlo associations (dashed red line).

matches. By comparing the P-statistic of our associations to those P '-statistics from the randomised sample, we examine the ratio of sources with a particular value of *P* to the similar value of *P '* from the spurious identifications. If this ratio is high, i.e. there are many associations with a particular value of *P* compared to that of *P '*, then we can mark that particular association as a secure identification. This is shown for a matching radius of 30" in Fig.3.2.

3.2.3.2 Separation Cut-Off

A useful outcome from the use of P-statistics is that it allows for the determination of the separation cut-off for each dataset; essentially the maximum matching radius at which one considers the majority of associations found to be reliable. The selection of the separation cut-off depends on several factors. Clearly a smaller cut-off gives rise to fewer counterparts, increasing the likelihood of missing a true counterpart. Conversely, a larger cut-off increases the risk of associating to a very bright but unrelated counterpart. From the P-statistics we are then able

Table 3.1: Optimum matching radius for each data set to the Hi-GAL G305 field.

Data Set	True ID	False ID	Optimum Matching Radius (”)
ATCA	11	2	15
MMB	14	2	15
RMS	9	2	5
H_2O Masers	4	1	15
MIPS	500	63	10

to derive the optimum matching radius for the data using the technique described by Dye et al. (2009). Firstly, we match between the Hi-GAL and ATCA data at a minimum matching radius of 1”. By then comparing the P-statistic of our associations to those P’-statistics from the randomised sample, we examine the ratio of sources with a particular value of *P* to the similar value of *P ’* from the spurious identifications. If this ratio is high, i.e. there are many associations with a particular value of *P* compared to that of *P ’*, then we can suggest that particular association as a secure identification. This process is stepped through, at intervals of 1” up to a maximum matching radius of 30” . As a result of this we are then able to compute a true and false ID rate as a function of separation.

The result is shown in Fig.3.3, with the true ID rate, the false ID rate, and the separation between Hi-GAL and ATCA true associations in the G305 field shown as a function of the separation cut-off. From this we can see that the true ID rate levels out at 15” (with a total of eleven true associations), and only increases again at 25” onward (with a further three true associations being found). These additional three true associations found at radii $\geq$ 25” correspond to Hi-GAL matches to the brightest ATCA radio sources found in the G305 field. In choosing the search radius, we wish to maximize the number of secure, unambiguous identifications and to minimize the number of real counterparts missed. It is not seemingly clear as to why there is a well-defined P-statistic peak at a lower matching radii; being due to faint, real radio identifications, contesting (in terms of low P-statistic) with rare, brighter sources, which are unrelated to the Hi-GAL source (such as background radio galaxies). By increasing our matching radius, any correct identifications will tend to drop off, with the levelling out

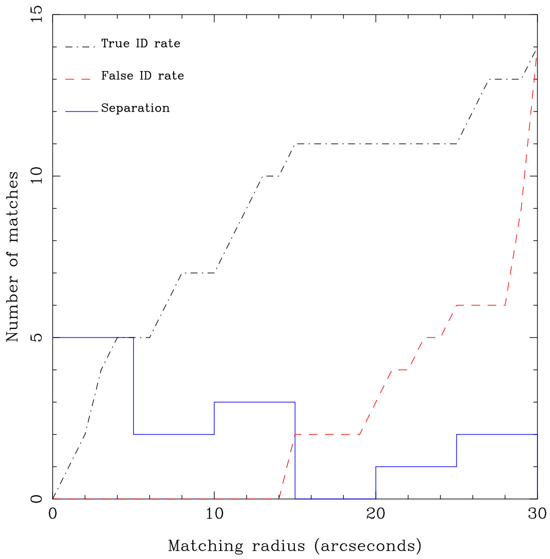

Figure 3.3: Distribution of radial offsets between Hi-GAL sources and ATCA radio counterparts (open histogram). The dashed line gives the expected cumulative number of false radio IDs as a function of the separation cut-off, while the dot-dashed line shows the cumulative number of true radio IDs for each separation cut-off. In this context, the optimum matching radius is found to be 15".

in true identifications being balanced by those bright unrelated radio sources present; since they are very bright, their P-statistic tends to zero as soon as they are within the matching radius. Therefore allowing a matching radius well beyond 15" is not suggested, as the amount of secure associations tend to level out, while matches to contaminant radio sources will preserve the number of perceived true associations (Ivison et al., 2010).

We also note from Fig.3.3 that the false ID rate only becomes noticeable for 15" onwards, with two possible false IDs found at 15". Finally, the separation between Hi-GAL and ATCA true associations, shown in the open histogram, emphasises the fact that the majority of true associations are found within a matching radius of $\leq$ 15". The outcome of the matching procedure returns an optimal separation cut-off of 15" for the radio counterparts in the Hi-GAL field.

Suggesting that a radio source some 15" from an IR source is a secure match may seem counter-intuitive, but two factors need to be taken into consideration;

the *Herschel* beam size, and the physical nature of the IR sources. Our goal is the identification of a sample of embedded massive star-forming regions that themselves are extended in nature, on average around 29” in size, and with the beam size some 18” at 250 μm (Traficante et al., 2011), a secure match within 15” is acceptable.

The approach is repeated for the MMB, RMS, H_2O Masers, and MIPS data sets, with the total number of associations found and the optimum matching radius shown in Table 3.1. The result of the technique is a statistically robust sample of true associations that have been identified over multiple datasets, which can later be investigated and analysed.

3.3 Spectral Energy Distributions of Sources

To obtain estimates of the physical properties of our associations, the observed SEDs were fitted with firstly a simple modified blackbody, incorporating the *Herschel* Hi-GAL observations at 70, 160, 250, 350, and 500 μm. We then can obtain estimates of the bolometric luminosity of each association, by broadening the SED coverage with both the MSX 21 and MIPS 24 μm fluxes, and fitting to the grid of SED models from Robitaille et al. (2006). We find that the modified blackbody fails to reproduce the observed flux at $\lambda \leq 70\,\mu$m, hence associations with solely *Herschel* detections are best suited to modified blackbody fits. Those associations with detections at 21 and 24 μm, suggesting a warm embedded YSO, are more reliably reproduced with the Robitaille et al. (2006) SED models, that incorporate both the central embedded source, and the surrounding envelope.

3.3.1 Modified Blackbody Fitting

In order to firstly be able to derive the basic physical properties for each of our associations such as dust temperature and emissivity index, it was necessary to model the SEDs with a modified blackbody. We are justified in taking the approach of a simple modified blackbody, since the wavelength coverage measured by both PACS and SPIRE trace the peak of the dust SED. Far-IR emission is due to large dust grains (15 - 100 μm), which are more stable and tend to dominate

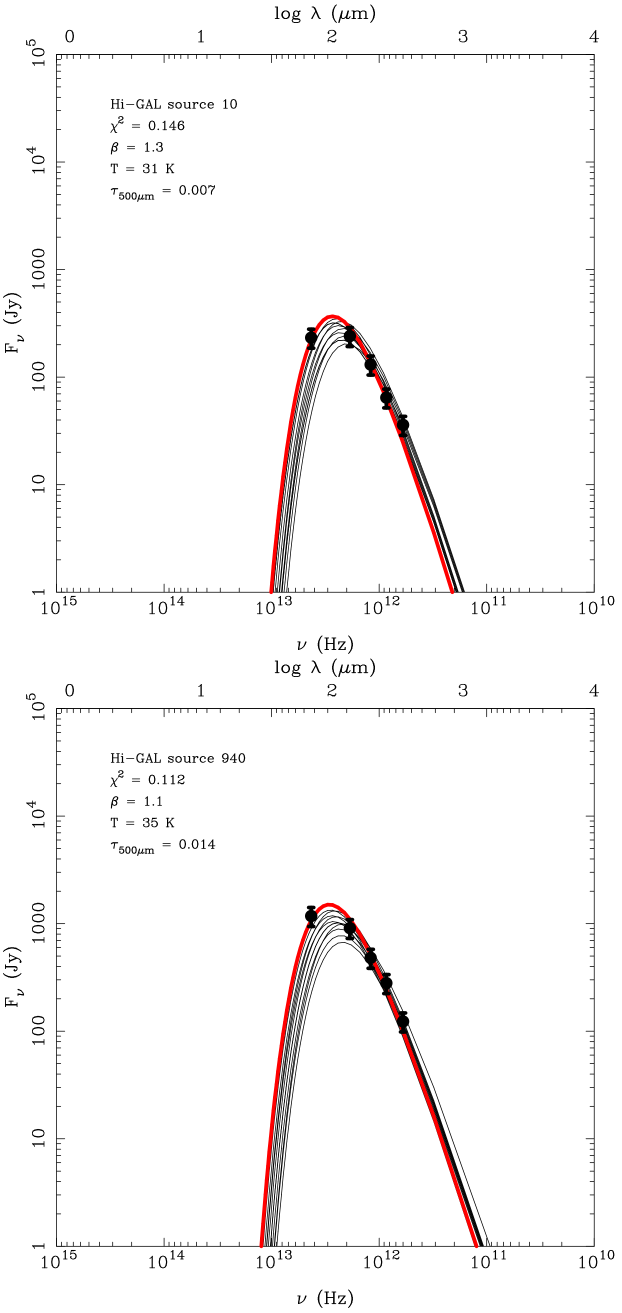

Figure 3.4: Fits to two associations using a modified blackbody SED. Physical properties derived from the fit are shown, along with minimum χ^2 for the best fit. The red solid line represents the best fit model, while the grey solid lines represent other models with a good fit to the data.

the total dust mass, while also tending to trace all phases of the ISM. Therefore, measurements in Hi-GAL will be most sensitive to temperature variations, while also providing an accurate tracer of the overall ISM column density.

Since we have a embedded massive star within a dust cocoon we cannot assume a blackbody, but rather a modified blackbody that takes into consideration the optical depth, and the dust emissivity, as clearly emission is not optically thick at all frequencies. Thus we adopt a modified blackbody fit to the SED of the form (Ward-Thompson & Robson, 1990):

$$F_\nu = \Omega\, B_\nu(T)(1 - e^{-\tau}) \text{ [Jy]} \tag{3.4}$$

where Ω is the effective solid angle of the source (obtained as part of the CuTEx source extraction of Molinari et al. 2011), in sr, $\mathrm{B}_\nu(\mathrm{T})$ is the Planck function, T is the dust temperature, and τ is the optical depth such that:

$$\tau = \left(\frac{\nu}{\nu_c}\right)^\beta \tag{3.5}$$

where β is the dust emissivity index, and ν_c is the critical frequency at which $\tau = 1$.

The free parameters that are derived from the fit include the dust temperature, the dust emissivity index, and the critical frequency. We also note that throughout the calculations each *Herschel* flux was assigned an uncertainty of 20%, this being the calibration error at the time of observation; for reference, the present error is found to be $\approx 15\%$ (Swinyard et al., 2010).

Fitting was performed via a χ^2 minimisation, by considering the observed flux at each of the five Hi-GAL wavebands available for every individual association. The χ^2 minimisation was such that (Hunter et al., 2000):

$$\chi^2 = \sum_n \left[1 - \left(\frac{F_{\nu_n,\mathrm{model}}}{F_{\nu_n,\mathrm{observed}}}\right)\right]^2 \tag{3.6}$$

where the ratio of the model flux to the observed flux is used to give equal weighting to each different wavelength regime.

With these parameters we can then derive the total (gas + dust) mass for each association using both the *Herschel* fluxes at 500 μm, and the corresponding free parameters derived from the minimum χ^2 fit. We note that dust masses were calculated with an opacity $\tau_{500\mu m}$, since at this wavelength all sources were found to be optically thin, allowing for us to sample the dust at all depths. If dust masses were calculated at shorter wavelengths, where some sources were found to be optically thick, we would simply be tracing the dust distribution in the outer layers, and not in fact determining a total dust mass value. Therefore, by following the method highlighted in Hildebrand (1983):

$$M = \frac{F_\nu D^2}{B_\nu(T)} C_\nu \tag{3.7}$$

where D is the source distance, and C_ν is the mass coefficient (a factor that combines dust opacity and gas-to-dust ratio) (Kerton et al., 2001):

$$C_\nu = \frac{M_{\rm g}}{M_{\rm d}\kappa_\nu} \tag{3.8}$$

where M_g is the gas mass, M_d is the dust mass, and κ_ν is the dust opacity. A value of the mass coefficient of $\mathrm{C}_\nu = 50\,\mathrm{g\,cm^{-2}}$ at $850\,\mu$m was initially chosen from those quoted in Kerton et al. (2001), assuming a gas to dust ratio of 100 and a dust emissivity index β of 2. At wavelengths greater than $250\,\mu$m, the frequency dependence can be characterised by a power-law function of (Kramer et al., 2003);

$$C_\nu = C_0 \left(\frac{\nu}{\nu_0}\right)^\beta \tag{3.9}$$

this value was then scaled to a value at $500\,\mu$m, by adopting the value of β from the minimum χ^2 fits. We note that current dust models, such as those of Ossenkopf & Henning (1994), suggest that grain evolution in cold, dense prestellar cores leads to changes in the value of $\mathrm{C}_{850\,\mu\mathrm{m}}$ while β remains constant.

Fig.3.4 shows the result of the modified blackbody model SED fit for a sample of associations, with both the best fit model and those models deemed good fits from the criterion $\chi^2\,/\,\mathrm{N}_{data}\ \leq 2$ (Povich et al., 2011) shown. Included are the corresponding free parameters of the minimum χ^2 fit, being the dust temperature, emissivity index, and source opacity at $500\,\mu$m ($\tau_{500\mu m}$).

3.3.2 SED Fitting

We next obtain estimates of the bolometric luminosity by fitting the observed SEDs with the grid of young stellar object (YSO) model SEDs of Robitaille et al. (2006). Since the SEDs of embedded YSOs tend to peak at 100 μm ,we require photometric data at $\lambda \geq 10\,\mu$m (Mottram et al., 2011b; Povich et al., 2011), hence to broaden the SED coverage we incorporate the 21 and 24 μm fluxes obtained from MSX and MIPS. For these sources, the standard modified blackbody adopted earlier will fail to produce accurate SEDs at wavelengths $\lambda \leq 70\,\mu$m. As a result, to model these sources a multi-component fit using the model SEDs of Robitaille et al. (2006) that are then fit with the online SED fitting tool of Robitaille et al. (2007), that are based on the YSO/disk/envelope models of Whitney et al. (2003), are employed.

The model grid of Robitaille et al. (2006) consists of some 200,000 model SEDs incorporating a vast range of possible evolutionary stages, from an embedded protostellar phase to pre-main-sequence stars with low-mass circumstellar disks. Fitting of models to the data is done by varying the visual extinction, A_V, for a number of distances d between d_{min} - d_{max}, in order to determine the optimum SED model and parameters set. A range of 0 - 20 is selected for the visual extinction (Leistra et al., 2005), while an averaged distance of 3.2 - 4.4 kpc derived from both the kinematic distance to G305 and the spectroscopic distance of Danks 1 & 2 is used (Davies et al., 2012). The optimum SED model is determined through linear regression, with the result shown in Fig.3.5, where all models that fitted with a χ^2 value satisfying $\chi^2 - \chi^2_{best} \leq 3 \times n_{data}$ shown also.

The majority of sources, with no 21, 24, or 70 μm emission, have fitted SEDs that peak at wavelengths $\lambda \geq 160\,\mu$m and are found to have an averaged temperature of ≈ 14 K. Bontemps et al. (2010) characterise YSOs within the Aquila rift complex from pre-stellar sources on the presence of either a 24 or 70 μm counterpart, with this emission originating from warm dust within the inner regions of the YSO envelope. Moreover, such emission is unlikely the result of external heating from the interstellar radiation field producing a detectable 70 μm counterpart (Giannini et al., 2012), making sources with 21, 24, or 70 μm emission likely embedded massive stellar sources. Indeed, Dunham et al. (2008) show

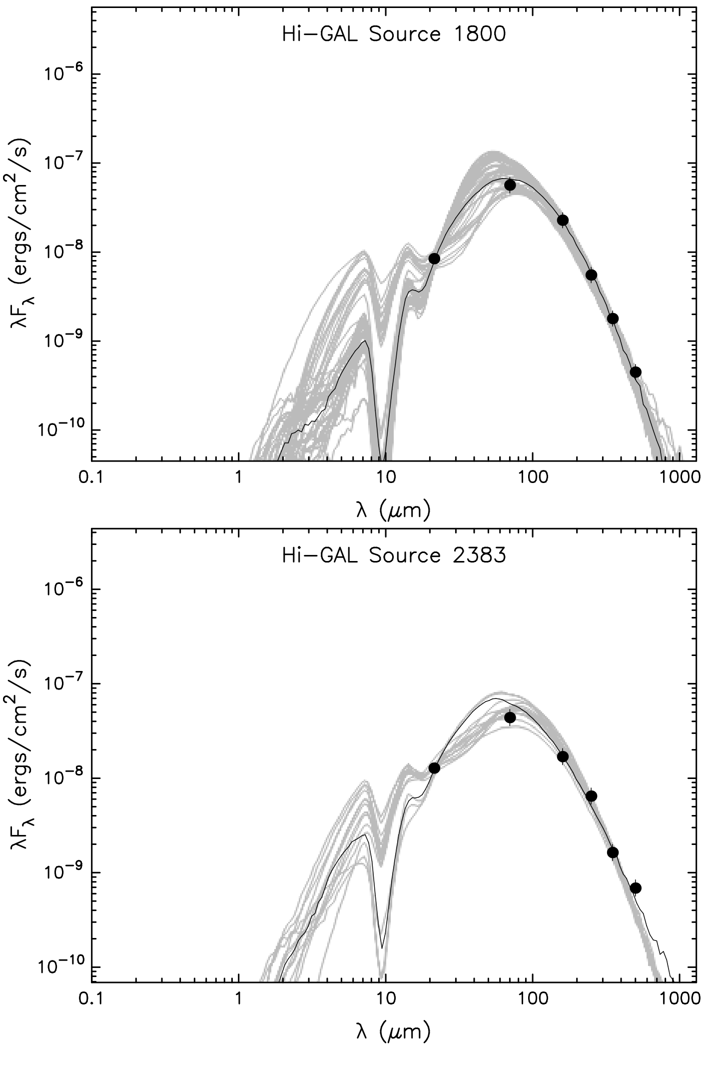

Figure 3.5: Fits for two associations using the Robitaille et al. (2007) fitting technique. Black solid line represents the best fit model, with the grey solid lines showing all other models providing a good fit to the data. The black filled circles show the Hi-GAL and MSX/MIPS data with error bars shown.

that 70 μm emission is closely correlated to the overall luminosity of protostellar sources. Using this selection criteria, the suggestion is that these identified sources correspond to an earlier stage (possibly pre-stellar) that are poorly fitted by a protostar embedded in a dust envelope, and are more suited to a simple modified blackbody fit, yielding values of dust mass, temperature, and emissivity index.

3.4 Discussion

In this section we discuss the global distribution of the embedded massive star-forming population within the G305 complex, and the general method of identification of this population; through the combination of the SED morphology and derived parameters. Using these identified sources, we are able to comment on the present-day star formation activity of G305, and place it into the context of Galactic star formation.

3.4.1 General Properties Of Sources Within G305

We firstly consider the global properties of G305 obtained from SED fitting, by both modified blackbody and Robitaille et al. (2006) YSO models, for each association identified within the G305 region. For our fitting we consider sources with detections of $\mathrm{N}_{data} \geq 3$ as acceptable to fit an SED to, since we have three free parameters in our modified blackbody fitting, sources with limited detections are unlikely to produce a reliable SED; this leaves us with some 503 sources. From these fits, we deem sources with $\chi^2 \, / \, \mathrm{N}_{data} \; \leq 2$ (Povich et al., 2011), as having a reliably fitted SED, yielding a total of 359 well fitted sources.

In Fig.3.6 we present the distribution of the modified blackbody parameters of the dust temperature, dust emissivity index, and the dust temperature, along with the bolometric luminosities obtained from Robitaille et al. (2006) model SED fitting. We find that dust temperatures lie within the range of 10 to 42 K, with a median value of $\approx$ 21 K. For the dust emissivity index, a range between 0.8 to 2.8 is found, with the median of $\approx$ 1.8. The bolometric luminosity is sampled between 10 to $10^4\,\mathrm{L}_\odot$, with a median of $\approx 300\,\mathrm{L}_\odot$, while the dust mass lies between

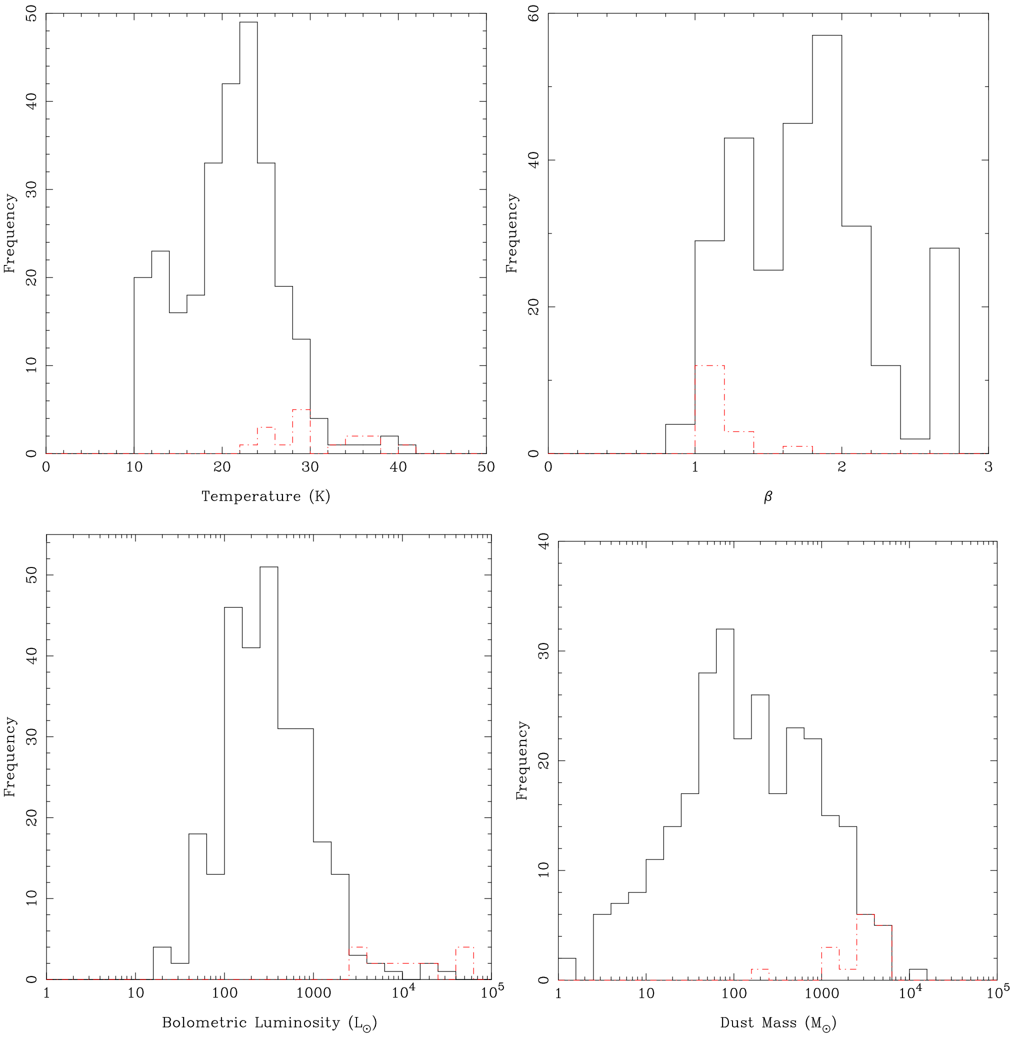

Figure 3.6: Distribution of parameters for all sources with a reliable SED fit within G305 (solid black line), compared to the 16 identified candidate embedded massive star-forming regions (red dot-dashed line). *Top left*: dust temperature. *Top right*: dust emissivity index. *Bottom left*: bolometric luminosity. *Bottom right*: dust mass.

1 to $10^4\,M_\odot$, with a median of $\approx 540\,M_\odot$.

3.4.2 A Far-IR Selection Criterion For Embedded Massive Star Formation

Previous studies that have attempted to distinguish a sample of MYSOs have relied on colour selection criteria based on IRAS data (Palla et al., 1991; Molinari et al., 1996b; Walsh et al., 1997; Sridharan et al., 2002), however these are restricted by selection effects, limitations in sensitivity and resolution, and also their incomplete Galactic coverage. The majority of these studies are biased in that they rely on bright IRAS sources, that with a resolution of 5' at $100\,\mu$m , are often found removed from the dense, confused regions along the Galactic plane where the majority of star formation is expected to be found. The result of these studies is a restricted sample that, due to selection issues, may not entirely represent the general MYSO population, making any extension to study massive star-formation problematic (Urquhart et al., 2008a).

It has been suggested that both the SED morphology, and the bolometric luminosity can prove effective in determining a sample of embedded massive star-forming objects (Molinari et al., 2008a). With the bulk of the YSO emission being in the far-IR portion of the SED, due to cold dust (Molinari et al., 2008b), the *Herschel* Hi-GAL observations are ideal in accurately constraining the luminosity.

From the candidate associations identified, those sources found to have either a radio, MMB, H_2O maser, or RMS counterpart are known sites of massive star formation; tending to be luminous sources (i.e. $> 10^3\,L_\odot$). Using this sub-sample we are able to identify a sample of known embedded massive star-forming regions from the physical properties derived from, and morphology of, their SEDs (shown to peak at $100\,\mu$m , as shown in Fig.3.5). We refer to this population of Hi-GAL sources that are associated with radio, MMB, H_2O maser or RMS counterparts as the embedded population. Added to this, we employ a selection cut in the bolometric luminosity of $10^3\,L_\odot$, that corresponds to the minimum spectral type that we define as a massive star (i.e. $M > 8\,M_\odot$). In total we find some 16 candidate embedded massive star-forming regions, that match these selection criteria; their respective properties and relative associations are shown in Table

3.2. We also note the location of these associations, shown in Fig.3.7, with the majority being located in the hot dust locations along the periphery of the central cavity, suggesting an interaction between the central sources of Danks 1 & 2, and the surrounding material.

Based on this sample of 16 embedded massive star-forming regions, we are able to derive a two-colour selection criterion to identify the overall embedded population of the G305 complex. We find that the 70 - 500 μm and 160 - 350 μm colours are most sensitive to the embedded population, shown as asterisks in Fig.3.8. As can be seen from Fig.3.8, the embedded population are tightly confined to one area of the colour plot, and can be distinguished from the remaining G305 population, shown as circles. From this we suggest a far-IR colour selection criterion for embedded massive star-forming regions of $\log(F_{70}/F_{500}) \geq 1$ and $\log(F_{160}/F_{350}) \geq 1.6$, yielding a further 31 embedded massive star candidates with no associated emission and luminosities $> 10^3\,L_\odot$, as shown in Fig.3.8. From these 31 candidates we find the faintest source to have a peak 70 μm flux of 1.02 Jy/pixel, and compared to the 90% recovery rate of sources discussed in Sect. 2.1, we do not expect any further more deeply-embedded massive star-forming regions to be found within G305.

Currently, the nature of these 31 candidate embedded massive star-forming regions with no associated emission is unclear; from Fig.3.8 these candidates are predominately found with bolometric luminosities of $\approx 10^3\,L_\odot$ however at least 3 sources are found a luminosities $\geq 10^4\,L_\odot$ with no corresponding tracer of massive star formation. A lack of association to ATCA radio sources could be accounted for by localised noise found towards bright large-scale emission present with G305, confusing possible associations to real compact emission present (see Hindson et al. (2012) Sect. 2.2 for a detailed discussion of the ATCA data reduction process). Another possibility could be the strong variability of both methanol (Green et al., 2012) and water masers (Breen et al., 2010), to such an extent that they display no common features at the present epoch. Aside from the possible reasons for lack of associated tracers, this sample of candidates may also suggest an earlier, very young embedded phase present within G305. The possible nature of these additional candidates is particularly interesting; Gaczkowski et al. (2013) identify a sample of highly embedded Class 0 protostars within the Carina Nebula, which are found to have no associated *Spitzer* IRAC and MIPS counterparts, and exhibit luminosities of $\approx 10^3$ - $10^4\,L_\odot$. Such a population of highly embedded sources warrants further investigation using available LABOCA (Siringo et al., 2009) observations of G305 at a later date, as we propose in section 5.3.3. We list the physical parameters of these 31 candidate embedded massive star-forming regions in Appendix B.3.

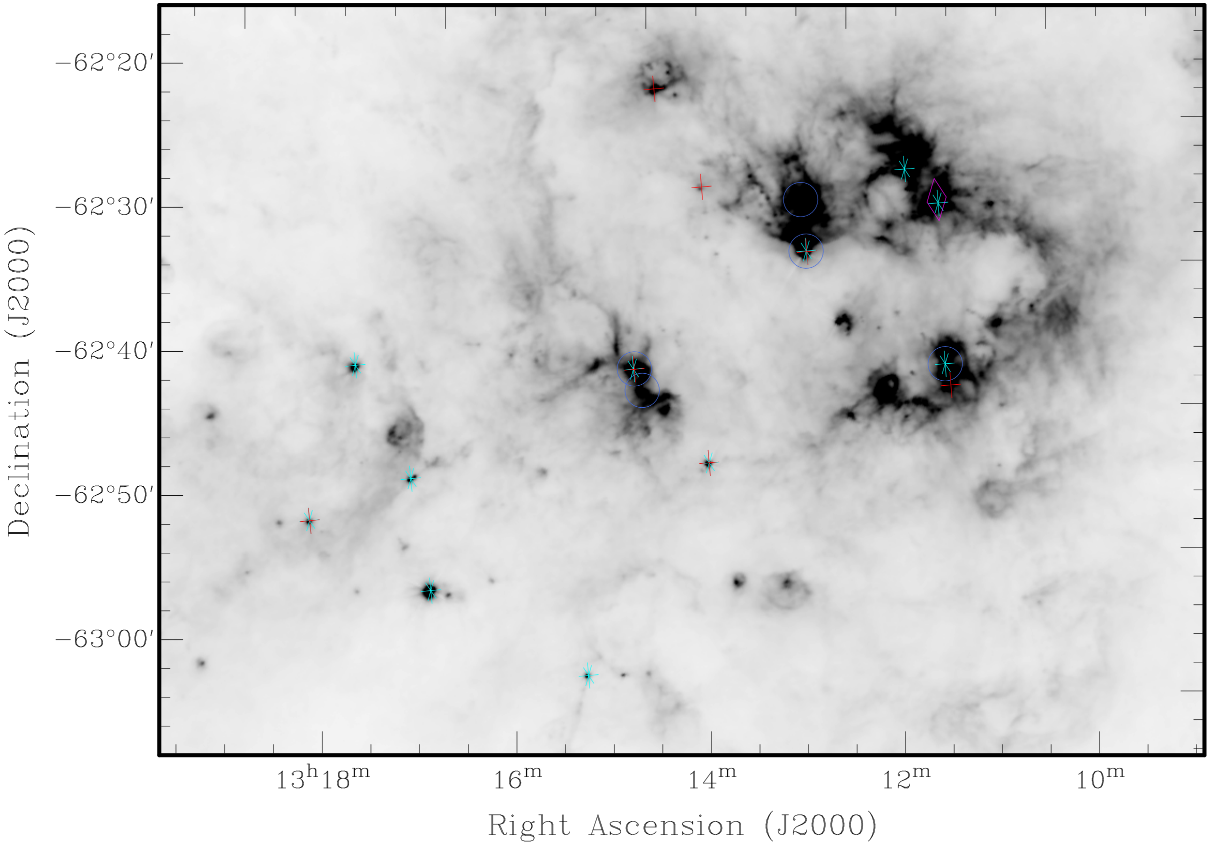

Figure 3.7: Location of candidate embedded massive star-forming regions and their relative association overlaid onto a 160 μm greyscale Hi-GAL image; ATCA radio data (blue circles), MMB methanol masers (cyan asterisks), RMS sources (red crosses), H_2O masers (purple diamonds). Numerous regions are found to be associated with multiple star formation tracers.

Table 3.2: Derived physical properties for all identified embedded massive star-forming regions, from both modified blackbody fits and Robitaille et al. (2007) SED fitting technique, along with found associations.

Hi-GAL Source Index	RA (J2000)	Dec (J2000)	β	T (K)	$\tau_{500\mu m}$ (10^{-3})	M_{Dust} ($M_{\odot}$)	L_{Bol} ($10^3\,L_{\odot}$)	Association(s)
938	197:48:24.2	-62:34:41	1.0	35	20.1	4300	48.6	MMB, H_2O maser
945	197:48:37.19	-62:47:25.2	1.1	29	15.4	3900	7.95	RMS
972	197:49:13.6	-62:45:54.4	1.2	41	11.4	1200	20.8	ATCA, MMB
1184	197:53:6.7	-62:32:10	1.1	25	27.1	4700	11.1	MMB
1800	198:8:56.4	-62:37:18.3	1.4	35	29.4	3500	60.8	ATCA, MMB, RMS
1804	198:9:5	-62:33:32.7	1.0	32	24.8	5200	17.4	ATCA
2114	198:24:0.4	-62:32:14.7	1.7	24	1.29	200	2.91	RMS
2153	198:26:26	-62:51:27.2	1.2	29	9.14	3700	4.13	MMB, RMS, MIPS
2212	198:29:51.7	-62:25:8.4	1.1	23	14.3	4400	4.68	RMS, MIPS
2363	198:35:42.5	-62:46:0.2	1.1	27	14.2	3200	12.2	ATCA, RMS
2383	198:36:37.3	-62:44:29	1.0	36	20.0	1700	57.7	ATCA, MMB, RMS
2627	198:47:49.6	-63:5:29	1.4	28	4.18	1500	3.65	MMB
2902	199:10:47.3	-62:58:31.9	1.0	37	42.2	4200	48.6	MMB
2923	199:12:9.7	-62:50:37	1.1	24	16.1	3700	3.24	MMB
2994	199:18:52.3	-62:42:25.4	1.0	29	23.1	3900	7.95	MMB, MIPS
3032	199:28:12.9	-62:52:50.6	1.4	28	4.57	1500	3.75	MMB, RMS

3.4.3 The Present-day Star Formation Rate Of The G305 Complex

With a sample of embedded massive star-forming objects, one opportunity that is available is to study the recent star-forming history of the complex. Determining the star formation rate (SFR) at a local level is crucial in determining the global Galactic SFR, helping to unveil any mechanisms that may lead to global scaling laws (Molinari et al., 2010b). The SFR, along with the IMF, express the population of massive stars within the Galaxy, and determine what the impact on the local environment is, such as the composition of the ISM, the rate of feedback from massive stars, and the rate of conversion of gas into stars (Calzetti et al., 2010a).

Given our position within the Galactic disk, direct SFR indicators using optical/UV tracers will fail to reproduce an accurate SFR due to high extinction rates of the dusty ISM. However, far-IR observations, unaffected by extinction, provide us with the ability to resolve the YSO population associated with HII regions, allowing constraints on the IMF and stellar ages, yielding a detailed star formation rate of Galactic HII regions (Chomiuk & Povich, 2011).

A SFR derived from a resolved, YSO counting approach, or from that inferred from the total infrared luminosity has to assume a ‘steady-state’ approximation to reliably trace the star formation activity of the region. The assumption in these calculations is that both the rate of massive star formation, and the rate that massive stars evolve off the main sequence, is in approximate equilibrium (Krumholz, Dekel & McKee, 2012). For this to be true, the requirement is that the age of the region be longer than that of the UV emitting population used to trace the SFR (Kennicutt, 1998a). We show below that this is the case for a realistic star-forming timescale.

3.4.3.1 The Embedded Massive Star Formation Rate

With our sample of 16 identified embedded massive star-forming regions, and the further 31 embedded massive star candidates found, we are able to comment on the present star formation history of the G305 complex. If we make the assumption that for each embedded massive star-forming region identified, the

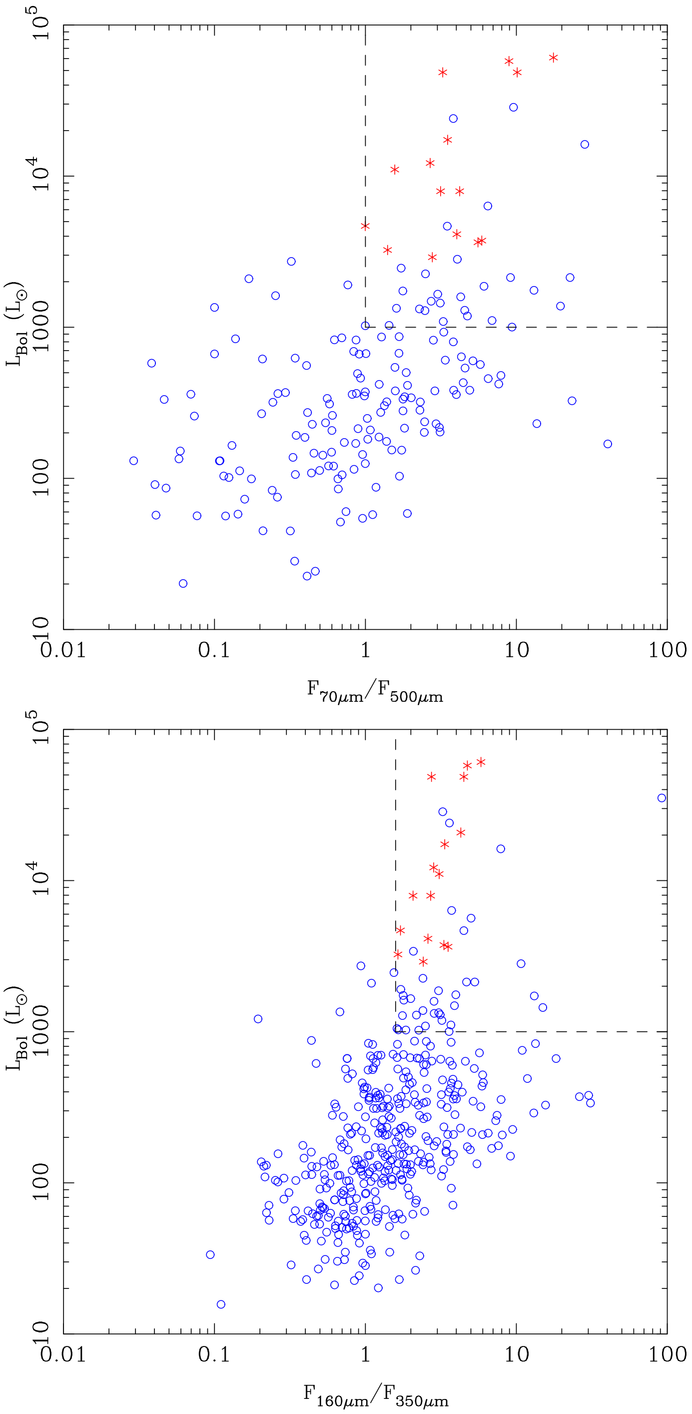

Figure 3.8: Colour - colour plots of all Hi-GAL sources found in the G305 field (blue circles), and known sites of massive star formation (red asterisks). Dashed lines indicates the boundary of the region used for distinguishing sites of embedded massive star formation from other sources, at a luminosity of $> 10^3\,L_\odot$.

most massive star present produces the majority of the bolometric luminosity and is also accompanied by a cluster of lower mass stars, we are able to scale the IMF accordingly; for our calculations, we adopt a simple IMF proposed by Salpeter (1955). By comparing the calculated bolometric luminosity for each candidate region found, to the luminosities calculated for a sample of main-sequence stars from Mottram et al. (2011a), we are then able to estimate the most massive star for each region.

In order to extrapolate the IMF from observed mass to lower mass, we are obliged to select both a lower and upper mass limit that all observed YSOs fall within the selected range. For our purposes we adopt a lower mass of $0.1\,\mathrm{M}_\odot$ and an upper limit of $50\,\mathrm{M}_\odot$, as used when calculating the Galactic SFR (Robitaille & Whitney, 2010).

By adopting a Salpeter IMF, which best samples the high-mass tail of the IMF (Zinnecker & Yorke, 2007), and assuming a constant SFR therefore, we arrive at $\approx 10^4$ YSOs present, which corresponds to a total mass in stars of $\approx\ 8 \times 10^3$ $\mathrm{M}_\odot$. Since we consider the total mass in stars, we select a typical timescale for that mass to assemble, which would be the time to reach the pre main-sequence of 0.5 Myr (Offner & McKee, 2011), from this we attain a SFR for G305 of $\approx$ 0.01 - 0.02 $\mathrm{M}_\odot$ yr^{-1}. In this scenario, the 'steady-state' approximation should hold since the timescales of both MYSOs, $\approx 10^4$ yr (Mottram et al., 2011a), and UC HII regions, $\approx 10^5$ yr (Churchwell, Wolfire & Wood, 1989; Comerón & Torra, 1996; Churchwell, 2002b), are some 5 - 50 times shorter than our assumed timescale for the star formation within G305 of $\approx$ 0.5 Myr.

A similar approach has been taken in Hindson et al. (2012), using the identified UC HII population (some five identified in total) of G305 to derive a SFR, over the last 0.5 Myr, of 0.002 - 0.004 $\mathrm{M}_\odot$ yr^{-1}. This rate is considered a lower limit due to the incompletenesses in the ATCA radio data, with a *uv* cut implemented to emphasise the compact, small scale radio emission associated with UC HII regions. For comparison, Davies et al. (2012), have determined the SFR for the G305 complex over the last 5 Myr from the calculated age and mass of the two central open clusters Danks 1 & 2. The SFR was found to be $\approx$ 0.002 - 0.005 $\mathrm{M}_\odot$ yr^{-1}, which is comparable to our derived SFR from counting the embedded YSO population. However, taking our derived SFR of $\approx$ 0.01 - 0.02 $\mathrm{M}_\odot$ yr^{-1}, it is clear that the star formation activity of G305 has not remained constant over the last 5 Myr. If this were to be the case, then we would expect to observe some 75 000 $M_\odot$ of stars to be observed within the complex, which is entirely not the case. The 'collect and collapse' model of star formation, proposed by Elmegreen & Lada (1977), requires a period of time, of 1.5 - 3 Myr (Elmegreen & Lada, 1977; Whitworth et al., 1994a), after the formation of the central ionising source(s) for material within the surrounding molecular clouds to be swept-up by the expansion of the HII region. If this expansion continues for a sufficient time, the swept-up shell of material becomes self-gravitating and is then expected to fragment, entering a phase of collapse possibly leading to the formation of new stars. Following the approach taken by Dale, Bonnell & Whitworth (2007), who have calculated this 'fragmentation time-scale' for a uniform molecular cloud of pure molecular hydrogen, we take the ionising photon flux of the G305 complex from Clark & Porter (2004) to estimate a similar timescale. We find that after the formation of Danks 1 & 2, there would be a delay of ≈ 2.4 Myr until the next generation of star formation occurred within the complex. This would support the scenario that the star formation within G305 was not continuous, but more likely characterised by punctuated star formation over the lifetime of the complex. One could also speculate on such a scenario, with the clear age difference present between Danks 1 & 2; with the age of Danks 2 found to be 3^{+3}_{-1} Myr, while Danks 1 found at $1.5^{+1.5}_{-0.5}$ Myr (Davies et al., 2012), such an age difference could also imply evidence towards a 'collect and collapse' mechanism.

We find also that our derived SFR for G305 is comparable to other well known massive star-forming complexes in the Galaxy, namely the Carina complex (Povich et al., 2011), and M17 (Chomiuk & Povich, 2011). We stress that the derived SFR value is based on a small sample of high mass stars, and has been extrapolated over a large range of stellar masses; when considering the lower mass stars present, their lifetimes may well be 1-2 orders of magnitude longer.

For completeness, the Galactic SFR is found to be ≈ 2 $M_\odot$ yr^{-1} (Chomiuk & Povich, 2011; Davies et al., 2011), suggesting that a few tens to hundreds of G305 complexes are analogous to the entire star formation rate of the Milky Way. Using results from the Wilkinson Microwave Anisotropy Probe (WMAP), Murray & Rahman (2010) identify some 14 Galactic HII regions with an ionising flux greater than that of G305, of which some 18 WMAP sources constitute over half the total Galactic ionising flux. Just as the IMF is dominated by the more massive stars present, the Galactic SFR is probably dominated by the few rigorous star-forming regions present.

3.4.4 Alternative Star Formation Rate Indicators Within G305

Clearly the value for the SFR derived from the population of embedded massive star-forming regions identified will be an upper limit, since we have assumed a power-law slope (i.e. Salpeter IMF), and by extrapolating the IMF over a small sample of massive stars have overestimated the total mass in stars. To this must also be added issues of completeness, and assuming a timescale of $\approx 10^5$ yrs will be unrepresentative of the intermediate to low-mass YSOs present; as was shown in section 1.7.1, other forms of the IMF that are more representative of the intermediate and low-mass stellar population do exist. Our approach focuses specifically on the embedded massive star-forming population, which is best represented by a Salpeter IMF, and should prove a good assumption for the upper limit of the SFR. With this result, we can then compare to other SFR tracers that are independent of the resolved massive stellar population within G305, such as those derived from the classic Kennicutt (1998a) SFR relation, which itself assumes a Salpeter IMF.

What is key here is that we are able to resolve the YSO population within Galactic HII regions, such as G305, and use both the IMF and stellar timescales to derive a SFR. This can then be contrasted and calibrated to extragalactic emission tracers, such as the total IR luminosity, to determine whether Galactic SFRs are consistent with extragalactic SFR indicators. We next consider the SFR using tracers that are independent of the identified YSO population. Table 3.3 lists the calculated SFRs for G305 using numerous tracers, with reference to each approach.

3.4.4.1 The Relation Between Star Formation Rate and Molecular Cloud Mass

Recent work by Heiderman et al. (2010) and Lada, Lombardi & Alves (2010) on the star formation activity of molecular clouds within 0.5 kpc of the Sun, suggest that the star formation rate scales linearly with the molecular cloud mass. Lada (1992) showed that active star formation is to be found primarily in high volume density regions of molecular clouds, with star formation favouring very massive, dense cores. The expectation for the star formation activity is thus that there is a tight correlation with the amount of high extinction material present in molecular clouds.

Lada, Lombardi & Alves (2010) illustrate for a sample of local molecular clouds, that by comparison of the cumulative mass to YSO content as a function of extinction (see Lada, Lombardi & Alves (2010) Fig. 3), a marked minimum dispersion of the cumulative mass is found at $A_V = 7.3 \pm 1.8$ mag. The proposition is that above this minimum, the cloud mass is directly related to the star formation activity and hence the SFR within the clouds. It is shown that this high extinction value corresponds to an equally high volume density of $n(H_2) \approx 10^4\,cm^{-3}$ (Lada, Lombardi & Alves, 2010). There is also evidence this linear relation holds for extragalactic molecular clouds. A tight correlation between the total IR luminosity and the luminosity of the HCN molecule, which itself requires high densities ($> 10^4\,cm^{-3}$) to be excited to a detectable level, has been found for both Galactic cores (Wu et al., 2005), and for a sample of normal spirals and starburst galaxies (Gao & Solomon, 2004). These studies suggest that the linear relation holds for dense interstellar gas both on a Galactic and extragalactic scale, underlying a physical relation that links star formation and galaxy evolution.

From this linear correlation, a SFR is derived of the form:

$$SFR = 4.6 \pm 2.6 \times 10^{-8}\, M_{0.8}\ [\mathrm{M_\odot\ yr^{-1}}] \tag{3.10}$$

where $M_{0.8}$ corresponds to the cloud mass, in solar masses, above an extinction threshold of $A_K \approx 0.8$ mag, which is derived from the visual extinction of $A_V = 7.3 \pm 1.8$ mag mentioned earlier. We note also, that this relation is in agreement with the well known Larson (1981) relations, that molecular clouds obey three scaling laws: *i)* the velocity dispersion is proportional to cloud size; *ii)* the velocity dispersion is proportional to cloud mass; *iii)* the cloud size is inversely proportional to the density of the cloud. Specifically, regarding the third Larson relation, Lombardi, Alves & Lada (2010) find for a sample of molecular clouds of differing mass and size, that above an extinction threshold of $A_K \approx 0.1 - 1.0$ mag, differing clouds have near identical average column densities.

For each IR source identified by *Herschel* across the G305 complex we determine the physical radius at 250 μm, as this wavelength offers the optimum combination of signal-to-noise, and angular resolution. To estimate the physical diameter for each source, we firstly deconvolve the source size from the Gaussian beam (Thompson et al., 2004):

$$\Theta^2_{\rm Source} = \Theta^2_{\rm Obs} - \Theta^2_{\rm Beam} \tag{3.11}$$

where Θ^2_{Obs} is the source size estimated from the FWHM of the Gaussian fitting, and Θ^2_{Beam} is the *Herschel* beam size at 250 μm. If we then place each source at a distance of 4 kpc, and assume spherical geometry and a uniform density, we can determine those sources found to be above the critical density threshold. From this we are able to determine the mass of the dense gas within G305, then using the Lada, Lombardi & Alves (2010) assumption that dense gas is associated with the star formation activity, we find a dense gas mass of $\approx 3 \times 10^5$ M$_\odot$; for comparison, the total molecular mass traced by NH$_3$ is found to be $\approx 6 \times 10^5$ M$_\odot$ (Hindson et al., 2010). We note that this mass is an approximation, since it is unlikely that the density of each source is uniform.

By combining this mass with Equation (3.10), we obtain a dense gas derived SFR of 0.006 - 0.02 M$_\odot$ yr^{-1}. The result is found to be in good agreement with the embedded massive star formation rate derived earlier, and goes some way toward confirming the Lada, Lombardi & Alves (2010) assumption by extension to the star formation activity of embedded massive star-forming regions.

3.4.4.2 The 70 μm Emission Star Formation Rate

In contrast to deriving a value of the SFR from all identified embedded massive star-forming regions, we can also approach measuring the SFR by considering the total infrared flux (TIR) of the giant G305 HII region. On an extra-galactic perspective current SFRs are calculated using a tracer of UV photon emission from YSOs, and also spectral synthesis models (Kennicutt, 1998a). In this case, observations of HII regions prove ideal measures of current star formation. However, some fraction of the total UV emission will be obscured by the presence of dust, thus bolometric IR observations of dust (i.e. TIR) will provide an excellent means to recover the extinguished UV photon emission, with the dust absorption highly peaked in the UV and re-emission being in a broad spectral range of mid-to-far-IR (Kennicutt, 1998a). The conclusion from this is that the TIR will provide the best indicator of SFR obscured by the presence of dust.

Observationally, an advantage would be the use of a single-band star formation indicator, such as UV, Hα, 8 μm, 24 μm etc., however each of these has its own complications. In the case of UV and optical lines, corrections need to be taken into consideration due to large extinction. Whereas 8 and 24 μm emission strongly depends on the local environment, since the abundances of small dust grains that contribute to their emission depend greatly on metallicity and the presence of ionising radiation (Calzetti et al., 2005; Dale et al., 2005; Calzetti et al., 2007).

Calzetti et al. (2007) and Dale et al. (2005) note that 8 μm emission makes for an inaccurate SFR indicator since there is a large degree of variability of emission in galaxies with respects to SED shape and metallicity. The strong variability at 8 μm is emphasised in Fig.3.5, where variations of an order of magnitude exist between the best fit and good fit SED models. This variation can be accounted for by the disk inclination to the line of sight for the centrally embedded object, where the observed flux from a pole-on view can be 2 - 4 times greater than a more edge-on viewing angle (Whitney et al., 2003).

Calzetti et al. (2005) find that the SFR calculated from 24 μm emission itself varies strongly from galaxy to galaxy. On a local scale, the ratio of the 24 μm luminosity to SFR is found to be a reasonably accurate tracer, however when applied to other systems, such as starbursts and ultraluminous infrared galaxies (ULIRGs), the ratio is systematically higher. This variation in the 24 μm is found to be a factor of a few with respects to the observed SEDs, and may be grounded in the strong dependence on local galactic conditions; with ionising stars heating dust to different averaged temperatures, the 24 μm emission will be most sensitive to this. However, Dale et al. (2005) find that 70 μm emission may be an accurate monochromatic star formation indicator, since the 70-to-160 μm ratio is found to correlate well with local SFRs.

Recent work by Lawton et al. (2010) have determined an accurate monochromatic IR band that best approximates the obscured SFR in the Large Magellanic (LMC) and Small Magellanic Clouds (SMC), through IR aperture photometry of 16 LMC and 16 SMC HII regions, using *Spitzer* IRAC (3.6, 4.5, 8 μm) and MIPS (24, 70, 160 μm) bands. It is found from the IR SEDs of each HII region, that the majority peak at around 70 μm at all radii (10 - 400 pc) from the centrally ionising sources, and that the 70 μm emission most closely traces the size of each HII region as found using the TIR. The conclusion from this is that the 70 μm emission is the most likely suitable IR band to utilise as a monochromatic SFR indicator.

It has been argued by Kennicutt (1998a) that the TIR is the best obscured SFR indicator available for starburst galaxies. However, dust obscured star formation in HII regions are found to behave similarly, in that their environments are both very dusty and are sites of recent star formation. The Kennicutt (1998a) obscured SFR equation is of the form:

$$SFR = 4.5 \times 10^{-44} \, L_{\rm TIR} \; [{\rm M}_\odot \; {\rm yr}^{-1}] \tag{3.12}$$

where L_{TIR} is the TIR luminosity in erg s^{-1}, and the value 4.5×10^{-44} is a constant derived from synthesis models, with assumptions on the IMF and star formation timescales (Kennicutt, 1998a).

The TIR luminosity in Equation (3.12) can be substituted with the averaged 70μm luminosity, normalised by the TIR, while also applying an IR band specific constant. The monochromatic obscured SFR equation of Lawton et al. (2010) is found to be:

$$SFR = 9.7(0.7) \times 10^{-44} \, L(\lambda) \; [{\rm M}_\odot \; {\rm yr}^{-1}] \tag{3.13}$$

where L(λ) is the observed luminosity in erg s^{-1}.

By employing aperture photometry of the whole G305 region, we obtain the cumulative 70 μm flux, $f_\nu(\lambda)$, and from this are able to calculate the monochromatic luminosity at 70 μm (Calzetti et al., 2010b):

$$L(\lambda) = 4\,\pi\,d^2\,\left(\frac{c}{\lambda}\right)\,f_\nu(\lambda)\ [\mathrm{erg\ s^{-1}}] \tag{3.14}$$

where d is the distance to the G305 complex, in m.

Using the value found for the observed luminosity at 70 μm, with Equation (3.13), we obtain an obscured SFR for G305 of 0.002 - 0.005 $\mathrm{M_\odot\ yr^{-1}}$. A similar approach has been suggested by Li et al. (2010), who also determine a monochromatic SFR indicator at 70 μm , yet calibrate their SFR tracer not with the TIR luminosity but rather with the combined Hα, and 24 μm luminosity. For completeness, using the Li et al. (2010) tracer, we derive a SFR of 0.004 - 0.008 $\mathrm{M_\odot\ yr^{-1}}$, which is in approximate agreement with that using the Lawton et al. (2010) approach.

We can directly compare these results to that derived from the total Lyman continuum photon rate of G305, where we find an SFR of 0.002 - 0.004 $\mathrm{M_\odot\ yr^{-1}}$ (Hindson et al. in prep). We note that both these two independent tracers are in excellent agreement, however are found to be a factor of ≥ 2 lower than that derived from the embedded massive star-forming population. A similar result is found by Chomiuk & Povich (2011), who find that the SFR for M17 estimated from both the Lyman continuum and 24 μm emission is underestimated by a factor of ≥ 2 in comparison to the SFR derived from YSO counting.

This discrepancy may simply be that there are elementary differences in the measurements between Galactic and extragalactic observations. Lawton et al. (2010) note that Equation (3.13) extends to HII regions measured at projected distances of 52 kpc and 61 kpc for the LMC and SMC respectively. With G305 some $\sim$4 kpc distant, the relation between the SFR and luminosity at 70 μm may indeed break down, with the effects of individual protostars becoming more important, due to the larger spatial resolution. It may also be the case that the 'steady-state' assumption breaks down in this comparison. Though it is normally true that the lifetime of the region observed is longer than for the individual objects for extragalactic realms, this may not hold for observations of Galactic regions that tend to be smaller, and with shorter dynamical timescales.

3.4.4.3 A Galactic - Extragalactic Comparison

By comparing the derived SFR from numerous tracers, shown in Table 3.3, what is immediately apparent is the disparity between the rates derived from the resolved stellar population and those from extragalactic tracers; there is lack of consistency between the two, with extragalactic tracers tending to underestimate the SFR derived from resolved Galactic SFRs. This circumstance between the two SFR regimes has been noted by several authors (Heiderman et al., 2010; Lada, Lombardi & Alves, 2010; Chomiuk & Povich, 2011), where there appears a distinct underestimation for Galactic H II regions. Heiderman et al. (2010) make the suggestion that this difference may be accounted for by the inclusion of diffuse gas, in the standard Kennicutt-Schmidt relation, that is below the critical density threshold for star formation, as suggested by Lada, Lombardi & Alves (2010). Since extinction maps are not readily available to determine the surface density of gas in extragalactic studies, CO maps are often employed instead. Heiderman et al. (2010) find that using CO as a gas tracer, for a sample of local molecular clouds, leads to an underestimate in mass of $\gtrsim 30\,\%$ compared to that obtained using extinction maps. The result of this would essentially push down the estimated SFR from the Kennicutt (1998a) relation, and may go some way in accounting for the dissimilarity between extragalactic regions and more local, Galactic ones.

However, recent work by Krumholz, Dekel & McKee (2012) seems to suggest a unified star formation law, with objects ranging from both low mass Solar neighbourhood clouds through to sub-mm galaxies in agreement with one distinct star formation law. What is advocated in this law is that the SFR, within a variety of scales, is simply $\approx 1\,\%$ of the molecular gas mass per local free-fall time. This volumetric approach suggests a local, universal star formation law that is applicable to Galactic and extragalactic observations (see Krumholz, Dekel & McKee (2012) Fig. 3), bridging the gap between the apparent disparity in the two regimes. This law is affected solely by local variations, such as the gas condition, with more global Galactic/galaxy-scale properties, such as the orbital period, having no impact on the SFR in so far as they do not change the local properties of star-forming regions.

Conversely, Lada et al. (2012) conclude that a universal star formation law that is applicable from the Milky Way through to near-IR selected (BzK) galaxies, is simply directed by the amount of dense molecular gas that can accumulate within a star-forming region. In the majority of situations, only 10 % of the total mass within a molecular cloud is at a sufficient density, $n(H_2) \geq 10^4\,cm^{-3}$ (Lada, Lombardi & Alves, 2010), to actively form stars. Clearly there is a disparity between the two proposed universal SFR laws; Krumholz, Dekel & McKee (2012) favouring gas surface densities and local free-fall times as crucial, while Lada et al. (2012) advocate gas surface densities and the fraction of dense gas as the pivotal factors. It therefore seems that more work is needed to describe the underlying nature of a universal star formation law, if such a law is to be found.

What is apparent, when measuring the Galactic SFR, is the need for an accurate means to compare the Milky Way to other galaxies, in order to allow us to extend the more detailed Galactic analysis to other systems and to test the discrepancy between the two regimes. Continued, multi-wavelength analysis of Galactic HII regions, now including *Herschel* Hi-GAL, will in part aid with this. Through extended study across a wide range of star-forming regions, an accurate determination of the IMF, and with that the SFR, can be achieved, which scaled up from a more local level to a global, Galactic level, will allow for the consideration of how these crucial properties vary as a function of environment across the Milky Way (see Veneziani et al. (2013) for a detailed study of the Herschel Science Demonstration Phase fields). This should help in a better understanding of how the SFR can accurately be measured on both Galactic, and extragalactic scales, and lead to a more unified calibration.

3.5 Summary

We have studied the G305 star-forming complex, using *Herschel* Hi-GAL far-IR data in search of an embedded massive star-forming population. In total, we identify some 16 embedded massive star-forming regions from their associations to radio, maser, and RMS counterparts across the region (Fig.3.7). From this sample of known embedded massive stars we suggest a far-IR colour selection of $\log(F_{70}/F_{500}) \geq 1$ and $\log(F_{160}/F_{350}) \geq 1.6$ that can be utilised across similar

Table 3.3: Calculated SFR for G305 using multiple SFR tracers.

SFR Tracer	SFR ($M_\odot$ yr^{-1})	Reference
Embedded Massive Stars	0.01 - 0.02	Faimali et al. (2012)
Dense Gas	0.006 - 0.02	Lada, Lombardi & Alves (2010)
UC HII Regions	$\geq$ 0.002 - 0.004	Hindson et al. (2012)
Danks 1 & 2	0.002 - 0.005	Davies et al. (2012)
70 μm Emission	0.002 - 0.005	Lawton et al. (2010)
	0.004 - 0.008	Li et al. (2010)
Lyman Continuum	0.002 - 0.004	Hindson et al. in prep.

regions within the *Herschel* Hi-GAL survey, to identify embedded massive star-forming candidates across the Galactic plane.

With our sample of embedded massive stars, we derive the present-day SFR for the complex of $0.01 - 0.02\,M_\odot$ yr^{-1}, which is found to be in good agreement with other well known massive star-forming complexes such as the Carina complex (Povich et al., 2011), and M17 (Povich & Whitney, 2010). In comparison to other well known extragalactic SFR tracers, based on the Kennicutt (1998a) relation, there is a noted discrepancy between the two regimes, with extragalactic tracers tending to underemphasise the SFR. We note however, the use of the Lada, Lombardi & Alves (2010) relation for SFR that is in good agreement with the resolved SFR derived from our study, suggesting the key to the SFR is the total amount, and production of, dense gas within molecular clouds. We find that the Milky Way SFR (Chomiuk & Povich, 2011; Davies et al., 2011) is comparable to tens to hundreds of G305 complexes, emphasising the fact that the Galactic SFR is most likely dominated by similar massive star-forming complexes.

Our results in this chapter have focused on identifying the embedded star-forming population within G305, taking advantage of *Herschel* Hi-GAL observations to constrain the physical parameters of this sample. As a result of this, we have been able to constrain the upper limit of the SFR, that reflected the high-mass component of the complex. This result allows us to directly compare the derived SFR, to extragalactic SFR indicators that solely tracer the high-mass content within external star-forming regions. To fully understand both the nature of star formation within G305, and comment on the highly suggestive morphology of the complex, we need to address the issues of incompleteness that were first raised in section 3.4.4. In the following chapter we outline our approach to conducing a complete census of the YSO population of G305, with a view to better understanding star formation, and the star formation history, of G305.

Chapter 4

Young Stellar Objects, And The Nature Of Star Formation Within G305

"A human is a system for converting dust billions of years old, into dust billions of years from now, via a roundabout process which involves checking email a lot."
- xkcd

4.1 Motivation

As was shown in Chapter 3, we began the process of identifying the embedded massive star-forming component of G305, by proposing a two-colour selection criterion to identify such regions within *Herschel* Hi-GAL observations, and derived a SFR that reflected the high-mass component of the complex. In using the *Herschel* Hi-GAL far-IR observations, to derive a simple colour selection criterion, we will inevitably be biased towards the deeply embedded earlier stages of star formation within the complex. Having focused on the massive stellar content, and fixing the IMF to this high-mass, Salpeter IMF, we will have inevitably overestimated the total mass in stars within G305; the usefulness of the approach is in providing an upper limit to the SFR, that can then be compared to other SFR tracers, which are independent of the resolved massive stellar population within star-forming regions. Therefore, the SFRs that have been derived so far either rely on scaling from the high-mass end of the IMF, or by assuming that the Lada, Lombardi & Alves (2010) dense gas - SFR relation holds in G305. In this chapter, by undertaking a complete census of the YSO content of G305, we can go beyond these two assumptions by directly determining the YSO mass function, and hence the SFR.

In this chapter we outline our approach to cataloguing the YSO content of G305, where we have combined our *Herschel* Hi-GAL observations, with *Spitzer* data, 2MASS, and VVV observations, to identify candidate YSOs from their characteristic IR excess emission present from both dusty circumstellar disks and envelopes. In section 1.4.1 we discussed the evolution of the low-mass SED, and showed how the presence of dusty envelopes and disks can lead to strong mid-IR emission, making *Spitzer* data very sensitive to this population, while the more evolved, T Tauri sources became apparent in the near-IR. Our approach to YSO identification follows that approach taken in the Carina nebula (Povich et al., 2011), and M17 (Povich & Churchwell, 2009; Povich & Whitney, 2010), however we propose an extension of the technique by including both VVV and *Herschel* Hi-GAL data in our analysis.

In section 1.7.1, we discussed the shape of the IMF, and how the presently accepted view is that of an IMF that can be broken into three components that constitute differing mass regimes (see equation (1.19)). More importantly, as can be seen in Fig.1.9, at low-mass regimes we need to address the issue of completeness, and sensitivity in detecting the ever lower mass stellar component of the complex. What is needed is a complete census of the intermediate-, to low-mass YSO component of G305, so as to more accurately define the total mass in stars for the region, and deal with any incompleteness found.

The importance in identifying this population in G305 is not only, as mentioned in section 1.7.2, the role that the intermediate-, to low-mass population plays in chemically enriching their surroundings and manufacturing a significant proportion of the dust content, but also in understanding the star-forming environment of the surrounding molecular cloud. A number of authors (Davies et al., 2012; Longmore et al., 2007; Clark & Porter, 2004) have suggested that the morphology of G305, and the distribution of massive stars within is highly suggestive of triggered star formation. The feedback from these massive stars can disrupt the natal environment, destroying the reservoir of material for future formation, and halting star formation entirely; YSOs themselves are susceptible to destructive UV radiation that can disperse their disks (Whitworth & Zinnecker, 2004). However, the energy input derived from these sources may also promote and induce sequential star formation in the surrounding molecular cloud, before it is dispersed. In identifying the YSO content of G305, and reproducing the YSO IMF (YMF), we are better able to understand the morphology and evolution of star-forming complexes, and can use the spatial distribution of these sources in an attempt to identify signs of sequential star formation. Therefore, a complete census of the YSO population in G305 is crucial in understanding the star-forming environment on a large scale.

4.2 Observations & Data Analysis

As was shown in section 1.4.1, the evolution of the SED for YSOs can be tracked by observations from near-IR through to far-IR, accounting for the presence of circumstellar envelopes and disks. Below we discuss the data we use, to conduct a region-wide census of the population of YSOs found within G305. For each source found, every available wavelength is included in SED fitting. That is further discussed in section 4.3.

4.2.1 GLIMPSE & 2MASS

We start our YSO identification by extracting data (a 2° tile, similar to the *Herschel* Hi-GAL frame) from the *Spitzer* telescope GLIMPSE survey (Benjamin et al., 2003), utilising the four mid-IR bands (3.6, 4.5, 5.8, and 8.0 μm) of IRAC (Fazio et al., 2004). Within the Point Source Catalogue, point-spread function fitting photometry is conducted for individual sources, using the GLIMPSE point-source extractor, which is a modified version of DAOPHOT (Stetson, 1987), that has been optimised for crowded fields that suffer from strong variations of background nebular emission[1]. From this, the 5σ detection limits of the GLIMPSE

---

[1] Details of data processing are available at http://www.astro.wisc.edu/glimpse/docs.html

images are 0.2, 0.2, 0.4, and 0.4 mJy for the respective bands. Sources that are found to have a flux density of greater than 5σ, in at least two neighbouring bands, of the four IRAC bands, are included into the GLIMPSE Point Source Catalogue. The GLIMPSE Point Source Catalogue is also band-merged with the JHK_s photometry from the 2MASS Point Source Catalogue (Skrutskie et al., 2006), providing us with an initial G305 catalogue of sources in seven near-, to mid-IR bands across 1.2 μm to 8.0 μm.

4.2.2 VVV

To complement the 2MASS near-IR observations of G305, we also have at our disposal JHK_s photometry from the Vista VVV survey[1]. We fold this additional near-IR photometry into our analysis to provide us with greater sensitivity; the K_s - band sensitivity within crowded fields reaches ≈ 16.5 mag, as opposed to the 2MASS photometry which reaches a limit of $K_s \approx 14.3$ mag. As is discussed in the following section, Skrutskie et al. (2006) show that the 2MASS photometric error becomes noticeable at $K_s > 13$ mag; therefore we perform a selection cut in our near-IR detections, where 2MASS photometry is taken for sources with $K_s < 13$ mag, while VVV photometry is taken for sources with $K_s \geq 13$ mag.

4.2.3 MIPSGAL & MSX

As will be shown later, photometry at 24 μm will be vital in our ability to constrain both the evolutionary stage, and luminosities of our YSO sample. We obtain 24 μm mosaics of the MIPSGAL survey (Carey et al., 2009) taken from the MIPS instrument on board *Spitzer* (Rieke et al., 2004), with the mosaics having a high-resolution of 2.4” per pixel, and a quoted 5σ sensitivity of 1.7 mJy (Carey et al., 2009).

In addition to the MIPSGAL 24 μm data, we also include 21 μm mosaics from the Spirit III instrument on board the MSX satellite, which has a 5σ point-source detection limit of 200 mJy at 21 μm. We find that the sensitivity of the MSX

---

[1] We note that at the time of submission, we have worked with Vista v1.1; the current release is v1.3. Minor changes in the JHK_s zero-points exist that will change the photometry slightly.

21 μm band is below the saturation limits of IRAC and MIPS, which allows us to combat the saturation present at the 24 μm band within G305.

Fig.4.1 shows the saturation present at 24 μm in G305, caused by the presence of bright diffuse emission towards the complex. All MIPS observations use the same exposure time of 1.2s, with the pixel saturation level independent of position across the survey; however, the maximum flux a source obtains will depend on the level of background emission. In this case, for a region that has bright background emission, found to be close to saturation, only the faint point sources present will avoid being saturated. As the level of diffuse emission will be a strong function of position, then the point source flux saturation limit will be dependent on the position within the complex (Robitaille et al., 2008). This can be seen in Fig.4.1, where the saturation towards the main lobes situated along the periphery of the central cavity, which were shown to exhibit strong 70 μm emission in Fig.3.1, have effectively burnt a hole through the MIPSGAL mosaic.

Taking the MSX 21 μm data to fill the gaps in the MIPSGAL observations, we note that the spatial correlation of the MSX mosaics is found to be $\approx$ 18.3" making a direct correlation of the GLIMPSE Point Source Catalogue with that of MSX a somewhat confusing state of affairs. We therefore decide not to use the MSX Point Source Catalogue in our work, since this low resolution would cause confusion with multiple GLIMPSE sources, but rather we perform aperture photometry to extract the 21 μm flux density.

4.2.4 Hi-GAL

Finally, to complete our SED coverage, we incorporate the *Herschel* Hi-GAL far-IR observations at 70, 160, 250, 350, and 500 μm, to serve us in identifying highly embedded YSOs within G305. To include this far-IR photometry we again utilise the cross-matching technique first highlighted in section 3.2.3, where the optimum matching radius is selected for those sources found to have either a MIPSGAL or MSX counterpart.

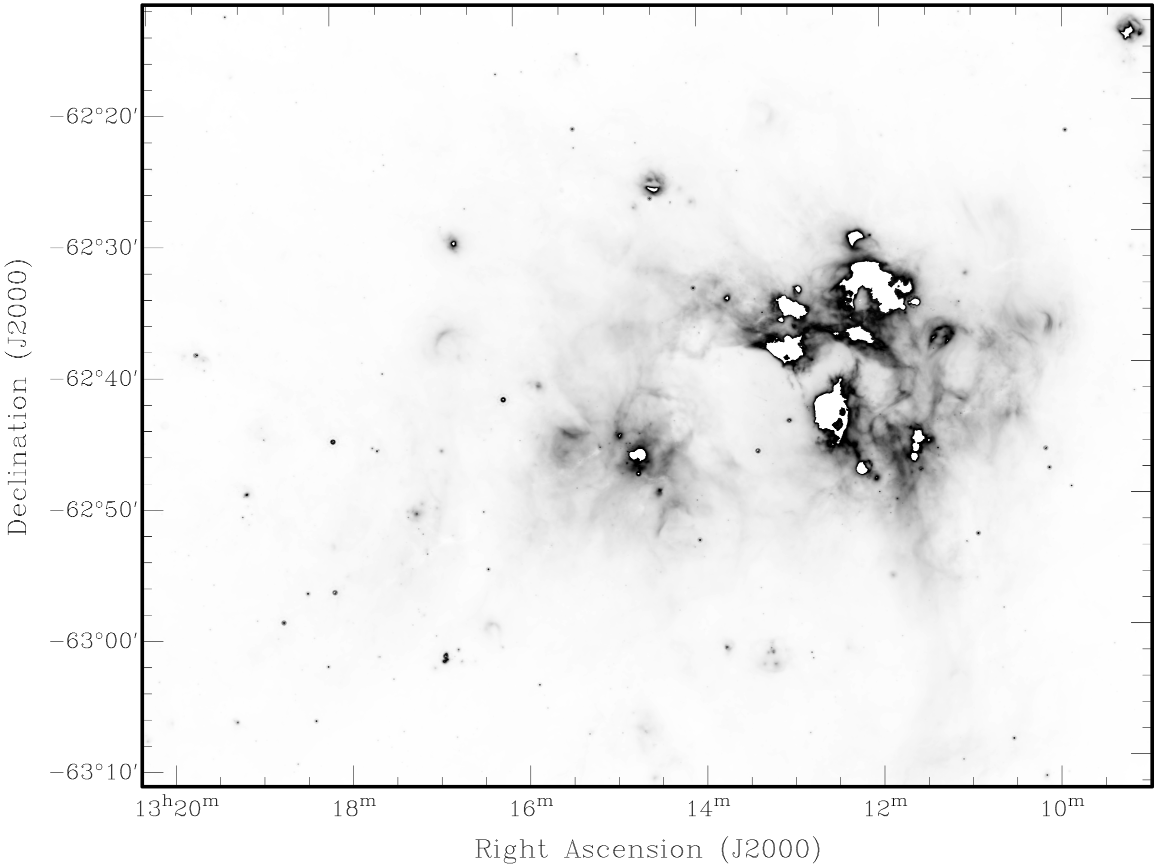

Figure 4.1: The saturation of MIPS 24 μm towards G305, caused by bright, diffuse emission present within the complex.

Table 4.1: Break-down of sources at each stage of obtaining the G305 YSO catalogue.

Stage	Number	Description
GLIMPSE Archive	451,789	99.5% Reliable Point Source Catalogue
2MASS Sources	231,624	Sources with $K_s < 13\,$mag
VVV Sources	220,165	Sources with $K_s \geq 13\,$mag
Fit with SED model	187,106	Detections of ≥ 4 in 2MASS/VVV + IRAC bands
Stellar Photosphere	182,692	Sources well fit by stellar atmosphere SEDs
Possible IR excess	4,414	Sources poorly fit by stellar atmosphere SEDs
Marginal IR excess	2,450	Excess emission in IRAC [5.8] or [8.0] band only
Saturated $24\,\mu$m sources	241	Sources requiring MSX $21\,\mu$m aperture photometry
Contaminating IR excess	873	Contaminating IR sources
Reliable IR excess	1,091	Sources fitted with YSO models
Candidate YSOs	599	Well fit by YSO SEDs
Stage 0/I	157	Well-fit by Stage 0/I SED
Stage II	303	Well-fit by Stage II SED
Stage III	24	Well-fit by Stage III SED
Ambiguous	115	Inconclusive SED Fit

4.3 Identifying Candidate YSOs

The aim of this chapter is to identify the YSO population associated with G305, and to this end we utilise the characteristic IR excess emission that is indicative of a YSO. Below we outline the steps taken to identify a final sample of candidate YSOs, with Table 4.1 providing an overview of the steps taken, and the sources removed.

YSOs are characterised by dusty circumstellar disks, and surrounding infalling natal envelopes that will reprocess the radiation from the central source, to produce a distinguishable IR excess emission; making for their identification via their SEDs possible (see Fig.1.3). Our main tool to identify these sources are the YSO models of Robitaille et al. (2006), in combination with the YSO SED fitting tool of Robitaille et al. (2007).

4.3.1 2MASS & VVV Source Selection

Our start point for our analysis begins with the GLIMPSE Point Source Catalogue, with the additional band-merged 2MASS detections; we find within the 2° tile of G305, that some 451,789 sources are detected. We immediately decide to perform a selection cut on this sample, to address the issue of photometric error

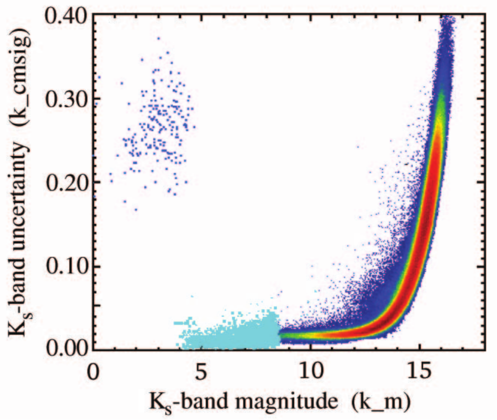

Figure 4.2: Photometric uncertainty as a function of magnitude for 2MASS K_s band from Skrutskie et al. (2006).

that is most noticeable in the K_s - band detections.

Skrutskie et al. (2006) find, for 2MASS observations, that at fainter magnitudes (i.e. $K_s \geq 13$ mag), uncertainties begin to rise due to the dominance of background noise; this uncertainty is shown in Fig.4.2. As can also been seen in Fig.4.3, VVV observations are shown to be some four magnitudes deeper than 2MASS, while within crowded fields (shown in red in Fig.4.2) the photometric error only begins to becomes noticeable at $K_s \geq 14$ mag. From the GLIMPSE Point Source Catalogue, we find that as much as 49 % of the detections within G305 are found at magnitudes of $K_s \geq 13$ mag, as shown in Fig.4.4. For massive star-forming regions such as G305, the observed field is likely crowded, therefore to obtain more reliable observations at fainter magnitudes we employ a selection cut at $K_s \geq 13$ mag.

From the Point Source Catalogue, we retain the 2MASS observations of some 231,624 sources found with a photometry $K_s < 13$ mag, while some 220,165 sources with $K_s \geq 13$ mag are selected for cross-matching to our VVV dataset. The positional accuracy of 2MASS sources is well defined, found to be ≈ 0.5” on average (Varricatt et al., 2010); based on the average FWHM measured in the K_s - band, which is found to be ≈ 2” (Skrutskie et al., 2006; Varricatt et al., 2010), a matching radius of 2” is selected.

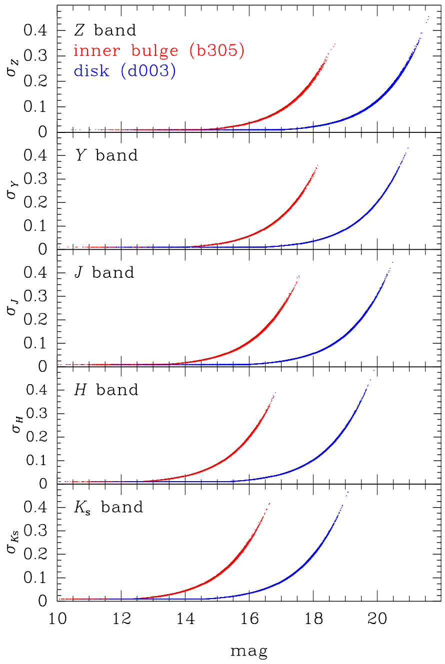

Figure 4.3: Photometric uncertainty as a function of magnitude for VVV $ZYJHK_s$ bands for a Galactic disk field, in blue, and a crowded field close to the Galactic centre, in red; from Saito et al. (2012).

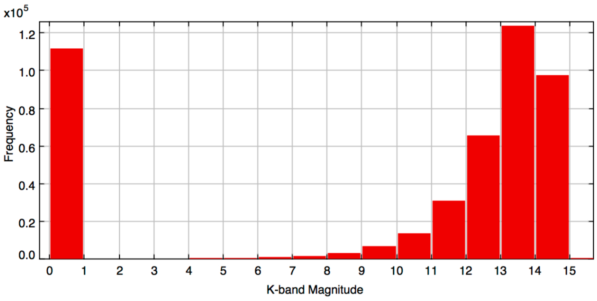

Figure 4.4: Distribution of 2MASS K_s - band detections within G305.

4.3.2 Fitting Stellar Sources

The technique we employ to identify our YSO sample follows an adapted version that has previously been conducted in both the Carina nebula (Smith et al., 2010; Povich et al., 2011), and M17 (Povich & Churchwell, 2009; Povich & Whitney, 2010). Previous work attempting to define a set of IRAC mid-IR colour criteria to identify YSOs within nearby young embedded clusters, such as NGC 1333, has been attempted by Allen et al. (2004); Gutermuth et al. (2008). However, the issue with extending these criteria to other regions such as G305, has been shown to be problematic. Povich & Churchwell (2009) applied the Allen et al. (2004); Gutermuth et al. (2008) colour criteria to identify YSOs within the M17 star-forming regions and showed that it failed to reproduce a similar number of YSOs as had been achieved using the Robitaille et al. (2007) SED fitting tool, while some highly reddened stellar photospheres are also incorrectly identified as YSOs. The issue with the applicability of the IRAC mid-IR colour criteria is that it was derived from a close complex, 1 kpc, that was located within relatively low-density molecular clouds situated away from the Galactic plane. The power of a model based YSO identification is the capacity to include interstellar extinction as a free parameter into the SED modelling, before matching the results to observation. This allows us to provide a consistent matching approach over a wide range of Galactic environments, without having to empirically redefine colour criteria.

The aim in following the approach taken in these studies is to provide a comparative analysis of other galactic star-forming region, but with the addition of new observations in the form of both Hi-GAL and VVV data. By doing so, we hope to demonstrate both in this chapter, and the last, the power of multi-wavelength analysis, and how these studies can easily be rolled out to other Galactic regions, with the aim of building a better picture of star formation across the Milky Way.

The first major source of contamination within the field is that of highly reddened stars, which we first attempt to address. YSOs are distinguishable from the reddened photosphere of both main-sequence and giant stars, since YSOs require a thermal emission component that originates from the circumstellar dust of their surrounding envelope, to reproduce the shape of their mid-IR excess found from their SED. Within the YSO fitting tool of Robitaille et al. (2007), we have an additional set of some 7,853 model stellar atmospheres (Castelli & Kurucz, 2004) that we firstly fit to our sample. So as to distinguish between YSOs and sources that are consistent with stellar photospheres that have been reddened by interstellar dust, we follow the mid-IR extinction law of Indebetouw et al. (2005), and select a range of $A_V = 0 - 30$ mag for the visual extinction (obtained from the Schlegel, Finkbeiner & Davis 1998 extinction maps), so as to exclude highly reddened stellar sources from our models.

The Castelli & Kurucz (2004) model stellar atmospheres consist of a grid of ATLAS9 models that encompass several metallicities [M/H], and microturbulence velocities ξ, where for the models a range in T_{eff} and $\log g$ of 3,500 - 50,000 K and 0.0 - 0.5 are chosen respectively. Throughout the fitting process we again take an averaged distance of 3.2 - 4.4 kpc to G305, similar to that in Chapter 3. We firstly apply a selection cut to our data to provide us with a highly reliable point-source catalogue that we fit to, where sources with $N_{data} \geq 4$ in the combined 2MASS/VVV + IRAC detections are considered for model fits; applying this strict cut leaves some 187,106 viable sources to fit to. We next apply the Castelli & Kurucz (2004) models, and consider a source to be well fit by a reddened stellar atmosphere if the goodness-of-fit parameter, normalised by the total number of detections, is found to be $\chi^2 / N_{\rm data} \leq 2$. In total, some 182,692 sources are deemed to be well-fitted by reddened stellar photospheres, examples of which are shown in Fig.4.5, leaving some 4,414 sources as possible YSOs.

This remaining sample of some 4,414 sources, were not fitted well by these reddened stellar photospheres either because:

- These sources posses IR emission that originates from their circumstellar dust envelope, that creates an excess emission which is found to be above that of the stellar photosphere.
- The sources suffer from photometric uncertainties larger than the default 10 % from the catalogue; this produces spurious IR excess emission, which we address in the following section.

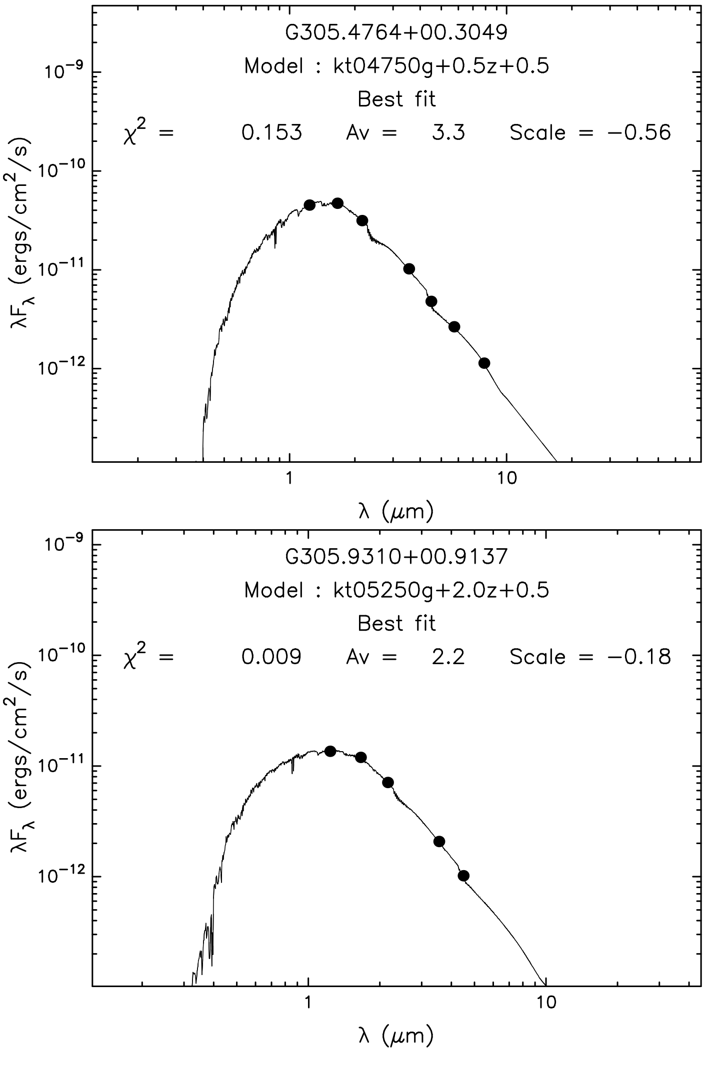

Figure 4.5: Examples of sources well-fit by the Castelli & Kurucz (2004) reddened stellar photospheres.

4.3.3 Removing Marginal IR Excess Sources

As mentioned above, one possible reason for sources failing to be fitted by reddened stellar models can be attributed to sources with excess IR emission, with this excess appearing in only one of the IRAC bands. These 'marginal' IR excess sources tend to be stellar sources that have been detected at both 3.6, and 4.5 μm bands, while their flux density tends to be significantly overestimated in the 8.0 μm band, or less commonly in the 5.8 μm band. The source of this overestimate is due to poor source extraction at the 8.0, and 5.8 μm bands, where a noise peak or diffuse emission has been extracted at the position of the actual source. This most commonly affects faint point sources that are found to be close to the 5σ detection limit, especially in regions of bright diffuse emission. As stars tend to be fainter at 8.0 μm, the IRAC 5.8 and 8.0 μm detections will become less sensitive to point sources, and will instead become more affected by nebular emission, compared to the 3.6, and 4.5 μm bands. The consequence of this is the extraction of a noise peak or diffuse emission feature, at 8.0 μm, being extracted from the position of the star observed at the lower bands, causing an artificially high flux to be recorded at 8.0 μm.

In order to remove these spurious 8.0 μm detections, we employ the Smith et al. (2010) colour criteria, derived within the Carina nebula, to our candidate YSO catalogue for G305. In Smith et al. (2010), these spurious 8.0 μm detections are defined as:

- Excess found only at 8.0 μm, while all remaining detections are consistent with those of a reddened stellar photosphere.
- Excess found only at 5.8 μm, while all remaining detections are consistent with those of a reddened stellar photosphere. In this situation, the source tends not to be detected at 8.0 μm.
- Excess found in both 5.8, and 8.0 μm bands, yet the difference in the bands is negligible (i.e. $[5.8] - [8.0] = 0$), as is the case in a stellar photosphere.

Following on from this definition, only sources detected at both the 3.6, and 4.5 μm bands are considered, to provide us with a highly reliable sample of candidate YSOs. We employ the modified selection criteria of Povich et al. (2011), which de-reddens the [3.6] - [4.5] colours, so as to consider background field stars that have been viewed through the G305 complex by up to a visual extinction $A_V = 0$ - 20 mag (as was used in our earlier stellar model fitting). The selection criteria are defined as:

- $[3.6]\text{-}[4.5] > \delta([3.6]\text{-}[4.5]) + \mathrm{E}([3.6]\text{-}[4.5])$,
- Or $[4.5]\text{-}[5.8] > \delta([4.5]\text{-}[5.8])$,
- And $[5.8]\text{-}[8.0] > \delta([5.8]\text{-}[8.0])$.

where $[\lambda]$ is the magnitude, and $\delta([\lambda_i] - [\lambda_j])$ are the uncertainties calculated from the 10 % error placed on the Point Source Catalogue flux densities. The colour excess for the de-reddening is calculated:

- $\mathrm{E}([3.6]\text{-}[4.5]) = \mathrm{A}_V\,(\kappa_{3.6} - \kappa_{4.5})\,/\,\kappa_V = 0.0135\,\mathrm{A}_V$

where κ_λ is the opacity given by the Indebetouw et al. (2005) extinction law.

The result of this strict selection criteria is the removal of some 2,450 'marginal' IR excess sources, leaving us with some 1,964 candidate sources that we begin to fit with YSO models.

4.3.4 Mid-IR Aperture Photometry

Crucial to identifying candidate YSOs is the inclusion of mid-IR data from MIPSGAL & MSX, and removing the final remnants of contaminating sources within our sample. As was shown in Fig.1.3, the SED of highly embedded YSOs will tend to peak at $\approx 100\,\mu$m in the thermal IR; this makes photometry at $\lambda > 100\,\mu$m key to determining the evolutionary stage of the source. Robitaille et al. (2006) show for some 200,000 model SEDs, for YSOs of varying mass and some 10 viewing angles (pole-on through to edge-on), that for fluxes found at $\lambda > 10\,\mu$m the dominant mechanism is the reprocessing of absorbed stellar flux by surrounding circumstellar dust (i.e. the envelope dominated Class 0/I). At wavelengths shorter than $10\,\mu$m, the flux is found to be dominated by the warm dust that originates from the circumstellar disk. Providing a constraint, at either 21 or $24\,\mu$m, has been shown to be critical in constraining the SED of a YSO; the Robitaille et al.

(2006) YSO models exhibit a variation on the order of magnitude in the 24 μm flux, even when all IRAC fluxes have been accurately constrained.

Extracting the 24 μm flux is done using aperture photometry on the enhanced MIPSGAL 24 μm, mosaic, shown in Fig.4.2 (Carey et al., 2009). Extracting the 24 μm flux density, and estimating the background level within a crowded field such as G305, is done by utilising the Daophot MMM algorithm (Stetson, 1987). We positionally located all candidate YSOs within the MIPSGAL mosaic, and centred an extraction aperture of 3.5" in radius, with a background annulus of inner and outer radii of 7 and 13" respectively; Povich & Whitney (2010); Povich et al. (2011) find such an extraction technique provides excellent agreement with fluxes extracted via point-spread function (PSF) fitting with the GLIMPSE pipeline, and also that aperture photometry detects more 24 μm sources than PSF fitting. With having a small sample of candidate sources at this stage, and the importance that mid-IR data has in determining the evolutionary stage of a YSO (Carey et al., 2009), we feel justified in taking this approach to maximise the number of 24 μm detections.

However, as we discussed earlier, and can be clearly seen in Fig.4.2, the *Spitzer* detections at 24 μm do suffer from saturation within G305. In applying our aperture photometry, we find that some 12 % of candidate YSOs are found to be saturated at 24 μm, and rather than failing to accurately constrain the SEDs of these sources, or discarding them for fear of being genuine YSOs, we use MSX 21 μm observations to replace this key mid-IR measurement. We again employ aperture photometry where an extraction aperture of 18" in radius (corresponding to the MSX beam size) is selected, with thin annuli of 3 pixel radii (18") are used to estimate the background flux levels (Crowther & Conti, 2003).

4.3.5 Contaminating IR Excess Sources

With this additional mid-IR information, we are now able to weed out the remaining contaminants within our sample of candidate YSOs. Much work has gone in to identifying contaminating IR excess sources, which have been misidentified as YSOs in the past, with such spurious objects as variable stars, planetary nebula, background active galactic nuclei (AGN), and dusty asymptotic giant (AGB)

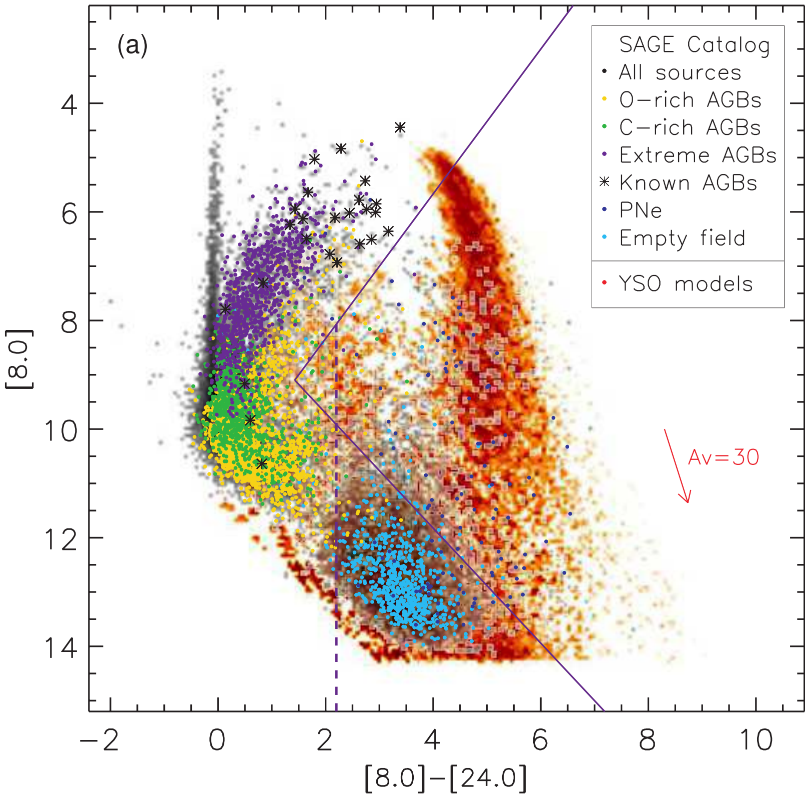

Figure 4.6: The colour-magnitude diagram of Whitney et al. (2008). Stellar sources are plotted in grey scale, while YSO models are plotted in orange scale; subsets of these catalogues are plotted in other colours (as denoted in the key). The vertical dashed line indicates the AGB selection cut of [8.0] - [24] $<$ 2.2 mag.

stars (Harvey et al., 2006, 2007a; Porras et al., 2007; Robitaille, 2008; Whitney et al., 2008; Povich & Churchwell, 2009; Povich & Whitney, 2010; Anderson et al., 2012); the main culprits that we focus our attention towards are both AGB, and AGN sources.

The main source of spurious identifications can be found from luminous AGB stars, which masquerade as massive YSOs. Working from the Gutermuth et al. (2008) colour classification scheme of YSOs, Povich & Churchwell (2009) find that the distinction between Class II YSOs and AGB stars somewhat blurs, making misinformed identification more likely; the mismatching of these two distinctly

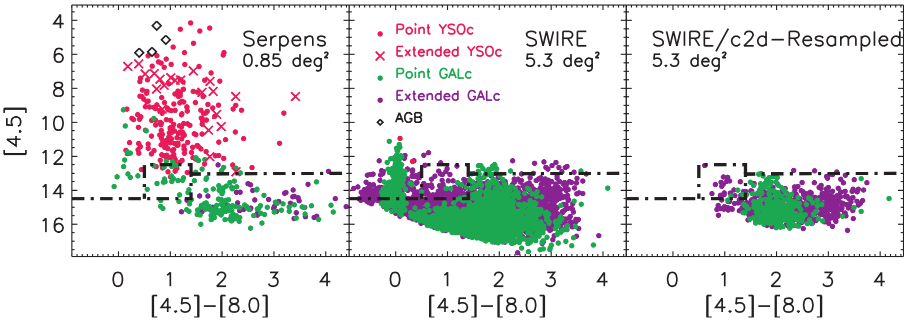

Figure 4.7: The colour-magnitude diagram of Harvey et al. (2007a). Observations of Galactic sources within the Serpens star-forming region (left) are compared to two control SWIRE regions (middle, and right) to compare the colour-magnitude properties of the galaxy component observed within Serpens. The black line shows the colour-magnitude selection criterion that is employed to identify YSOs from interloping background galaxy sources.

different sources supports the view of AGB stars being typically surrounded by dust shells, of smaller radii, than the disk and envelopes of YSOs (Robitaille, 2008). In order to discard these sources from our sample, we employ the AGB selection criterion of Whitney et al. (2008), see Fig.4.6. The study involved the identification of some 1,000 YSOs within the LMC, as part of the Surveying the Agents of a Galaxys Evolution (SAGE) Legacy program of *Spitzer*, where it was found that the majority of AGB stars have [8.0] - [24] < 2.2 mag. By employing this strict cut, we find that some 671 sources are immediately removed from our sample, leaving us with 1,293 possible YSOs.

Much work, as part of the *Spitzer* “From Molecular Cores to Planet- forming Disks” (c2d) (Evans et al., 2003), has been focused on the removal of AGN background source from YSO identification using *Spitzer* IRAC and MIPS data. Identification, and the derivation of a selection criterion, has been conducted in two Galactic regions, namely the Chamaeleon II molecular cloud (Porras et al., 2007), and the Serpens star-forming region (Harvey et al., 2006, 2007a). Both these regions are found at a tenth the distance that G305 is situated at, 178 ± 18 pc and 260 ± 10 pc, however Chamaeleon II is found to be highly removed from the Galactic plane (found at b = -14°); this removed position makes any criterion derived from Chamaeleon II somewhat tenuously applicable to a region, such as G305, located within the Galactic plane.

The colours of possible background galaxies are identified in c2d study of Serpens, by employing data from the *Spitzer* Wide-Area Infrared Extragalactic Survey (SWIRE), namely the Elais N1 data set (Surace et al., 2004). In order to make the properties of Galactic source, and background galaxies comparable, Harvey et al. (2007a) process this one field through the same c2d pipeline, with similar processing parameters, while still retaining the longer integration times required to identify fainter sources within SWIRE. As a result of this, we employ the AGN selection criterion of Harvey et al. (2007a), as seen in Fig.4.7, namely that background star-forming galaxies and dusty AGN are found to very faint sources, tending to be below the selection limit of $[4.5] > 13.05$ mag. Applying this selection to our data removes a further 202 possible background galaxies from our catalogue, leaving us with a final some of some 1,091 reliable IR excess sources that can now be fit with the YSO models of Robitaille et al. (2006).

4.3.6 Far-IR Matching

Finally, we extend our candidate YSO catalogue into the far-IR, by folding in the *Herschel* Hi-GAL observations of G305, from Chapter 3. The addition of this data will be beneficial in the identification of highly embedded YSOs, where the peak of the SED is found beyond 100 μm; in order to include these additional observations, we employ the optimised cross-matching technique that was discussed in section 3.2.3. We note that we previously found optimum matching radii between MIPS and Hi-GAL of 10", and for associations of MSX and Hi-GAL an optimum radius of 5" was also found (Faimali et al., 2012); we identify some 240 sources that have associated emission within the *Herschel* Hi-GAL bands.

4.4 Classification Of Candidate YSOs

With this sample of 1,091 reliable IR excess sources, we can begin to decipher the YSO content of G305 using the Robitaille et al. (2007) fitting tool, where we fit the YSO models of Robitaille et al. (2006) to our candidate sources. We again, as in Chapter 3, fit with chosen parameters of 0 - 20 for the visual extinction (Leistra et al., 2005), and averaged kinematic and spectroscopic distance of 3.2 - 4.4 kpc to G305. The 200,000 Monte Carlo radiative transfer models of Robitaille et al. (2006) model the propagation of photons from the central source, through the surrounding circumstellar environment. These models solve for the temperature of this circumstellar material, along with the inclusion of the dust absorption and emission characteristics, and the properties of photons produced by circumstellar disk accretion and backwarming of the stellar photosphere (Whitney et al., 2003; Whitney et al., 2003, 2004). By fitting these Monte Carlo models we are effectively bypassing the effects of the circumstellar envelope, and placing the central stellar source on the Hertzsprung Russell diagram, by interpolating between the pre-main-sequence evolutionary tracks of Bernasconi & Maeder (1996); Siess, Dufour & Forestini (2000).

When we are fitting these YSO models, our results are effectively constrained within the parameter space that the Robitaille et al. (2006) models are built upon; having inherent assumptions, degeneracies, and multidimensional parameters spaces to fit within. As a result of this, when we fit these models to the available photometry that we have, inevitably there will be multiple combinations within this parameter space that can accurately describe the properties of the YSO. Therefore, the more logical approach to defining the parameters of a YSO is not to pinpoint the sole, unique solution, for each candidate, but rather to define how well we can constrain the physical properties of each candidate. As a result of this we define, for each YSO, a set of i well-fit parameters, a well-fit criterion of:

$$\chi_i^2 - \chi_0^2 \leq 3 \times n_{data} \tag{4.1}$$

By doing this, we are then able to construct a χ^2 weighted, normalised probability P_i of each model fit, such that:

$$P_i\,(\chi^2) = e^{-(\chi_i^2 - \chi_{min}^2)/2} \tag{4.2}$$

where we normalise this distribution, for each model, such that $\sum P = 1$. Using this probability distribution, we can begin to constrain the key parameters that will be required to determine the evolutionary phase of candidate YSOs, namely the stellar mass, bolometric luminosity, circumstellar envelope accretion rate, and circumstellar disk mass.

We define the characteristic values for the stellar parameters, mass ($X = M_*$), and bolometric luminosity ($X = L_{bol}$), as the probability-weighted means of the parameter distributions:

$$\langle X \rangle = \sum P_i \, X_i \tag{4.3}$$

For the circumstellar parameters derived from our YSO fits, such as the envelope accretion rate ($Y = \dot{M}_{env}$) and circumstellar disk mass ($Y = M_{disk}$), we find that these results tend to be across many orders of magnitude. Such a large spread in results makes deriving a probability-weighted means somewhat implausible, therefore we decide to define these values as the found medians of the parameter distribution. By taking such an approach, the value derived will not be affected by any extreme, outlying values, that were obtained during the fitting process. We define these parameters such as:

$$\langle Y \rangle = \mu_{1/2} \, (Y) \tag{4.4}$$

For both the stellar and circumstellar parameter distributions, we also derive the $1\,\sigma$ uncertainty as the standard deviation on the characteristic parameter values $\langle X, Y \rangle$. From our YSO fitting, we find that some 599 of the 1,091 reliable IR excess sources, are well fit by a Robitaille et al. (2006) YSO model, satisfying the criterion of $\chi^2 \text{-} \chi^2_{best} \leq 3 \times n_{data}$; Table 4.2 lists the derived parameters for a sample of YSOs that we discuss, while the parameters for all our sources are given in Table C.6.

4.4.1 YSO Evolutionary Stage

With this sample of 599 well fit candidate YSOs, we can use the physical properties derived earlier to divide these sources into evolutionary stages that follow the Robitaille et al. (2006) classification scheme. As we discussed in section 1.4.1, YSOs have traditionally been defined according to the spectral index (Equation

Table 4.2: Examples of the derived physical properties for all candidate YSOs identified within G305; full YSO table available in Table C.6.

ID	$\langle M_* \rangle$ ($M_\odot$)	$\sigma\,(M_*)$ ($M_\odot$)	$\langle log\,L_{bol} \rangle$ ($L_\odot$)	$\sigma\,(log\,L_{bol})$ ($L_\odot$)	$\left\langle log\,\dot{M}_{env} \right\rangle$ ($M_\odot\,y^{-1}$)	$\sigma\left(log\,\dot{M}_{env}\right)$ ($M_\odot\,y^{-1}$)	$\langle log\,M_{disk} \rangle$ ($M_\odot$)	$\sigma\,(log\,M_{disk})$ ($M_\odot$)	Stage
G305.1108+00.7893	1.4	0.08	1.36	0.17	-5.48	-4.18	-2.50	-1.72	Stage 0/I
G305.0741+00.6131	2.9	0.09	1.32	-0.23	-8.24	-5.39	-2.15	-1.54	Stage II
G305.8324-00.1616	3.7	0.10	2.21	0.64	0.00	0.00	-6.35	-2.70	Stage III

1.14) of their SED, however this approach can lead to a blurring of boundaries between the classes. The limitation of the spectral index classification approach is the dependence on viewing angle, where the same object may be grouped into differing evolutionary stages according to the viewing angle of the observer. Calvet et al. (1994) find for a source accompanied with a circumstellar disk viewed edge on would display an SED characteristic of a Class I object, while if the same source were to be observed pole-on, we would observed a flat SED, rather than a rising one, leading to a misclassified source.

The classification scheme of Robitaille et al. (2006) mirror that of the classical T Tauri scheme, but rather than defining an observational "Class", what is instead defined is an evolutionary "Stage" that is defined according to the physical parameters from the model (i.e. the circumstellar disk mass, and envelope accretion rate). These Stages are defined as according to the envelope accretion rate, M_{env}, and the circumstellar disk mass, M_{disk}, both of which are normalised by the mass of the central star, M_*;

- **Stage 0/I**: $\dot{M}_{env}\,/\,M_* > 10^{-6}$ yr^{-1}
- **Stage II**: $\dot{M}_{env}\,/\,M_* < 10^{-6}$ yr^{-1} ; $M_{disk}\,/\,M_* > 10^{-6}$ yr^{-1}
- **Stage III**: $\dot{M}_{env}\,/\,M_* < 10^{-6}$ yr^{-1} ; $M_{disk}\,/\,M_* < 10^{-6}$ yr^{-1}

In this, Stage 0/I sources are protostars that are still heavily embedded within their infaling natal dust and gas cocoons, Stage II sources are similar to classical T Tauri sources in having, in the optical and near IR, optically thick circumstellar disks that dominate the near-, to mid-IR portion of the SED, while Stage III sources display an optically thin remnant disk and have an SED that is dominated

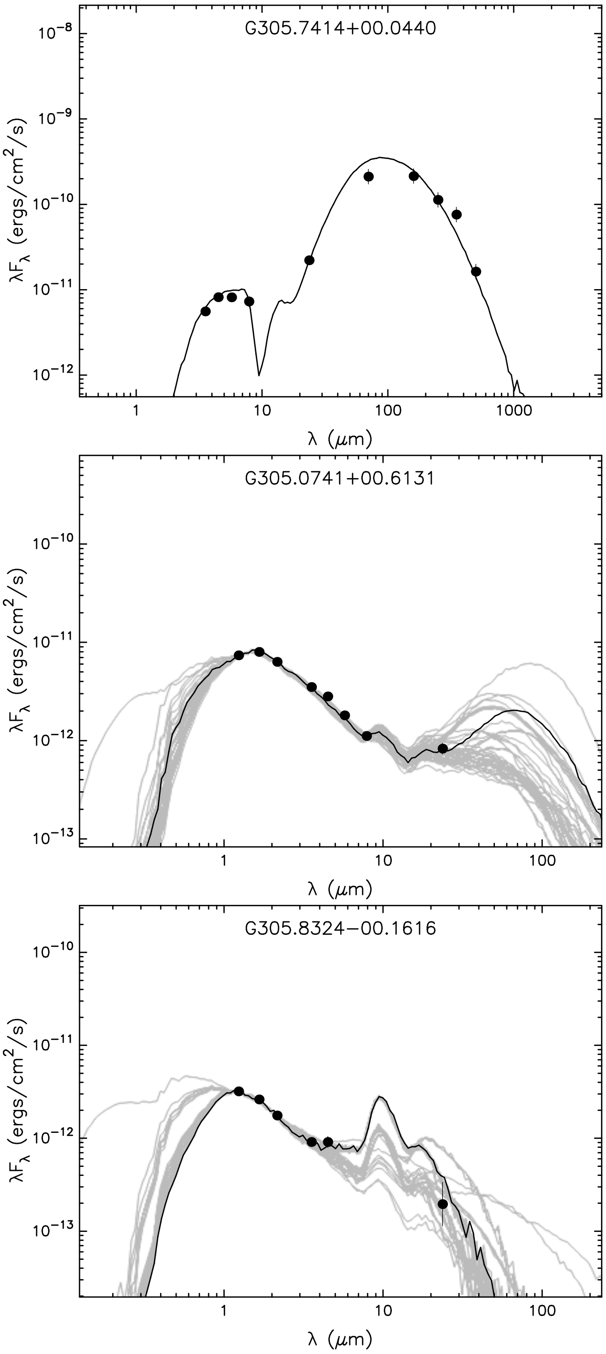

Figure 4.8: Examples of best-fit model SEDs for YSOs identified in G305, each at a various evolutionary stage; *Top*: Stage 0/I SED, *Middle*: Stage II, *Bottom*: Stage III.

by photospheric emission (thus making detection by IR emission alone difficult) (Smith et al., 2010). This classification scheme provides us the ability to identify and describe a physical and evolutionary frame for intermediate-, to high-mass YSOs in a similar way to the classical T Tauri approach, which itself may not be applicable to these mass regimes.

Since each candidate YSO has been fit with multiple models, we can again construct a probability distribution of the evolutionary stage for each YSO. A candidate YSO is defined as a Stage 0/I, II, or III if $\sum P_i(Stage)\ \geq 0.67$; if a source fails to meet this condition, then we define this source as "Ambiguous"; the majority of sources found to be Ambiguous are probably found to be between the Stage 0/I to II classifications, with Stage III sources tending to be far harder to identify solely in the IR. The inclusion of this Ambiguous class allows us to acknowledge the limitations of attempting to impose a set of distinct classes on a continuously evolving sequence (Povich et al., 2011). The YSO evolutionary stage composition found in G305 is shown in Table 4.1, while examples of the SEDs of various identified YSO stages is shown in Fig.4.8.

4.5 The Global Properties Of G305 YSOs

Starting with a sample of some 187,106 sources that were detected in a minimum of four 2MASS/VVV + IRAC bands, we have obtained a catalogue of some 599 YSOs within G305, whose positions are shown in Fig.4.9. As is quite apparent, the vast majority of sources within G305 have been removed from our catalogue, with the vast majority of these sources being removed as likely contaminating foreground sources, or fainter background objects. This final sample is rather small, being less than 1 % of the initial catalogue, but what we must state clearly is that this is most likely the minimum number of YSOs present within G305. The reason we can state this is an underestimate of the YSO content is the pursuit of a meticulous set of criteria for inclusion of candidate sources, and the rigorous constraints that were placed on the SEDs.

The stringent selection criteria we employed allowed us to identify a sample that was highly reliable, rather than pursuing a complete sample, making us far more likely to omit true YSOs from our sample, rather than include false IR excess sources. A clear example of this is the issue of sources with excess $8\,\mu$m emission; bright diffuse PAH emission, as is seen in Fig.2.6, causes us to reject many sources, in our case some 2,450 in total. We also find that our sample can be found to be slightly biased against Stage 0/I sources, since these sources can be found to be very red, and are likely only detected at longer wavelengths, thus making the requirement of a minimum of four 2MASS/VVV + IRAC band detections rather prohibitive. Finally, those sources found to be highly embedded, high-mass YSOs would also be systematically omitted from the candidate YSO catalogue from the very beginning. Having started from a Point Source 2MASS catalogue, these embedded sources that are found to be extended objects, would have not have been included in this catalogue, meaning they were simply not included to begin with. Clearly such an approach to identifying YSOs has its drawbacks, and we have mentioned them, however the strength of this approach is the reliability that these strict criteria placed on the final sample. With this reliable catalogue of YSOs we are able to study, and draw strong conclusions, about the physical properties of YSO population of G305 and the nature of star formation within the complex. As Chapter 3 allowed us to comment on the upper end of star formation in the complex, the work in Chapter 4 will allow us to draw conclusions on the lower limit of star formation within G305.

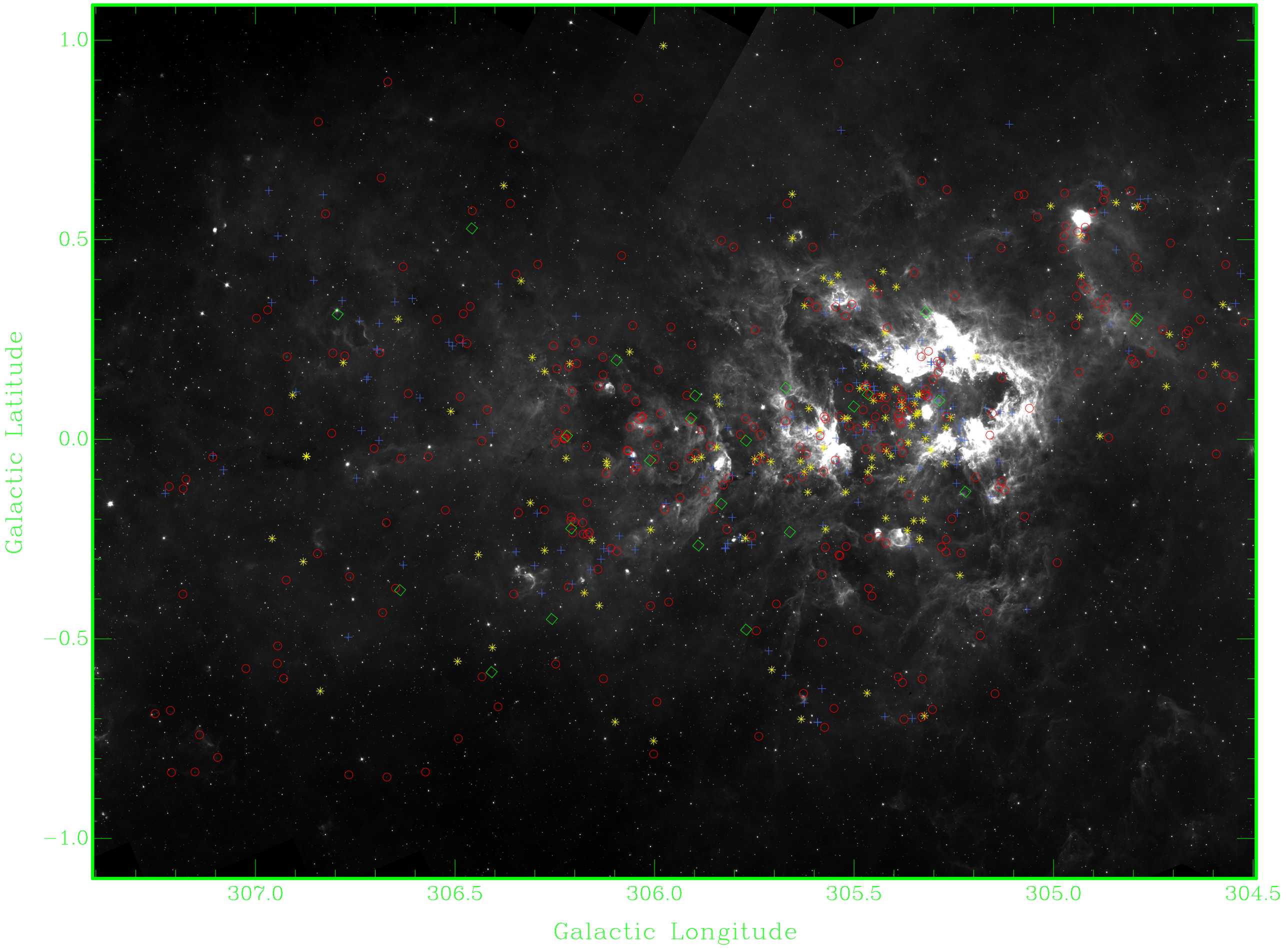

Figure 4.9: A *Spitzer* IRAC 8 μm image of G305, with all 599 identified YSOs shown also. The various symbols represent the evolutionary stages of each YSO: blue crosses = Stage 0/I, red circles = Stage II, green diamonds = Stage III, yellow asterisks = Ambiguous sources.

4.5.1 The YSO Mass Function

Following on from the results of our probability distribution approach to YSO parameter derivation (section 4.4), we can employ the derived stellar masses for each YSO to construct the YSO mass function (YMF), following a similar approach employed by Shepherd et al. (2007); Whitney et al. (2008) for all 599 YSOs identified. The YMF is defined in a similar form to the stellar IMF, such that:

$$\xi\left(log\, m\right) = \frac{dN}{d\, log\, m} \propto m^{-\Gamma} \tag{4.5}$$

where dN is the number of stars in the logarithmic mass interval $\log m$, $\log m + d \log m$, and Γ is the power-law slope (Bastian, Covey & Meyer, 2010).

In constructing the YMF, we are able to determine the power-law slope of the G305 YMF, however care needs to be taken in that we do not include significant numerical biases when uniformly binning our data. Our process requires us to bin the derived YSO masses, and using χ^2 minimisation, we fit a power-law to this binned data to obtain our index value. The origin of this bias is caused by the strong anticorrelation present between the binned stellar masses, and the weights in χ^2 minimisation for these derived values with an associated Poisson uncertainty (Wheaton et al., 1995). This situation is particularly important for our results, as the most noticeable biases occur when the number of stars in each mass bin is small, compared to other populated mass bins (Wheaton et al., 1995); this is the case for sources found beyond our completeness limit, or for scarce high-mass YSOs. Many studies that have focused their attention to deriving an accurate power-law slope for the IMF, and reported strongly varying results (Massey, 2003), sometimes being dramatic variations in the same region; for NGC 6611 a value of -1.1 ± 0.1 was indentified by Hillenbrand et al. (1993), while Massey, Johnson & Degioia-Eastwood (1995) find a power-law of -0.7 ± 0.2. Therefore, strong biases introduced from calculating an IMF where some mass bins are underpopulated, while others are heavily populated can go some way in explaining the apparent variations in results (Kroupa, 2001; Elmegreen, 2004). To minimise the uncertainty in our analysis, we adopt the approach of Maíz Apellániz & Úbeda (2005), who propose the use of variable-sized bins in the analysis. In this,

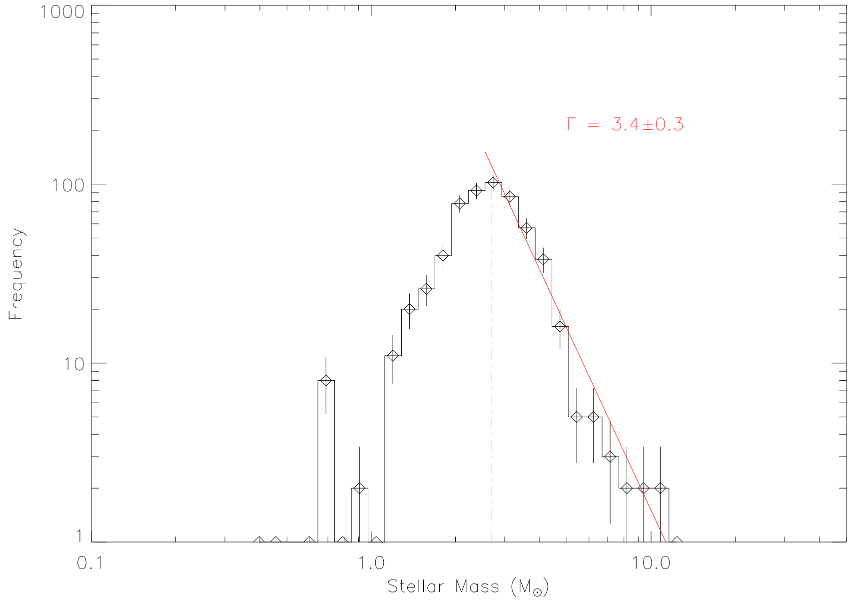

Figure 4.10: YMF plot for all 599 YSOs identified within G305. The power-law fit to our results with accompanying power-law slope, Γ, is shown, along with completeness limit of ≈ 2.6 M⊙ shown as the dashed line.

by using variable-sized bins, the division of stellar mass is more evenly spread over the bin intervals, thus reducing any biases present and breaking the strong dependence that variation has on the number of YSOs per mass bin. In this technique, Maíz Apellániz & Úbeda (2005) note that the ideal number of bins to divide the sources amongst is $\approx 2\,N^{2/5}$, where N is the total number of YSOs.

The resulting YMF for G305 is shown in Fig.4.10, and from our χ^2 minimisation fitting, we find a power-law slope $\Gamma\ \approx 3.4 \pm 0.3$. We find from χ^2 minimisation that the YMF is fit with a power-law up for $M_c \leq 10\,\mathrm{M}_\odot$; the departure from the power-law is found a for $M_c\ \approx 2.6\,\mathrm{M}_\odot$, which does not signify a real break in the YMF, but rather reflects the incompletenesses in our YSO catalogue, due to the detection of lower-mass sources. We firstly note that, as discussed in section 1.7.1, for the Galactic IMF a turnover of $\approx 0.1\,\mathrm{M}_\odot$ is observed (Kroupa, 2002; Chabrier, 2003; Kroupa & Weidner, 2005). Therefore, our observed turnover at $M_c\ \approx 2.6\,\mathrm{M}_\odot$ for G305 seems more likely due to incompleteness, rather than a physical phenomena that is observed within this star-forming complex.

We can test how reasonable this completeness limit is by comparing to the sensitivity of MIPSGAL observations to YSOs as a function of luminosity. Dunham et al. (2008) identify a sample of low-mass YSOs from data taken as part of the *Spitzer c2d* survey of Serpens (Harvey et al., 2006, 2007b,a), Lupus I, Lupus III, Lupus IV clouds (Chapman et al., 2007; Merín et al., 2008), Chamaeleon II (Young et al., 2005; Porras et al., 2007; Alcalá et al., 2008), Ophiuchus (Padgett et al., 2008), and Perseus (Jørgensen et al., 2006; Rebull et al., 2007) at distances of 260 ± 10, 150 ± 20, 200 ± 20, 150 ± 20, 178 ± 18, 125 ± 25, and 250 ± 50 pc respectively. From this sample Dunham et al. (2008) find an approximately linear relationship between MIPS 24 μm observations, and the total internal luminosity of this identified sample of YSOs; this result is consistent with predictions of radiative transfer models of low-mass YSOs (Crapsi et al., 2008). From least square fitting to the observations, Dunham et al. (2008) find the following relation:

$$log(\nu f_\nu) \;=\; [(0.87 \,\pm\, 0.20)\, log\,(L) \;-\; (10.05 \,\pm\, 0.17)]\ \mathrm{erg\,cm^{-1}\,s^{-1}} \tag{4.6}$$

where this result has been normalised to a distance of 140 pc. We can extend this result, by substituting the relationship $f_\nu \,\propto\, d^{-2}$, to obtain:

$$f_{24\,\mu m} \;=\; \frac{1}{\nu}\,\left(10^{(log(L^{0.87})\,-\,10.05)}\right)\left(\frac{140^2}{d^2\,(pc)}\right)\left(10^{23}\right)\ \mathrm{Jy} \tag{4.7}$$

From our YMF results, we can see that the vast majority of YSOs are found in the Stage 0/I and Stage II evolutionary stages, therefore with a completeness limit of 2.6 $\mathrm{M}_\odot$ and a mass-luminosity relation for pre-main-sequence stars of $L_* \,\propto\, M_*^{2.5}$ (Bernasconi & Maeder, 1996), we obtain a luminosity $L_* \,\approx 11\,\mathrm{L}_\odot$. By placing this luminosity into Equation (4.7), we obtain a detection at our completeness limit of $f_{24\,\mu m} \,\simeq 7$ mJy. We compare this to the quoted 5σ sensitivity of 1.7 mJy at 24 μm for MIPSGAL (Carey et al., 2009), suggesting that our YSO completeness limit of 2.6 $\mathrm{M}_\odot$ is within the sensitivity limit of *Spitzer*; the implication being that MIPSGAL is not sensitive to YSOs with masses $< 2\,\mathrm{M}_\odot$.

Our results are in good agreement with similar YSO studies that have been conducted in other Galactic star-forming regions: Povich & Whitney (2010) find

Galactic HII region M17, a power-law slope $\Gamma \approx 3.5 \pm 0.6$ to a completeness limit of $M_c \approx 3.9\,\mathrm{M}_\odot$, while Povich et al. (2011) find for the Carina Nebula a power-law of $\Gamma \approx 3.2 \pm 0.3$ up to a limiting mass $M_c \approx 3.1\,\mathrm{M}_\odot$. In comparing the power-law slope, we find a significant disparity between the result for G305, and those found in across a range of environments that include young open clusters and field stars. Across these varying environments, the power-law slope is found to be practically consistent, and is best described by the standard Salpeter-Kroupa IMF of slope $\Gamma = 1.3$ (Kroupa, 2001). We can directly compare our results with similar determinations of the IMF within G305; Davies et al. (2012) conducted an analysis of the populations of Danks 1 & 2, and found a power-law slope of 1.4 ± 0.17 and 1.38 ± 0.16 respectively, while Leistra et al. (2005) focused on the young stellar cluster G305.3+00.2 and find a power-law slope of 1.5 ± 0.3 (the massive stellar populations of these targets are given in Table A.1). A YMF power-law slope for G305 of $\Gamma \approx 3.4 \pm 0.3$, before turning over due to incompletenesses at $M_c \approx 2.6\,\mathrm{M}_\odot$, is notably steeper than these other cases within G305, and suggests an apparent deficit of high-mass YSOs within G305.

What must be noted at this stage is, as mentioned earlier, any results obtained here are strictly lower limits, where we cannot be certain to have fully identified the intermediate-, to high-mass YSO content of G305 because of the strict selection criteria we have imposed in identifying candidate YSOs. Aside from the potential loss of sources during the selection process, the estimate of YSO mass may also be off due to issues such as multiple systems. In this case we have treated the system as a single YSO, and thought the final mass obtained via SED fitting may overestimate the mass of the most massive source within a multiple system, it will most certainly underestimate the combined stellar mass of the system (Whitney et al., 2008).

4.5.2 Present-Day SFR

The YMF that we have constructed for G305, and show in Fig.4.10, contains our 599 candidate YSOs across the G305 complex, and is not concentrated in one single volume of space, or single cluster. The sources that have been identified, however, are drawn from a coeval stellar population, that represents the recent generation of star formation within G305; therefore taking this sample should allow us to determine a present-day SFR for G305.

In order to accurately estimate a present-day SFR from the YSO sample, a realistic timescale for each evolutionary stage is required. As mentioned earlier, the presence of a circumstellar disk and/or infalling envelope was a prerequisite for inclusion in the G305 YSO catalogue, therefore an estimate of the accretion phase and disk lifetime should provide us with reliable timescales for each evolutionary phase. In the classical case of low-mass, Class I YSOs, the phase is found to typically exhibit a lifetime of $\approx 0.1\,\mathrm{Myr}$ (Kenyon & Hartmann, 1995; Haisch, Lada & Lada, 2000), we can use this as a sanity check for our own estimate of the Stage 0/I lifetime. To place a characteristic timescale on the lifetime of Stage 0/I, we use an accretion age, t_A such that (Povich & Churchwell, 2009):

$$t_A = 10^{-6}\,\frac{M_*}{\dot{M}_{env}} \tag{4.8}$$

where we assume that the circumstellar envelope accretion rate remains constant over this accretion age, and that all accreting material will eventually reach the central stellar source. By combining the probability derived parameters for all Stage 0/I YSOs identified, we obtain an average accretion age $t_A \approx 0.07\,\mathrm{Myr}$, which we find is in good agreement with the estimated lifetime of Class I YSOs.

We next need to derive a characteristic disk lifetime for Stage II sources, and by assuming a constant SFR within G305, the ratio of Stage II to Stage 0/I sources should allow us to compare the relative lifetimes. In attempting to study the ratio of the two populations, we must take care that populations of a similar mass range are not compared, we therefore need to implement a limit where we can compare the two distinct populations. In Fig.4.11 we have reproduced the G305 YMF, with the contribution to the YMF shown for each evolutionary stage. As we can see, the bulk of Stage 0/I sources are found below our completeness limit $M_c \approx 2.6\,\mathrm{M}_\odot$, while at $M_* \geq M_c$ the main constituent of the YMF is of Stage II sources. Taking this completeness limit as our boundary, we find that the ratio of Stage II to Stage 0/I YSOs in G305 is 4.3. From this ratio, we can estimate the disk lifetime as follows (Povich & Churchwell, 2009):

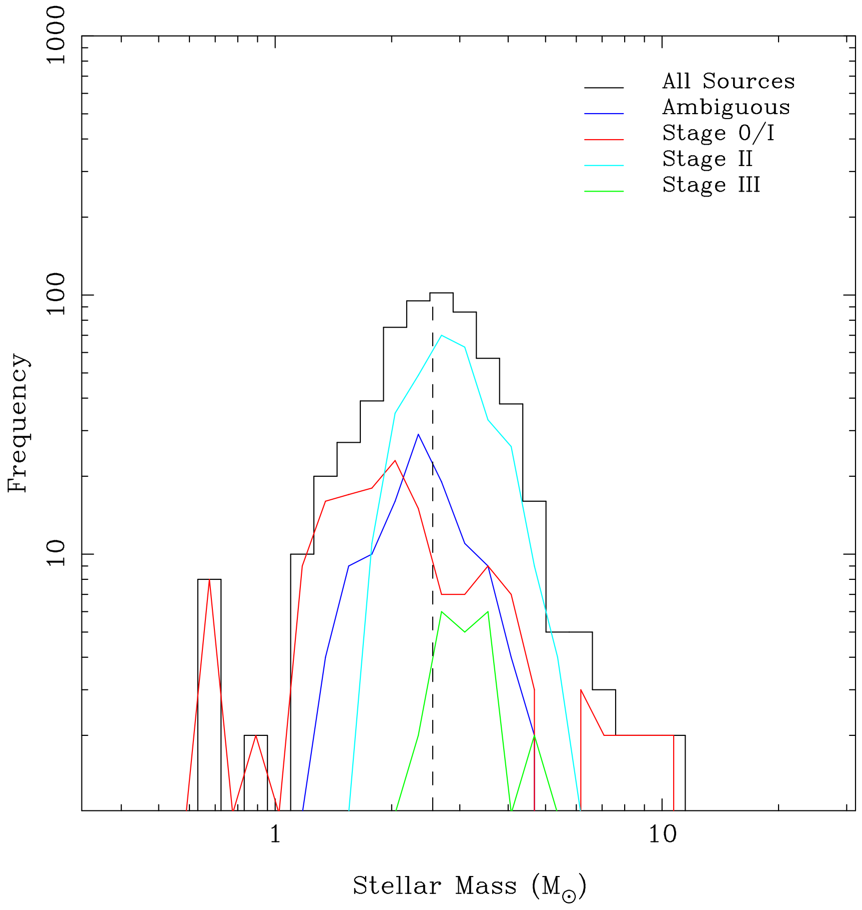

Figure 4.11: YMF plot for all 599 YSOs identified within G305, along with completeness limit of $\approx 2.6\,\mathrm{M}_\odot$ shown as the dashed line. In this example, the YMF is also broken down into evolutionary stages, with the contributions from Stage 0/I, Stage II, Stage III, and Ambiguous sources shown also.

$$t_D = 4.3\, t_A \tag{4.9}$$

from this we obtain a $t_D \approx 0.3\,\mathrm{Myr}$. In this calculation we have neglected to include the Ambiguous classified sources that, as can be seen in Fig.4.11, straddle the Stage 0/I to Stage II models.

With these two values, we can derive a characteristic age for the YSO population of G305 as $t_A + t_D \approx 0.37\,\mathrm{Myr}$. From our derivation of the stellar masses for each YSO identified, we found that our 599 YSOs represented some $1656 \pm 63\,\mathrm{M_\odot}$ in total, and by combining this stellar mass with our characteristic YSO age, we arrive at a YSO derived SFR of $0.005 \pm 0.001\,\mathrm{M_\odot\ yr^{-1}}$. As has been mentioned earlier, the incompletenesses present in our YSO sample, and the potential of having removed genuine YSOs under strict selection criteria, make this derived SFR a strict lower limit. This result again has good agreement with similar YSO studies of both M17 and Carina, where a respective SFR of 0.002 and $0.008\,\mathrm{M_\odot\ yr^{-1}}$ have been found (Povich & Churchwell, 2009; Povich et al., 2011). We can directly compare this result to the embedded massive SFR of Faimali et al. (2012) that was strictly an upper limit to the SFR of G305, since it was based on the population of embedded massive star-forming regions identified, and having assumed a Salpeter IMF that was extrapolated over a small sample of stars, we will have overestimated the total mass in stars. By comparing these two results we find that for these separate populations we constrain the SFR of G305 to $0.005 \pm 0.001 \leq \mathrm{SFR} \leq 0.015 \pm 0.005\,\mathrm{M_\odot\ yr^{-1}}$.

4.6 Discussion

4.6.1 Characterising The YSO Mass Function

As we have shown, the derived YMF for G305 shows a considerably steeper power-law slope than that found in the case of regular field stars, which tend to follow a Salpeter-Kroupa IMF (Scalo, 1986, 1998; Kroupa, 2001); we do find agreement with other star-forming complexes, such as M17 and the Carina Nebula, where we share the same YSO SED modelling technique. We now address the implications of this steep power-law slope, and test whether such a result can be understood in terms of physical phenomena within massive star-forming regions, or whether inherent biases in our YSO identification have propagated such observed steepness.

4.6.1.1 A Physical Interpretation

The overall composition of the YMF, as seen in Fig.4.11, shows the YMF is dominated by a narrow Stage II component, with a much broader component of Stage 0/I sources; Ambiguous defined YSOs are characterised by both these components. These Ambiguous sources are shown to be found more towards the lower-mass regimes, below our completeness limit, and this can be explained due to a lack of associated $24\,\mu$m detections for these sources, making a significant constraint on their physical properties during SED fitting somewhat problematic. We also find that the population of Stage 0/I sources is preferentially detected at lower masses than Stage II YSOs, since redder sources tend to be more dominant in the mid-IR, for a given mass (Povich et al., 2011). The steepness of the intermediate-mass component of the YMF, dominated by both Stage II and Ambiguous sources (themselves likely Stage II objects at this mass range, given the Stage 0/I and Stage II ratios) suggests that the presence of a circumstellar disk and its lifetime is a strong influence on the observed steepness of the YMF.

The timescale to which circumstellar disks are destroyed is inversely related to the mass of the central source, if we assume that photoevaporative dissipation caused by radiation from the central star is the driving force (Hollenbach et al., 1994; Monnier & Millan-Gabet, 2002); solar-mass YSOs are typically characterised by a timescale $\leq 2\,$Myr (Haisch, Lada & Lada, 2001). The suggestion, therefore, is that intermediate-, to high-mass YSOs have a much shorter timescale, with T Tauri like stars exhibiting circumstellar disk lifetimes of $\leq 1\,$Myr (Hernández et al., 2007). By following the estimate of disk lifetimes taken in section 4.5.2, we find the average disc lifetime $t_D \approx 0.16$ - $0.2\,$Myr at an intermediate mass-range of $4\,\mathrm{M}_{\odot}$; this result is found to be comparable to the typical accretion age for low-mass Class 0/I YSOs of $\approx 0.1\,$Myr (Kenyon & Hartmann, 1995; Haisch, Lada & Lada, 2000). We also find that our population of Stage 0/I sources all typically exhibit a similar accetion age $t_A \approx 0.1$ - $0.2\,$Myr. We also note that the ratio of Stage II to Stage 0/I sources does begin to steadily decrease with mass, with $m \geq 4\,\mathrm{M}_{\odot}$, and in fact this ratio inverts at $m > 6\,\mathrm{M}_{\odot}$, suggesting that the more massive YSOs are indeed younger. The conclusion from this, therefore, is that the much shorter disc lifetimes at increasing mass results in a shorter evolutionary phase for these intermediate-, to high-mass YSOs. This rapid disc destruction at higher masses would therefore mean that high-mass YSOs would be preferentially removed from our identified YSO catalogue, and may go some part in explaining the apparent steepness of the YMF in G305.

In adopting the Robitaille et al. (2006) SED models, we have assumed that a scaled-up version of the standard accretion model is applicable to the high-mass YSOs that we have identified. Within our sample, we identify sources with high envelope accretion rates in the order of $\approx 10^{-3.2}\,\mathrm{M}_{\odot}\,\mathrm{yr}^{-1}$, which is found to be consistent with an accretion-based theory of massive star formation. Such a result is consistent with a picture of high accretion rates for massive YSOs (Churchwell, 1999; Henning et al., 2000; Beuther et al., 2002; Zhang et al., 2005), while is further supported by observations of spectral line infall characteristic of high infall rates (Zhang & Ho, 1997; Keto, 2002; Fuller, Williams & Sridharan, 2005; Beltrán et al., 2006; Keto & Wood, 2006; Zapata et al., 2008), and is also a requirement for theoretical models also (Yorke & Sonnhalter, 2002; McKee & Tan, 2003). The observed high accretion rates may also further explain the lack of high-mass YSOs and apparent steepness of the YMF, as discussed above; a much shorter accretion age for massive YSOs would lead to a shorter evolutionary phase for these intermediate-, to high-mass YSOs.

However, when discussing these high accretion rates we need to take into consideration the limitations of the models, where our results are only as good as the input parameters of the models (Robitaille, 2008). Within the Robitaille et al. (2006) SED models, the stellar mass is modelled between $0.1 - 50\,\mathrm{M}_{\odot}$, while the accretion rates obtained typically vary from $10^{-4} - 10^{-5}\,\mathrm{M}_{\odot}\,\mathrm{yr}^{-1}$; the accretion rate is modelled to an upper limit of $20\,\mathrm{M}_{\odot}$, placing a maximum value of $\dot{\mathrm{M}}_{\mathrm{env}}/\mathrm{M}_{*} = 5 \times 10^{-4}\,\mathrm{yr}^{-1}$. From the SED fitting results, we see accretion rates much higher than typical values, with some sources reaching as high as $10^{-3.2}\,\mathrm{M}_{\odot}\,\mathrm{yr}^{-1}$. At these values the mass-radius relation for a massive YSO is expected to differ, and other models such as Hosokawa & Omukai (2009), consider accretions rates $> 3 \times 10^{-3}\,\mathrm{M}_{\odot}\,\mathrm{yr}^{-1}$ for an upper mass limit of $\approx 60\,\mathrm{M}_{\odot}$. In our sample of identified YSOs, typical upper limits in the stellar mass of $\approx 11\,\mathrm{M}_{\odot}$ are observed, therefore the model limitations of Robitaille et al. (2006) are deemed acceptable in this situation.

4.6.1.2 Possible Selection Effect?

Disc evolution clearly plays a part in the steepness observed in the YMF, however it alone cannot explain the lack of high-mass YSOs identified. Another competing factor, that effects the observed YMF composition, is the inherent biases present in detecting YSOs at various evolutionary phases. The wavelength coverage of *Spitzer* observations included in our analysis, upon which we begin the process of catalogue building, have been shown to be excellent at identifying the mid-IR excess emission that originates from the circumstellar material around YSOs (Allen et al., 2004; Harvey et al., 2007a; Koenig et al., 2008). A combination of the mid-IR extinction law of Indebetouw et al. (2005), along with the IRAC 4.5 μm and 5.8 μm bands proves crucial in identifying YSOs, where the flattening of the observed extinction curve between the 4.5 μm and 8.0 μm bands is important in reducing the degeneracies between interstellar extinction and intrinsic IR excess emission.

As discussed earlier, selection of candidate YSOs was made on the basic of reliable IR excess emission, and the apparent lack of Stage III sources identified points to a YMF populated with YSOs that exhibit excess emission either from optically thick circumstellar disks and/or emission due to infalling from the circumstellar envelope. Having such a detection emphasis on the presence of circumstellar material, be it in the form of an accreting envelope or disk, does place a completeness limit, that is dependent on the evolutionary stage of object, on the finality of our YSO catalogue for G305. The 2 - 24 μm coverage is ideal for the detection of Stage II YSOs, where the IR excess of circumstellar disks around young stars provides a tell-tale tracer, while the detection of the earlier stage of YSO evolution requires longer, far-IR, to fully identify the entire Stage 0/I content of G305; this earlier, embedded stage, is particularly underestimated in our catalogue based on IRAC and MIPSGAL data.

Though far-IR Hi-GAL observations are included in our catalogue, helping to populate the SEDs of Stage 0/I sources, the inclusion of the data followed on from a series of stringent near- and mid-IR selection criteria, that helped provide us with a highly reliable sample of sources. These embedded sources are preferentially detected towards longer wavelengths, where the SED is found to peak at $\lambda \geq 100\,\mu$m, and the selection criteria that we impose, most noticeably the requirement of a detection in at least four of the seven 2MASS/VVV and IRAC bands, will have an effect in filtering out these embedded sources. Adding to this issue is that the bulk of these highly embedded MYSOs are found to have extended structures, and will have simply not been included within the YSO catalogue from its inception. A clear example of this can be seen by comparing the 599 YSOs within the final G305 catalogue to the embedded massive star-forming regions identified in Chapter 3, where we find that of the 16 candidates identified, only 3 are found to be reproduced within the G305 YSO catalogue (i.e. only 3 have a GLIMPSE counterpart). The combination of having extended structures that are not included in point source catalogues, and the fact that these embedded MYSOs tend to be detectable at longer wavelengths, and so fail initial near-IR and mid-IR selection criteria, means that some embedded high-mass candidates will have been removed from our initial YSO catalogue. We note also that the lack of high-mass candidates may also be the result of saturation in the datasets. For GLIMPSE passbands, a brightness limit of 7.0 mag at $3.6\,\mu$m and 6.5 mag at $4.5\,\mu$m is found (Benjamin et al., 2003), which may mean that a few more massive candidates are missed from our sample.

As stated from the outset, our approach has been to produce a comparable study in G305 to those of the Carina nebula (Povich et al., 2011), and M17 (Povich & Churchwell, 2009; Povich & Whitney, 2010), while also extending the approach to both VVV and *Herschel* Hi-GAL observations. In making our study comparable, we adopt certain selection criteria to remove contaminating sources (i.e. highly reddened stars, AGB stars, background AGN), and eventually this provides us with a sample of candidate YSOs. We must note however, that any errors or selection bias that may have been inadvertently introduced into both the studies of Carina and M17, will also exist within our study of G305, and this must be raised as a potential source of error in our final YSO sample.

In this chapter, we started our selection process with the requirement that a candidate YSO must have been detected in either GLIMPSE, 2MASS, or VVV. As a result of this, we have been biased towards later stage YSOs, and not necessarily the earliest, embedded phases of star formation. Ideally, to address this issue, we would produce a single YSO catalogue that will combine the populations identified in this chapter, and that of Chapter 3. In order to do this, we would continue our analysis as discussed here, but in order to select those earlier embedded sources, we would not require a candidate to have an initial GLIMPSE, 2MASS, or VVV detection, but rather consider candidates detected at $\lambda \geq 24\,\mu$m or $\lambda \geq 70\,\mu$m, which could then be fit to the Robitaille et al. (2006) SED models with GLIMPSE upper limits. Due to time constraints we have been unable to produce this single YSO catalogue, yet this is a clear avenue of immediate future work, as we propose in section 5.3.1.

4.6.2 YSO Spatial Distribution

Our results, the identification of some 599 YSOs, confirms that G305 is a rich and active star-forming region, where the distribution of the identified YSOs is not random, but in fact belies some structure and possible evidence towards the the formation process within the complex. The content of G305 suggests that star formation is in its early stages, where we find that the ratio of Stage 0/I to Stage II sources is ≈ 0.5 shows that a substantial fraction of star-forming content is found in an initial evolutionary phase. This youth in formation is found to agree with other similar massive star-forming regions such as W51 (0.8; Kang et al. 2009), M17 (0.5; Povich & Whitney 2010), and N66 in the SMC (0.7; Simon et al. 2007). What we also find, and share in common with these other examples, is a preference for YSO candidates to be found towards both Danks 1 & 2, within the central HII region of G305. Within this central cavity we estimate an averaged surface density of YSOs that is found to be $\approx 6.3\,\mathrm{YSO\,pc^{-2}}$, again in good agreement with other regions such as Vulpecula OB 1 ($7.4\,\mathrm{YSO\,pc^{-2}}$; Billot et al. 2010), Serpens ($13.0\,\mathrm{YSO\,pc^{-2}}$; Harvey et al. 2007a), and Lupus ($3.3\,\mathrm{YSO\,pc^{-2}}$; Merín et al. 2008). Studying Figs.4.12 - 4.15, we can begin to get a better understanding of the evolutionary distribution of YSOs across G305, and there appears to be tentative evidence of certain evolutionary stages being preferentially located either within, or outside of, the central cavity of G305.

What we firstly see from Figs.4.12 - 4.15, is that Stage 0/I sources are more readily detected towards the central cavity of G305, and that even moving outwards from here, Stage 0/I sources in the majority of cases are found to be located within regions of higher density that the surrounding environment; which to certain extent can be expected from a population that is highly embedded, and in its infancy. Comparing this to the Stage II population, we see a significant fraction within the central region, however the extent of the clustering is not equivalent to that of their earlier siblings. The Stage II population seems more distributed across G305, and not necessary confined to the natal material of G305. As argued by Robitaille et al. (2008), these candidate YSOs may in fact be AGB stars that have managed to find themselves within the final YSO catalogue, even with the implementation of stringent selection criteria. However, Koenig et al. (2008) argue that such a population of YSOs could either be due to formation in isolation, or a population that have been ejected from their formation site via gravitational interactions with other members within the natal cluster; assuming a ejection velocity of $10\,\mathrm{kms}^{-1}$(Goodman & Arce, 2004), a YSO could travel the projected size of G305, 30 pc, in a timescale of $\approx 3\,$Myr. Considering the Ambiguous YSO population, we also see a stronger preference towards the central region, which can be accounted for by the increase of bright mid-IR emission as was shown in Fig.4.2. The strong saturation of the $24\,\mu$m observations towards the central region meant that, in some cases, crucial mid-IR emission was absent from the construction of the YSO SED, and as has been discussed earlier, this region of the SED is crucial in determining the evolutionary class between either a Stage 0/I or Stage II YSO; this effect becomes less of a concern for highly luminous YSOs (Indebetouw et al., 2007).

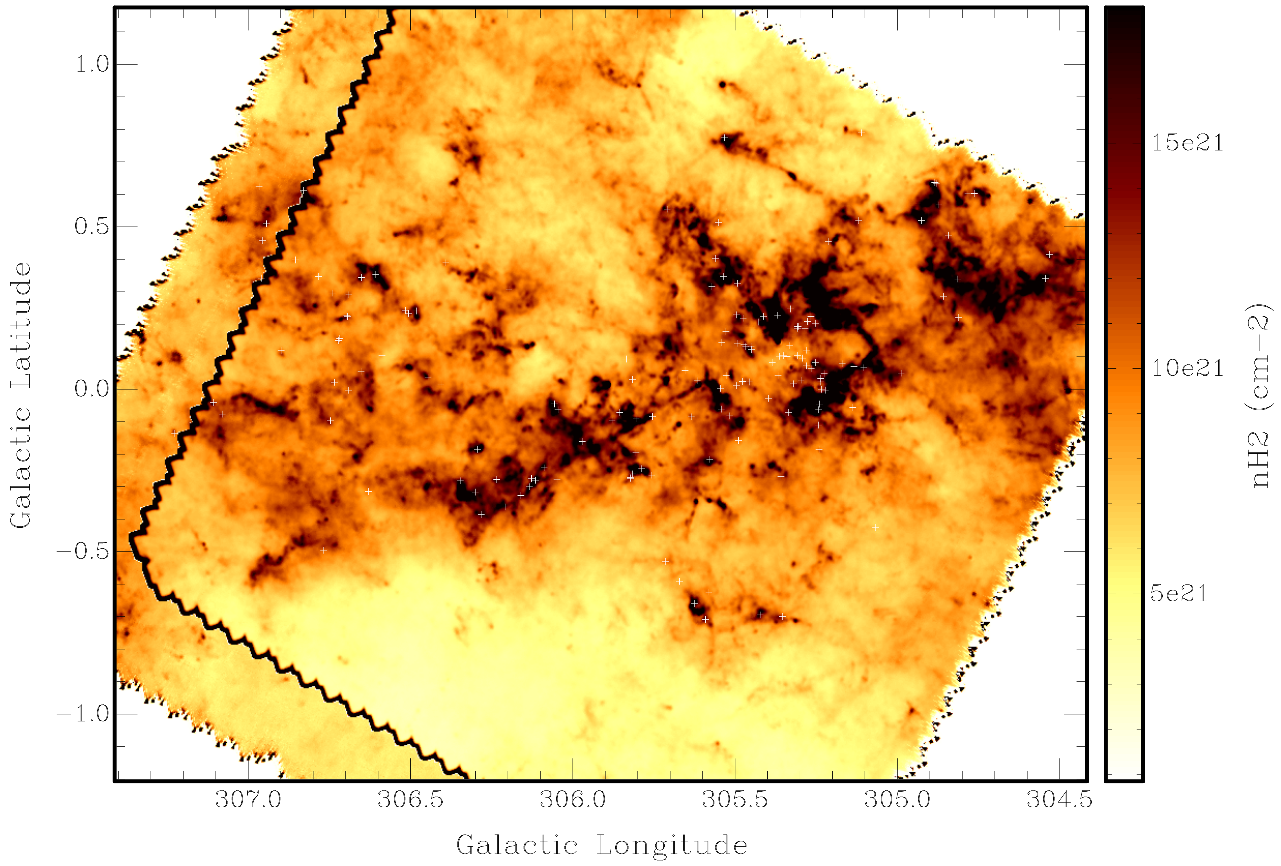

Figure 4.12: G305 column density map derived from *Herschel* Hi-GAL PACS/SPIRE observations, with Stage 0/I YSOs shown as crosses.

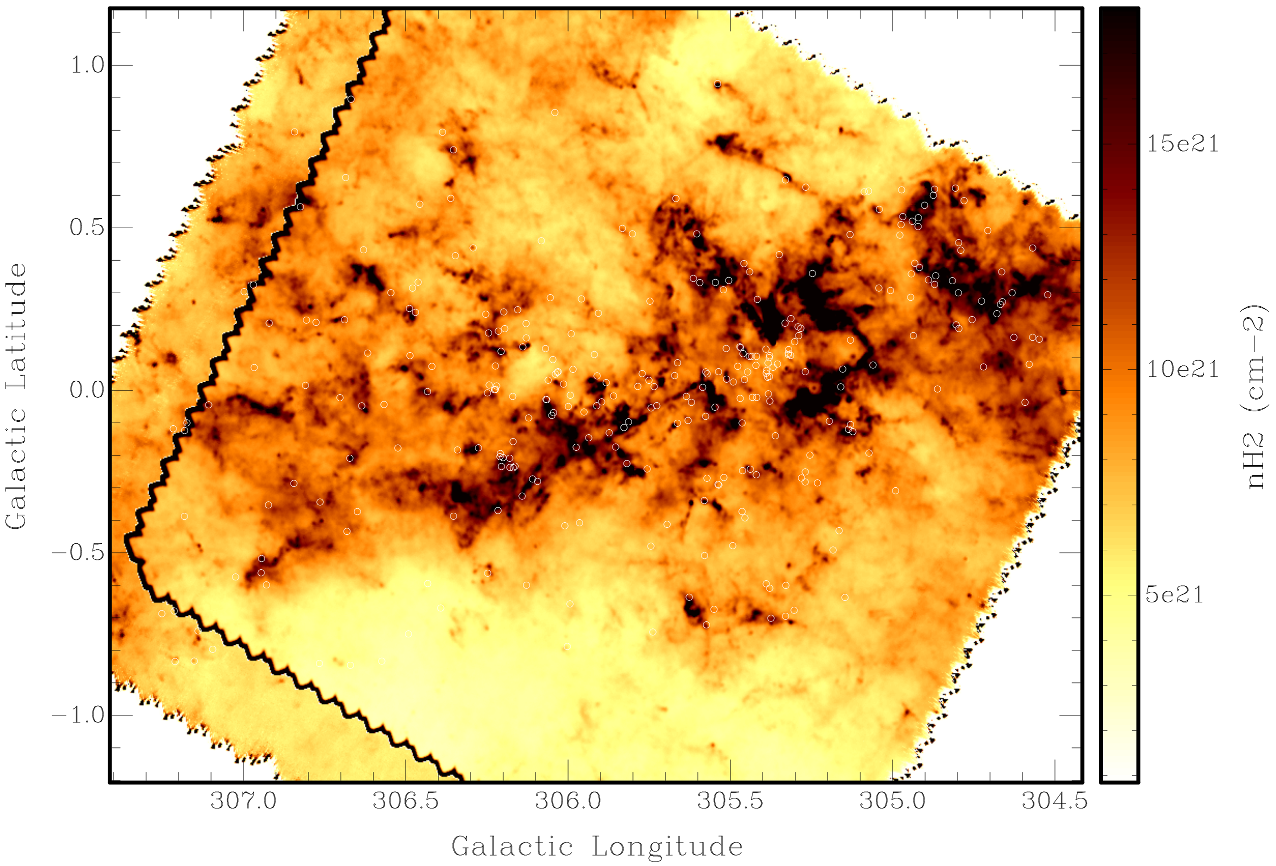

Figure 4.13: Similar plot to Fig.4.12, yet with the distribution of Stage II YSOs, shown as circles.

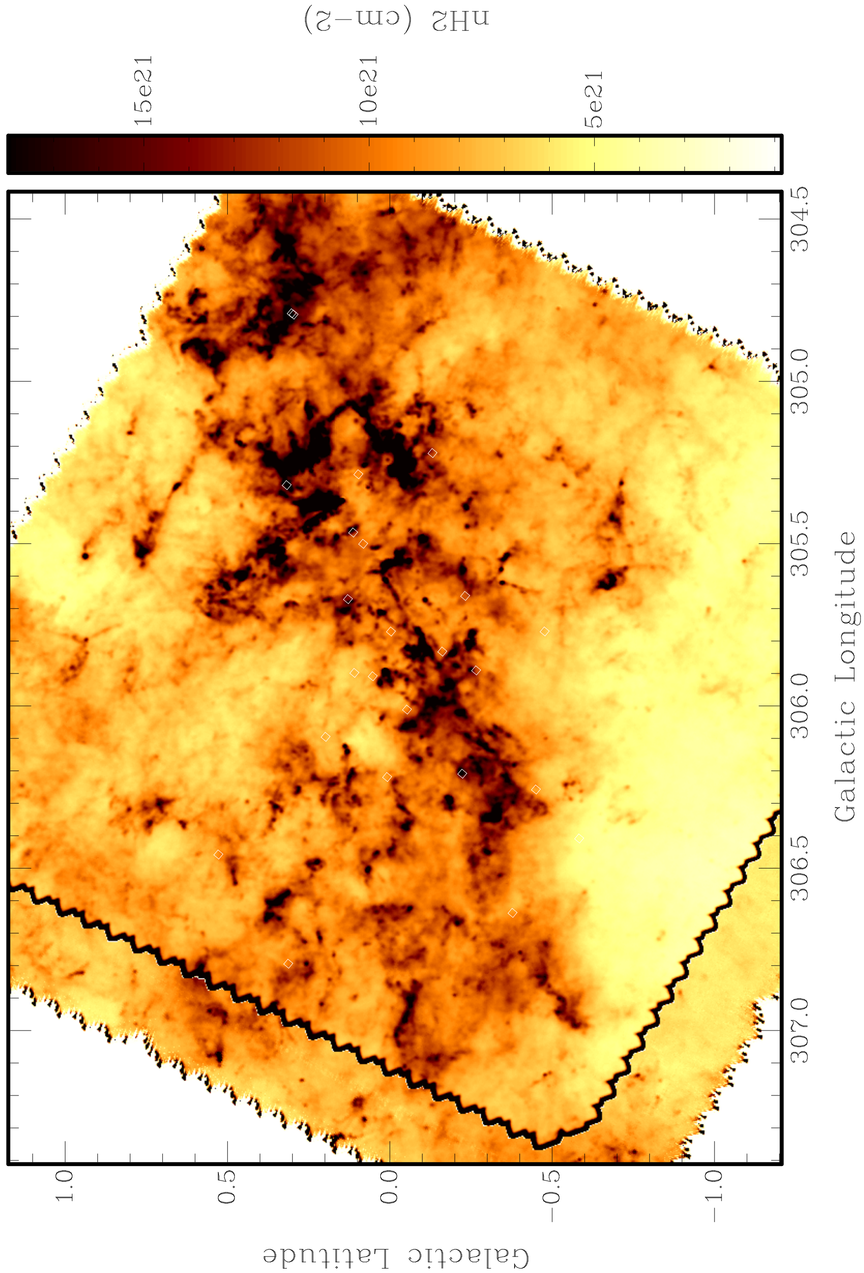

Figure 4.14: Similar plot to Fig.4.12, yet with the distribution of Stage III YSOs, shown as diamonds.

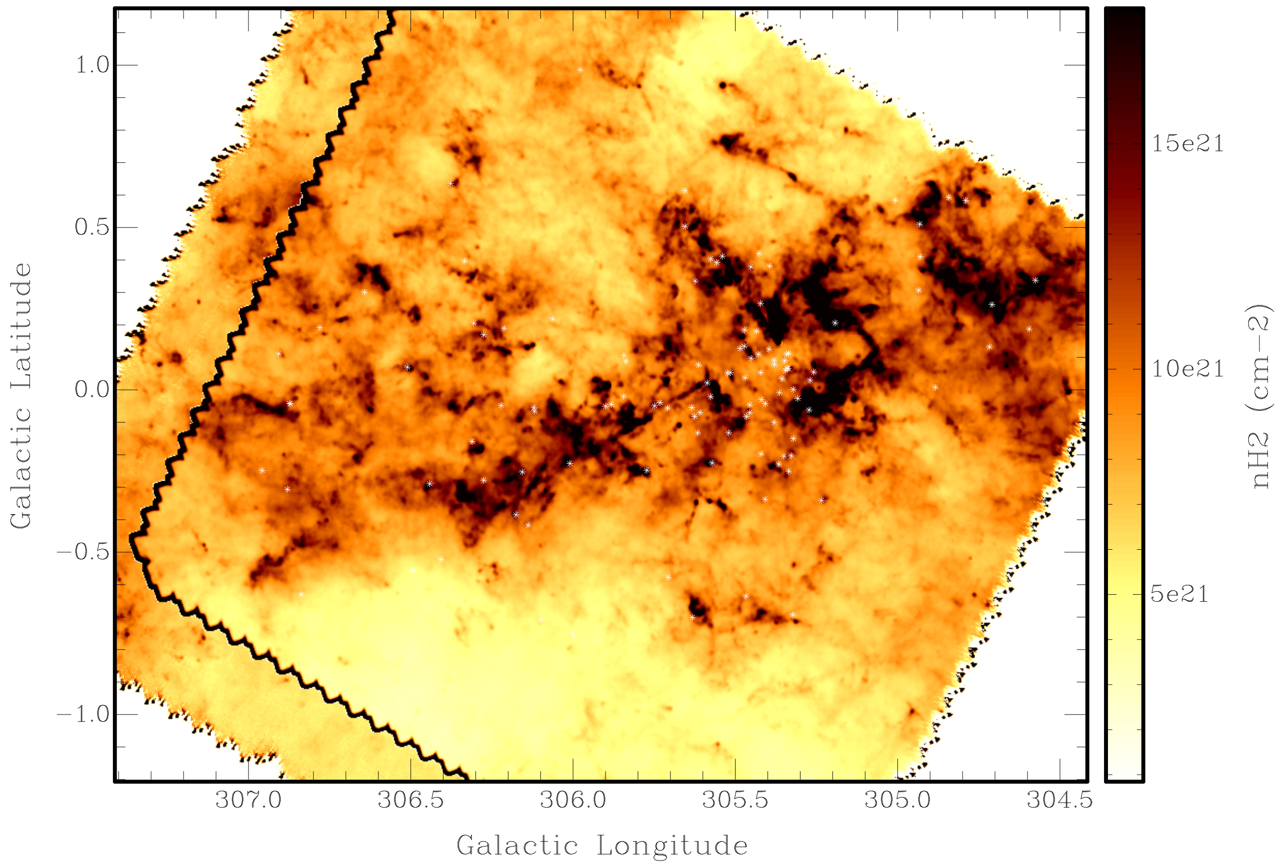

Figure 4.15: Similar plot to Fig.4.12, yet with the distribution of Ambiguous YSOs, shown as asterisks.

The distribution of YSOs within G305 does provide tentative evidence of an ordered distribution, that does follow an underlying property. However, there is also a contribution from detection bias, within certain regions, that can also play a significant role in the overall positioning of YSOs within the complex. The issue with detection bias is most noticeable when considering the GLIMPSE Point Source Catalogue, which is greatly affected by the presence of bright diffuse emission within a region. This issue is discussed by Robitaille et al. (2008) who, rather serendipitously, consider the effect of bright diffuse emission in the G305 complex. Bright diffuse emission, particularly at 8 μm, has a strong influence on the sensitivity of IRAC observations, and hence the inclusion of a source within the GLIMPSE Point Source Catalogue. The brighter the background emission is found to be, the larger the Poisson noise, thus reducing the sensitivity of observations; this affect is clearly demonstrated for G305 in Fig.4.16. The bright background emission has a strong affect on source detection for objects fainter than 10 mJy at 8 μm, and as can clearly be seen in Fig.4.16, the detection of faint point sources within the trilobed cavity structure of G305 is indeed very low; this will inevitably have an affect on any spatial distribution conclusions we may draw from our results. The increase in Stage 0/I sources over Stage II towards the central region of G305 could in part be explained by detection bias, where towards regions of bright diffuse emission, the preference is towards detecting sources of a positive spectral index (Kang et al., 2009). In the inception of the YSO catalogue, the inclusion of a candidate source was strongly influenced by the presence of a circumstellar disk or envelope, meaning that candidate YSOs will be found preferentially towards bright mid-IR emission in comparison to their more evolved siblings. Since this mid-IR emission originates from thermal emission of small dust grains, that have been excited by UV radiation, the trend for YSOs to be found more towards bright mid-IR emission means that such candidates will be strongly associated with the PDRs and HII regions. Such a correlation of YSOs with HII regions is seen within G305, and may go in some part towards explaining the distribution of YSOs within the region.

What we can summarise about the distribution, whether solely physical or in some part due towards detection bias, is that Stage 0/I sources are found preferentially towards the central HII region of G305, while Stage II sources see more of a distribution across the complex. We also see that within the central cavity, that is delineated by the strong 8 μm emission in Figs.4.12 - 4.15, there is a significant level of clustering. This strong clustering of sources is associated with the central sources of G305, namely the open clusters of Danks 1 & 2, and WR 48a.

4.6.2.1 Evidence Of Mass Segregation?

In studying the spatial distribution of YSOs, we can take an alternative approach, and consider the YSO distribution as a function of mass within G305. In Figs.4.17 - 4.19 we again analyse the YSO distribution, shown against the IRAC 8 μm image of G305, where we have defined three distinct mass regimes for our YSO sample, based on the mass of the central star. Our subgroups are defined as $\mathrm{M}_* < 2.6\,\mathrm{M}_\odot$, which is our completeness limit, $2.6 \leq \mathrm{M}_* < 8\,\mathrm{M}_\odot$ for the intermediate mass regime, and $\mathrm{M}_* > 8.0\,\mathrm{M}_\odot$ defined as the high-mass YSOs. As we can see, the most massive YSOs are found towards the centre of the region, while the majority of the intermediate-mass YSOs are also tightly correlated towards the central cavity; the low-mass sample does show a population within the central cavity of G305, however there is more of an even spread across the region also. Taking the spatial division of our YSO sample, along with the distribution of massive stars within G305 (see Table A.1), which are shown to be centrally located in Fig.2.8, we can see that there is a degree of massive stellar clustering towards the central region of G305. The mass distribution that we find within G305, and the strong evidence for concentration towards the central HII region, provides significant evidence for mass segregation within G305. This segregation of mass, shown by our YSO sample, can be further quantified by deriving the YMF both within the central HII cavity, and also for the surrounding complex.

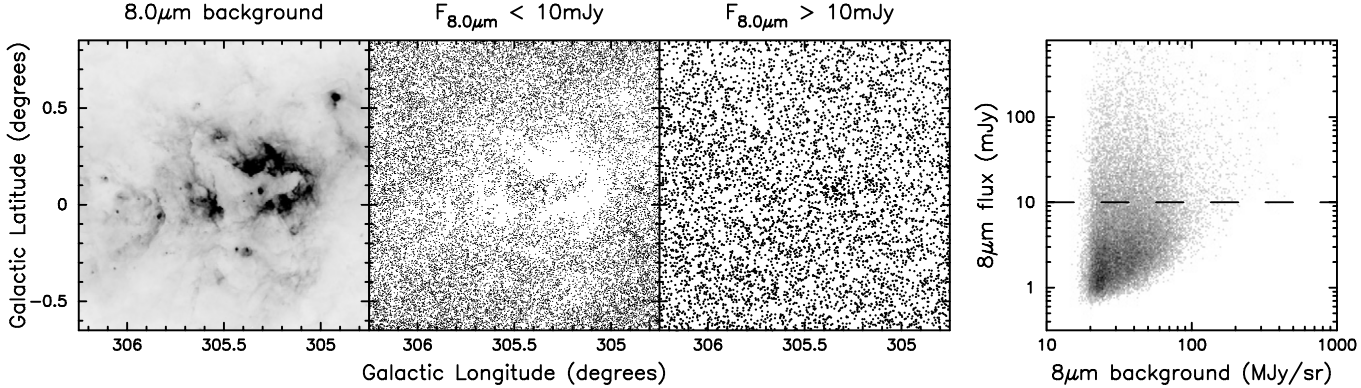

Figure 4.16: The dependence of *Spitzer* GLIMPSE observations on diffuse emission within G305. *From left to right*: 8 μm greyscale image of G305; GLIMPSE point sources, as black points, extracted with flux densities less than 10 mJy; point sources extracted with flux densities greater than 10 mJy; flux density against diffuse emission brightness for all sources in G305, where the detection threshold of 10 mJy is shown as the dashed line (Robitaille et al., 2008).

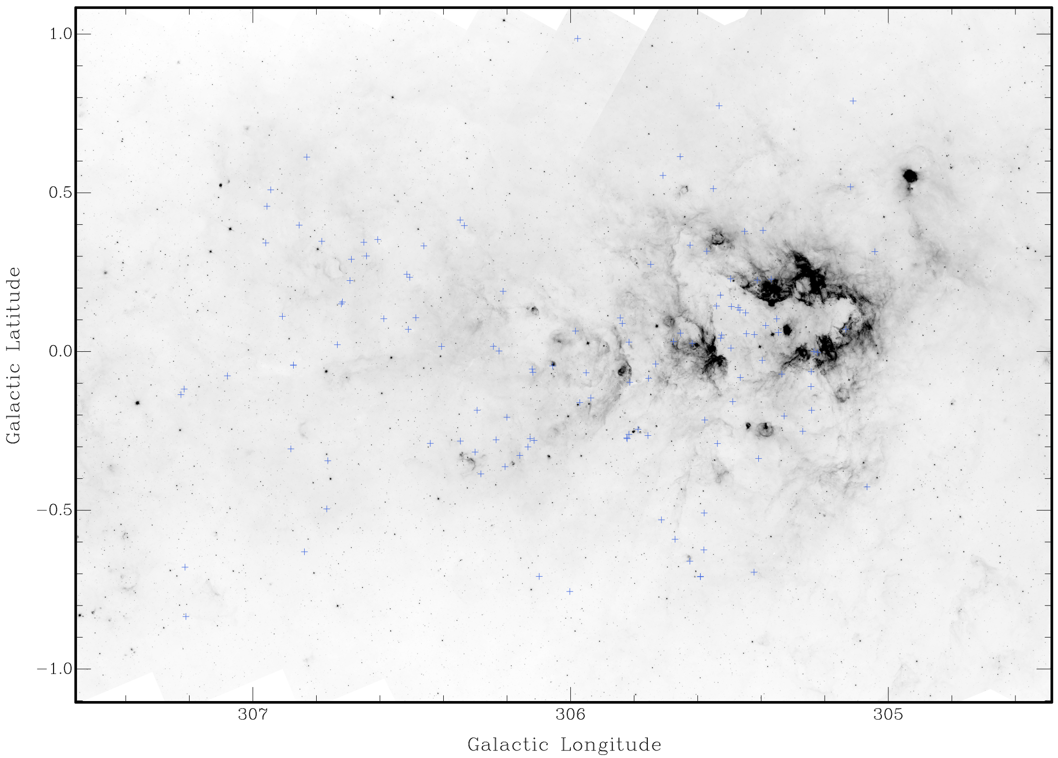

Figure 4.17: Mass distribution of YSOs with $M_* < 2.6\,M_\odot$, shown on a *Spitzer* IRAC 8 μm greyscale images of G305, as blue crosses.

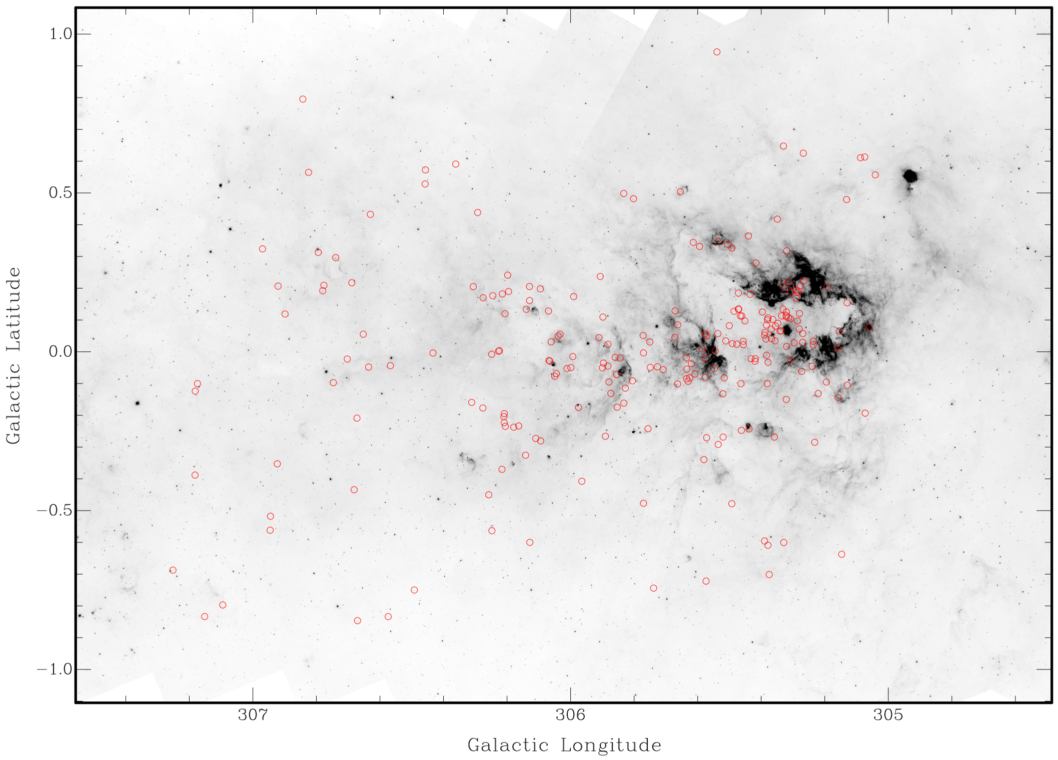

Figure 4.18: Similar plot to Fig.4.17, but with the distribution of YSOs with masses of $2.6 \leq M_{*} < 8\,M_{\odot}$ shown as red circles.

Figure 4.19: Similar plot to Fig.4.17, but with the distribution of YSOs with masses of $M_* > 8.0\,M_\odot$ shown as green diamonds.

In Fig.4.20 we have constructed the YMF for both the inner region of G305 (the central HII region that is defined by the surround peripheral materiel), and the surrounding outer material of G305. We have again adopted a similar approach as taken in section 4.5.1, where our completeness limit of $M_c \approx 2.6\,\mathrm{M}_\odot$ is again adopted for power-law fits. As we can see, there is a significant difference in the YMF between the two regions where the inner region exhibits a power-law slope $\Gamma \approx 2.7 \pm 0.3$, while the outer slope is found to be $\Gamma \approx 3.6 \pm 0.4$. The YMF slope for the inner region is not as steep as initially found for G305 in its entirety, yet still some way off from that of a standard Salpeter-Kroupa IMF; yet both the issues of disc lifetime and detection bias, as discussed in section 4.6.1, may explain this result. We also find that the YMF slope for the surrounding G305 complex does indeed exhibit a very steep power-law slope. This clear difference in MFs has been noted by other authors; Kang et al. (2009) find a YMF slope for the central star-forming region of $\Gamma \approx 1.26 \pm 0.12$, while an outer region characterised by a slope of $\Gamma \approx 2.36 \pm 0.26$. Massey (2002) also find a large disparity between IMF slopes in the SMC and LMC, where a very steep slope of $\Gamma \approx 4.0 \pm 0.5$ is observed outside of the OB associations.

This observed mass segregation, with the YMF derived from the central region of G305 observed to be much shallower, can occur either because the massive stellar content of G305 has been formed towards the centre of the complex, or that this population has migrated towards the centre over time. This places the mechanism for mass segregation as either down to initial conditions, or some form dynamical evolution over the lifetime of the region. As we have seen earlier, in Figs.4.12 - 4.15, the bulk of the intermediate-, to high-mass content of G305 is found to be in the early stages of evolution, and concentrated towards the central region. With the majority of these Stage 0/I sources found to be within the central region, this spatial variation could suggest that the observed mass segregation within G305 is not the result of a dynamical effect, but rather symptomatic of initial conditions of star formation within the complex.

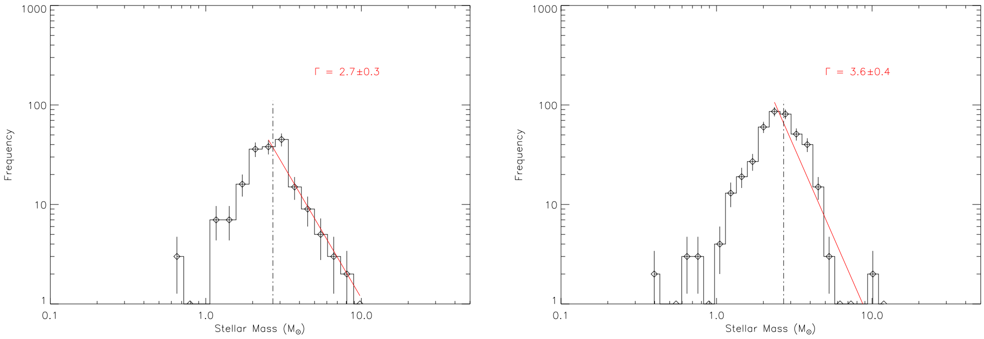

Figure 4.20: YMF plot for all 599 YSOs identified within G305, with the completeness limit of $\approx 2.6\,\mathrm{M}_\odot$ shown as the dashed line. We have derived two separate YMFs for the central region; *left*, and for the surrounding outer complex; *right*. The power-law fit to our results with accompanying power-law slope, Γ is shown for both cases.

4.6.3 The Nature Of Star Formation In G305

Star formation that is driven by the presence of massive stars has been a concept raised by many authors (e.g. Zinnecker & Yorke 2007), where the strong stellar winds and radiation from such a population can provide the driving force for ongoing star formation. The morphology of G305, and the presence of a centralised population of massive stars clearly presents a sight suggestive of triggered star formation, and many authors have proposed this. Clark & Porter (2004) firstly proposed such a mechanism for star formation within G305, with a large complex comprising of a centrally ionisning HII regions, two populations of massive stars, and sites of ongoing star formation such as UC HII regions as evidence for this. Many other authors has also suggested as much, with both the distribution of massive stars, and the ionised component of G305 acting as a means to potentially trigger further star formation within the surrounding molecular cloud (Longmore et al., 2007; Davies et al., 2012; Hindson et al., 2012). We attempt to address this suggested triggered star formation scenario within G305, by taking our identified YSO population, and testing whether any evidence can be provided to support this theory.

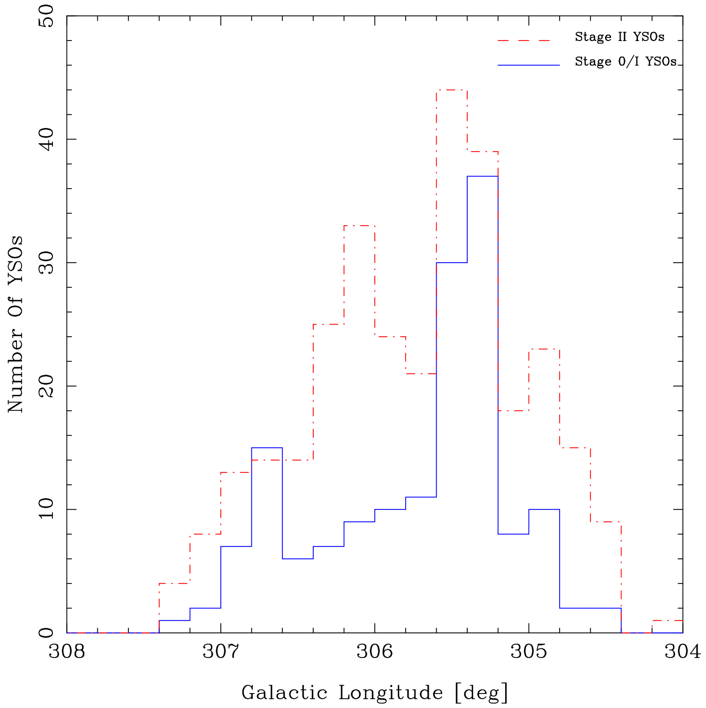

Figure 4.21: The distribution of Stage 0/I and Stage II YSOs as a function of Galactic longitude; for reference, Danks 1 & 2 are found at $l = 305.3$ and $l = 305.4$ respectively.

4.6.3.1 Propagating Star Formation

If triggering were indeed the main proponent for star formation within G305, then we would expect to observe some relation between the population of YSOs and the feedback from the massive stellar population, where YSOs will be left in the wake of the retreating molecular material eroded away by the advancing ionisation front (Smith et al., 2010).

We see from Fig.4.21 both the evolution and number of YSOs as a function of Galactic longitude within G305. For reference we note that both Danks 1 & 2 are found at longitudes of $l = 305.3$ and $l = 305.4$ respectively, and we can see from this that there is clearly a concentration of YSOs towards these two open clusters. Concentration of YSOs towards both Danks 1 & 2 does seem to suggest some form of interaction between the embedded population and the surrounding material, where this large number of YSOs may be the direct consequence of feedback from Danks 1 & 2. Though the proximity of this population of YSOs could suggest some form of propagating star formation, it may also point to the fact that G305 is simply an active star-forming complex, and there is no physical propagating star formation within the region.

Another way to which we can study this can be by comparing the typical lifetimes of the YSO population, that we derived earlier, to an averaged timescale needed for star formation to have propagated throughout G305. In order to test this, we follow the approach taken by Nomura & Kamaya (2001), who study the nature of sequential star formation within the ISM and quantify this effect through numerical simulations. From these simulations Nomura & Kamaya (2001) quantify propagating star formation across star-forming regions, and find for scales up to 50 pc that the time delay between the formation of the original site of star formation (i.e. Danks 1 & 2), and subsequent sequential star formation can be defined as:

$$\Delta\, t \;\approx\; 50\,\mathrm{Myr}\,[\Delta\,\mathrm{x}/(0.5\,\mathrm{kpc})]^{0.5} \tag{4.10}$$

where $\Delta\, t$ is the time delay between the original star formation and subsequent formation, and $\Delta\, x$ is the separation between this central source and the surrounding populations. A similar relation has been derived from star clusters within the LMC, where Efremov & Elmegreen (1998) find that the time delay can be described by $\Delta\, t \;\approx\; 26\,\mathrm{Myr}\,[\Delta\,\mathrm{x}/(0.5\,\mathrm{kpc})]^{0.4}$.

For G305, we have a projected diameter of $\approx$30 pc (Clark & Porter, 2004), which using the above relation suggests that star formation would take $\approx$8-12 Myr to propagate across G305; we directly compare this result to the average lifetime of a YSO, which is found to be $\approx$1-3 Myr, that has been derived from a statistically large sample of mainly low-mass YSOs identified as part of the *Spitzer* c2d survey (Evans et al., 2009). If, within G305, the main mechanism for star formation originated from one single burst propagating across the complex from the central sources of Danks 1 & 2, then we would have expected to identify one confined slice in longitude that constituted the star forming activity of G305; this would be expected as other sources would evolve over time, and fade away in their IR presence as this propagating front extended across the region. As we have clearly seen from our results, we do not identify such a narrow component of star formation in G305, but rather a distribution throughout the complex. This differing could, however, be explained if star formation were propagating at a far quicker pace than that derived above, and this could certainly be the case for an inhomogeneous region such as G305. In order for the propagating timescale to be more in agreement with the averaged lifetime of our YSO population, we would expect to observe YSOs distributed across the region with an observed age gradient, that quantified the evolutionary phases of the YSO population as a function of Galactic longitude. Again, consulting Fig.4.21, we do observe a preference for Stage 0/I YSOs towards the positions of Danks 1& 2, while a stronger Stage II presence accompanied with decreasing Stage 0/I sources as we move outwards in longitude. Regardless of this, we do still observe a large fraction of Stage 0/I YSOs at larger longitudes, and also a significant presence of Stage II YSOs towards Danks 1& 2. It is unlikely, therefore, that star formation within G305 can be characterised by one single burst of star formation originating from Danks 1& 2 which then propagated throughout the surrounding molecular environment, but rather, as suggested in section 3.4.3.1, a scenario of punctuated star formation across the complex.

4.6.3.2 Star Formation History Of G305

Based on the observational data to hand, and the conclusions we have drawn from this, we present a very broad picture to the nature of star formation within G305, and a possible sequence of events in the region.

Initially, the central parts of the natal GMC, with an initial mass $> 6 \times 10^5\,\mathrm{M}_\odot$ (Hindson et al., 2010), collapsed to first form Danks 2 some ≈ 3 Myr ago, followed by Danks 1 some ≈ 1.5 Myr ago (Davies et al., 2012). Over the last ≈ 3 - 6 Myr, the massive stellar component of these two open clusters have ionised an expanding HII region, which has swept up the surrounding molecular material into the present-day structure that G305 exhibits. It is from this interaction that a second generation of star formation has occurred, with the presence of classical and compact HII regions, with lifetimes of 0.1 - 2.4 Myr, present around the central cavity of G305 providing the evidence for further massive star formation (Clark & Porter, 2004). Whether the feedback originating from Danks 1 & 2 played the key role in inducing the formation of this second population, or whether this was simply spontaneous star formation, remains unclear. Although, we do note that the separation in age of these populations is consistent with triggering via the 'collect and collapse' model of star formation (Elmegreen & Lada, 1977; Whitworth et al., 1994a), as discussed earlier in section 3.4.3.1.

It is around the central sources of Danks 1 & 2, and the classical HII regions that we then observe a third, more recent stage of star formation within G305. This third generation of star formation is populated by observational tracers of embedded high-mass star formation, namely the presence of UC HII regions and maser emission with lifetimes of $\leq 0.1\,$Myr (Hindson et al., 2012; Faimali et al., 2012) and a strong component of low- to intermediate-mass YSOs found predominately in an evolutionary Stage II or Stage 0/I phase with a derived lifetime of 0.1 - 0.2 Myr. This final generation of sources comprises of multiple epochs of star formation, which are spatially distributed across the complex. As we have shown earlier, this population is not confined to one select region of the complex, nor do we observe a clear distribution in age across G305, suggesting that rather than one singular event of triggered star formation with a constant SFR, the main mechanism is likely a number of distinct bursts of star formation across the lifetime of the region.

Proving that triggered star formation is the driving mechanism within a massive star-forming complex is indeed a taxing task; whether the sources we observe are simply the result of spontaneous star formation and are merely revealed by expanding HII regions, that leads to a somewhat suggestive morphology. Indeed, the morphology of G305, and the presence of numerous star-forming candidates along the rim of the central cavity of the complex is highly suggestive of triggered star formation within G305 (Elmegreen & Lada, 1977). Certainly the presence of star-forming tracers around classical HII regions within G305 suggests that the presence of an ionising component is enhancing star formation within the surrounding molecular material (Clark & Porter, 2004; Hindson et al., 2012). However simply considering the morphology of the complex alone does not provide us with a firm ground to base any conclusions. A combination of the morphology of

G305, and the cataloguing of the star-forming population of the complex does allow us to draw some conclusions about the nature of star formation within G305. Having firmly identified both the high-, and low-mass component of the complex, it seems unlikely that G305 is solely a site of sequential star formation. Smith et al. (2010) propose for the Carina Nebula, that if we were indeed observing sequential star formation, one would expect to observe a population of YSOs within the central cavity, and none outside of this; a combination of spontaneous and sequential star formation could be plausible. As we have shown, this is certainly not the case for G305; we observe a crowding of YSOs within the central cavity, but also a population outside of this region too.

Sabbi et al. (2007) propose an alternative theory to triggered star formation, for the hierarchical fragmentation and collapse of a GMC, and the subsequent star formation within such a region. In this approach, the presence of an initial population of massive stars does not necessarily lead to the triggering of a subsequent population of star-forming regions, but rather provide a means to regulate the star-forming process. The central massive stellar population provide the energy input, through stellar winds and radiation, to sweep-up and clear the surrounding molecular material, revealing and possibly unbinding an underlying cluster of YSOs within the complex (Smith et al., 2010; Povich et al., 2011).

From our identified YSO candidates we are able to derive a lower limit to the SFR of G305, which in combination with the upper limit obtained from the embedded high-mass population of G305, from Chapter 3, allows us to constrain the present-day SFR of G305 to $0.005 \pm 0.001 \leq \mathrm{SFR} \leq 0.015 \pm 0.005\,\mathrm{M}_{\odot}\,\mathrm{yr}^{-1}$. Perhaps such a regulated star-forming scenario can better explain the history of star formation in G305, where initial fragmentation and collapse of the GMC lead to the formation of Danks 1 & 2, with an average SFR of $0.002 - 0.005\,\mathrm{M}_{\odot}\,\mathrm{yr}^{-1}$ (Davies et al., 2012). This population was followed by a series of punctuated bursts of star formation, that leads us to the present-day picture of G305. The distributed population of YSOs, and the embedded massive star-forming component identified, lead to a time-averaged present-day SFR of $0.007 - 0.01\,\mathrm{M}_{\odot}\,\mathrm{yr}^{-1}$. The feedback from both Danks 1 & 2 has at the very least driven the expansion of the central HII region, leading to a clearing of the natal molecular material, which in turn has regulated the subsequent star formation within G305.

4.7 Summary

We have conducted a complete YSO census of the G305 star-forming complex, combining available information from both 2MASS and VVV, *Spitzer* GLIMPSE and MIPSGAL, MSX, and *Herschel* Hi-GAL to identify a sample of highly reliable YSOs. By employing a series of stringent selection criteria, we are able to remove numerous contaminating sources and background galaxies to obtain a population of some 599 YSOs from an initial catalogue of some 451,789 sources. By employing the Robitaille et al. (2007) fitting tool, we are able to fit the YSO models of Robitaille et al. (2006), and determine the physical properties, and associated evolutionary stages of these YSO, following a classification scheme that mirrors the taxonomy of the classical T Tauri classification scheme. This YSO catalogue is the first that has been produced for the G305 complex, and highlights the power of adopting a multi-wavelength analysis to massive star-forming regions such as G305.

Utilising this complete census of YSOs we are able to reproduce the YMF for the complex, and find that the power-law slope for G305 is significantly steeper than the standard Salpeter-Kroupa IMF found for field stars. We derive a power-law slope $\Gamma_{G305} \approx 3.4 \pm 0.3$, which is in good agreement with similar massive star-forming complexes, that follow a similar YSO identification process to that which we adopt in G305; namely both the Carina Nebula, and M17. We interpret this result as an apparent lack of high-mass YSO candidates within G305, which in part can be explained by selection affects in compiling our YSO catalogue, which is biased towards IR excess emission originating from circumstellar disks and accreting envelopes; the apparent dearth in a high-mass YSO component could also be attributed to a rapid disk evolutionary timescale within the intermediate-mass YSO component, thus removing these sources from our final sample. From our sample we also determine a characteristic YSO lifetime of ≈ 0.37 Myr, which provides us with a YSO derived SFR of $0.005 \pm 0.001\,\mathrm{M}_{\odot}\ \mathrm{yr}^{-1}$.

From the spatial distribution of our sample, we also find some evidence of mass segregation present within the complex; we note that from a spatial argument, the few high-mass YSO candidates, and the majority of the intermediate-mass YSOs are concentrated towards the central cavity of G305, with a low-mass YSO component found more distributed across the complex. We quantify this observation by deriving the YMF from the central cavity of G305, and also an associated YMF for the surrounding natal molecular cloud. With the YSO sample divided into these two populations, we clearly see a far shallower YMF power-law within the central region of G305 ($\Gamma_{Inner} \approx 2.7 \pm 0.3$), while a far steeper component is observed in the outer parts of the complex ($\Gamma_{Outer} \approx 3.6 \pm 0.4$). We find that the majority of the intermediate- to high-mass YSO component towards the centre of G305 is comprised of Stage 0/I sources, suggesting that is not the result of a dynamical effect, but rather an indication that the distribution is dependent on the initial conditions of star formation within the molecular cloud.

We also observe a strong concentration of YSOs towards both Danks 1 & 2, which would seem to suggest some form of triggered star formation occurring within the complex. If such a scenario were the case, and we were truly observing evidence indicative of propagating star formation, one would expect to find a clear age gradient from the distribution of YSOs across the complex. Such a phenomena is not observed within G305, instead we observe a slightly more distributed age of YSOs; a preference for Stage 0/I sources towards Danks 1 & 2, with a further Stage II component moving away from this is observed, yet accompanying this we observe a large fraction of Stage 0/I YSOs at larger longitudes, and also a significant presence of Stage II YSOs towards Danks 1& 2.

In considering the star formation history of G305, we suggest that rather than one single event of triggered star formation, leading to the propagation of a subsequent generation of star-forming objects, the more likely scenario is that of a non-constant star forming environment, where G305 has been characterised by punctuated bursts of star formation over the lifetime of the complex. Though it is indeed difficult to ever draw a conclusion to whether the subsequent star-forming population is the direct consequence of feedback from both Danks 1 & 2, or whether this population would have formed regardless, it seems likely that the central massive stellar population of G305 has played some part in regulating the star-forming activity of the complex.

Chapter 5

Summary & Conclusions

"There are things we know we know. We also know there are known unknowns; that is to say we know there are some things we do not know. But there are also unknown unknowns - the ones we don't know we don't know." - Donald Rumsfeld

5.1 Summary Of Main Results

The main aim of this thesis has been to perform a detailed analysis of the star-forming content of a Galactic star-forming region, such as G305, with a view to further understanding the nature of star formation and the star-forming history of the region. In order to do this, we have conducted a multiwavelength study of the region, where we have catalogued both the embedded massive star-forming population of G305, and the low- to intermediate-mass YSO population also, with a view to deriving the SFR of the region. In conducting this study, the hope has been to show the power of a multiwavelength analysis of Galactic regions, and we propose the adoption of such an approach to other regions across the Galactic plane. By extension of such a study to other regions, we can begin to study fundamental parameters such as the SFR, and nature of the IMF, across all environments within the Milky Way.

Our investigation began in Chapter 3, where we focused on identifying the embedded massive star-forming population within G305, by combining *Herschel* 70, 160, 250, 350, and 500 μm observations from the Hi-GAL survey of the Galactic plane with 5.5 GHz radio continuum, 22 GHz H_2O maser, 6.7 GHz methanol maser observations of the Methanol Multi-Beam survey, 24 μm observations from the *Spitzer* MIPS Galactic Plane Survey, and 21 μm observations from the Red MSX Source survey. In order to identify a sample of candidate objects, we firstly apply a frequentist technique that allows us to identify a sample of the most likely associations within our multiwavelength dataset, that can then be classified from the derived properties obtained from fitted SEDs. By SED modelling using both a simple modified blackbody and fitting to a comprehensive grid of YSO SED models from Robitaille et al. (2006), some 16 candidate associations are identified as embedded massive star-forming regions. The properties of this sample of candidate embedded massive star forming objects are given in Table 3.2. We use this sample to derive a two-colour selection criterion of $\log(\mathrm{F}_{70}/\mathrm{F}_{500}) \geq 1$ and $\log(\mathrm{F}_{160}/\mathrm{F}_{350}) \geq 1.6$, and identify an additional 31 embedded massive star candidates with no associated star-formation tracers. Using this result we can build a picture of the present day star-formation of the complex, and derive a star formation rate (SFR) of 0.01 - 0.02 $\mathrm{M}_\odot\ \mathrm{yr}^{-1}$ from the embedded population of G305. We find that the Milky Way SFR (Chomiuk & Povich, 2011; Davies et al., 2011) is comparable to tens to hundreds of G305 complexes, emphasising the fact that the Galactic SFR is most likely dominated by similar massive star-forming complexes. Comparing this Galactic SFR to extragalactic SFR tracers, based on the Kennicutt-Schmidt relation, we find they are a factor of ≥ 2 lower than that derived from the embedded massive star-forming population. The disparity between extragalactic SFR tracers, and the SFRs derived from Galactic tracers is shown in Table 3.3. The lack of consistency between the two regimes has been noted by several authors (Lada, Lombardi & Alves, 2010; Chomiuk & Povich, 2011), with extragalactic tracers tending to underestimate the SFR derived from resolved Galactic SFRs.

In Chapter 4 we continue our analysis, by focusing on identifying the intermediate-to-low-mass YSO content of G305, and construct the YSO mass function (YMF) to estimate the present-day star formation rate of G305. In order to conduct this analysis, we have extended the YSO identification technique of Povich et al. (2011), to a broader multiwavelength extraction of YSOs that includes VVV and Hi-GAL observations, covering YSO SEDs from the near-IR through to the sub-mm; this approach has not been repeated in other Galactic complexes to date.

YSOs possess dusty circumstellar disks and infalling envelopes, that reprocess radiation from the central star, and produce characteristic IR excess emission. We can identify such YSOs from this characteristic excess, and from modelling their SEDs. By combining 2MASS and VISTA VVV *JHK* photometry with *Spitzer* GLIMPSE, alongside our present dataset, we conduct a complete census of the YSO population of G305. By employing reddened stellar atmosphere models, and a series of colour criteria (Smith et al., 2010; Whitney et al., 2008), we remove contaminating objects such as stellar sources, luminous AGB stars, and background AGN sources. Using the Robitaille et al. (2006) YSO model SEDs, we are able to fit some 599 sources with YSO model SEDs, and constrain the physical properties such as the luminosity, stellar mass, envelope accretion rate, and the circumstellar disk mass, and combine these parameters to divide YSOs into evolutionary stages. The evolutionary stages parallel the empirical T Tauri classification scheme, and in total we identify within G305 some 157 Stage 0/I, 303 Stage II, and 24 Stage III YSOs, with an additional 115 Ambiguous sources found. The breakdown of our final YSO catalogue for G305, with the number of sources removed at each stage is given in Table 4.1. Using this sample of candidate YSOs, we determine a characteristic YSO lifetime of $\approx 0.37\,\mathrm{Myr}$, which provides us with a present-day SFR of $0.005 \pm 0.001\,\mathrm{M_\odot\ yr^{-1}}$ from the intermediate-, to low-mass YSO component of G305. By comparing the results of Chapter 3, with those in Chapter 4, we are able to constrain the present-day SFR of G305, which is found to be $0.005 \pm 0.001 \leq \mathrm{SFR} \leq 0.015 \pm 0.005\,\mathrm{M_\odot\ yr^{-1}}$. By constructing the YMF of the complex, we observe a far steeper power-law slope of $\Gamma \approx 3.4 \pm 0.3$, which is in good agreement with similar massive star-forming complexes such as the Galactic HII region M17 with a power-law slope $\Gamma \approx 3.5 \pm 0.6$ (Povich & Whitney, 2010), and the Carina Nebula a power-law of $\Gamma \approx 3.2 \pm 0.3$ (Povich et al., 2011). This significantly steeper YMF power-law slope than the classical Salpeter-Kroupa IMF for fields stars can be explained by a combination of a lack of high-mass YSOs within the region, and also due to selection bias in our sample. The apparent dearth in high-mass YSOs could be due to rapid disk evolution that removes these sources from our final sample, while selection bias, towards IR excess emission originating from circumstellar disks and accreting envelopes, in compiling our initial catalogue may also remove these sources. Finally, we go on to discuss the possible star-formation history of the complex, and suggest that G305 has been characterised by punctuated events of star formation over it's lifetime, rather than one triggered event characterised by a constant star formation rate.

5.2 Conclusions

Prior to this study, G305 was identified as one of the most massive and luminous star- forming regions in the Galaxy, with at least two known generations of star-formation occurring within (Clark & Porter, 2004). The morphology of the complex, with a central massive stellar population that had caused the expansion of a HII region into the surrounding natal material, was highly suggestive of a site of triggered star formation. Yet, up until this point, the nature of star formation within the region, and the exact nature of the high-mass and low-mass component of G305, was largely unknown. Without such a firm knowledge of the populations of star formation within the region, we have been unable to comment on the nature of star formation of the region. The main conclusion from our study has been to identify and catalogue each star-forming component of G305, confirms that there is in fact three generations of star formation within the complex, draw conclusions about the star-forming history and environment of the complex, and confirm that G305 is indeed one of the most massive star-forming complexed within the Milky Way, just as was first suggested by Clark & Porter (2004).

A substantive amount of work on G305 has focused on the nature of the ionising, radio continuum emission within the complex, with emphasis on both the classical and UC HII regions, and the role these play within the complex (Caswell & Haynes, 1987; Clark & Porter, 2004; Hindson et al., 2012). For the first time, we have conducted a far-IR analysis of the G305 complex, where we utilised *Herschel* Hi-GAL observations in conjunction with star-forming tracers provided by radio, maser, and RMS observations, to identify the embedded massive star-forming population of G305. Utilising this sample of known embedded massive stars, we have been able to derive a far-IR colour selection of $\log(\mathrm{F}_{70}/\mathrm{F}_{500}) \geq 1$ and $\log(\mathrm{F}_{160}/\mathrm{F}_{350}) \geq 1.6$. With the plethora of data available currently, such a criteria can be utilised across similar regions within the *Herschel* Hi-GAL survey, to identify embedded massive star-forming candidates across the Galactic plane; an example of this has been the application of said criteria within the G29.96-0.02 high-mass star-forming cloud (Beltrán et al., 2013).

From this identified embedded star-forming population, we have been able to constrain an upper limit on the SFR for G305, which is found to be $0.01 - 0.02\,\mathrm{M_{\odot}\ yr^{-1}}$. What is crucial from this finding is that not only do we find G305 comparable to other well known massive star-forming complexes such as the Carina complex (Povich et al., 2011), and M17 (Povich & Whitney, 2010), but that conclusions can be drawn with the Galactic SFR. We find that the Milky Way SFR (Chomiuk & Povich, 2011; Davies et al., 2011) is comparable to tens to hundreds of G305 complexes, which suggests that to better understand the Galactic SFR, we need only study a select sample of the most massive star-forming regions within the Galaxy; the majority of such sources have already been identified, for example via the WMAP results of Rahman & Murray (2010). Aside from this, we also find evidence for a clear disparity in derived SFR by comparing our results to other well known extragalactic SFR tracers, based on the Kennicutt (1998a) relation. There is a clear disagreement between the two regimes, with extragalactic tracers tending to underestimate the SFR of Galactic star-forming regions. We do find strong evidence that our resolve Galactic SFR is in good agreement with that of Lada, Lombardi & Alves (2010), who assert that the total amount of dense gas within a star-forming region provides an accurate tracer of the SFR. Such work may present a unified star formation law, that is applicable to both low-mass Solar neighbourhood clouds through to sub-mm galaxies, yet the current form of this is open to debate; Krumholz, Dekel & McKee (2012) advocated an approach where the SFR, within a variety of scales, is simply $\approx 1\,\%$ of the molecular gas mass per local free-fall time, while Lada et al. (2012) conclude that the SFR is dictated by the amount of dense molecular gas that can accumulate within a star-forming region. What is clear from our results though, is that when measuring the Galactic SFR, there is a clear disparity between this and extragalactic realms; making accurate comparison of the Milky Way to other galaxies problematic. Clearly more study will be needed to ascertain the nature of such a unified star formation law, if such a law were to indeed exist.

In combining 2MASS, VVV, *Spitzer* GLIMPSE and MIPSGAL, MSX, and *Herschel* Hi-GAL observations, we have also conducted the first complete YSO census of G305, allowing us to address the issues of completeness at intermediate-, and low-mass that have existed in previous studies. Such a population is important to the evolution and dynamics of the complex, with the bulk of the stellar matter dedicated to the low-mass population, which is also responsible for the manufacturing of interstellar dust and chemical enrichment. Studying the distribution of identified YSOs within G305, we find evidence of mass segregation within the complex where the majority of high-, and intermediate-mass YSOs are concentrated towards the central cavity of G305, with a low-mass YSO component found more distributed across the complex. Observationally, we also identify a strong concentration of YSOs towards the positions of Danks 1 & 2, suggesting that the initial massive stellar population of G305 may have contributed some form of triggered star formation within the complex.

With this identified population, we are able to comment on the possible star-forming history of the complex. As discussed by previous authors (e.g. Clark & Porter 2004; Hindson et al. 2012) the morphology of G305 is highly indicative of triggered star formation, however without analysis of the low-mass YSO population, we have been unable to address the issue of triggering and sequential star formation. From our results we find that G305 is most likely not characterised by a constant SFR, due to a single triggering event, but rather that the complex has been marked by bursts of star formation; accounting for the three separate generations of star formation present within the complex, namely Danks 1 & 2, the classical and compact HII regions, and both the embedded massive star-forming regions and the intermediate-, to low-mass YSO population. Our results cannot definitively suggest whether this population is the direct impact of triggering due to feedback from Danks 1 & 2, or whether these population were spontaneous formed. When considering the 'collect and collapse' model of star formation (Elmegreen & Lada, 1977), we find that some form of triggering and regulation of star formation within G305, caused by Danks 1 & 2, does seem a conceivable mechanism for the star formation activity that we observe. The future of G305 is likely to be dictated by the continued feedback from Danks 1 & 2, and other forming high-mass sources; to what extent this population will eventually clear and destroy the complex is unknown. Elmegreen (2007) suggest that the feedback from massive stars eventually leads to a swift destruction of the natal molecular material, with lifetimes < 10 Myr. Conversely, Krumholz, Matzner & McKee (2006) argue that feedback from high-mass stars, in the form of energy injection from HII regions and photoevaporation, can conspire to create a quasi-static equilibrium between gravitational collapse and turbulent support, leading to longer lifetimes (i.e. 10 - 20 Myr). Continued analysis of regions such as G305 will prove crucial in understanding the role that high-mass populations have in affecting GMCs, and this in turn will dictate the evolution of the Galaxy.

Our study serves as an excellent example of what can be achieved through dedicated multiwavelength analysis of Galactic star-forming regions, and with the presence of current and future large-scale multiwavelength datasets such as Hi-GAL (Molinari et al., 2010b), GLIMPSE (Benjamin et al., 2003), UKIDSS GPS (Lucas et al., 2008), MIPSGAL (Carey et al., 2009), VVV (Minniti et al., 2010), CORNISH (Purcell & Hoare, 2010), MMB (Green et al., 2009; Caswell et al., 2010), ATLASGAL (Schuller et al., 2009), SCUBA-2 (Holland et al., 2013), BOLOCAM GPS (Aguirre & Bolocam Galactic Plane Survey Team, 2008; Rosolowsky et al., 2010), and MALT90 (Foster et al., 2011), we will be able to study massive star formation across the Galactic plane. By building the wealth of observational data available, more stringent and complex models of star-formation (e.g. Dale, Ercolano & Bonnell 2013, 2012; Dale & Bonnell 2012) can be developed to test the initial stages of star formation within complexes such as G305. Such continued analysis will be crucial in understanding some of the fundamental questions of Galactic star formation, such as how does the SFR vary as a function of environment and galactocentric distance, what is the origin and shape of the IMF, what are the physical process involved in triggered star formation, and is there a unified approach to determining the SFR in the Milky Way and other external galaxies. The results could conceivably give rise to global star-formation scaling laws that could then allow us to extend the detailed knowledge of our Galaxy to more distant extragalactic realms.

5.3 Future Work

Below I outline a number of possible areas that can continue the study of the G305 complex, while also proposing potential studies to extend our multiwavelength analysis to other Galactic star-forming complexes.

5.3.1 Final G305 YSO Catalogue

As was discussed in Chapter 4, due to time constraints we have been unable to produce a single, unified YSO catalogue. Our first area of future work, would be the creation of such a catalogue that considered not only the more evolved YSO stages of Chapter 4, but that also considered those earlier, highly embedded YSO stages that were discussed in Chapter 3, but failed to be reproduced in Chapter 4 due to a lack of GLIMPSE, 2MASS, or VVV detections. We would identify this sample of embedded sources as those identified at $\lambda \geq 24\,\mu$m or $\lambda \geq 70\,\mu$m, which could then be fit with Robitaille et al. (2006) SED models with GLIMPSE upper limits. These upper limits would provide crucial information to constrain the variation in fitting SED models to these sources. In doing this, we would produce a complete catalogue of star formation within G305, that would allow us to consider both the earliest phases of star formation within G305, along with the more evolved stages also identified.

5.3.2 Additional Galactic Star-Forming Complexes

What is apparent, when measuring the Galactic SFR, is the need for an accurate means to compare the Milky Way to other galaxies. Continued, multiwavelength analysis of Galactic HII regions across a wide range of star-forming regions, will lead to an accurate determination of the SFR, which scaled up from a more local level to a global, Galactic level, will allow for the consideration of how the SFR and SFE vary as a function of environment across the Milky Way. This should help in a better understanding of how the SFR can accurately be measured on both Galactic, and extragalactic scales, and aid in the calibration of far-IR SFR indicators in galaxy studies such as the *Herschel* Reference Survey (Boselli et al., 2010), and *Herschel* ATLAS (Eales et al., 2010), with a view towards a unified star formation law. At present, there is a large body of multiwavelength data of the Galactic plane available, covering multiple star-forming complexes, that can be exploited to conduct this investigation.

- We can extend the multiwavelength YSO identification work across other Galactic star-forming complexes, drawn from the *WMAP* results of Rahman & Murray (2010), which suggest there are some 31 Galactic HII regions with a greater ionising flux than G305. The first region that we identify for analysis is the G34 complex, ranked the 6^{th} luminous HII region in *WMAP*, located some 2.2 kpc away, at $l = 34.7°$, $b = -0.2°$. Currently, this region has data in hand from 2MASS, UKIDSS GPS, GLIMPSE, MIPSGAL, RMS, Hi-GAL, ATLASGAL, SCUBA-2, BOLOCAM GPS, CORNISH, and MMB surveys.

5.3.3 LABOCA Analysis

We currently have LABOCA 870 μm (Siringo et al., 2009) data that has recently been reduced, the result is shown in Fig.5.1. With this additional data, we can address issues regarding:

- By combining *Herschel* Hi-GAL observations with the LABOCA 870 μm data, we aim to produce a detailed analysis of the dust and gas content of the G305 complex. Focus will be on the identification of prestellar, cold dense cores and young protostars within the star-forming clouds, including those candidate embedded massive star-forming regions with no associated emission that are discussed in section 3.4.2. We will be able to constrain the total mass of dense clouds within G305, and with previous estimations of the total molecular mass of the complex, derived from NH_3 observations (Hindson et al., 2010), we can constrain the overall total (gas+dust) mass of the complex.
- Identifying these dense clouds will allow us to identify the fraction of the complex that is sufficiently dense and massive enough for further star formation to occur. Such a comparison with the reservoir of future star formation,

with the present star forming complex, allows us to determine the efficiency of star formation within G305, which can be compared to the star-formation efficiency (SFE) determined for other OB associations (Gaczkowski et al., 2013; Preibisch et al., 2011). With a knowledge of the material available for future star formation, and the efficiency of the complex, we can also begin to comment on the future role of feedback from both Danks 1 & 2 on enhancing, regulating, or inhibiting future star formation within G305.

- Investigate results of André et al. (2010) that suggest the origin of the stellar IMF can be addressed by understanding the formation process of prestellar cores, and the prestellar core mass function (CMF). The suggestion is that the CMF and IMF are directly related by an approximate one-to-one formation relationship between the core mass and stellar mass ($\mathrm{M}_* = \epsilon_{Core}\,\mathrm{M}_{Core}$), with a local star formation efficiency ϵ_{Core}.

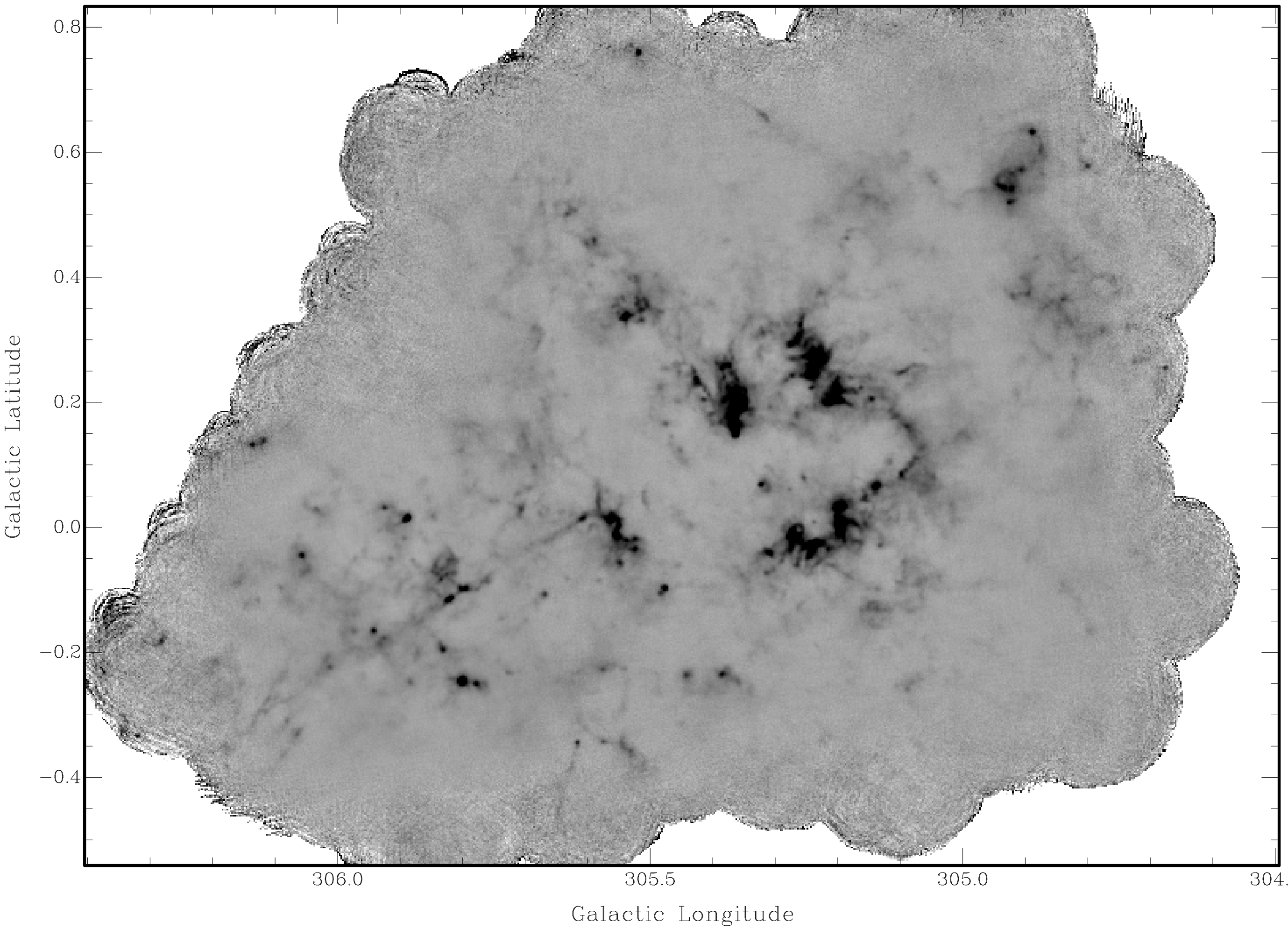

Figure 5.1: LABOCA 870 μm image of the G305 complex.

Appendix A

.1 High-Mass Stellar Content Of G305

Table 1: Positions and spectral type of the massive stars within G305 (Leistra et al., 2005; Mauerhan, van Dyk & Morris, 2009; Mauerhan, Van Dyk & Morris, 2011; Davies et al., 2012). The stellar populations of both Danks 1 & 2 are given in Table 2 of Davies et al. (2012).

ID	l (°)	b (°)	Spectral Type
Danks 1	305.338	0.072	Open Cluster
Danks 2	305.393	0.087	Open Cluster
L05-A1	305.26	0.23	O5 - 6
L05-A2	305.25	0.22	B0 - 1
L05-A3	305.26	0.22	B2 - 3
WR48A	305.36	0.06	WC6
MDM3	305.30	0.05	WN8 - 9
MDM4	305.33	0.10	WC8
MDM5	305.33	0.03	WN9
MDM6	305.34	0.03	WC7
MDM7	305.34	0.08	WN9
MDM8	305.34	0.08	WN9h
MDM9	305.65	0.35	WC8
J13125770 6240599	305.40	0.09	WC8

.2 Star Formation Tracers Found In G305

Table 2: Properties of Hindson et al. (2012) UC HII regions identified in G305

ID	Source Name	Spectral Type
8	G305.362+00.150	B0.5
9	G305.368+00.213	B0.5
17	G305.562+00.013	B0.5
20	G305.55300.012	B0.5
26	G304.930+00.552	B1
37	G305.200+00.019	B1

Table 3: Positions and source classifications of RMS sources found within G305 (Hindson et al., 2012).

ID	Source Name	Spectral Type
912	G305.2017 + 00.2072	YSO
981	G305.5610 + 00.0124A	HII Region/YSO
981	G305.5610 + 00.0124B	Null
963	G305.3719 + 00.1837	HII Region
972	G305.4748 - 00.0961	YSO
954	G305.3500 + 00.2240	HII Region
980	G305.5528 - 00.0109	HII Region
917	G305.1997 + 00.0216	HII Region
975	G305.5393 + 00.3394	YSO
990	G305.9402 - 00.1634	YSO
915	G305.1967 + 00.0335	HII Region
992	G306.1160 + 00.1386	YSO
916	G305.1940 - 00.0051	YSO
939	G305.2694 - 00.0072	HII Region

Table 4: The positions of masers identified towards G305: H_2O (Hindson et al., 2010), Methanol (Green et al., 2012), OH (Caswell, 1998).

Maser	l (°)	b (°)
H_2O	305.22	0.28
	305.21	0.21
	305.41	0.25
	305.35	0.20
	305.35	0.15
	305.33	0.07
	305.09	0.10
	305.13	0.08
	305.20	0.00
	305.26	0.10
	305.72	0.09
	305.89	0.03
	305.83	0.08
	305.75	0.08
	305.81	0.11
	305.80	0.24
CH_3OH	305.199	0.005
	305.200	0.019
	305.202	0.208
	305.208	0.206
	305.248	0.245
	305.362	0.150
	305.366	0.184
	305.475	0.096
	305.563	0.013
	305.573	0.342

	305.615	0.344
	305.634	1.645
	305.646	1.589
	305.799	0.245
	305.822	0.115
	305.887	0.017
	305.940	0.164
OH	305.200	0.019
	305.202	0.208
	305.208	0.206
	305.362	0.150
	305.799	-0.245

Appendix B

.3 Candidate Embedded Massive Star-Forming Regions In G305

Table 5: Derived physical properties for all candidate embedded massive star-forming regions, with no associated emission tracers found, from both modified blackbody fits and Robitaille et al. (2007) SED fitting techniques.

Hi-GAL Source Index	RA (J2000)	Dec (J2000)	β	T (K)	$\tau_{500\mu m}$ (10^{-3})	M_{Dust} ($M_\odot$)	L_{Bol} (10^3 $L_\odot$)
10	196:22:45.1	-62:30:0.3	1.3	31	7.0	646	6.3
131	197:7:46.4	-62:14:20.9	1.7	26	1.3	186	1.6
158	197:9:40.5	-62:15:37.6	1.3	28	6.3	803	4.7
159	197:9:57.3	-62:15:21.6	1.6	37	2.2	71	5.6
583	197:40:12.6	-62:34:52.7	1.4	25	4.3	375	1.5
658	197:42:16.1	-62:46:7.9	2	28	0.5	64	1.3
940	197:48:28.9	-62:45:7.3	1.1	35	14	2448	29
1134	197:52:18.2	-62:33:20.9	2.7	23	2.3	48	2.1
1233	197:54:11.5	-62:32:18.5	2.1	39	0.4	5	1.7
1303	197:56:5.1	-62:29:2.9	1.2	24	9.5	976	2.5
1306	197:56:13.6	-62:32:8.2	1.4	27	4.2	189	1.9

1346	197:57:0.2	-62:36:44	1.9	30	0.6	62	2.1
1350	197:57:2.6	-62:46:39.1	1.6	25	2.0	246	1.7
1409	197:58:33	-62:47:18.8	1	32	2.3	3594	24
1437	197:59:5.4	-62:33:45.5	1.9	28	0.6	45	1.4
1588	198:3:13.8	-62:42:50.8	1.8	29	0.9	54	1.8
1651	198:4:36.3	-62:42:17.7	1.6	41	2.1	208	16
1711	198:6:23.3	-62:32:58	1.9	38	0.6	28	3.4
2108	198:23:40.6	-62:59:54.8	1.4	23	4.4	518	1.3
2261	198:32:8.8	-62:47:27.7	1.4	25	5.0	610	2.3
2349	198:35:16.2	-62:45:10	2.6	23	2.9	68	2.8
2454	198:38:53.2	-62:42:44.4	2.7	24	0.4	48	1.4
2688	198:50:29.8	-63:26:17.9	1.6	26	2.1	173	1.3
2865	199:8:12.4	-62:59:1.8	1.3	24	6.3	429	1.0
2967	199:14:27.6	-62:47:17.5	1.5	24	2.9	208	1.1
3064	199:41:19.6	-62:44:44	1.5	24	2.9	374	1.3
3077	199:46:45.8	-63:1:55.4	1.8	26	0.9	130	1.2
3079	199:47:10.3	-62:33:41.9	1.5	24	2.9	289	1.3
3201	200:20:45.2	-63:0:26.2	1.3	23	6.2	877	1.7
3214	200:23:30.1	-62:59:50.6	1.4	21	4.3	824	1.0
3271	201:18:35.6	-63:1:12.5	1.7	27	1.5	87	1.1

Appendix C

.4 Candidate YSOs Identified Within G305

Table 6: Derived physical properties for all candidate YSOs identified within G305.

ID	$\langle M_* \rangle$ (M$_\odot$)	$\sigma(M_*)$ (M$_\odot$)	$\langle log\, L_{bol} \rangle$ (L$_\odot$)	$\sigma(log\, L_{bol})$ (L$_\odot$)	$\left\langle log\, \dot{M_{env}} \right\rangle$ (M$_\odot$ y^{-1})	$\sigma\left(log\, \dot{M_{env}}\right)$ (M$_\odot$ y^{-1})	$\langle log\, M_{disk} \rangle$ (M$_\odot$)	$\sigma(log\, M_{disk})$ (M$_\odot$)	Stage
G304.4133+00.3288	2.8	0.03	1.23	-0.77	0.00	0.00	-6.45	-2.04	Stage II
G304.4248+00.2427	2.3	0.11	1.39	0.07	0.00	0.00	-4.89	-2.01	Stage II
G304.4392+00.2664	1.8	0.10	1.73	0.35	-4.98	-4.13	-2.75	-1.47	Ambiguous
G304.4991+00.0299	2.4	0.00	1.25	-1.62	-6.33	-4.86	-2.93	-1.66	Stage II
G304.5224+00.2940	2.2	0.02	1.42	-0.51	0.00	0.00	-5.65	-1.92	Stage II
G304.5313+00.4152	2.1	0.05	1.63	0.00	-4.79	-4.06	-1.80	-1.47	Stage 0/I
G304.5436+00.3403	10.8	1.09	3.48	2.51	-3.28	-2.96	-1.62	-0.61	Stage 0/I
G304.5486+00.1572	2.3	0.00	1.15	-1.80	-6.20	-5.05	-3.13	-1.71	Stage II
G304.5687+00.4378	2.2	0.00	1.29	-1.47	-7.69	-5.27	-3.27	-1.82	Stage II
G304.5689+00.1630	2.4	0.04	1.41	-0.32	0.00	0.00	-2.69	-1.54	Stage II
G304.5755+00.3373	2.5	0.00	1.64	-1.47	-6.91	-4.92	-3.34	-1.75	Ambiguous
G304.5792+00.0800	2.2	0.00	1.17	-2.01	-6.54	-4.99	-3.05	-1.73	Stage II
G304.5922-00.0369	3.3	0.13	2.00	0.59	0.00	0.00	-2.64	-1.65	Stage II
G304.5948+00.1873	2.7	0.02	1.29	-0.97	-6.06	-4.94	-3.18	-1.72	Ambiguous
G304.6266+00.1629	1.7	0.00	1.00	-1.58	-6.34	-5.27	-2.94	-1.77	Stage II
G304.6322+00.3000	2.6	0.01	1.63	-1.00	0.00	0.00	-4.15	-1.70	Stage II
G304.6620+00.2725	2.7	0.05	1.87	0.24	0.00	0.00	-3.23	-1.76	Stage II

G304.6640+00.3645	3.7	0.25	1.57	0.39	-6.86	-4.65	-2.11	-1.54	Stage II
G304.6681+00.2643	3.1	0.02	2.11	0.16	0.00	0.00	-2.88	-1.71	Stage II
G304.6788+00.2356	3.8	0.12	2.46	1.15	0.00	0.00	-2.63	-1.48	Stage II
G304.7070+00.4916	2.9	0.01	1.90	-0.47	0.00	0.00	-3.54	-1.71	Stage II
G304.7094+00.2625	2.4	0.01	1.27	-1.15	-6.03	-4.82	-3.38	-1.80	Ambiguous
G304.7173+00.1323	2.6	0.00	1.53	-1.25	-6.76	-5.33	-3.60	-1.75	Ambiguous
G304.7201+00.0719	4.0	1.33	1.58	1.10	0.00	0.00	-2.66	-1.16	Stage II
G304.7261+00.2743	2.6	0.10	1.66	0.26	0.00	0.00	-4.23	-1.86	Stage II
G304.7552+00.2175	2.6	0.08	1.75	0.24	0.00	0.00	-3.61	-1.88	Stage II
G304.7633+00.6026	0.6	0.05	1.47	0.39	-4.50	-4.24	-1.95	-1.45	Stage 0/I
G304.7799+00.5835	2.7	0.01	1.69	-0.83	0.00	0.00	-3.36	-1.70	Stage II
G304.7826+00.6015	1.4	0.01	1.27	-0.99	-5.52	-4.39	-2.47	-1.53	Stage 0/I
G304.7899+00.4311	3.1	0.12	1.93	0.50	0.00	0.00	-2.78	-1.79	Stage II
G304.7900+00.5829	3.4	0.03	2.10	0.06	0.00	0.00	-4.89	-1.83	Ambiguous
G304.7903+00.3023	2.6	0.04	1.64	-0.26	0.00	0.00	-5.43	-2.11	Stage III
G304.7943+00.2964	2.8	0.06	1.81	0.13	0.00	0.00	-6.97	-2.29	Stage III
G304.7960+00.1901	3.9	0.13	2.03	0.58	0.00	0.00	-2.64	-1.56	Stage II
G304.7966+00.4544	2.0	0.22	1.15	0.18	0.00	0.00	-2.73	-1.91	Stage II
G304.7975+00.3000	1.9	0.08	1.18	-0.28	0.00	0.00	-5.24	-2.21	Stage II
G304.8044+00.2014	2.5	0.04	1.61	-0.17	0.00	0.00	-5.59	-2.12	Stage II
G304.8064+00.6220	11.9	2.01	4.04	3.24	0.00	0.00	-2.23	-1.04	Stage II
G304.8112+00.2212	3.7	0.69	2.03	1.30	-4.37	-3.78	-2.51	-1.40	Stage 0/I
G304.8138+00.3393	2.2	0.12	1.68	0.43	-5.66	-4.25	-1.51	-1.39	Stage 0/I

G304.8159+00.3372	2.2	0.28	1.38	0.50	0.00	0.00	-3.82	-2.14	Stage II
G304.8429+00.4743	3.0	0.08	1.93	0.48	-4.85	-4.18	-1.98	-1.34	Stage 0/I
G304.8431+00.5928	2.3	0.00	1.60	-1.23	-7.47	-5.09	-3.36	-1.73	Ambiguous
G304.8582+00.2862	2.0	0.08	1.30	-0.18	0.00	0.00	-3.30	-1.81	Stage 0/I
G304.8619+00.0040	1.7	0.00	1.07	-2.08	-6.50	-4.96	-3.07	-1.80	Stage II
G304.8672+00.3524	2.2	0.01	1.76	-0.34	0.00	0.00	-3.14	-1.64	Stage II
G304.8707+00.3257	2.9	0.04	1.83	0.02	0.00	0.00	-3.56	-1.99	Stage II
G304.8709+00.6186	2.4	0.00	1.35	-1.78	-6.96	-4.76	-3.11	-1.66	Stage II
G304.8720+00.5673	0.9	0.08	1.34	0.35	-4.41	-3.93	-1.98	-1.40	Stage 0/I
G304.8747+00.6000	2.9	0.11	1.89	0.46	0.00	0.00	-6.14	-2.29	Stage II
G304.8806+00.6341	1.3	0.00	1.28	-1.28	-5.46	-4.45	-2.54	-1.68	Stage 0/I
G304.8837+00.0079	1.6	0.00	1.09	-2.13	-6.26	-4.87	-3.07	-1.74	Ambiguous
G304.8842+00.6364	5.8	0.08	2.76	1.11	-4.09	-3.65	-1.71	-0.95	Stage 0/I
G304.8866+00.6359	9.8	0.10	3.38	1.37	-3.42	-3.52	-1.46	-0.59	Stage 0/I
G304.8899+00.3399	3.7	0.08	2.21	0.55	0.00	0.00	-3.25	-1.74	Stage II
G304.9016+00.5693	4.2	0.01	1.84	-0.62	-6.18	-4.30	-2.94	-1.39	Stage II
G304.9174+00.3780	3.1	0.01	1.91	-0.59	0.00	0.00	-3.54	-1.48	Stage II
G304.9208+00.5311	2.2	0.08	1.66	0.28	0.00	0.00	-4.15	-2.10	Stage II
G304.9215+00.5040	2.5	0.02	1.66	-0.27	0.00	0.00	-4.45	-1.82	Stage II
G304.9260+00.5192	4.0	0.38	1.89	0.85	-7.58	-4.13	-3.09	-1.36	Stage 0/I
G304.9307+00.4100	2.3	0.00	1.69	-0.89	-8.31	-4.11	-3.28	-1.31	Ambiguous
G304.9317+00.5103	3.2	0.08	2.14	0.57	-8.56	-4.02	-4.12	-1.24	Ambiguous
G304.9318+00.3909	1.7	0.06	1.24	-0.37	0.00	0.00	-5.33	-1.48	Stage II

G304.9349+00.3065	2.6	0.00	1.43	-1.85	-7.67	-5.33	-3.92	-1.84	Ambiguous
G304.9360+00.1683	2.3	0.03	1.33	-0.53	-8.06	-5.37	-2.66	-1.59	Stage II
G304.9395+00.5201	3.1	0.02	1.94	-0.25	0.00	0.00	-3.41	-1.80	Stage II
G304.9426+00.3582	2.7	0.26	1.70	0.70	0.00	0.00	-4.65	-2.74	Stage II
G304.9444+00.2861	2.7	0.17	1.68	0.45	0.00	0.00	-4.51	-2.23	Stage II
G304.9688+00.5346	2.5	0.32	1.09	0.19	0.00	0.00	-1.76	-1.76	Stage II
G304.9723+00.6168	3.2	0.02	1.90	-0.31	0.00	0.00	-4.46	-1.75	Stage II
G304.9740+00.5096	2.6	0.13	1.62	0.33	0.00	0.00	-3.11	-1.74	Stage II
G304.9777+00.4776	2.9	0.01	1.85	-0.56	0.00	0.00	-3.40	-1.71	Stage II
G304.9884+00.0497	1.9	0.02	1.38	-0.68	-6.76	-4.65	-2.55	-1.63	Stage 0/I
G304.9909-00.3090	2.2	0.00	1.19	-1.85	-6.77	-5.06	-3.17	-1.79	Stage II
G305.0065+00.3071	2.1	0.05	1.49	0.07	0.00	0.00	-3.25	-1.84	Stage II
G305.0071+00.5843	2.0	0.02	1.13	-0.96	-6.96	-5.36	-2.40	-1.57	Ambiguous
G305.0409+00.5569	3.7	0.44	2.21	1.28	0.00	0.00	-3.66	-1.56	Stage II
G305.0424+00.3147	2.0	0.11	1.15	-0.11	0.00	0.00	-3.17	-1.53	Stage II
G305.0605+00.0777	3.7	0.00	2.29	-1.19	0.00	0.00	-3.14	-1.41	Stage II
G305.0670-00.4261	1.1	0.15	1.10	0.24	-4.42	-3.88	-2.31	-1.78	Stage 0/I
G305.0728-00.1931	3.0	0.00	1.63	-1.16	0.00	0.00	-3.17	-1.65	Stage II
G305.0741+00.6131	2.9	0.09	1.32	-0.23	-8.24	-5.39	-2.15	-1.54	Stage II
G305.0875+00.6107	3.3	0.12	1.77	0.36	0.00	0.00	-3.46	-1.61	Stage II
G305.1032+00.0659	2.3	0.01	1.55	-0.69	-5.35	-4.46	-3.10	-1.54	Stage 0/I
G305.1108+00.7893	1.4	0.08	1.36	0.17	-5.48	-4.18	-2.50	-1.72	Stage 0/I
G305.1190+00.5188	1.8	0.02	1.55	-0.46	-7.51	-4.43	-2.53	-1.56	Stage 0/I

G305.1226-00.1272	2.6	0.02	1.80	-0.36	0.00	0.00	-3.63	-1.79	Stage II
G305.1297+00.1542	3.5	0.04	2.20	0.27	0.00	0.00	-2.46	-1.19	Stage II
G305.1297-00.1054	3.1	0.00	1.41	-1.49	-6.06	-4.36	-3.15	-1.58	Stage II
G305.1312+00.4793	4.3	0.56	2.44	1.55	0.00	0.00	-2.90	-1.50	Stage II
G305.1336+00.0702	0.8	0.00	1.42	-0.87	-4.72	-3.63	-1.96	-1.18	Stage 0/I
G305.1360-00.1199	2.6	0.03	1.68	-0.31	0.00	0.00	-3.07	-1.62	Stage II
G305.1371-00.0563	2.1	0.04	1.57	-0.13	-5.33	-4.20	-1.95	-1.46	Stage 0/I
G305.1467-00.6374	3.3	0.11	2.15	0.86	0.00	0.00	-3.01	-1.72	Stage II
G305.1537+00.0652	4.4	0.04	2.47	0.45	0.00	0.00	-2.91	-1.42	Stage II
G305.1583-00.1440	4.3	0.38	1.89	0.83	-4.63	-4.05	-1.98	-1.41	Stage 0/I
G305.1597+00.0105	3.2	0.01	1.99	-0.45	0.00	0.00	-2.93	-1.51	Stage II
G305.1649-00.4322	2.7	0.01	1.41	-0.93	0.00	0.00	-2.82	-1.59	Stage II
G305.1702+00.0784	2.1	0.05	1.55	-0.07	-5.02	-3.61	-3.30	-1.52	Stage 0/I
G305.1835-00.4915	2.6	0.00	1.42	-1.65	-8.47	-5.19	-3.52	-1.72	Stage II
G305.1926+00.2062	3.3	0.03	2.32	0.50	-5.26	-4.26	-2.43	-1.23	Ambiguous
G305.1950-00.0953	3.6	0.04	2.18	0.24	0.00	0.00	-3.81	-1.62	Stage II
G305.2131+00.4544	2.2	0.08	1.47	-0.05	0.00	0.00	-2.55	-1.64	Stage 0/I
G305.2208-00.1314	2.7	0.01	1.89	-0.50	0.00	0.00	-5.10	-1.58	Stage III
G305.2221-00.0027	1.3	0.12	1.41	0.41	-4.79	-3.96	-2.79	-1.68	Stage 0/I
G305.2257+00.0478	2.2	0.11	1.59	0.35	-5.02	-4.42	-3.29	-1.80	Stage 0/I
G305.2317-00.2849	3.2	0.04	1.94	0.04	0.00	0.00	-3.02	-1.70	Stage II
G305.2341+00.0001	1.3	0.09	1.45	0.26	-5.06	-4.17	-2.09	-1.28	Stage 0/I
G305.2346-00.3408	2.6	0.02	1.60	-0.50	-6.14	-4.52	-2.58	-1.57	Ambiguous

G305.2360+00.0224	3.7	0.12	1.80	0.31	-4.76	-4.21	-2.15	-1.25	Stage 0/I
G305.2361+00.0331	7.8	0.61	2.82	1.69	-3.68	-3.52	-1.25	-0.70	Stage 0/I
G305.2395-00.0455	2.8	0.31	2.25	1.29	-4.53	-3.67	-2.00	-1.41	Stage 0/I
G305.2413-00.1850	1.7	0.03	1.27	-0.45	0.00	0.00	-3.08	-1.77	Stage 0/I
G305.2425-00.0633	1.5	0.03	1.37	-0.44	-5.31	-4.31	-3.14	-1.72	Stage 0/I
G305.2433-00.1102	0.6	0.02	1.31	-0.16	-5.11	-4.06	-2.13	-1.74	Stage 0/I
G305.2471+00.3595	2.3	0.00	1.43	-1.85	-5.93	-4.55	-2.92	-1.67	Stage II
G305.2518+00.2031	2.2	0.01	1.71	-0.46	-5.46	-4.26	-2.51	-1.44	Stage 0/I
G305.2519+00.0818	11.4	0.39	3.77	2.33	-4.00	-3.57	-1.58	-0.79	Stage 0/I
G305.2548-00.1994	2.7	0.11	1.67	0.30	0.00	0.00	-5.58	-2.06	Stage II
G305.2585+00.0547	2.1	0.01	1.49	-0.68	0.00	0.00	-3.27	-1.53	Ambiguous
G305.2657+00.0633	2.3	0.00	2.00	-1.09	-5.39	-3.77	-2.60	-1.25	Stage 0/I
G305.2662+00.2239	3.0	0.09	1.77	0.15	-7.81	-4.19	-2.52	-1.34	Stage 0/I
G305.2674+00.6251	2.8	0.01	1.53	-0.99	-7.44	-4.79	-2.71	-1.61	Stage II
G305.2691+00.0573	2.8	0.05	1.80	0.13	0.00	0.00	-3.86	-1.82	Stage II
G305.2692-00.2511	1.9	0.00	1.20	-2.08	-6.24	-4.74	-3.05	-1.81	Stage II
G305.2695-00.2821	2.4	0.00	1.31	-1.70	-7.72	-5.03	-3.16	-1.70	Stage II
G305.2698+00.0297	2.8	0.01	2.11	-0.35	-5.10	-4.08	-2.47	-1.25	Ambiguous
G305.2727-00.0618	3.3	0.01	1.82	-0.53	-4.97	-4.01	-2.23	-1.34	Ambiguous
G305.2767+00.2084	3.6	0.16	2.13	0.85	-4.74	-4.21	-2.00	-1.31	Stage 0/I
G305.2794+00.1204	3.6	0.01	2.04	-0.41	-4.45	-3.79	-1.80	-1.09	Stage 0/I
G305.2801+00.0719	4.9	0.05	2.34	0.30	-4.14	-3.81	-1.79	-0.95	Stage 0/I
G305.2808-00.2698	2.4	0.01	1.52	-0.80	0.00	0.00	-3.41	-1.73	Stage II

G305.2828+00.1908	4.6	0.06	2.58	0.69	0.00	0.00	-2.89	-1.52	Stage II
G305.2846+00.1864	5.8	1.41	2.35	1.74	-3.24	-3.44	-2.02	-0.91	Stage 0/I
G305.2862+00.0969	4.6	0.83	2.69	1.95	-4.28	-4.42	-1.95	-0.85	Stage III
G305.2894+00.1682	3.4	0.13	2.04	0.63	0.00	0.00	-4.02	-2.22	Stage II
G305.2913+00.1953	3.7	0.04	2.35	0.41	0.00	0.00	-3.86	-1.86	Stage II
G305.2926+00.0958	2.1	0.01	1.51	-0.70	-4.89	-4.00	-2.43	-1.54	Stage 0/I
G305.2966+00.0282	4.7	0.19	1.96	0.57	-4.28	-3.67	-2.01	-1.22	Stage 0/I
G305.3017+00.1494	2.2	0.06	1.33	-0.26	0.00	0.00	-4.28	-1.87	Stage II
G305.3034-00.6769	2.2	0.00	1.23	-1.99	-7.24	-5.04	-3.39	-1.80	Stage II
G305.3052+00.1940	9.5	0.19	3.56	1.90	-3.37	-3.49	-1.59	-0.61	Stage 0/I
G305.3071+00.1877	4.2	0.04	2.13	0.17	0.00	0.00	-2.93	-1.32	Stage 0/I
G305.3073+00.1930	8.2	1.27	3.06	2.25	-3.55	-3.28	-1.49	-0.66	Stage 0/I
G305.3075-00.0266	3.1	0.03	2.06	0.10	0.00	0.00	-3.54	-1.65	Ambiguous
G305.3082+00.1035	3.6	0.13	1.92	0.46	0.00	0.00	-5.78	-1.78	Stage 0/I
G305.3133+00.2205	3.8	0.02	2.39	0.31	0.00	0.00	-3.34	-1.54	Stage II
G305.3140+00.1072	5.0	0.04	2.72	0.78	0.00	0.00	-2.90	-1.36	Stage II
G305.3197+00.3178	3.1	0.10	1.95	0.54	0.00	0.00	-6.64	-2.08	Stage III
G305.3203+00.0165	2.7	0.07	1.69	0.05	-4.70	-4.33	-2.11	-1.34	Stage 0/I
G305.3204+00.1252	3.4	0.00	2.07	-0.81	0.00	0.00	-3.22	-1.48	Stage II
G305.3210-00.1500	2.8	0.00	1.45	-1.12	-6.55	-5.04	-3.71	-1.88	Ambiguous
G305.3211+00.0014	2.2	0.04	1.46	-0.25	0.00	0.00	-6.45	-1.80	Ambiguous
G305.3212+00.1099	3.3	0.03	2.02	-0.03	0.00	0.00	-2.64	-1.46	Stage II
G305.3215+00.1143	3.2	0.45	1.90	1.05	0.00	0.00	-3.00	-1.51	Stage II

G305.3234-00.6927	2.2	0.00	1.32	-1.98	-6.88	-5.08	-3.50	-1.89	Ambiguous
G305.3278-00.2032	1.9	0.00	1.33	-1.26	-6.03	-4.65	-2.58	-1.59	Ambiguous
G305.3289-00.6004	3.2	0.67	2.29	1.63	-5.46	-4.28	-1.73	-1.24	Stage II
G305.3296+00.2472	2.7	0.16	1.68	0.44	-5.00	-4.22	-1.74	-1.34	Stage 0/I
G305.3297-00.6955	2.5	0.00	1.44	-1.59	0.00	0.00	-3.74	-1.75	Stage II
G305.3300+00.6475	3.6	0.07	2.13	0.42	0.00	0.00	-4.07	-2.23	Stage II
G305.3314+00.1338	5.8	0.92	2.50	1.71	-4.08	-4.43	-1.27	-0.91	Stage 0/I
G305.3314+00.2066	5.3	0.18	3.01	1.84	0.00	0.00	-2.55	-1.32	Stage II
G305.3350-00.0712	2.0	0.02	1.51	-0.38	-5.20	-4.14	-2.73	-1.66	Stage 0/I
G305.3354-00.2507	2.6	0.01	1.72	-0.73	-7.47	-4.45	-2.63	-1.43	Ambiguous
G305.3357+00.1127	5.9	0.42	2.71	1.56	-7.46	-4.68	-1.86	-1.56	Ambiguous
G305.3376+00.0661	3.5	0.01	1.91	-0.58	-5.31	-4.11	-2.52	-1.32	Ambiguous
G305.3400+00.1008	2.4	0.00	1.77	-0.98	-5.55	-4.13	-2.63	-1.29	Stage 0/I
G305.3408+00.0651	3.7	0.00	2.29	-0.48	-5.74	-4.16	-3.25	-1.40	Ambiguous
G305.3423+00.1094	2.6	0.00	1.98	-0.66	-5.47	-4.16	-2.58	-1.30	Ambiguous
G305.3457+00.0598	2.0	0.01	1.43	-0.82	0.00	0.00	-4.07	-1.82	Ambiguous
G305.3475+00.0897	3.2	0.03	1.85	-0.25	0.00	0.00	-3.01	-1.45	Ambiguous
G305.3493+00.4175	5.0	0.21	2.90	1.82	-8.66	-4.97	-2.80	-1.35	Stage II
G305.3503-00.2043	2.6	0.07	2.32	0.91	0.00	0.00	-2.93	-1.73	Ambiguous
G305.3511+00.1032	1.9	0.22	1.45	0.51	-6.02	-5.01	-2.17	-1.57	Stage 0/I
G305.3542-00.6996	2.5	0.06	1.78	0.23	-5.72	-4.11	-2.12	-1.40	Stage 0/I
G305.3550+00.0808	3.6	0.02	2.15	-0.11	0.00	0.00	-3.08	-1.56	Stage II
G305.3561+00.0344	3.4	0.07	2.16	0.50	0.00	0.00	-3.72	-1.73	Ambiguous

G305.3586-00.2684	4.7	0.06	2.68	0.90	-5.43	-4.23	-3.01	-1.63	Stage 0/I
G305.3612-00.1399	2.4	0.02	1.57	-0.55	-6.85	-4.54	-2.77	-1.68	Stage II
G305.3634+00.1017	3.0	0.21	1.58	0.39	-6.13	-4.38	-2.85	-1.50	Stage 0/I
G305.3643-00.0087	2.2	0.02	1.69	-0.33	-5.14	-4.37	-2.98	-1.54	Ambiguous
G305.3662-00.2286	2.2	0.04	1.76	0.13	0.00	0.00	-4.17	-1.43	Ambiguous
G305.3676+00.0417	3.2	0.24	2.10	1.11	0.00	0.00	-2.17	-1.60	Stage 0/I
G305.3683+00.0710	3.6	0.01	1.80	-0.85	0.00	0.00	-3.65	-1.52	Stage II
G305.3687+00.2280	1.6	0.02	1.31	-0.47	-5.20	-4.25	-2.55	-1.54	Stage 0/I
G305.3749-00.7014	2.8	0.01	1.24	-1.06	-6.68	-5.26	-3.08	-1.69	Stage II
G305.3783-00.0332	3.5	0.11	2.14	0.57	0.00	0.00	-5.79	-1.56	Stage II
G305.3786-00.6091	2.7	0.01	1.81	-0.36	0.00	0.00	-3.42	-1.74	Stage II
G305.3788+00.1066	3.1	0.01	1.95	-0.61	0.00	0.00	-3.65	-1.73	Stage II
G305.3792+00.0781	2.3	0.02	1.64	-0.32	-8.38	-4.65	-2.82	-1.67	Ambiguous
G305.3794+00.0424	2.2	0.02	1.36	-0.78	0.00	0.00	-6.08	-1.83	Stage II
G305.3800+00.1006	3.0	0.00	1.74	-1.58	-5.81	-4.25	-2.88	-1.42	Stage II
G305.3804+00.0914	2.5	0.00	1.33	-1.61	-5.77	-4.58	-2.99	-1.54	Ambiguous
G305.3808-00.1001	3.3	0.03	2.06	0.07	0.00	0.00	-6.00	-2.03	Ambiguous
G305.3830-00.0109	3.4	0.04	1.73	-0.17	-6.78	-4.31	-2.78	-1.43	Stage II
G305.3838+00.0841	3.3	0.05	1.99	0.27	0.00	0.00	-2.84	-1.55	Stage II
G305.3850+00.0401	4.1	0.21	2.39	1.11	0.00	0.00	-2.46	-1.41	Stage II
G305.3857+00.0819	1.2	0.00	1.07	-1.98	-5.28	-4.48	-2.77	-1.71	Stage 0/I
G305.3882+00.0611	3.3	0.03	2.04	0.06	0.00	0.00	-3.44	-1.57	Stage II
G305.3893+00.0525	2.8	0.25	1.76	0.70	0.00	0.00	-3.06	-1.54	Stage II

G305.3894-00.5954	3.3	0.05	2.09	0.29	0.00	0.00	-4.65	-2.12	Stage II
G305.3902+00.1266	2.5	0.00	1.45	-2.04	-5.96	-4.56	-3.04	-1.65	Stage II
G305.3943+00.3814	1.7	0.03	1.30	-0.50	-5.46	-4.60	-2.99	-1.76	Ambiguous
G305.3963+00.1253	3.0	0.03	1.58	-0.40	-5.73	-4.21	-2.32	-1.44	Ambiguous
G305.3967-00.0277	1.3	0.04	1.09	-0.40	-5.43	-4.12	-3.20	-1.51	Stage 0/I
G305.4076-00.0422	2.2	0.02	1.43	-0.55	0.00	0.00	-4.36	-1.55	Ambiguous
G305.4083-00.3368	1.7	0.01	1.18	-1.06	-6.17	-5.01	-2.65	-1.71	Ambiguous
G305.4122+00.2245	1.5	0.02	1.41	-0.40	-5.54	-4.24	-2.17	-1.26	Stage 0/I
G305.4167+00.2798	3.3	0.05	2.04	0.19	0.00	0.00	-5.10	-2.25	Stage II
G305.4186-00.0218	2.9	0.01	1.58	-1.01	0.00	0.00	-3.61	-1.60	Stage II
G305.4193+00.1043	2.2	0.08	1.43	-0.04	0.00	0.00	-4.16	-1.88	Stage II
G305.4193-00.0298	3.5	0.12	2.14	0.69	0.00	0.00	-5.49	-2.40	Ambiguous
G305.4201-00.2600	2.6	0.01	1.54	-1.12	0.00	0.00	-2.97	-1.60	Stage II
G305.4205-00.1976	2.5	0.01	1.27	-1.03	-5.41	-4.61	-2.90	-1.68	Ambiguous
G305.4211+00.0768	2.4	0.01	1.50	-0.69	0.00	0.00	-3.62	-1.84	Stage II
G305.4216+00.0535	1.6	0.00	1.13	-2.15	-5.65	-4.63	-2.87	-1.72	Ambiguous
G305.4223+00.2664	2.4	0.01	1.64	-0.50	0.00	0.00	-4.17	-1.53	Ambiguous
G305.4227-00.6949	1.8	0.01	1.58	-0.52	-6.38	-4.68	-2.66	-1.73	Stage 0/I
G305.4272+00.4200	2.3	0.11	1.42	0.15	0.00	0.00	-5.58	-2.34	Ambiguous
G305.4286+00.2070	2.3	0.04	1.65	-0.22	-5.00	-4.44	-2.33	-1.55	Stage 0/I
G305.4290+00.1095	2.1	0.00	1.72	-1.17	-5.37	-4.00	-2.51	-1.28	Ambiguous
G305.4320-00.0217	2.8	0.05	1.83	0.08	0.00	0.00	-3.23	-1.70	Stage II
G305.4343+00.1042	2.5	0.00	1.49	-1.76	-5.91	-4.43	-2.93	-1.63	Stage II

G305.4350+00.1810	2.9	0.03	2.11	0.08	-5.70	-4.05	-2.43	-1.34	Ambiguous
G305.4384-00.2429	4.0	0.06	2.27	0.65	0.00	0.00	-3.36	-1.48	Stage II
G305.4403+00.3645	3.9	0.16	1.55	0.16	-6.38	-4.60	-2.43	-1.56	Stage II
G305.4415+00.1047	2.3	0.00	1.43	-2.18	-6.03	-4.40	-3.12	-1.70	Stage II
G305.4466+00.0563	1.9	0.00	1.27	-2.02	-5.71	-4.08	-2.86	-1.53	Stage II
G305.4491+00.1219	0.7	0.09	1.24	0.24	0.00	0.00	-2.46	-1.57	Stage 0/I
G305.4508+00.1326	2.1	0.24	1.91	0.97	-3.40	-3.70	-2.03	-1.25	Stage 0/I
G305.4513+00.0972	3.0	0.01	2.29	-0.05	0.00	0.00	-3.78	-1.47	Ambiguous
G305.4522+00.3786	1.8	0.00	1.28	-1.48	-5.75	-4.30	-2.85	-1.53	Ambiguous
G305.4550-00.3928	2.3	0.01	1.46	-1.14	-6.96	-4.93	-3.04	-1.65	Stage II
G305.4552-00.0465	2.1	0.01	1.66	-0.65	-6.96	-4.38	-3.17	-1.50	Ambiguous
G305.4556-00.0701	2.2	0.00	1.81	-0.96	-5.23	-3.97	-2.31	-1.18	Ambiguous
G305.4564+00.0224	3.0	0.24	1.33	0.15	0.00	0.00	-4.55	-1.55	Stage 0/I
G305.4564+00.0330	3.0	0.01	1.73	-0.67	0.00	0.00	-3.81	-1.55	Stage II
G305.4582+00.3899	2.4	0.02	1.52	-0.50	0.00	0.00	-4.62	-2.10	Stage II
G305.4609+00.1128	3.7	0.23	1.93	0.69	0.00	0.00	-3.73	-1.92	Stage II
G305.4624-00.2472	2.9	0.05	1.69	-0.13	-6.78	-4.22	-2.16	-1.30	Stage II
G305.4637-00.1005	3.1	0.00	1.91	-1.20	0.00	0.00	-3.26	-1.50	Stage II
G305.4638-00.3730	2.6	0.03	1.26	-0.72	0.00	0.00	-5.84	-2.08	Stage II
G305.4656-00.0818	1.8	0.01	1.34	-0.90	-5.69	-4.72	-2.53	-1.63	Ambiguous
G305.4657+00.1129	3.4	0.10	2.07	0.54	0.00	0.00	-4.79	-2.02	Stage III
G305.4670+00.1306	1.8	0.00	1.45	-1.24	-5.65	-4.39	-2.38	-1.51	Stage 0/I
G305.4671-00.6358	2.1	0.03	1.69	-0.03	-8.68	-4.47	-2.63	-1.65	Ambiguous

G305.4687+00.1315	2.1	0.06	1.30	-0.24	0.00	0.00	-2.69	-1.57	Stage II
G305.4696-00.0249	2.2	0.09	1.29	-0.16	0.00	0.00	-2.66	-1.74	Stage II
G305.4698+00.0369	2.5	0.00	1.83	-1.20	-5.49	-4.07	-2.58	-1.24	Ambiguous
G305.4706+00.1338	5.5	0.05	2.89	0.90	0.00	0.00	-2.47	-1.08	Stage II
G305.4716+00.1846	2.8	0.04	1.74	-0.15	0.00	0.00	-3.01	-1.78	Ambiguous
G305.4722+00.1343	3.9	0.00	2.00	-1.01	-5.45	-4.09	-2.58	-1.38	Ambiguous
G305.4726+00.1384	0.9	0.04	1.14	-0.19	-4.86	-4.18	-2.48	-1.62	Stage 0/I
G305.4753+00.2188	2.4	0.08	1.69	0.19	-4.68	-4.20	-2.03	-1.33	Stage 0/I
G305.4769+00.0239	4.0	0.13	2.11	0.71	0.00	0.00	-3.62	-1.46	Stage 0/I
G305.4772+00.0738	2.5	0.08	1.31	-0.34	-4.98	-3.97	-1.71	-1.25	Stage II
G305.4855+00.1274	2.9	0.06	1.75	0.32	-7.40	-4.33	-2.74	-1.33	Ambiguous
G305.4896-00.1575	1.9	0.10	1.59	0.09	-5.40	-4.22	-2.28	-1.63	Stage 0/I
G305.4910+00.0256	3.4	0.01	2.01	-0.72	0.00	0.00	-3.01	-1.39	Stage II
G305.4923+00.3264	6.8	0.27	2.66	1.23	-4.10	-3.73	-1.68	-0.87	Stage 0/I
G305.4926-00.4782	2.9	0.02	1.40	-0.64	-7.44	-5.50	-3.09	-1.61	Stage II
G305.4937+00.1417	1.9	0.18	1.27	0.21	0.00	0.00	-2.69	-1.87	Stage 0/I
G305.4952+00.0108	1.3	0.01	1.60	-0.46	-5.96	-4.46	-3.36	-1.41	Stage 0/I
G305.4961+00.2289	1.9	0.05	1.30	-0.30	-5.13	-4.71	-3.03	-1.74	Stage 0/I
G305.5004+00.0821	2.9	0.04	1.83	-0.05	0.00	0.00	-4.89	-1.98	Stage III
G305.5049+00.3380	3.0	0.02	1.91	-0.25	0.00	0.00	-3.59	-1.78	Stage II
G305.5116+00.0342	5.8	0.13	3.09	1.58	0.00	0.00	-2.48	-1.43	Stage II
G305.5127+00.1286	2.1	0.02	1.25	-0.85	0.00	0.00	-5.58	-1.82	Stage II
G305.5154+00.0529	2.2	0.00	1.56	-1.21	0.00	0.00	-3.60	-1.63	Ambiguous

G305.5164-00.0821	3.1	0.29	2.26	1.21	-3.61	-3.43	-1.65	-1.23	Stage 0/I
G305.5199-00.2684	2.8	0.14	1.83	0.61	-5.60	-4.39	-1.95	-1.40	Stage II
G305.5207-00.1323	4.7	0.09	2.63	1.01	0.00	0.00	-3.37	-1.66	Ambiguous
G305.5215+00.3095	2.1	0.03	1.33	-0.49	0.00	0.00	-5.58	-2.03	Stage II
G305.5246+00.0519	2.0	0.04	1.51	-0.15	-5.46	-4.35	-2.82	-1.52	Ambiguous
G305.5276+00.0419	1.6	0.00	1.20	-1.30	-5.34	-4.44	-2.54	-1.56	Stage 0/I
G305.5282+00.1775	1.5	0.00	1.18	-2.34	-5.42	-4.24	-2.69	-1.64	Stage 0/I
G305.5324+00.7741	0.7	0.16	1.31	0.58	-5.06	-4.19	-3.03	-1.65	Stage 0/I
G305.5354-00.2916	3.0	0.04	1.34	-0.51	0.00	0.00	-3.42	-1.68	Stage II
G305.5361+00.3475	7.0	1.16	2.93	2.16	-3.83	-3.65	-1.47	-1.35	Stage 0/I
G305.5363+00.0573	3.0	0.29	1.84	0.84	0.00	0.00	-3.36	-1.65	Stage II
G305.5377-00.2897	1.9	0.00	1.24	-1.71	-6.33	-4.81	-2.99	-1.71	Stage II
G305.5393+00.9439	3.1	0.03	1.99	0.04	0.00	0.00	-2.49	-1.40	Stage II
G305.5404+00.4116	2.5	0.01	1.45	-0.93	-6.12	-4.52	-2.32	-1.56	Ambiguous
G305.5408+00.1434	1.1	0.03	1.22	-0.40	0.00	0.00	-3.46	-1.87	Stage 0/I
G305.5424-00.0610	2.5	0.01	1.86	-0.50	-4.82	-4.11	-2.29	-1.16	Stage 0/I
G305.5447+00.0030	4.1	0.11	2.15	0.49	-4.27	-4.09	-1.61	-0.99	Stage 0/I
G305.5460+00.3319	2.1	0.01	1.38	-0.92	-8.06	-4.54	-2.79	-1.45	Stage II
G305.5503-00.6740	2.1	0.00	1.27	-1.71	-7.13	-5.17	-3.19	-1.81	Stage II
G305.5506+00.5129	1.8	0.12	1.38	0.14	-5.41	-4.04	-2.67	-1.77	Stage 0/I
G305.5578+00.3924	2.5	0.03	1.79	-0.21	0.00	0.00	-2.68	-1.64	Ambiguous
G305.5608+00.4032	2.5	0.08	2.17	1.00	-7.02	-4.21	-2.08	-1.38	Stage 0/I
G305.5713+00.3159	1.3	0.00	1.30	-1.15	-5.45	-4.25	-3.15	-1.52	Stage 0/I

G305.5714+00.0506	3.3	0.01	2.04	-0.30	0.00	0.00	-3.25	-1.48	Stage II
G305.5715-00.2249	2.5	0.32	2.27	1.45	-4.16	-3.91	-1.85	-1.53	Ambiguous
G305.5719-00.2705	2.9	0.02	1.38	-0.70	-6.12	-4.92	-2.74	-1.61	Stage II
G305.5737-00.7218	3.1	0.06	1.50	-0.19	0.00	0.00	-3.02	-1.58	Stage II
G305.5755+00.0566	3.1	0.02	1.97	-0.27	0.00	0.00	-3.67	-1.72	Stage II
G305.5761+00.4036	2.2	0.00	1.43	-1.38	-6.68	-4.77	-3.09	-1.72	Ambiguous
G305.5761-00.0214	4.7	0.02	2.15	-0.31	0.00	0.00	-2.82	-1.36	Ambiguous
G305.5761-00.0802	2.9	0.08	1.88	0.34	0.00	0.00	-2.89	-1.44	Stage II
G305.5777-00.2155	1.8	0.04	1.72	0.32	0.00	0.00	-2.47	-1.50	Stage 0/I
G305.5794-00.5085	1.9	0.03	1.70	0.04	-6.68	-4.38	-2.29	-1.75	Stage II
G305.5803-00.3393	2.8	0.00	1.74	-0.97	0.00	0.00	-3.24	-1.67	Stage II
G305.5805-00.6247	1.5	0.09	1.31	0.07	-5.69	-5.02	-2.18	-1.47	Stage 0/I
G305.5852+00.0090	2.7	0.65	1.69	1.07	0.00	0.00	-3.48	-1.62	Stage II
G305.5867+00.0215	2.5	0.01	1.82	-0.45	-6.14	-4.47	-3.17	-1.52	Ambiguous
G305.5912-00.7083	1.8	0.06	1.57	0.10	-5.57	-4.10	-2.14	-1.82	Stage 0/I
G305.5913-00.7093	0.7	0.01	0.97	-0.99	-5.42	-4.33	-2.29	-1.68	Stage 0/I
G305.5941+00.3315	3.2	0.27	1.97	0.91	0.00	0.00	-2.57	-1.63	Stage II
G305.6033+00.4814	2.6	0.01	1.72	-0.42	0.00	0.00	-3.56	-1.78	Stage II
G305.6087-00.0700	3.1	0.00	2.03	-1.39	-5.79	-4.27	-3.00	-1.52	Ambiguous
G305.6133+00.0769	2.3	0.03	1.61	-0.27	0.00	0.00	-3.60	-1.91	Ambiguous
G305.6140+00.3444	3.1	0.02	2.03	-0.01	0.00	0.00	-2.77	-1.62	Stage II
G305.6159-00.1325	2.4	0.00	1.42	-1.51	-6.38	-4.65	-2.82	-1.62	Ambiguous
G305.6170+00.0260	2.0	0.32	1.53	0.75	0.00	0.00	-4.35	-1.69	Stage 0/I

G305.6197-00.0371	3.4	0.05	2.05	0.24	0.00	0.00	-2.82	-1.43	Stage II
G305.6239+00.3350	1.8	0.01	1.30	-1.11	-5.68	-4.41	-2.53	-1.48	Ambiguous
G305.6246-00.6603	1.5	0.28	1.65	0.94	-4.02	-3.98	-1.99	-1.84	Stage 0/I
G305.6251-00.0822	2.8	0.05	1.83	0.10	0.00	0.00	-4.02	-1.59	Ambiguous
G305.6266-00.6368	2.0	0.00	1.48	-1.20	-5.46	-4.07	-2.55	-1.51	Stage II
G305.6301-00.0929	3.1	0.00	1.68	-1.55	-6.23	-4.41	-2.97	-1.53	Stage II
G305.6324-00.7011	2.4	0.00	1.65	-0.98	-7.88	-5.31	-3.27	-1.73	Ambiguous
G305.6340-00.0546	2.8	0.01	1.82	-0.45	-6.83	-4.42	-2.78	-1.63	Ambiguous
G305.6351-00.0850	2.9	0.00	2.49	-0.49	-4.62	-3.59	-2.11	-1.06	Stage 0/I
G305.6356-00.0188	3.1	0.09	1.92	0.42	0.00	0.00	-3.81	-1.75	Stage II
G305.6541+00.0579	1.7	0.14	1.39	0.27	-5.29	-4.81	-2.60	-1.58	Stage 0/I
G305.6545+00.5036	4.2	0.06	2.22	0.34	-7.20	-4.17	-2.46	-1.33	Ambiguous
G305.6551+00.6140	1.6	0.00	1.36	-1.84	-5.94	-3.94	-3.04	-1.43	Ambiguous
G305.6609-00.2320	2.2	0.04	1.34	-0.38	0.00	0.00	-5.68	-2.43	Stage III
G305.6625+00.0848	2.7	0.08	1.71	0.21	0.00	0.00	-5.48	-1.86	Stage II
G305.6631-00.1013	4.7	0.15	2.68	1.17	0.00	0.00	-3.15	-1.59	Stage II
G305.6677+00.5904	2.4	0.00	1.38	-1.27	-6.50	-4.85	-2.84	-1.68	Stage II
G305.6709+00.1290	5.0	0.17	2.79	1.34	0.00	0.00	-5.80	-1.58	Stage III
G305.6712-00.5912	1.6	0.04	1.56	0.17	-5.55	-4.28	-2.19	-1.76	Stage 0/I
G305.6716+00.0453	3.3	0.01	2.03	-0.44	0.00	0.00	-3.21	-1.48	Stage II
G305.6760+00.0315	2.0	0.01	1.32	-1.03	-5.52	-4.18	-3.16	-1.70	Stage 0/I
G305.6948-00.4124	2.6	0.02	1.63	-0.55	0.00	0.00	-3.35	-1.64	Stage II
G305.7062-00.5775	2.2	0.01	1.66	-0.29	0.00	0.00	-2.60	-1.55	Ambiguous

G305.7085-00.0562	2.7	0.00	1.75	-1.32	-6.25	-4.51	-3.04	-1.65	Ambiguous
G305.7092+00.5547	0.7	0.00	0.86	-1.47	-5.25	-4.31	-2.27	-1.66	Stage 0/I
G305.7140-00.5300	1.2	0.10	1.61	0.50	-4.12	-3.89	-2.60	-1.87	Stage 0/I
G305.7267-00.0472	3.1	0.02	2.25	0.38	0.00	0.00	-2.57	-1.48	Stage II
G305.7321-00.0391	2.0	0.00	1.17	-1.47	-5.72	-4.73	-2.93	-1.68	Ambiguous
G305.7347+00.0114	2.1	0.06	1.35	-0.22	0.00	0.00	-3.66	-1.98	Stage II
G305.7387-00.7440	4.0	0.18	2.31	0.95	0.00	0.00	-3.45	-1.62	Stage II
G305.7441-00.0541	2.4	0.01	1.51	-1.10	-7.03	-4.62	-2.69	-1.61	Stage II
G305.7448-00.4796	2.7	0.02	1.27	-0.76	-7.70	-5.90	-3.48	-1.82	Stage II
G305.7477+00.2743	2.0	0.00	1.30	-1.74	-6.37	-4.85	-3.02	-1.70	Stage II
G305.7489-00.0490	3.2	0.01	2.16	-0.12	-5.86	-4.57	-2.93	-1.60	Ambiguous
G305.7506+00.0308	5.1	0.27	2.71	1.46	0.00	0.00	-2.42	-1.41	Stage II
G305.7544-00.0844	2.0	0.03	1.57	-0.23	-5.67	-4.18	-2.17	-1.48	Stage 0/I
G305.7563-00.2421	2.7	0.27	1.69	0.69	0.00	0.00	-4.83	-3.82	Stage II
G305.7565-00.2644	2.0	0.03	1.36	-0.44	-4.63	-4.37	-2.67	-1.63	Stage 0/I
G305.7704-00.4769	3.7	0.10	2.25	0.68	-7.85	-5.58	-5.18	-2.21	Stage III
G305.7706-00.0034	3.9	0.02	2.46	0.20	0.00	0.00	-4.28	-1.62	Stage III
G305.7716+00.0514	3.4	0.01	1.60	-0.84	-6.93	-4.62	-3.24	-1.54	Stage II
G305.7725-00.2477	2.3	0.01	1.64	-0.31	0.00	0.00	-2.58	-1.49	Ambiguous
G305.7851+00.0119	2.6	0.09	1.64	0.18	0.00	0.00	-3.82	-1.94	Stage II
G305.7877-00.2449	1.7	0.38	2.07	1.47	-3.51	-3.63	-1.88	-1.56	Stage 0/I
G305.8019+00.4816	4.7	0.91	2.58	1.87	0.00	0.00	-3.15	-1.97	Stage II
G305.8051-00.0914	4.0	0.00	2.72	0.15	-4.23	-3.48	-1.79	-0.92	Stage 0/I

G305.8053-00.1956	2.0	0.01	1.58	-0.86	-5.40	-4.20	-2.31	-1.54	Stage 0/I
G305.8136-00.0968	2.0	0.13	1.12	-0.08	0.00	0.00	-5.24	-2.16	Stage II
G305.8161+00.0295	1.7	0.01	1.41	-0.77	-5.91	-4.25	-2.22	-1.43	Stage 0/I
G305.8164-00.2609	1.3	0.00	1.40	-1.05	-4.82	-3.86	-2.11	-1.40	Stage 0/I
G305.8187-00.2254	2.5	0.12	1.55	0.23	0.00	0.00	-3.82	-2.01	Stage II
G305.8218-00.2743	2.0	0.07	1.54	0.06	-4.78	-3.88	-1.93	-1.36	Stage 0/I
G305.8231-00.2720	1.4	0.00	1.19	-1.30	-5.73	-4.61	-2.60	-1.69	Stage 0/I
G305.8278-00.1145	4.2	0.15	2.44	1.04	0.00	0.00	-2.82	-1.71	Stage II
G305.8324-00.1616	3.7	0.10	2.21	0.64	0.00	0.00	-6.35	-2.70	Stage III
G305.8326+00.4983	3.7	0.10	2.25	0.68	0.00	0.00	-3.60	-1.78	Stage II
G305.8343+00.0930	2.0	0.03	1.44	-0.43	-4.87	-3.97	-2.71	-1.28	Stage 0/I
G305.8371+00.0884	1.6	0.01	1.20	-0.92	-5.83	-4.83	-3.12	-1.72	Ambiguous
G305.8436+00.1060	1.9	0.00	1.57	-1.40	-6.34	-4.30	-3.36	-1.73	Ambiguous
G305.8442-00.0197	2.7	0.04	1.91	0.15	0.00	0.00	-4.28	-1.37	Ambiguous
G305.8532-00.1745	3.3	0.21	2.00	0.82	0.00	0.00	-4.11	-1.94	Stage II
G305.8552-00.0715	3.5	0.27	2.00	0.88	-4.76	-3.95	-2.00	-1.29	Stage 0/I
G305.8599-00.0174	3.2	0.05	2.00	0.15	0.00	0.00	-3.53	-1.61	Stage II
G305.8731-00.1307	3.0	0.41	1.86	1.01	0.00	0.00	-4.68	-3.80	Stage II
G305.8791-00.0950	3.4	0.98	1.97	1.43	-3.20	-3.54	-1.83	-1.15	Stage 0/I
G305.8824+00.0236	3.9	0.04	2.33	0.37	0.00	0.00	-3.52	-1.56	Stage II
G305.8825-00.0450	4.1	0.15	1.70	0.22	-6.12	-4.57	-2.19	-1.48	Ambiguous
G305.8904-00.2659	3.0	0.16	1.83	0.57	0.00	0.00	-4.89	-2.05	Stage III
G305.8964-00.0355	2.7	0.01	1.43	-0.91	0.00	0.00	-3.42	-1.72	Stage II

G305.8981+00.1093	3.2	0.10	1.99	0.49	0.00	0.00	-2.63	-1.67	Stage III
G305.8997-00.0504	3.1	0.01	2.06	-0.42	0.00	0.00	-3.52	-1.67	Ambiguous
G305.9065+00.2370	4.1	1.85	2.00	1.65	-7.86	-7.82	-2.30	-1.27	Stage II
G305.9085+00.0527	2.7	0.09	1.76	0.32	0.00	0.00	-5.24	-1.83	Stage III
G305.9105+00.0443	3.4	0.69	2.07	1.38	0.00	0.00	-3.79	-2.02	Stage II
G305.9116-00.0475	2.6	0.03	1.63	-0.31	0.00	0.00	-4.23	-1.83	Stage II
G305.9190+00.1100	2.4	0.12	1.06	-0.27	0.00	0.00	-3.48	-1.83	Stage II
G305.9362-00.1461	1.8	0.00	1.34	-1.55	-5.47	-3.86	-2.66	-1.34	Stage II
G305.9508-00.0667	2.0	0.07	1.24	-0.23	0.00	0.00	-3.09	-1.83	Stage II
G305.9590+00.2813	2.3	0.10	1.45	0.07	0.00	0.00	-3.09	-1.79	Stage II
G305.9646-00.4076	3.0	0.02	1.34	-0.87	-6.20	-4.75	-3.20	-1.68	Stage II
G305.9711-00.1608	1.5	0.02	1.36	-0.47	0.00	0.00	-2.97	-1.68	Stage 0/I
G305.9749-00.1751	3.1	0.00	1.92	-0.89	0.00	0.00	-3.59	-1.56	Stage II
G305.9776+00.9858	1.9	0.00	1.15	-1.64	-6.14	-4.73	-2.79	-1.68	Ambiguous
G305.9847+00.0646	2.0	0.00	1.28	-2.13	-5.92	-4.17	-3.03	-1.69	Stage II
G305.9902+00.1738	2.9	0.20	1.18	0.09	0.00	0.00	-3.46	-1.77	Stage II
G305.9930-00.0151	4.5	0.15	2.58	1.11	0.00	0.00	-2.84	-1.49	Stage II
G305.9941-00.6576	2.1	0.00	1.35	-1.17	-6.72	-4.87	-2.81	-1.69	Stage II
G305.9991-00.0498	3.0	0.04	1.86	0.02	0.00	0.00	-3.00	-1.65	Stage II
G306.0023-00.7884	2.6	0.00	1.37	-1.68	-7.42	-5.29	-3.42	-1.75	Stage II
G306.0024-00.7558	1.6	0.12	1.50	0.19	-4.79	-4.23	-2.63	-1.37	Ambiguous
G306.0097-00.2268	2.4	0.01	2.01	-0.08	0.00	0.00	-2.62	-1.56	Ambiguous
G306.0098-00.4170	2.6	0.00	1.58	-1.02	-8.26	-4.98	-3.12	-1.69	Stage II

G306.0112-00.0528	2.9	0.11	1.83	0.41	0.00	0.00	-5.98	-5.18	Stage III
G306.0138+00.0191	2.7	0.09	1.66	0.15	0.00	0.00	-4.46	-2.43	Stage II
G306.0307+00.0572	2.7	0.09	1.67	0.16	0.00	0.00	-4.42	-2.18	Stage II
G306.0330+00.0553	3.0	0.01	1.81	-0.73	0.00	0.00	-4.07	-1.60	Stage II
G306.0392+00.0498	2.7	0.44	1.36	0.51	0.00	0.00	-2.21	-1.56	Stage II
G306.0407+00.8549	2.1	0.00	1.12	-2.30	-6.97	-5.05	-3.34	-1.81	Stage II
G306.0447-00.0686	4.0	0.15	1.84	0.44	-7.36	-4.53	-2.50	-1.31	Stage II
G306.0454-00.0632	2.5	0.08	1.64	0.17	-4.99	-4.16	-2.45	-1.50	Stage 0/I
G306.0468+00.0945	2.2	0.22	1.32	0.32	0.00	0.00	-4.97	-2.08	Stage II
G306.0486-00.2771	2.3	0.02	1.85	-0.12	-4.91	-3.56	-2.50	-1.15	Stage 0/I
G306.0499-00.0772	7.5	2.11	3.33	2.78	0.00	0.00	-1.60	-2.25	Stage II
G306.0547+00.2850	2.3	0.00	1.29	-1.61	-8.32	-5.48	-3.68	-1.82	Stage II
G306.0564-00.0452	1.9	0.00	1.54	-1.03	-4.79	-3.67	-2.18	-1.47	Stage 0/I
G306.0613+00.0312	2.7	0.00	1.49	-1.31	-7.36	-4.78	-2.88	-1.58	Stage II
G306.0624+00.2188	2.4	0.01	1.62	-0.83	-6.51	-5.13	-3.23	-1.71	Ambiguous
G306.0656-00.0291	2.9	0.06	1.85	0.13	0.00	0.00	-2.70	-1.62	Stage II
G306.0679-00.0275	3.7	0.02	2.21	0.02	0.00	0.00	-3.03	-1.55	Stage II
G306.0694+00.1283	3.1	0.15	1.47	0.14	-7.40	-5.65	-2.29	-1.50	Stage II
G306.0824+00.4603	2.3	0.00	1.18	-2.06	-7.42	-5.41	-3.50	-1.90	Stage II
G306.0884-00.2421	2.1	0.09	1.40	0.00	-6.66	-4.47	-2.02	-1.54	Stage 0/I
G306.0941-00.2805	2.7	0.01	1.87	-0.49	-5.47	-4.15	-2.44	-1.53	Stage II
G306.0952+00.1979	3.1	0.04	1.92	-0.02	0.00	0.00	-3.09	-1.63	Stage III
G306.0987-00.7082	1.7	0.00	1.19	-1.30	-6.55	-4.89	-2.71	-1.71	Ambiguous

G306.1093-00.2728	3.5	0.19	2.14	0.90	0.00	0.00	-2.76	-1.55	Stage II
G306.1148-00.2800	0.7	0.03	1.29	-0.06	-5.22	-4.79	-1.94	-1.57	Stage 0/I
G306.1186-00.0656	1.9	0.00	1.16	-1.66	-6.16	-4.67	-2.81	-1.67	Ambiguous
G306.1208-00.0552	1.6	0.00	1.13	-1.64	-6.23	-4.71	-2.66	-1.64	Ambiguous
G306.1213-00.0849	2.2	0.14	1.38	0.23	0.00	0.00	-5.07	-1.94	Stage II
G306.1272-00.2743	1.2	0.00	1.11	-1.44	-5.61	-4.66	-2.74	-1.76	Stage 0/I
G306.1281-00.5999	3.9	0.06	2.36	0.65	0.00	0.00	-3.69	-1.74	Stage II
G306.1290+00.1612	2.8	0.00	1.48	-1.27	0.00	0.00	-3.24	-1.65	Stage II
G306.1292+00.2053	3.4	0.36	1.84	0.85	0.00	0.00	-4.23	-1.95	Stage II
G306.1341-00.3003	0.6	0.05	1.23	0.14	-5.03	-3.90	-2.58	-1.67	Stage 0/I
G306.1385-00.4168	2.3	0.30	1.39	0.53	0.00	0.00	-5.24	-3.79	Ambiguous
G306.1394+00.1337	3.4	0.32	1.81	0.78	0.00	0.00	-4.12	-1.57	Stage II
G306.1416-00.3256	3.3	0.01	2.02	-0.34	0.00	0.00	-3.40	-1.66	Stage II
G306.1551+00.2479	2.6	0.01	1.51	-1.06	0.00	0.00	-3.11	-1.68	Stage II
G306.1564-00.2528	2.3	0.04	1.92	0.26	0.00	0.00	-2.72	-1.66	Ambiguous
G306.1599-00.3272	1.7	0.03	1.53	-0.28	-5.14	-4.04	-2.03	-1.45	Stage 0/I
G306.1634-00.2335	4.3	0.10	2.43	0.81	0.00	0.00	-3.60	-1.73	Stage II
G306.1686-00.2383	2.6	0.04	1.34	-0.48	-8.33	-5.23	-2.60	-1.56	Stage II
G306.1693-00.1579	2.6	0.03	1.77	-0.16	0.00	0.00	-3.16	-1.66	Stage II
G306.1706-00.0187	2.2	0.06	1.35	-0.23	0.00	0.00	-5.59	-2.04	Stage II
G306.1758-00.3848	2.2	0.02	1.75	-0.07	-6.25	-4.49	-2.57	-1.61	Ambiguous
G306.1789-00.2374	4.2	0.22	1.78	0.50	0.00	0.00	-3.02	-1.36	Stage II
G306.1798-00.2090	2.4	0.35	1.52	0.71	0.00	0.00	-2.17	-2.15	Stage II

G306.1951+00.1897	3.2	0.07	1.86	0.18	0.00	0.00	-3.44	-1.61	Stage II
G306.1965+00.3084	2.6	0.05	1.54	-0.20	-4.81	-4.23	-1.84	-1.52	Stage 0/I
G306.1980+00.2412	3.3	0.07	1.29	-0.40	-7.54	-5.50	-2.66	-1.62	Stage II
G306.2003-00.2070	1.9	0.04	1.21	-0.45	0.00	0.00	-3.17	-1.82	Stage II
G306.2053-00.2345	3.8	0.20	1.60	0.30	-7.78	-5.07	-3.02	-1.51	Stage II
G306.2062-00.3626	1.9	0.04	1.65	0.07	-5.57	-4.15	-2.18	-1.69	Stage 0/I
G306.2064+00.1200	3.8	0.22	1.93	0.69	0.00	0.00	-3.15	-1.60	Stage II
G306.2086-00.1946	2.8	0.02	1.75	-0.29	0.00	0.00	-4.42	-1.83	Stage II
G306.2088-00.2232	3.3	0.17	2.20	0.91	0.00	0.00	-5.47	-2.08	Stage III
G306.2097-00.2041	2.9	0.34	1.26	0.35	0.00	0.00	-3.57	-1.81	Stage II
G306.2124+00.1897	1.6	0.01	0.99	-1.40	-6.66	-5.06	-2.79	-1.72	Ambiguous
G306.2148+00.1820	4.0	0.14	1.78	0.32	-6.68	-5.03	-2.40	-1.55	Stage II
G306.2159-00.3701	3.6	0.05	2.21	0.32	0.00	0.00	-3.59	-1.68	Stage II
G306.2190+00.0083	2.4	0.06	1.56	-0.00	0.00	0.00	-2.51	-1.73	Stage III
G306.2200+00.0132	2.2	0.20	1.33	0.30	0.00	0.00	-3.86	-2.29	Stage II
G306.2217-00.0477	2.4	0.05	1.56	-0.12	0.00	0.00	-4.51	-1.96	Ambiguous
G306.2239+00.0035	3.0	0.03	1.29	-0.67	-6.43	-5.22	-2.31	-1.58	Stage II
G306.2241+00.0747	2.6	0.01	1.31	-1.13	0.00	0.00	-3.14	-1.69	Stage II
G306.2251+00.0017	1.9	0.02	0.83	-1.08	-8.63	-5.22	-2.45	-1.72	Stage II
G306.2267+00.0018	3.2	0.21	1.94	0.80	0.00	0.00	-3.02	-1.79	Stage II
G306.2344-00.2779	0.4	0.03	0.97	-0.34	-4.68	-3.83	-2.00	-1.26	Stage 0/I
G306.2448+00.1765	3.8	0.57	1.92	1.11	-7.16	-6.30	-2.58	-1.52	Stage II
G306.2477-00.5631	4.1	0.13	2.41	0.88	0.00	0.00	-3.74	-1.81	Stage II

G306.2484-00.0078	2.9	0.02	1.86	-0.24	0.00	0.00	-4.11	-1.97	Stage II
G306.2535+00.2342	2.1	0.00	1.14	-1.77	-8.26	-5.09	-3.18	-1.76	Stage II
G306.2574-00.4501	3.5	0.17	2.20	0.89	0.00	0.00	-7.25	-2.66	Stage III
G306.2752+00.1700	3.7	0.18	2.30	1.13	-5.22	-4.23	-2.10	-1.54	Ambiguous
G306.2754-00.2785	2.2	0.03	1.24	-0.67	-5.35	-4.63	-3.06	-1.79	Ambiguous
G306.2761-00.1770	3.4	0.05	2.23	0.51	-8.10	-4.30	-2.27	-1.65	Stage II
G306.2823-00.3853	0.4	0.00	0.86	-1.19	-5.27	-4.31	-2.22	-1.85	Stage 0/I
G306.2924+00.4382	3.9	0.20	2.30	1.03	0.00	0.00	-3.25	-1.87	Stage II
G306.2942-00.1849	1.4	0.21	1.34	0.51	-4.29	-3.71	-2.02	-1.33	Stage 0/I
G306.3004-00.3166	1.3	0.04	1.19	-0.34	0.00	0.00	-2.72	-1.58	Stage 0/I
G306.3062+00.2051	4.3	0.18	2.01	0.69	-6.51	-4.98	-2.53	-1.18	Ambiguous
G306.3113-00.1593	3.8	0.08	2.26	0.62	0.00	0.00	-3.69	-1.60	Ambiguous
G306.3343+00.3966	1.4	0.00	1.07	-1.82	-6.03	-4.77	-2.83	-1.72	Ambiguous
G306.3409-00.1835	2.1	0.00	1.35	-1.24	-6.88	-4.86	-2.82	-1.67	Stage II
G306.3468-00.2820	1.5	0.02	1.41	-0.44	-6.19	-4.17	-2.18	-1.60	Stage 0/I
G306.3473+00.4142	2.0	0.00	1.21	-1.41	-7.73	-5.21	-3.04	-1.74	Stage II
G306.3529-00.3876	2.6	0.00	1.37	-1.51	-8.31	-4.98	-3.06	-1.66	Stage II
G306.3530+00.7401	2.1	0.00	1.19	-1.89	-7.57	-5.34	-3.42	-1.86	Stage II
G306.3614+00.5908	2.9	0.03	1.79	-0.10	0.00	0.00	-2.82	-1.61	Stage II
G306.3777+00.6357	2.4	0.00	1.32	-1.45	-6.61	-4.94	-2.92	-1.67	Ambiguous
G306.3868+00.7941	2.3	0.00	1.29	-1.83	-7.92	-5.35	-3.55	-1.88	Stage II
G306.3910+00.3891	2.3	0.49	1.42	0.75	-4.76	-4.20	-1.56	-1.54	Stage 0/I
G306.3922-00.6701	2.3	0.02	1.64	-0.25	0.00	0.00	-4.13	-1.97	Stage II

G306.4060+00.0160	1.6	0.06	1.40	0.02	-5.48	-4.08	-2.12	-1.74	Stage 0/I
G306.4061-00.5220	2.2	0.08	1.37	-0.09	0.00	0.00	-5.07	-1.72	Ambiguous
G306.4084-00.5833	2.6	0.11	1.66	0.29	0.00	0.00	-5.24	-1.99	Stage III
G306.4195+00.0736	2.3	0.00	1.30	-1.28	0.00	0.00	-3.09	-1.71	Stage II
G306.4324-00.5948	2.3	0.00	1.33	-1.46	0.00	0.00	-3.73	-1.76	Stage II
G306.4330-00.0039	2.7	0.00	1.48	-1.30	0.00	0.00	-3.69	-1.70	Stage II
G306.4415-00.2892	1.3	0.02	1.52	-0.30	-7.73	-4.45	-2.83	-1.73	Ambiguous
G306.4461+00.0373	2.0	0.15	1.76	0.56	-5.31	-4.35	-2.11	-1.61	Stage 0/I
G306.4568+00.5725	3.2	0.01	1.66	-0.92	0.00	0.00	-3.11	-1.64	Stage II
G306.4577+00.5282	5.7	0.42	2.89	1.76	0.00	0.00	-5.94	-2.13	Stage III
G306.4619+00.3328	1.9	0.00	1.23	-1.28	-6.26	-4.70	-2.63	-1.64	Stage II
G306.4701+00.2399	2.4	0.00	1.39	-1.41	0.00	0.00	-3.69	-1.78	Stage II
G306.4791+00.3145	2.0	0.01	1.60	-0.47	-7.50	-4.63	-2.79	-1.70	Stage II
G306.4810+00.2409	2.1	0.04	1.64	-0.03	-8.14	-4.47	-2.55	-1.63	Stage 0/I
G306.4870+00.1066	2.0	0.00	1.25	-1.69	-6.51	-4.97	-3.05	-1.74	Stage II
G306.4887+00.2519	2.1	0.00	1.29	-1.45	-6.80	-4.95	-2.97	-1.73	Stage II
G306.4917-00.7498	4.1	0.14	2.43	0.93	0.00	0.00	-3.10	-1.61	Stage II
G306.4936-00.5564	2.2	0.00	1.50	-0.86	-8.15	-5.26	-3.21	-1.76	Ambiguous
G306.5062+00.2338	2.0	1.16	2.16	1.92	-3.69	-4.32	-1.72	-2.11	Stage 0/I
G306.5106+00.0699	2.0	0.04	1.78	0.26	0.00	0.00	-2.85	-1.60	Ambiguous
G306.5153+00.2432	1.6	0.04	1.35	-0.26	-6.20	-4.42	-2.19	-1.60	Stage 0/I
G306.5242-00.1775	2.6	0.02	1.79	0.09	-7.13	-4.60	-2.88	-1.72	Stage II
G306.5458+00.3003	2.2	0.00	1.39	-1.52	-7.67	-5.22	-3.21	-1.75	Stage II

G306.5670-00.0436	3.1	0.03	1.88	-0.13	0.00	0.00	-3.02	-1.52	Stage II
G306.5739-00.8336	3.2	0.01	1.90	-0.63	0.00	0.00	-3.36	-1.65	Stage II
G306.5878+00.1034	1.3	0.01	1.23	-0.80	-5.54	-4.55	-2.38	-1.65	Stage 0/I
G306.6070+00.3529	1.6	0.78	1.63	1.33	-3.43	-4.22	-1.19	-1.04	Stage 0/I
G306.6172+00.1146	2.5	0.00	1.58	-0.89	0.00	0.00	-4.11	-1.80	Stage II
G306.6297-00.3150	2.4	0.01	1.55	-0.67	-4.92	-4.14	-2.61	-1.58	Stage 0/I
G306.6300+00.4324	3.8	0.11	2.46	1.03	-5.75	-4.20	-2.62	-1.43	Stage II
G306.6356-00.0479	2.8	0.01	1.46	-1.20	0.00	0.00	-3.24	-1.65	Stage II
G306.6376-00.3779	2.3	0.07	1.43	-0.03	0.00	0.00	-6.45	-4.31	Stage III
G306.6423+00.3010	1.4	0.00	1.04	-1.61	-5.94	-4.90	-3.39	-1.82	Ambiguous
G306.6491-00.3732	2.5	0.01	1.14	-1.44	-6.75	-5.45	-3.65	-1.86	Stage II
G306.6507+00.3440	1.3	0.00	1.15	-1.50	-5.58	-4.57	-2.58	-1.67	Stage 0/I
G306.6524+00.0553	3.5	0.24	1.78	0.59	-4.95	-4.28	-1.78	-1.21	Stage 0/I
G306.6685+00.8956	2.5	0.00	1.58	-1.12	-8.25	-5.18	-3.17	-1.72	Stage II
G306.6705-00.8463	4.0	0.04	2.36	0.37	0.00	0.00	-3.21	-1.73	Stage II
G306.6724-00.2089	4.1	0.14	2.01	0.53	0.00	0.00	-2.83	-1.56	Stage II
G306.6812-00.4342	3.6	0.31	2.24	1.15	0.00	0.00	-3.21	-1.58	Stage II
G306.6852+00.6548	2.6	0.00	1.55	-0.96	0.00	0.00	-3.86	-1.75	Stage II
G306.6885+00.2172	3.3	0.02	2.00	-0.26	0.00	0.00	-3.32	-1.68	Stage II
G306.6898+00.2905	1.1	0.18	1.64	0.89	-4.35	-4.35	-2.10	-1.15	Stage 0/I
G306.6906-00.0028	2.3	0.10	1.63	0.29	-5.68	-4.20	-2.20	-1.55	Stage 0/I
G306.6942+00.2235	1.5	0.02	1.30	-0.70	-6.72	-4.47	-2.58	-1.71	Stage 0/I
G306.6958+00.2263	2.4	0.57	1.80	1.11	-4.02	-3.89	-1.71	-1.57	Stage 0/I

G306.7027-00.0228	2.7	0.06	1.94	0.40	-8.26	-5.06	-2.58	-1.66	Stage II
G306.7181+00.1561	0.7	0.02	1.33	-0.13	-4.85	-4.13	-2.60	-1.45	Stage 0/I
G306.7216+00.1502	1.3	0.00	1.16	-1.41	-5.21	-4.45	-2.74	-1.77	Stage 0/I
G306.7340+00.0215	1.4	0.01	1.34	-0.61	-6.59	-4.65	-2.60	-1.70	Stage 0/I
G306.7391+00.2962	4.3	0.80	2.73	2.06	-4.65	-4.63	-1.22	-1.02	Stage 0/I
G306.7466-00.0971	2.8	0.33	1.77	0.84	-8.65	-4.72	-2.50	-1.48	Stage 0/I
G306.7641-00.3439	2.0	0.00	1.31	-1.53	-6.52	-4.81	-3.01	-1.72	Stage II
G306.7660-00.8407	2.4	0.01	1.33	-1.12	-6.28	-4.85	-2.79	-1.65	Stage II
G306.7674-00.4956	1.1	0.04	1.15	-0.26	-5.28	-4.38	-2.82	-1.74	Stage 0/I
G306.7763+00.2091	2.9	0.10	1.79	0.32	0.00	0.00	-3.21	-1.69	Stage II
G306.7800+00.1921	2.7	0.29	1.68	0.70	-5.35	-4.43	-1.85	-1.39	Ambiguous
G306.7831+00.3472	2.0	0.07	1.55	0.10	-5.18	-3.99	-2.14	-1.66	Stage 0/I
G306.7941+00.3129	3.5	0.01	1.66	-0.94	-6.46	-4.53	-3.90	-1.66	Stage III
G306.8061+00.2160	2.1	0.00	1.26	-1.79	-6.97	-4.99	-3.13	-1.71	Stage II
G306.8090+00.0151	2.2	0.01	1.41	-0.86	0.00	0.00	-3.17	-1.76	Stage II
G306.8246+00.5647	4.4	0.14	2.55	1.09	0.00	0.00	-2.84	-1.45	Stage II
G306.8301+00.6124	1.2	0.06	1.34	0.09	-4.85	-3.96	-1.96	-1.38	Stage 0/I
G306.8376-00.6306	1.8	0.01	1.04	-1.32	-5.64	-4.74	-3.19	-1.79	Ambiguous
G306.8426+00.7953	4.5	0.19	2.47	1.11	0.00	0.00	-2.18	-1.38	Stage II
G306.8447-00.2865	2.7	0.01	1.44	-1.08	0.00	0.00	-3.36	-1.70	Stage II
G306.8542+00.3981	1.9	0.12	1.39	0.20	-4.76	-4.22	-1.59	-1.52	Stage 0/I
G306.8722-00.0432	1.6	0.01	1.27	-0.96	-5.94	-4.75	-2.39	-1.64	Ambiguous
G306.8724-00.0422	1.2	0.00	1.01	-1.50	-5.82	-4.70	-2.46	-1.66	Ambiguous

G306.8803-00.3066	1.5	0.01	1.11	-1.20	-6.44	-5.02	-2.89	-1.74	Ambiguous
G306.8987+00.1187	3.4	0.09	1.84	0.22	-5.82	-3.95	-2.05	-1.17	Stage 0/I
G306.9070+00.1106	1.4	0.00	1.21	-1.20	-5.81	-4.58	-2.60	-1.68	Ambiguous
G306.9208+00.2066	3.7	0.15	2.32	0.90	0.00	0.00	-2.45	-1.77	Stage II
G306.9230-00.3527	2.9	0.03	1.34	-0.67	-7.38	-6.08	-4.16	-1.90	Stage II
G306.9293-00.5988	2.7	0.03	1.33	-0.71	0.00	0.00	-3.52	-1.76	Stage II
G306.9437+00.5093	1.1	0.14	1.53	0.59	-4.85	-3.97	-2.66	-1.88	Stage 0/I
G306.9443-00.5177	2.7	0.01	1.65	-0.93	0.00	0.00	-3.23	-1.65	Stage II
G306.9456-00.5616	3.2	0.02	1.95	-0.15	0.00	0.00	-3.26	-1.71	Stage II
G306.9555+00.4574	1.3	0.02	1.28	-0.48	-5.99	-4.42	-2.40	-1.59	Stage 0/I
G306.9582-00.2484	2.5	0.03	1.51	-0.39	-6.46	-5.44	-4.15	-1.71	Ambiguous
G306.9595+00.3421	1.3	0.01	1.15	-1.18	-6.50	-4.87	-2.82	-1.73	Stage 0/I
G306.9665+00.6235	2.2	0.10	1.59	0.19	-5.29	-4.32	-2.89	-1.81	Stage 0/I
G306.9669+00.0700	2.5	0.01	1.30	-1.04	-6.16	-5.03	-3.13	-1.73	Stage II
G306.9696+00.3240	3.1	0.01	1.66	-0.95	0.00	0.00	-4.41	-1.78	Stage II
G306.9978+00.3035	2.4	0.00	1.35	-1.59	-7.16	-5.01	-3.09	-1.68	Stage II
G307.0241-00.5744	2.3	0.00	1.29	-1.53	-7.50	-5.28	-3.31	-1.83	Stage II
G307.0801-00.0764	1.5	0.20	1.36	0.49	-4.40	-3.83	-2.02	-1.56	Stage 0/I
G307.0948-00.7969	3.2	0.03	1.99	-0.04	0.00	0.00	-3.36	-1.68	Stage II
G307.1063-00.0404	2.6	0.01	1.68	-0.65	-4.91	-4.15	-2.11	-1.41	Stage 0/I
G307.1070-00.0447	2.2	0.01	1.66	-0.22	-7.97	-4.99	-2.63	-1.64	Stage II
G307.1399-00.7404	2.2	0.00	1.35	-1.86	-8.18	-5.14	-3.52	-1.75	Stage II
G307.1517-00.8333	4.9	0.92	2.21	1.49	-4.98	-4.02	-1.35	-1.33	Stage II

G307.1742-00.1002	3.1	0.09	1.75	0.17	0.00	0.00	-3.56	-1.72	Stage II
G307.1813-00.1237	2.8	0.02	1.31	-0.86	0.00	0.00	-3.04	-1.70	Stage II
G307.1819-00.3880	3.4	0.29	2.10	1.02	0.00	0.00	-2.64	-1.56	Stage II
G307.2106-00.8346	1.8	0.00	1.05	-2.10	-6.67	-5.01	-3.12	-1.82	Stage II
G307.2135-00.6791	1.5	0.00	0.95	-2.23	-7.36	-4.10	-3.75	-1.87	Stage II
G307.2162-00.1182	1.9	0.00	1.09	-2.36	-7.13	-5.13	-3.36	-1.86	Stage II
G307.2262-00.1356	1.6	0.01	1.24	-0.96	-6.82	-4.81	-2.60	-1.64	Stage 0/I
G307.2514-00.6872	4.3	0.04	2.53	0.47	0.00	0.00	-3.81	-1.73	Stage II

Bibliography

Abergel A., Boulanger F., Mizuno A., Fukui Y., 1994, ApJL, 423, L59 8

Aguirre J. E., Bolocam Galactic Plane Survey Team, 2008, in Bulletin of the American Astronomical Society, Vol. 40, American Astronomical Society Meeting Abstracts #212, p. 198 176

Aguirre J. E. et al., 2011, ApJS, 192, 4 53

Alcalá J. M. et al., 2008, ApJ, 676, 427 140

Allamandola L. J., Tielens A. G. G. M., Barker J. R., 1985, ApJL, 290, L25 11

Allen L. E. et al., 2004, ApJS, 154, 363 122, 147

Anderson L. D., Zavagno A., Barlow M. J., García-Lario P., Noriega-Crespo A., 2012, A&A, 537, A1 128

André P. et al., 2010, A&A, 518, L102 179

André P., Men'shchikov A., Könyves V., Arzoumanian D., 2011, in IAU Symposium, Vol. 270, IAU Symposium, J. Alves, B. G. Elmegreen, J. M. Girart, & V. Trimble, ed., pp. 255–262 23

Andre P., Ward-Thompson D., Barsony M., 1993, ApJ, 406, 122 17

Anglada G., Villuendas E., Estalella R., Beltrán M. T., Rodríguez L. F., Torrelles J. M., Curiel S., 1998, AJ, 116, 2953 81

Ascenso J., Alves J., Lago M. T. V. T., 2009, A&A, 495, 147 24

Baldry I. K., Glazebrook K., 2003, ApJ, 593, 258 37, 39

Bally J., Cunningham N., Moeckel N., Smith N., 2005, Massive star birth: A crossroads of Astrophysics, 1, 12 3

Bastian N., Covey K. R., Meyer M. R., 2010, ARA&A, 48, 339 138

Bastian N., Gieles M., Efremov Y. N., Lamers H. J. G. L. M., 2005, A&A, 443, 79 35

Beltrán M. T., Cesaroni R., Codella C., Testi L., Furuya R. S., Olmi L., 2006, Nature, 443, 427 146

Beltrán M. T. et al., 2013, A&A, 552, A123 174

Benjamin R. A. et al., 2003, PASP, 115, 953 53, 71, 115, 148, 176

Benson P. J., Myers P. C., 1989, ApJS, 71, 89 2

Bergin E. A., Maret S., van der Tak F. F. S., Alves J., Carmody S. M., Lada C. J., 2006, ApJ, 645, 369 62

Bernasconi P. A., Maeder A., 1996, A&A, 307, 829 131, 140

Bertelli G., Bressan A., Chiosi C., Fagotto F., Nasi E., 1994, A&AS, 106, 275 60

Bertoldi F., 1989, ApJ, 346, 735 32

Beuther H., Linz H., Henning T., 2012, A&A, 543, A88 23

Beuther H., Schilke P., Sridharan T. K., Menten K. M., Walmsley C. M., Wyrowski F., 2002, A&A, 383, 892 146

Billot N., Noriega-Crespo A., Carey S., Guieu S., Shenoy S., Paladini R., Latter W., 2010, ApJ, 712, 797 149

Bisbas T. G., Wünsch R., Whitworth A. P., Hubber D. A., 2009, A&A, 497, 649 33

Bisbas T. G., Wünsch R., Whitworth A. P., Hubber D. A., Walch S., 2011, ApJ, 736, 142 33

Blitz L., 1993, in Protostars and Planets III, Levy E. H., Lunine J. I., eds., pp. 125–161 9, 14

Bloemhof E. E., Reid M. J., Moran J. M., 1992, ApJ, 397, 500 27

Bok B. J., Reilly E. F., 1947, ApJ, 105, 255 3

Bonnell I. A., Bate M. R., Clarke C. J., Pringle J. E., 1997, MNRAS, 285, 201 23

Bonnell I. A., Bate M. R., Clarke C. J., Pringle J. E., 2001, MNRAS, 323, 785 24

Bonnell I. A., Bate M. R., Zinnecker H., 1998, MNRAS, 298, 93 24

Bonnell I. A., Vine S. G., Bate M. R., 2004, MNRAS, 349, 735 23, 24

Bontemps S. et al., 2010, A&A, 518, L85 90

Boselli A. et al., 2010, PASP, 122, 261 177

Brand J., Blitz L., 1993, A&A, 275, 67 58, 59

Breen S. L., Caswell J. L., Ellingsen S. P., Phillips C. J., 2010, MNRAS, 406, 1487 95

Busfield A. L., Purcell C. R., Hoare M. G., Lumsden S. L., Moore T. J. T., Oudmaijer R. D., 2006, MNRAS, 366, 1096 59

Calvet N., Hartmann L., Kenyon S. J., Whitney B. A., 1994, ApJ, 434, 330 133

Calzetti D., Chandar R., Lee J. C., Elmegreen B. G., Kennicutt R. C., Whitmore B., 2010a, ApJ, 719, L158 99

Calzetti D. et al., 2007, ApJ, 666, 870 106

Calzetti D. et al., 2005, ApJ, 633, 871 106

Calzetti D. et al., 2010b, ApJ, 714, 1256 108

Carey S. J. et al., 2009, PASP, 121, 76 53, 72, 80, 116, 127, 140, 176

Castelli F., Kurucz R. L., 2004, ArXiv Astrophysics e-prints 123, 124

Caswell J. L., 1998, MNRAS, 297, 215 67, 183

Caswell J. L., 2009, PASA, 26, 454 28

Caswell J. L. et al., 2010, MNRAS, 404, 1029 74, 80, 176

Caswell J. L., Haynes R. F., 1987, A&A, 171, 261 173

Cesaroni R., 2005, in IAU Symposium, Vol. 227, Massive Star Birth: A Crossroads of Astrophysics, R. Cesaroni, M. Felli, E. Churchwell, & M. Walmsley, ed., pp. 59–69 26

Cesaroni R., Churchwell E., Hofner P., Walmsley C. M., Kurtz S., 1994, A&A, 288, 903 62

Chabrier G., 2003, PASP, 115, 763 37, 139

Chapman N. L. et al., 2007, ApJ, 667, 288 140

Chomiuk L., Povich M. S., 2011, AJ, 142, 197 99, 102, 108, 109, 111, 171, 174

Churchwell E., 1999, NATO ASIC Proc. 540: The Origin of Stars and Planetary Systems, -1, 515 146

Churchwell E., 2002a, The Stellar Initial Mass Function (38th Herstmonceux Conference), 267, 3 28, 30

Churchwell E., 2002b, ARA&A, 40, 27 27, 101

Churchwell E., Wolfire M., Wood D. O. S., 1989, in IAU Symposium, Vol. 135, Interstellar Dust, Allamandola L. J., Tielens A. G. G. M., eds., p. 195P 101

Clark J. S., Davies B., Thompson M. A., 2011, Société Royale des Sciences de Liège, 80, 223 63

Clark J. S., Porter J. M., 2004, A&A, 427, 839 55, 57, 60, 67, 75, 102, 114, 162, 164, 166, 173, 175

Cohen M., 1973, MNRAS, 161, 97 2

Cohen R. S., Cong H., Dame T. M., Thaddeus P., 1980, ApJL, 239, L53 4

Comerón F., Torra J., 1996, A&A, 314, 776 30, 31, 101

Crapsi A., van Dishoeck E. F., Hogerheijde M. R., Pontoppidan K. M., Dullemond C. P., 2008, A&A, 486, 245 140

Crowther P. A., Conti P. S., 2003, MNRAS, 343, 143 29, 80, 127

Crowther P. A., Schnurr O., Hirschi R., Yusof N., Parker R. J., Goodwin S. P., Kassim H. A., 2010, MNRAS, 408, 731, (c) Journal compilation © 2010 RAS 21

Cutri R. M. et al., 2003, VizieR Online Data Catalog, 2246, 0 70, 71

Dale D. A. et al., 2005, ApJ, 633, 857 106, 107

Dale J. E., Bonnell I. A., 2012, MNRAS, 422, 1352 35, 176

Dale J. E., Bonnell I. A., Whitworth A. P., 2007, MNRAS, 375, 1291 35, 102

Dale J. E., Clark, P. C., Bonnell I. A., 2007, MNRAS, 377, 535 35

Dale J. E., Ercolano B., Bonnell I. A., 2012, MNRAS, 427, 2852 35, 176

Dale J. E., Ercolano B., Bonnell I. A., 2013, MNRAS, 431, 1062 35, 176

Dalton G. B. et al., 2006, in Society of Photo-Optical Instrumentation Engineers (SPIE) Conference Series, Vol. 6269, Society of Photo-Optical Instrumentation Engineers (SPIE) Conference Series 70

Dame T. M., 2007, ApJL, 665, L163 57

Damineli A., Blum R. D., Figuerêdo E., Conti P. S., 2005, in IAU Symposium, Vol. 227, Massive Star Birth: A Crossroads of Astrophysics, Cesaroni R., Felli M., Churchwell E., Walmsley M., eds., pp. 407–412 59

Danks A. C., Dennefeld M., Wamsteker W., Shaver P. A., 1983, A&A, 118, 301 59

Danks A. C., Wamsteker W., Shaver P. A., Retallack D. S., 1984, A&A, 132, 301 55, 59

Davies B. et al., 2012, MNRAS, 419, 1871 53, 59, 60, 61, 66, 67, 90, 101, 102, 111, 114, 141, 162, 165, 167, 181

Davies B., Hoare M. G., Lumsden S. L., Hosokawa T., Oudmaijer R. D., Urquhart J. S., Mottram J. C., Stead J., 2011, MNRAS, 416, 972 21, 25, 30, 31, 102, 111, 171, 174

de Pree C. G., Mehringer D. M., Goss W. M., 1997, ApJ, 482, 307 57

Deharveng L., Zavagno A., Caplan J., 2005, A&A, 433, 565 32

Dewangan L. K., Ojha D. K., 2013, MNRAS, 429, 1386 35

Dewangan L. K., Ojha D. K., Anandarao B. G., Ghosh S. K., Chakraborti S., 2012, ArXiv e-prints 35

Dirienzo W. J., Indebetouw R., Brogan C., Cyganowski C. J., Churchwell E., Friesen R. K., 2012, AJ, 144, 173 35

Dobbs C., 2009, in The Evolving ISM in the Milky Way and Nearby Galaxies 9

Dobbs C. L., Pringle J. E., 2013, ArXiv e-prints 8, 9

Dobbs C. L., Pringle J. E., Burkert A., 2012, MNRAS, 425, 2157 8

Downes A. J. B., Peacock J. A., Savage A., Carrie D. R., 1986, MNRAS, 218, 31 81

Dunham M. M., Crapsi A., Evans, II N. J., Bourke T. L., Huard T. L., Myers P. C., Kauffmann J., 2008, ApJS, 179, 249 90, 140

Dupac X. et al., 2003, A&A, 404, L11 52

Duschl W. J., Gail H.-P., Tscharnuter W. M., 1996, A&A, 312, 624 11

Dye S. et al., 2009, ApJ, 703, 285 84

Eales S. et al., 2010, PASP, 122, 499 178

Efremov Y. N., Elmegreen B. G., 1998, MNRAS, 299, 588 164

Elia D. et al., 2010, A&A, 518, L97 79

Ellingsen S. P., Voronkov M. A., Cragg D. M., Sobolev A. M., Breen S. L., Godfrey P. D., 2007, Astrophysical Masers and their Environments, 242, 213 27

Elmegreen B. G., 1979, ApJ, 231, 372 8

Elmegreen B. G., 2002, Massive star birth: A crossroads of Astrophysics, 207, 390 68, 76

Elmegreen B. G., 2004, MNRAS, 354, 367 138

Elmegreen B. G., 2007, ApJ, 668, 1064 176

Elmegreen B. G., Lada C. J., 1977, ApJ, 214, 725 31, 34, 68, 76, 102, 166, 175

Emerson J. P., Sutherland W. J., 2010, in Society of Photo-Optical Instrumentation Engineers (SPIE) Conference Series, Vol. 7733, Society of Photo-Optical Instrumentation Engineers (SPIE) Conference Series 70

Evans, II N. J. et al., 2003, PASP, 115, 965 129

Evans, II N. J. et al., 2009, ApJS, 181, 321 164

Faimali A. et al., 2012, MNRAS, 426, 402 63, 73, 76, 111, 130, 144, 166

Fazio G. G. et al., 2004, ApJS, 154, 10 71, 115

Fontani F., Pascucci I., Caselli P., Wyrowski F., Cesaroni R., Walmsley C. M., 2007, A&A, 470, 639 26

Foster J. B. et al., 2011, ApJS, 197, 25 53, 176

Fraser H. J., Collings M. P., McCoustra M. R. S., Williams D. A., 2001, MNRAS, 327, 1165 12

Frerking M. A., Langer W. D., Wilson R. W., 1987, ApJ, 313, 320 7

Fuente A., 2001, in ESA Special Publication, Vol. 460, The Promise of the Herschel Space Observatory, Pilbratt G. L., Cernicharo J., Heras A. M., Prusti T., Harris R., eds., p. 177 18

Fuller G. A., Williams S. J., Sridharan T. K., 2005, A&A, 442, 949 146

Furuya R. S., 2003, The Stellar Initial Mass Function (38th Herstmonceux Conference), 287, 367 80

Gaczkowski B., Preibisch T., Ratzka T., Roccatagliata V., Ohlendorf H., Zinnecker H., 2013, A&A, 549, A67 95, 179

Gao Y., Solomon P. M., 2004, ApJ, 606, 271 104

Garay G., Reid M. J., Moran J. M., 1985, ApJ, 289, 681 27

Georgelin Y. M., Boulesteix J., Georgelin Y. P., Le Coarer E., Marcelin M., 1988, A&A, 205, 95 59

Giannini T. et al., 2012, A&A, 539, A156 65, 90

Goodman A. A., Arce H. G., 2004, ApJ, 608, 831 150

Goss W. M., Shaver P. A., 1970, Australian Journal of Physics Astrophysical Supplement, 14, 1 55, 56

Green J. A. et al., 2009, MNRAS, 392, 783 53, 74, 80, 176

Green J. A. et al., 2012, MNRAS, 420, 3108 67, 74, 95, 183

Griffin M. J. et al., 2010, A&A, 518, L3 72, 78

Guesten R., Mezger P. G., 1982, Vistas in Astronomy, 26, 159 31

Gutermuth R. A. et al., 2008, ApJ, 674, 336 122, 128

Gvaramadze V. V., Weidner C., Kroupa P., Pflamm-Altenburg J., 2012, MNRAS, 424, 3037 67

Haisch, Jr. K. E., Lada E. A., Lada C. J., 2000, AJ, 120, 1396 142, 145

Haisch, Jr. K. E., Lada E. A., Lada C. J., 2001, AJ, 121, 2065 145

Harper D. A., Low F. J., 1971, ApJL, 165, L9 2

Harvey P., Merín B., Huard T. L., Rebull L. M., Chapman N., Evans, II N. J., Myers P. C., 2007a, ApJ, 663, 1149 128, 129, 130, 140, 147, 149

Harvey P. M. et al., 2006, ApJ, 644, 307 128, 129, 140

Harvey P. M. et al., 2007b, ApJ, 663, 1139 140

Hatchell J., Millar T. J., Rodgers S. D., 1998, A&A, 332, 695 26

Heiderman A., Evans N. J. I., Allen L. E., Huard T., Heyer M., 2010, ApJ, 723, 1019 76, 104, 109

Henning T., Schreyer K., Launhardt R., Burkert A., 2000, A&A, 353, 211 146

Herbig G. H., 1952, JRASC, 46, 222 2

Herbig G. H., 1957, in IAU Symposium, Vol. 3, Non-stable stars, Herbig G. H., ed., p. 3 2

Hernández J. et al., 2007, ApJ, 662, 1067 145

Hildebrand R. H., 1983, QJRAS, 24, 267 14, 89

Hillenbrand L. A., Massey P., Strom S. E., Merrill K. M., 1993, AJ, 106, 1906 138

Hindson L., Thompson M. A., Urquhart J. S., Clark J. S., Davies B., 2010, MNRAS, 408, 1438 53, 55, 57, 61, 62, 63, 66, 67, 73, 75, 80, 105, 165, 178, 183

Hindson L., Thompson M. A., Urquhart J. S., Faimali A., Clark J. S., Davies B., 2012, MNRAS, 421, 3418 53, 57, 63, 66, 67, 73, 80, 82, 95, 101, 111, 162, 166, 173, 175, 182

Hoare M. G., Kurtz S. E., Lizano S., Keto E., Hofner P., 2007, Protostars and Planets V, -1, 181 28

Hoare M. G., Lumsden S. L., Oudmaijer R. D., Busfield A. L., King T. L., Moore T. L. J., 2004, in Astronomical Society of the Pacific Conference Series, Vol. 317, Milky Way Surveys: The Structure and Evolution of our Galaxy, Clemens D., Shah R., Brainerd T., eds., p. 156 72

Hoare M. G. et al., 2005, in IAU Symposium, Vol. 227, Massive Star Birth: A Crossroads of Astrophysics, Cesaroni R., Felli M., Churchwell E., Walmsley M., eds., pp. 370–375 59

Holland W. S. et al., 2013, MNRAS, 430, 2513 53, 176

Hollenbach D., Johnstone D., Lizano S., Shu F., 1994, ApJ, 428, 654 145

Hollenbach D. J., Tielens A. G. G. M., 1997, ARA&A, 35, 179 4

Hosokawa T., Omukai K., 2009, ApJ, 691, 823 146

Hunter T. R., Churchwell E., Watson C., Cox P., Benford D. J., Roelfsema P. R., 2000, AJ, 119, 2711 88

Indebetouw R. et al., 2005, ApJ, 619, 931 123, 126

Indebetouw R., Robitaille T. P., Whitney B. A., Churchwell E., Babler B., Meade M., Watson C., Wolfire M., 2007, ApJ, 666, 321 150

Indebetouw R., Whitney B. A., Robitaille T. P., Churchwell E., the GLIMPSE team, 2005, Massive star birth: A crossroads of Astrophysics, 1, 397 147

Ivison R. J. et al., 2010, MNRAS, 402, 245 85

Jeans J. H., 1902, Royal Society of London Philosophical Transactions Series A, 199, 1 13

Jørgensen J. K. et al., 2006, ApJ, 645, 1246 140

Joy A. H., 1945, ApJ, 102, 168 2

Jura M., 1986, ApJ, 303, 327 11

Kang M., Bieging J. H., Povich M. S., Lee Y., 2009, ApJ, 706, 83 149, 155, 161

Kendrew S. et al., 2012, ApJ, 755, 71 36

Kennicutt R. C., 2005, Massive star birth: A crossroads of Astrophysics, 1, 3 2

Kennicutt R. C., Evans N. J., 2012, ARA&A, 50, 531 43

Kennicutt, Jr. R. C., 1983, ApJ, 272, 54 37

Kennicutt, Jr. R. C., 1998a, ARA&A, 36, 189 40, 99, 103, 106, 107, 109, 111, 174

Kennicutt, Jr. R. C., 1998b, ApJ, 498, 541 39, 40, 41, 42

Kenyon S. J., Hartmann L., 1995, ApJS, 101, 117 142, 145

Kenyon S. J., Hartmann L. W., Strom K. M., Strom S. E., 1990, AJ, 99, 869 8

Kerton C. R., Martin P. G., Johnstone D., Ballantyne D. R., 2001, ApJ, 552, 601 16, 89

Keto E., 2002, ApJ, 568, 754 146

Keto E., Wood K., 2006, ApJ, 637, 850 146

Koenig X. P., Allen L. E., Gutermuth R. A., Hora J. L., Brunt C. M., Muzerolle J., 2008, ApJ, 688, 1142 147, 150

Kramer C., Richer J., Mookerjea B., Alves J., Lada C., 2003, A&A, 399, 1073 89

Kroupa P., 2001, MNRAS, 322, 231 39, 138, 141, 144

Kroupa P., 2002, Science, 295, 82 37, 139

Kroupa P., Tout C. A., Gilmore G., 1993, MNRAS, 262, 545 37

Kroupa P., Weidner C., 2005, in Astrophysics and Space Science Library, Vol. 327, The Initial Mass Function 50 Years Later, Corbelli E., Palla F., Zinnecker H., eds., p. 175 38, 139

Krumholz M. R., Dekel A., McKee C. F., 2012, ApJ, 745, 69 99, 109, 110, 174

Krumholz M. R., Klein R. I., McKee C. F., Offner S. S. R., Cunningham A. J., 2009, Science, 323, 754 23

Krumholz M. R., Matzner C. D., McKee C. F., 2006, ApJ, 653, 361 176

Krumholz M. R., McKee C. F., Klein R. I., 2005, ApJL, 618, L33 23

Krumholz M. R., McKee C. F., Tumlinson J., 2009, ApJ, 693, 216 4

Kuiper R., Klahr H., Beuther H., Henning T., 2010, ApJ, 722, 1556 23

Kurtz S., Cesaroni R., Churchwell E., Hofner P., Walmsley C. M., 2000, Protostars and Planets IV, -1, 299 21, 26, 30

Kurtz S., Hofner P., 2005, AJ, 130, 711 30

Kwan J., 1979, ApJ, 229, 567 8

Lacy J. H., Knacke R., Geballe T. R., Tokunaga A. T., 1994, ApJL, 428, L69 41

Lada C. J., 1987, in IAU Symposium, Vol. 115, Star Forming Regions, Peimbert M., Jugaku J., eds., pp. 1–17 17, 19

Lada C. J., Forbrich J., Lombardi M., Alves J. F., 2012, ApJ, 745, 190 110, 174

Lada C. J., Lombardi M., Alves J. F., 2010, ApJ, 724, 687 76, 104, 105, 109, 110, 111, 114, 171, 174

Lada E. A., 1992, ApJL, 393, L25 104

Larson R. B., 1981, MNRAS, 194, 809 104

Larson R. B., 1985, MNRAS, 214, 379 14

Lawton B. et al., 2010, ApJ, 716, 453 107, 108, 111

Lefloch B., Lazareff B., 1994, A&A, 289, 559 32

Leger A., Puget J. L., 1984a, A&A, 137, L5 11

Leger A., Puget J. L., 1984b, A&A, 137, L5 63

Leisawitz D., 1990, ApJ, 359, 319 9

Leistra A., Cotera A. S., Liebert J., Burton M., 2005, AJ, 130, 1719 59, 66, 90, 131, 141, 181

Leitherer C., Heckman T. M., 1995, ApJS, 96, 9 40

Li A., Greenberg J. M., 2003, in Solid State Astrochemistry, Pirronello V., Krelowski J., Manicò G., eds., pp. 37–84 11

Li Y., Calzetti D., Kennicutt R. C., Hong S., Engelbracht C. W., Dale D. A., Moustakas J., 2010, ApJ, 725, 677 108, 111

Lilly S. J., Eales S. A., Gear W. K. P., Hammer F., Le Fèvre O., Crampton D., Bond J. R., Dunne L., 1999, ApJ, 518, 641 81

Lombardi M., Alves J., Lada C. J., 2010, A&A, 519, L7 105

Longmore S. N., Burton M. G., Barnes P. J., Wong T., Purcell C. R., Ott J., 2007, MNRAS, 379, 535 26

Longmore S. N., Maercker M., Ramstedt S., Burton M. G., 2007, MNRAS, 380, 1497 114, 162

Lucas P. W. et al., 2008, MNRAS, 391, 136 53, 176

Lumsden S. L., Hoare M. G., Oudmaijer R. D., Richards D., 2002, MNRAS, 336, 621 72

Maíz Apellániz J., Úbeda L., 2005, ApJ, 629, 873 138, 139

Martins F., Schaerer D., Hillier D. J., 2005, A&A, 436, 1049 60

Massey P., 2002, ApJS, 141, 81 161

Massey P., 2003, ARA&A, 41, 15 138

Massey P., Johnson K. E., Degioia-Eastwood K., 1995, ApJ, 454, 151 138

Mathis J. S., Rumpl W., Nordsieck K. H., 1977, ApJ, 217, 425 10

Mathis J. S., Whiffen G., 1989, ApJ, 341, 808 10

Mauerhan J. C., van Dyk S. D., Morris P. W., 2009, PASP, 121, 591 66, 181

Mauerhan J. C., Van Dyk S. D., Morris P. W., 2011, AJ, 142, 40 66, 181

McKee C. F., Ostriker E. C., 2007, ARA&A, 45, 565 9

McKee C. F., Tan J. C., 2003, ApJ, 585, 850 22, 23, 146

Mendoza V. E. E., 1968, ApJ, 151, 977 2

Menten K., 1991, The Stellar Initial Mass Function (38th Herstmonceux Conference), 16, 119 27, 28, 80

Menten K. M., Pillai T., Wyrowski F., 2005, in IAU Symposium, Vol. 227, Massive Star Birth: A Crossroads of Astrophysics, Cesaroni R., Felli M., Churchwell E., Walmsley M., eds., pp. 23–34 25

Merín B. et al., 2008, ApJS, 177, 551 140, 149

Miao J., White G. J., Thompson M. A., Nelson R. P., 2009, ApJ, 692, 382 33

Miller G. E., Scalo J. M., 1979, ApJS, 41, 513, a&AA ID. AAA026.155.066 36, 37

Minier V., Burton M. G., Hill T., Purcell C. R., Longmore S., Walsh A. J., Herpin F., 2005, Star Formation from the Small to the Large Scale, 577, 201 3

Minier V., Ellingsen S. P., Norris R. P., Booth R. S., 2003, A&A, 403, 1095 80

Minniti D. et al., 2010, NewA, 15, 433 53, 70, 176

Mizuno A., Onishi T., Yonekura Y., Nagahama T., Ogawa H., Fukui Y., 1995, ApJL, 445, L161 8

Mizuno D. R. et al., 2008, PASP, 120, 1028 71, 80

Moffat A. F. J., Isserstedt J., 1980, A&A, 85, 201 67

Moffat A. F. J. et al., 1998, A&A, 331, 949 67

Moisés A. P., Damineli A., Figuerêdo E., Blum R. D., Conti P. S., Barbosa C. L., 2011, MNRAS, 411, 705 59

Molinari S., Brand J., Cesaroni R., Palla F., 1996a, A&A, 308, 573 26

Molinari S., Brand J., Cesaroni R., Palla F., 1996b, A&A, 308, 573 62, 94

Molinari S., Faustini F., Testi L., Pezzuto S., Cesaroni R., Brand J., 2008a, A&A, 487, 1119 94

Molinari S., Pezzuto S., Cesaroni R., Brand J., Faustini F., Testi L., 2008b, A&A, 481, 345 94

Molinari S., Schisano E., Faustini F., Pestalozzi M., Di Giorgio A. M., Liu S., 2011, A&A, 530, 133 78, 79, 88

Molinari S. et al., 2010a, A&A, 518, L100 78, 79

Molinari S. et al., 2010b, PASP, 122, 314 53, 72, 78, 99, 176

Monnier J. D., Millan-Gabet R., 2002, ApJ, 579, 694 145

Mottram J. C. et al., 2011a, ApJL, 730, L33 101

Mottram J. C. et al., 2011b, A&A, 525, A149 90

Murray N., 2011, ApJ, 729, 133 9

Murray N., Rahman M., 2010, ApJ, 709, 424 56, 102

Neugebauer G. et al., 1984, ApJL, 278, L1 2

Nomura H., Kamaya H., 2001, AJ, 121, 1024 164

Nürnberger D. E. A., Bronfman L., Yorke H. W., Zinnecker H., 2002, A&A, 394, 253 57

O'dell C. R., 2001, ARA&A, 39, 99 8

Oey M. S., Watson A. M., Kern K., Walth G. L., 2005, AJ, 129, 393 35

Offner S. S. R., McKee C. F., 2011, ApJ, 736, 53 101

Oort J. H., Spitzer, Jr. L., 1955, ApJ, 121, 6 33

Ossenkopf V., 1993, A&A, 280, 617 11

Ossenkopf V., Henning T., 1994, A&A, 291, 943 11, 89

Padgett D. L. et al., 2008, ApJ, 672, 1013 140

Palla F., Brand J., Comoretto G., Felli M., Cesaroni R., 1991, A&A, 246, 249 94

Panagia N., 1973, AJ, 78, 929 29, 80

Pilbratt G. L. et al., 2010, A&A, 518, L1 72, 76, 78

Poglitsch A. et al., 2010, A&A, 518, L2 72, 78

Pollack J. B., Hollenbach D., Beckwith S., Simonelli D. P., Roush T., Fong W., 1994, ApJ, 421, 615 11

Porras A. et al., 2007, ApJ, 656, 493 128, 129, 140

Povich M. S., Churchwell E., 2009, The Evolving ISM in the Milky Way and Nearby Galaxies, 53 114, 122, 128, 142, 144, 148

Povich M. S. et al., 2011, ApJS, 194, 14 76, 89, 90, 92, 102, 111, 114, 122, 125, 127, 135, 141, 144, 145, 148, 167, 171, 172, 174

Povich M. S. et al., 2007, ApJ, 660, 346 63

Povich M. S., Whitney B. A., 2010, ApJL, 714, L285 111, 114, 122, 127, 128, 140, 148, 149, 172, 174

Preibisch T., Hofmann K.-H., Schertl D., Weigelt G., Balega Y., Balega I., Zinnecker H., 2000, in IAU Symposium, Vol. 200, IAU Symposium, p. 106P 24

Preibisch T., Schuller F., Ohlendorf H., Pekruhl S., Menten K. M., Zinnecker H., 2011, A&A, 525, A92+ 179

Price S. D., Egan M. P., Carey S. J., Mizuno D. R., Kuchar T. A., 2001, AJ, 121, 2819 72

Purcell C. R., 2007, Thesis, 1 26, 29

Purcell C. R., Hoare M. G., 2010, Highlights of Astronomy, 15, 781 53, 176

Rahman M., Murray N., 2010, ApJ, 719, 1104 57, 174, 178

Rebull L. M. et al., 2007, ApJS, 171, 447 140

Reid M. A., Wilson C. D., 2006, ApJ, 644, 990 23

Rieke G. H. et al., 2004, ApJS, 154, 25 71, 116

Robitaille T. P., 2008, The Stellar Initial Mass Function (38th Herstmonceux Conference), 387, 290 128, 129, 146

Robitaille T. P. et al., 2008, AJ, 136, 2413 57, 117, 150, 155, 157

Robitaille T. P., Whitney B. A., 2010, ApJ, 710, L11 101

Robitaille T. P., Whitney B. A., Indebetouw R., Wood K., 2007, ApJS, 169, 328 90, 91, 98, 119, 122, 123, 130, 168, 185

Robitaille T. P., Whitney B. A., Indebetouw R., Wood K., Denzmore P., 2006, ApJS, 167, 256 86, 90, 92, 119, 126, 130, 131, 132, 133, 146, 147, 149, 168, 171, 172, 177

Rosolowsky E. et al., 2010, ApJS, 188, 123 176

Russeil D., Georgelin Y. M., Amram P., Gach J. L., Georgelin Y. P., Marcelin M., 1998, A&AS, 130, 119 59

Sabbi E. et al., 2007, AJ, 133, 44 167

Saito R. K. et al., 2012, A&A, 537, A107 70, 121

Salpeter E. E., 1955, ApJ, 121, 161 36, 37, 101

Sandell G., Wright M., Forster J. R., 2003, ApJL, 590, L45 23

Scalo J., 1998, The Stellar Initial Mass Function (38th Herstmonceux Conference), 142, 201 37, 144

Scalo J. M., 1986, , 11, 1 37, 144

Schlegel D. J., Finkbeiner D. P., Davis M., 1998, ApJ, 500, 525 123

Schmidt M., 1959, ApJ, 129, 243 40

Schuller F. et al., 2009, A&A, 504, 415 53, 176

Sellgren K., 1984, ApJ, 277, 623 11

Shaver P. A., Goss W. M., 1970, Australian Journal of Physics Astrophysical Supplement, 14, 133 55, 56

Shepherd D. S. et al., 2007, ApJ, 669, 464 138

Shu F. H., Adams F. C., Lizano S., 1987, ARA&A, 25, 23 2, 8, 16, 20, 22

Shu F. H., Ruden S. P., Lada C. J., Lizano S., 1991, ApJL, 370, L31 2, 16

Siess L., Dufour E., Forestini M., 2000, A&A, 358, 593 131

Simon J. D. et al., 2007, ApJ, 669, 327 149

Siringo G. et al., 2009, A&A, 497, 945 96, 178

Skrutskie M. F. et al., 2006, AJ, 131, 1163 71, 116, 120

Smith N. et al., 2010, MNRAS, 406, 952 122, 125, 135, 163, 167, 172

Sobolev A. M. et al., 2007, in IAU Symposium, Vol. 242, IAU Symposium, Chapman J. M., Baan W. A., eds., pp. 81–88 27

Sridharan T. K., Beuther H., Schilke P., Menten K. M., Wyrowski F., 2002, ApJ, 566, 931 94

Stahler S. W., Palla F., 2005, The Formation of Stars 7, 8, 61

Stetson P. B., 1987, PASP, 99, 191 115, 127

Stutzki J., Bensch F., Heithausen A., Ossenkopf V., Zielinsky M., 1998, A&A, 336, 697 9

Sung H., Sana H., Bessell M. S., 2013, AJ, 145, 37 24

Surace J. A. et al., 2004, VizieR Online Data Catalog, 2255, 0 130

Sutherland W., Saunders W., 1992, MNRAS, 259, 413 81

Swinyard B. M. et al., 2010, A&A, 518, L4 88

Thompson M. A., Urquhart J. S., Moore T. J. T., Morgan L. K., 2012, MNRAS, 2286 36

Thompson M. A., White G. J., Morgan L. K., Miao J., Fridlund C. V. M., Huldtgren-White M., 2004, A&A, 414, 1017 35, 105

Tielens A. G. G. M., 2008, ARA&A, 46, 289 63

Torrelles J. M., Gomez J. F., Rodriguez L. F., Curiel S., Ho P. T. P., Garay G., 1996, ApJL, 457, L107 27

Torrelles J. M., Gomez J. F., Rodriguez L. F., Ho P. T. P., Curiel S., Vazquez R., 1997, ApJ, 489, 744 27

Traficante A. et al., 2011, MNRAS, 416, 2932 86

Ungerechts H., Thaddeus P., 1987, ApJS, 63, 645 7

Urquhart J. S., Busfield A. L., Hoare M. G., Lumsden S. L., Clarke A. J., Moore T. J. T., Mottram J. C., Oudmaijer R. D., 2007, A&A, 461, 11 59, 72

Urquhart J. S. et al., 2007, A&A, 474, 891 57, 63, 72, 75

Urquhart J. S. et al., 2008a, A&A, 487, 253 80, 94

Urquhart J. S., Hoare M. G., Lumsden S. L., Oudmaijer R. D., Moore T. J. T., 2008b, Massive Star Formation: Observations Confront Theory ASP Conference Series, 387, 381 72

Urquhart J. S. et al., 2009, A&A, 507, 795 59, 63, 72

Urquhart J. S. et al., 2012, MNRAS, 420, 1656 58, 59

Urquhart J. S. et al., 2009, A&A, 501, 539 72

Urquhart J. S. et al., 2011a, MNRAS, 418, 1689 62

Urquhart J. S. et al., 2011b, MNRAS, 1644 72

Urquhart J. S., Morgan L. K., Thompson M. A., 2009, A&A, 497, 789 35

Urquhart J. S., Thompson M. A., Morgan L. K., White G. J., 2006, A&A, 450, 625 33

Urquhart J. S., White G. J., Pilbratt G. L., Fridlund C. V. M., 2003, A&A, 409, 193 63

van der Tak F. F. S., Menten K. M., 2005, A&A, 437, 947 25

van der Walt J., 2005, MNRAS, 360, 153 28

Varricatt W. P., Davis C. J., Ramsay S., Todd S. P., 2010, MNRAS, 404, 661 120

Vázquez-Semadeni E., 2010, in Astronomical Society of the Pacific Conference Series, Vol. 438, Astronomical Society of the Pacific Conference Series, Kothes R., Landecker T. L., Willis A. G., eds., p. 83 9

Veneziani M. et al., 2013, A&A, 549, A130 110

Walsh A. J., Hyland A. R., Robinson G., Burton M. G., 1997, MNRAS, 291, 261 94

Wang J., Townsley L. K., Feigelson E. D., Broos P. S., Getman K. V., Román-Zúñiga C. G., Lada E., 2008, ApJ, 675, 464 57

Ward-Thompson D., Robson E. I., 1990, MNRAS, 244, 458 88

Welty D. E., Hobbs L. M., Lauroesch J. T., Morton D. C., Spitzer L., York D. G., 1999, ApJS, 124, 465 7

Wheaton W. A., Dunklee A. L., Jacobsen A. S., Ling J. C., Mahoney W. A., Radocinski R. G., 1995, ApJ, 438, 322 138

Whitney B. A., Indebetouw R., Bjorkman J. E., Wood K., 2004, ApJ, 617, 1177 131

Whitney B. A. et al., 2008, AJ, 136, 18 128, 129, 138, 141, 172

Whitney B. A., Wood K., Bjorkman J. E., Cohen M., 2003, ApJ, 598, 1079 131

Whitney B. A., Wood K., Bjorkman J. E., Wolff M. J., 2003, ApJ, 591, 1049 90, 106, 131

Whittet D. C. B., 1992, Science, 257, 1148 12

Whittet D. C. B., Shenoy S. S., Clayton G. C., Gordon K. D., 2004, ApJ, 602, 291 12

Whitworth A. P., Bhattal A. S., Chapman S. J., Disney M. J., Turner J. A., 1994a, A&A, 290, 421 102, 166

Whitworth A. P., Bhattal A. S., Chapman S. J., Disney M. J., Turner J. A., 1994b, MNRAS, 268, 291 35

Whitworth A. P., Zinnecker H., 2004, A&A, 427, 299 115

Williams J. P., Blitz L., McKee C. F., 2000, Protostars and Planets IV, 97 14

Williams J. P., McKee C. F., 1997, ApJ, 476, 166 63

Wolfire M. G., Cassinelli J. P., 1987, ApJ, 319, 850 21

Wood D. O. S., Churchwell E., 1989a, ApJ, 340, 265 30

Wood D. O. S., Churchwell E., 1989b, ApJS, 69, 831 30

Wu J., Evans, II N. J., Gao Y., Solomon P. M., Shirley Y. L., Vanden Bout P. A., 2005, ApJL, 635, L173 104

Yorke H. W., Sonnhalter C., 2002, ApJ, 569, 846 23, 146

Young K. E. et al., 2005, ApJ, 628, 283 140

Zapata L. A., Palau A., Ho P. T. P., Schilke P., Garrod R. T., Rodríguez L. F., Menten K., 2008, A&A, 479, L25 146

Zavagno A. et al., 2010, A&A, 518, L101 35

Zavagno A., Deharveng L., Comerón F., Brand J., Massi F., Caplan J., Russeil D., 2006, A&A, 446, 171 35

Zavagno A. et al., 2010, A&A, 518, L81 35

Zhang Q., Ho P. T. P., 1997, ApJ, 488, 241 146

Zhang Q., Hunter T. R., Brand J., Sridharan T. K., Cesaroni R., Molinari S., Wang J., Kramer M., 2005, ApJ, 625, 864 146

Zinnecker H., Yorke H. W., 2007, ARA&A, 45, 481 2, 21, 25, 101, 162